核理研研究報告　第42&43巻　2010年

ISSN 0385-2105

TOHOKU

RESEARCH REPORT OF LABORATORY OF NUCLEAR SCIENCE

Vol.42&43　2010

TOHOKU UNIVERSITY

Editor

YAMAZAKI, Hirohito

Research Center for Electron Photon Science

Tohoku University

1-2-1 Mikamine, Taihaku, Sendai 982-0826

Japan

Phone: +81, 22-743-3400

Fax: +81, 22-743-3401

Web site: http://www.lns.tohoku.ac.jp/

982-0826 仙台市太白区三神峯1-2-1

東北大学電子光理学研究センター

電話 022-743-3400

Fax 022-743-3401

Preface

The Laboratory of Nuclear Science (LNS) affiliated to Graduate School of Science is aimed at promoting fundamental study and applied research of the various classes of materials in nuclear science. It was reorganized into a new laboratory directly operated by Tohoku University on December 1, 2009, keeping the main facilities unchanged. The laboratory operates two accelerators: a 300 MeV electron LINAC and an electron synchrotron ring capable of boosting and storing electrons up to 1.2 GeV. The accelerators have been in operation for more than 40 years for users not only in Tohoku University but also outside. The present Research Report is the final issue reporting on research activities at LNS for the academic years 2008 and 2009.

Two major experiments, FOREST and NKS2, have been successfully conducted on individual GeV photon beam lines during the period covered in this report. The first data analysis gives the basic performance of FOREST, a 4π electro-magnetic calorimeter. A vertex drift chamber, VDC, has been installed into a neutral kaon spectrometer, NKS2, to replace the previously used inner detectors. And data analysis is now going on for the NKS2 experiment equipped with the new detector system.

The electron LINAC provides also high-intensity electron and photon beams below 50 MeV, which have been used for basic research such as life-time measurements of various nuclei in a certain environment as well as for production of radioactive isotopes.

The capability of the laboratory has been considerably improved by operation of a positron beam line constructed in 2006. The positron beam is produced by utilizing GeV Bremsstrahlung photons with a converter placed in front of a charge sweeping magnet, RTAGX, in GeV-γ Experimental Hall. The positron beam of an energy up to 850 MeV has been used mainly for detector development by many users in various fields such as Astrophysics, High Energy Physics, Nuclear Physics, and Material Science.

I'd like to take this opportunity to thank Jirohta Kasagi, Professor Emeritus of Tohoku University, who stepped down from the position of LNS director at the end of November, 2009 and then retired in March 2010. He had been LNS director for about 12 years and made the best use of his deep understanding of science to lead the laboratory to what it is today. I'm fully convinced that this would not have been possible without his expertise as a scientist and leader.

SHIMIZU Hajime
Director of Research Center for Electron Photon Science

Research Report of Laboratory of Nuclear Science
Volume 42&43, 2010
Contents

I. Nuclear Physics

Ⅰ. Nuclear Physics

(LNS Experiment : #2623, #2640, #2655, #2694)

Current status of meson photoproduction experiments with FOREST

T. Ishikawa[1], H. Fujimura[1], R. Hashimoto[1], S. Kaida[1], J. Kasagi[1], K. Maeda[2], S. Ogushi[1], M. Sato[1], H. Shimizu[1], H. Sugai[1], K. Suzuki[1], S. Takahashi[1], and H. Yamazaki[1]

[1]*Laboratory of Nuclear Science (LNS), Tohoku University, Sendai 982-0826, Japan*
[2]*Department of Physics, Tohoku University, Sendai 980-8578, Japan*

Meson photoproduction experiments with FOREST started in May 2008. The main purpose of the FOREST experiments is to study a nucleon resonance $N^*(1670)$, which is a candidate of antidecuplet pentaquark baryons, via η photoproduction on the neutron. The 8 series of long term FOREST experiments were carried out from May 2008 to November 2009 to measure the differential and total cross sections for the $\gamma p \to \eta p$ and $\gamma d \to \eta pn$ reactions.

The photoproduction data were acquired with two STB circulating currents of 1200 and 920 MeV. The numbers of events collected were 1.88 G, 2.02 G, and 0.20 G events for hydrogen, deuterium, and empty targets in the high energy mode, and those were 100 M, 86 M, and 13 M events in the low energy one. In this report, the newly constructed plastic scintillator hodoscope in front of a backward calorimeter Rafflesia II is described, and the current status of the analysis on the performance of FOREST is presented.

§1. Nucleon resonance $N^*(1670)$

Study of exotic hadrons has been a subject of great interest in nuclear physics since the $S = +1$ baryon resonance Θ^+ was observed at SPring-8/LEPS for the first time [2]. Baryons might have other configurations than 3 valence quarks as a fraction such as 5 quarks, 7 quarks, and so on [1]. Since the observed Θ^+ has a narrow width, the Θ^+ is thought to be a member of antidecuplet pentaquark baryons with the lowest mass [3]. After the LEPS experiment, both the positive and negative results have been reported by many other facilities. Searching for other members is important to establish the pentaquark picture. Recently, a narrow bump was observed at GRAAL [4], LNS [5], and CB-ELSA [6] in η photoproduction on the deuteron. This bump would be attributed to a member of antidecuplet baryons with hidden strangeness since no signature corresponding to this bump has been observed so far in η photo-production on the proton [7].

Fig. 1 shows the baryon octet and anti-decuplet penta-quark baryons. Adjacent two baryons to the Θ^+ are members with hidden strangeness. We call the left one N_5^0 and the right one N_5^+. The N_5^0 can be photoproduced from the neutron because both the charge and U-spin are conserved in the reaction. On the other hand, photoproduction of N_5^+ having a U-spin of $3/2$ from the proton is forbidden since the

U-spins of the photon and the proton are zero and a half, respectively.

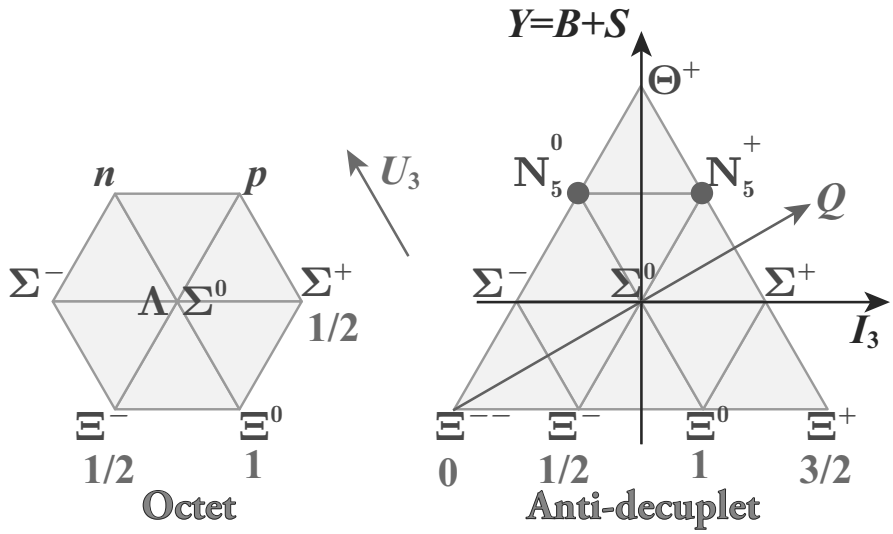

Fig.1. Octet baryons and anti-decuplet penta-quark baryons.

Thus, the nucleon resonance $N^*(1670)$ which is photoexcited only from the neutron and have a heavier mass than Θ^+ is a candidate of N_5^0. The FOREST experiments measure the total and differential cross sections of the $\gamma p \to \eta p$ and $\gamma d \to \eta pn$ reactions to investigate the properties of the relevant resonance: mass, width, spin, parity, and so on.

§2. Electromagnetic calorimeter FOREST

Meson photoproduction experiments were carried out at Laboratory of Nuclear Science (LNS), Tohoku University. Bremsstrahlung photons were used as a beam, being generated with a carbon thread moving into circulating 1200 or 920 MeV electrons in the STretcher booster (STB) ring. Each photon was tagged by detecting the corresponding post-bremsstrahlung electron inside a bending magnet of the ring. The details of the photon tagging counter STB-Tagger II are described elsewhere [10]. The energies of the tagged photon beam ranged from 740 to 1150 MeV for circulating 1200 MeV electrons and from 580 to 880 MeV for 920 MeV ones.

Two γ rays from $\pi^0 \to \gamma\gamma$ or $\eta \to \gamma\gamma$ were detected with an electromagnetic (EM) calorimeter SCISSORS II from 2003 July to December 2005. It consisted of 206 pure CsI crystals, and covered 12.6% of the total solid angle. It was difficult to detect all the γ's coming from π^0 and η decay due to the small solid angle of SCISSORS II. In addition to that the process of multi-π production is dominant in the GeV energy region. There is a huge background made up with wrong combinations of γ's, which do not form a peak of π^0 nor η in the $\gamma\gamma$ invariant mass distribution. To suppress the background due to the wrong combinations, a new EM calorimeter complex FOREST covering 90% of the total was constructed. The details of the design are described elsewhere [11] and the status report of FOREST achieved in 2006–2007 can be found in Ref. [12–15]. Fig. 2 shows the schematic view of FOREST.

Construction of a plastic scintillator hodoscope in front of Rafflesia II (LOTUS) has been much

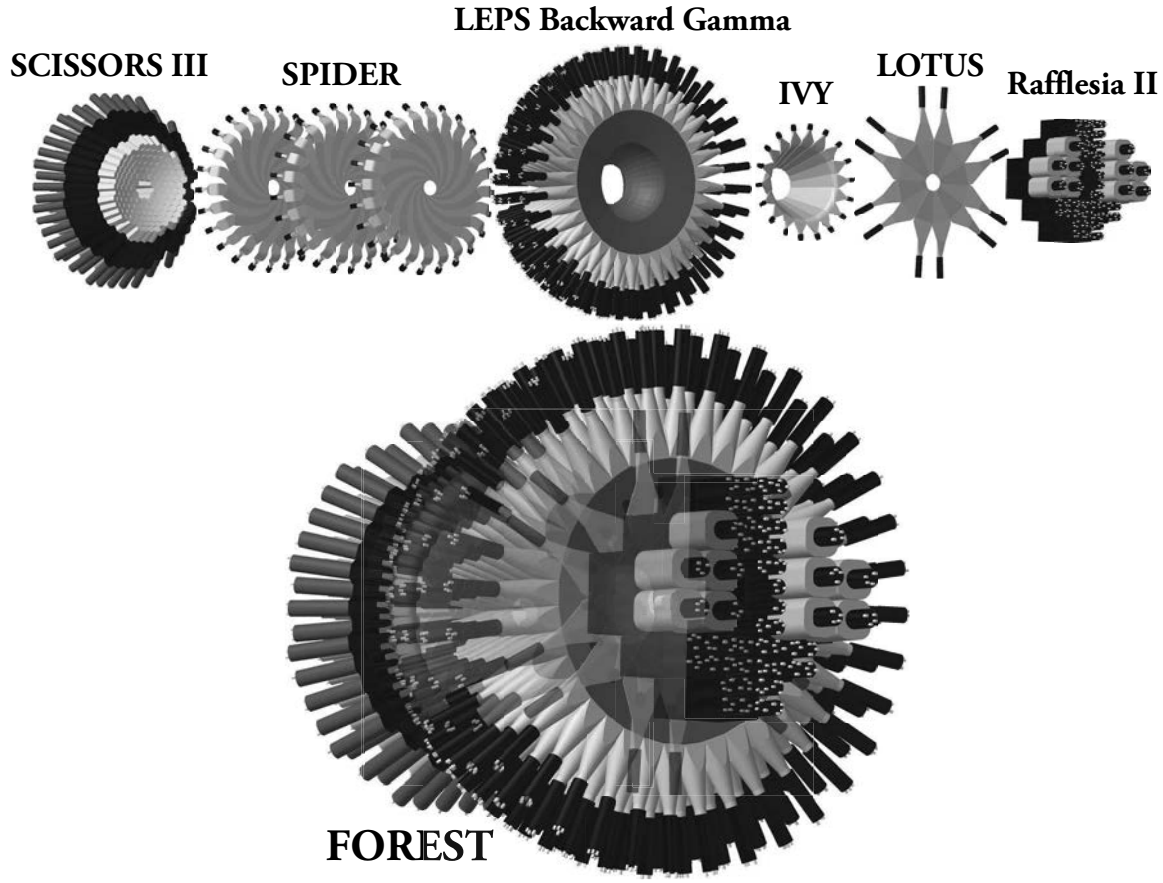

Fig.2. Schematic view of FOREST. It consists of three EM calorimeters: the forward one with 192 pure CsI crystals 'SCISSORS III,' the central one with 252 lead scintillating fiber modules 'LEPS Backward Gamma detector,' and the backward one with 62 lead glass Čerenkov counters 'Rafflesia II.' Plastic scintillator hodoscopes are placed in front of these calorimeters: SPIDER, IVY, and LOTUS.

delayed. This is because nucleons generated by the $\gamma N \to \pi^0 N$ and $\gamma N \to \eta N$ reactions do not come to Rafflesia II, and because the lead glass Čerenkov counters used in Rafflesia II is insensitive to charged hadrons. LOTUS was constructed from 9th to 10th September in 2009, it consists of 12 plastic scintillators with a thickness of 5 mm. To reject the inefficiency coming from a gap, adjacent scintillators have an overlap. Fig. 3 shows the schematic view and photo of LOTUS.

§3. Collected data

The 8 series of long period FOREST experiments were carried out from May 2008 to November 2009 to measure the differential and total cross sections for the $\gamma p \to \eta p$ and $\gamma d \to \eta pn$ reactions. The targets used were liquid hydrogen, deuterium, and empty. The developed FOREST cryogenic target system [16] enables us to change targets within 6 hours. The high speed data acquisition system (DAQ) FOREST-DAQ dedicated to the FOREST experiments [17] was used. The DAQ efficiency was 76% at the trigger rate of 2 kHz.

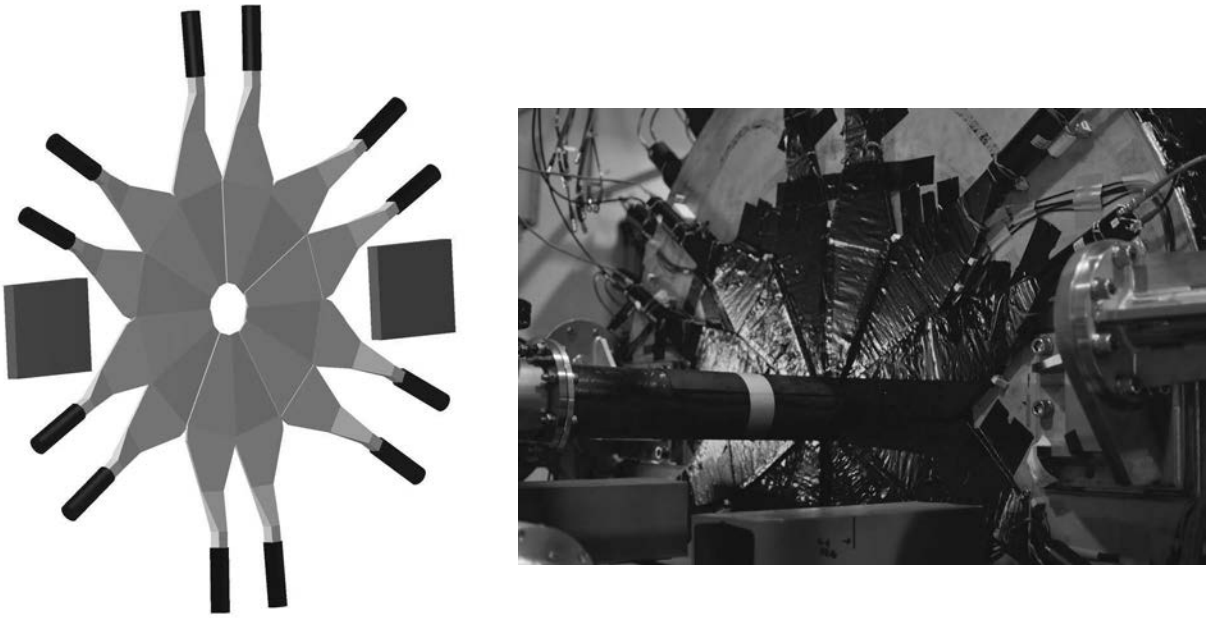

Fig.3. Schematic view and photo of LOTUS. It consists of 12 plastic scintillators with a thickness of 5 mm. Rafflesia II is removed temporarily for the contraction of LOTUS.

The trigger condition for the data acquisition was described as

$$\sum_{i} \{[\mathrm{ST}\ i] \otimes [\#\mathrm{Groups} \geq 2]\}\,. \tag{1}$$

Channels of STB-Tagger II were divided into 16 groups so that the counting rate of each group should be the same, and ST i ($i = 1, \ldots, 16$) denotes an OR signal of each group. Crystal signals of SCISSORS III (S3) were divided into 10 groups, and Lead/SciFi signals of LEPS Backward Gamma detector (BG) were divided into 18 groups. An output signal was generated in an S3 group when a linear sum of signals belonging to it exceeded the threshold. An output signal of a BG group was an OR signal of Lead/SciFi ones belonging to it. The $\#\mathrm{Groups} \geq 2$ stands for the signal which was generated when more than two output signals of S3 and BG groups were generated. Table 1 summarizes the number of spills and events in the FOREST experiments.

Construction of Rafflesia II finished after the 2008A term ended, and the readout of signals from all the counters in Rafflesia II was ready from the 2008C. LOTUS was constructed just before the 2009D started. The data taking with the deuterium target started in the 2008C, and the data for both the hydrogen and deuterium targets were acquired in a term except for a short term 2009C.

§4. Calibration of energy and timing

The calibration of the energy and timing of EM calorimeter modules and plastic scintillators is discussed in this section. The software alignment of the SPIDER plastic scintillators is also described.

Table 1. Numbers of spills and events collected in the FOREST experiments. The circulating electron energy of the STB ring was 1200 MeV for the periods from 2008A to 2009D, and was 920 MeV for the 2009E period. The targets used were liquid hydrogen, deuterium, and empty.

period	hydrogen		deuterium		empty	
	#spills	#events	#spills	#events	#spills	#events
2008A	10.83 k	76.49 M	—	—	3.50 k	30.43 M
2008B	29.17 k	234.48 M	—	—	7.96 k	27.48 M
2008C	25.52 k	388.15 M	11.43 k	282.93 M	19.93 k	73.20 M
2009A	23.16 k	225.14 M	20.28 k	297.43 M	6.00 k	13.58 M
2009B	23.98 k	211.34 M	35.47 k	548.43 M	5.99 k	13.31 M
2009C	27.45 k	254.13 M	—	—	4.93 k	13.84 M
2009D	56.38 k	492.71 M	45.28 k	891.66 M	7.31 k	23.40 M
2009E	34.84 k	100.37 M	22.89 k	85.89 M	16.48 k	12.76 M
total (1200 MeV)	196.48 k	1882.44 M	112.31 k	2017.50 M	55.63 k	195.22 M
total (920 MeV)	34.84 k	100.37 M	22.89 k	85.89 M	16.48 k	12.76 M

4.1 EM calorimeter modules

When a several hundred MeV photon is incident on an EM calorimeter module, it deposits its energy to some modules close to the incident position through the generation of the EM shower. Thus, several modules having energy information of the incident particle is treated as a cluster . A cluster is recognized in the following procedure:

1. the modules whose signals have timing information or exceed a certain threshold are selected,
2. all the modules adjacent to the ones selected in the condition 1 are added, and
3. the set of the modules selected in the conditions 1 and 2 are regarded as a cluster.

The charge of the cluster is determined from the response of the plastic scintillators in front of it.

The energy and momentum direction of the cluster is reconstructed from the energies of the modules belonging to it. The treatment of the SCISSORS III cluster is described in Ref. [18, 19] which has been developed originally for the previous EM calorimeter SCISSORS II. Since the particles generated in the target region are not injected perpendicularly to the front face of a CsI crystal, the reconstructed position assuming the particle is perpendicularly incident on a CsI crystal is modified by taking into account the maximum shower depth (a depth having the maximum energy deposit density) as a function of the particle energy. The energy of the Backward Gamma cluster is given by the sum of the module energies belonging to it, and the momentum direction is determined from the energy weighted average of the module positions (the center of the front face). The treatment of the Rafflesia II cluster is described in Ref. [20]. The energy is simply given by the sum of the module energies. The position given by the energy weighted sum of the module positions is modified in the same way as SCISSORS III.

The energy calibration of the EM calorimeter modules is made so that the π^0 peak in the $\gamma\gamma$ invariant mass distribution should be the π^0 mass where a neutral cluster is assumed as a photon [19–22]. The timing calibration of EM modules is made incorporating the pulse-height time-walk correlation for the photon clusters [23–26].

4.2 Plastic scintillators

A plastic scintillator is insensitive to the photon basically. The energy and timing calibrations of SPIDER and IVY plastic scintillators are made by using positron and electron clusters [27–31]. Charged pion clusters are suppressed by requiring the condition that the timing difference between STB-Tagger II and the associating EM cluster is the same as that of the photon (within $[-1, +1)$ ns) and that the energy leakage exists to adjacent modules. The calibration of LOTUS plastic scintillators are made by using the clusters that the energy deposit to the plastic scintillator is twice as that for the penetration of the minimum ionizing particle [32]. Both the energy and timing are calibrated by taking into account the polar angle dependence of the incident position for three hodoscopes.

4.3 Alignment of the SPIDER plastic scintillators

SPIDER consists of three layers, each of which is made up of 24 identical spiral-shaped plastic scintillators (PS) [13]. The first layer comprises the left-handed PS's, and the others comprise the right-handed ones. The actual placement of the PS's are investigated by using the collected events.

In the original design, a PS in the third layer is placed by rotating $+5^\circ$ about z axis with respect to a PS in the second one. Here, we define the responding PS numbers $n^-_{(1)}$, $n^+_{(2)}$, and $n^+_{(3)}$. When we assume the number of the incident particles is uniform in the azimuthal angle, the ratio of the number of events is expected to be 0.5 between $n^+_{(2)} - n^+_{(3)} \equiv 1$ and $n^+_{(2)} - n^+_{(3)} \equiv 0$ (mod 24). The actual ratio of the number of events are obtained by analyzing the collected data. To suppress the bias coming from the trigger condition for the data acquisition system, the events are analyzed that the number of clusters in BG is larger than 1. Fig 4a) shows the ratio of the number of events between $n^+_{(2)} - n^+_{(3)} \equiv 1$ and $n^+_{(2)} - n^+_{(3)} \equiv 0$. The ratio is almost constant independently of the PS number, and the average one is 0.600. This ratio suggests the rotation angle of the third layer is $+5.63^\circ$ with respect to the second.

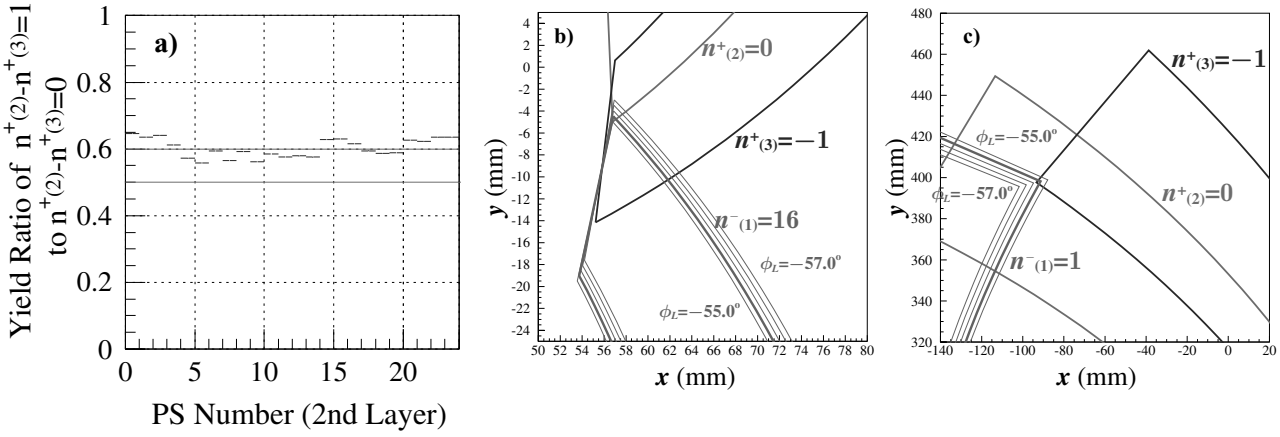

Fig.4. a) Ratio of the number of events between $n^+_{(2)} - n^+_{(3)} \equiv 1$ and $n^+_{(2)} - n^+_{(3)} \equiv 0$ (mod 24). b) Placement of the plastic scintillators in the case $n^-_{(1)} + n^+_{(2)} \equiv 1$ where the relative phase for the first layer $\phi^{(1)}_L$ is from -57.0° to -55.0° with a 0.5° step. c) Placement of the plastic scintillators in the case $n^-_{(1)} + n^+_{(2)} \equiv 1$ where $\phi^{(1)}_L$ ranges from -57.0° to -55.0°.

An overlap between two specified PS's are checked whether the events exist or not that they are

responding. The collected data suggests two PS's in the first and second layers have overlaps in the case $n^-_{(1)} + n^+_{(2)} \equiv 2$–$15$ for $n^+_{(2)} - n^+_{(3)} \equiv 1$, and in the case $n^-_{(1)} + n^+_{(2)} \equiv 1$–$15$ for $n^+_{(2)} - n^+_{(3)} \equiv 0$, respectively. Fig. 4b) and 4c) show the placements of PS's with the relative phase for the first layer $\phi^{(1)}_L$ ranging from -57.0° to -55.0° in the case that $n^-_{(1)} + n^+_{(2)} \equiv 1$ and $n^-_{(1)} + n^+_{(2)} \equiv 1$, respectively. The $\phi^{(1)}_L$ should be larger than -55.0° because the events do not exist that satisfies $n^-_{(1)} + n^+_{(2)} \equiv 16$, and it should be less than -56.0° because the events with three PS's responding in the three layers do not exist that satisfies $n^-_{(1)} + n^+_{(2)} \equiv 1$. Since a very little events are observed with $n^-_{(1)} + n^+_{(2)} \equiv 1$ and $n^+_{(2)} - n^+_{(3)} \equiv 1$, the value of -55.0° is adopted for $\phi^{(1)}_L$. The relative rotation angle of three layers have been determined.

To determine the absolute rotation angle of SPIDER about z axis, the difference of the azimuthal angles given by SPIDER and EM calorimeters are estimated. At first, the azimuthal angle given by SPIDER is compared with that of the SCISSORS III (S3) cluster. To enhance the electron and positron clusters, the events are selected that the number of members having TDC information in the S3 clusters is larger than 2. Fig. 5a) shows the difference distribution of the azimuthal angles given by SPIDER and S3. The shape of the peak is symmetric, and the mean $2.39^\circ \pm 0.01^\circ$ and width $6.60^\circ \pm 0.01^\circ$ are obtained by fitting it with a Gaussian function.

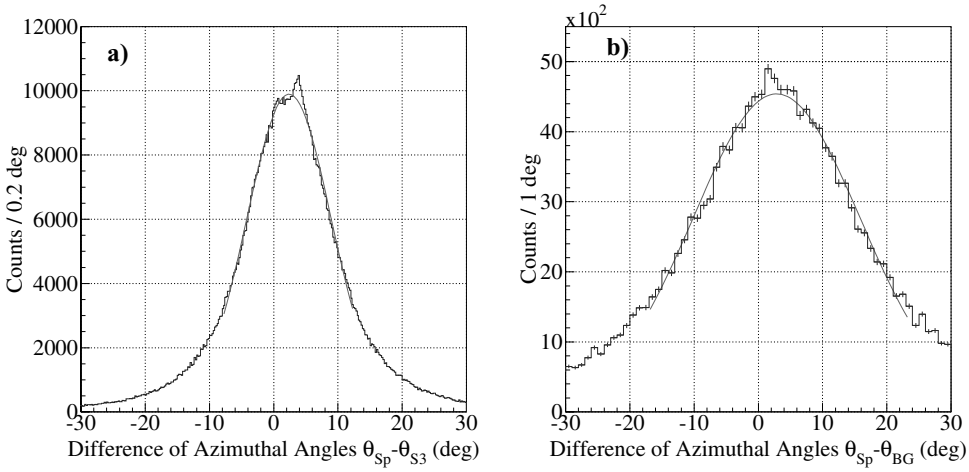

Fig.5. a) Difference distribution of the azimuthal angles given by SPIDER and SCISSORS III. The azimuthal angles are given by an overlap of three PS's of SPIDER and by the position of the front face of the maximum energy crystal in the SCISSORS III cluster. b) Difference distribution of the azimuthal angles given by SPIDER and the η missing momentum. The η missing momentum is calculated from the incident photon energy and the energy and position of two BG clusters.

The azimuthal angle given by SPIDER is also compared with that determined from cluster information of LEPS Backward Gamma detector (BG). The reaction of interest is $\gamma p \to \eta p$. The proton is detected with S3, and two γ's from η decays are detected with BG. The azimuthal angle of the proton is calculated from the η missing momentum. The events that satisfies the following condition are selected:

1. energy of each BG cluster is larger than 100 MeV,
2. the $\gamma\gamma$ invariant mass should be larger than 400 MeV, and
3. η missing mass is less than 1200 MeV.

Fig. 5b) shows the difference distribution of the azimuthal angles given by SPIDER and BG. The shape of the peak is broader than that in the SPIDER and S3 case, but it is also symmetric. The mean and width obtained by fitting the peak with a Gaussian function are $2.84^\circ \pm 0.01^\circ$ and $13.07^\circ \pm 0.01^\circ$, respectively. The means determined by two distributions have similar values, and the average 2.62° of them is adopted for the absolute rotation angle. The details of the analysis on the software alignment of SPIDER are described in Ref. [33, 34].

§5. Detection of nucleons with SCISSORS III

The performance of SPIDER and SCISSORS III has been investigated by using the $\gamma N \rightarrow \eta N$ reaction events. The detection efficiency and precise time of flight reconstruction are discussed in the case that the nucleon is incident on SCISSORS III.

5.1 Detection efficiency

At first, the detection efficiency of SCISSORS III in response to the proton is estimated. Here, the detection efficiency is defined as a probability of detecting the proton which is emitted within the effective coverage of SCISSORS III.

The protons generated in the $\gamma p \rightarrow \eta p$ reaction are used in the analysis from the events taken for the hydrogen target. The events are selected in the the same way as described in §4.3. It is determined from the η missing momentum whether the protons emit or not within the effective coverage of SCISSORS III. Fig. 6 shows the difference of radii at the SPIDER plane given by the SCISSORS III cluster and the η missing momentum under the condition that the protons are detected with SCISSORS III at the radius from 270 to 300 mm. Since the width of the residual distribution is 52.4 ± 0.9 mm, the protons coming to the radius from 270 to 300 mm at the SPIDER plane are selected by using the η missing momentum information.

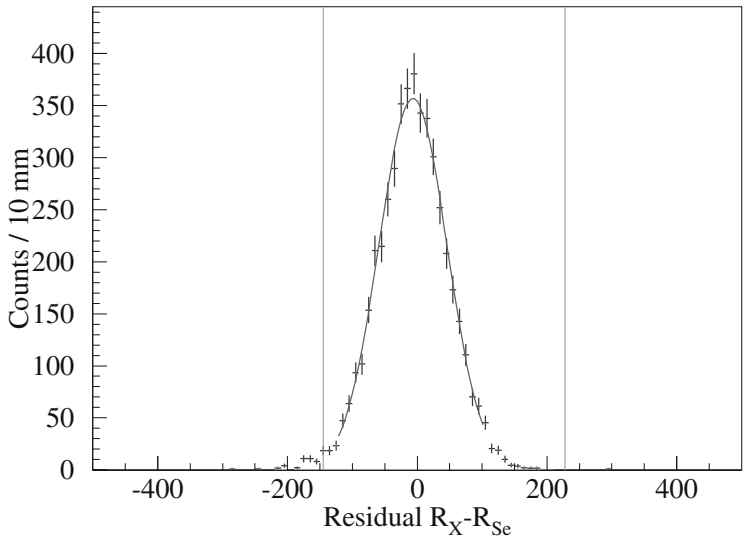

Fig.6. Difference of radii at the SPIDER plane given by SPIDER and the η missing momentum for the hydrogen target where the protons are detected with SCISSORS III at the radius from 270 to 300 mm.

Fig. 7 shows the detection efficiency of SCISSORS III in response to the proton as a function of the momentum. The proton detection efficiency of SPIDER requiring that one of the plastic scintillators responds is also estimated and shown in Fig. 7. Since the low momentum protons stop in the material on the way to SPIDER or SCISSORS III, the efficiency is not unity at the momentum less than 600 MeV/c, and that of SPIDER is higher than that of SCISSORS III especially at the momentum less than 500 MeV/c.

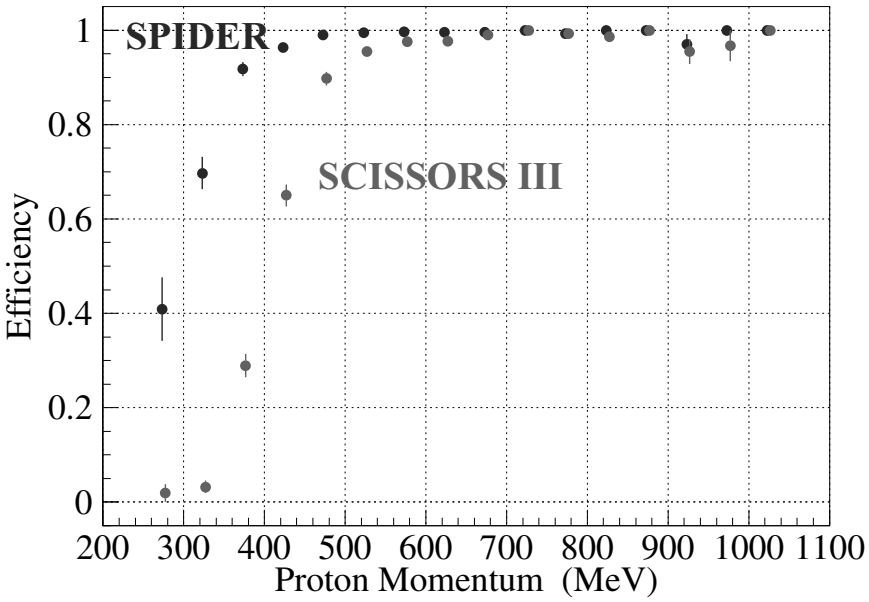

Fig.7. The detection efficiency of SCISSORS III and SPIDER in response to the proton as a function of the momentum. The efficiency of SPIDER is higher than that of SCISSORS III especially in the low momentum region.

As a next step, the detection efficiency of SCISSORS III in response to the neutron is estimated. The neutrons generated in the $\gamma n \rightarrow \eta n$ reaction are selected in the analysis from the events taken for the deuterium target. Since the neutron in the deuteron have some momentum due to the Fermi motion, the residual distribution of radii at the SPIDER plane becomes broader given by the SCISSORS III cluster and the η missing momentum. Fig. 8 shows the difference of radii at the SPIDER plane given by the SCISSORS III cluster and the η missing momentum under the condition that the protons are detected with SCISSORS III at the radius from 270 to 300 mm. The width of the residual distribution is 79.3 ± 1.4 mm.

The neutrons coming to the radius from 270 to 300 mm at the SPIDER plane are selected by using the η missing momentum information. The probability of the neutrons actually coming to the effective area of SCISSORS III in this selection is not unity, and it is found to be 94.1% from a GEANT3 based Monte-Carlo (MC) simulation. The detected nucleons are distinguished by using information on the SPIDER response. The neutron detection efficiency is estimated by taking the proton one into account. Fig. 9 shows the detection efficiency of SCISSORS III in response to the neutron as a function of the momentum. SCISSORS III has a 40% neutron detection efficiency in the high momentum region. This

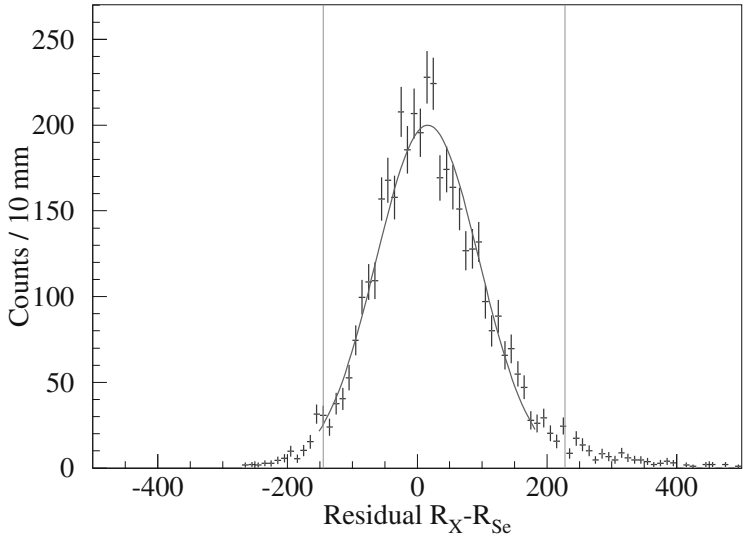

Fig.8. Difference of radii at the SPIDER plane given by SPIDER and the η missing momentum for the deuterium target where the protons are detected with SCISSORS III at the radius from 270 to 300 mm.

behavior can be qualitatively explained by the MC simulation, and the absolute values depend on the threshold values of CsI crystals. The details of the analysis on the detection efficiency of SCISSORS III in response to the nucleons are discussed elsewhere [35].

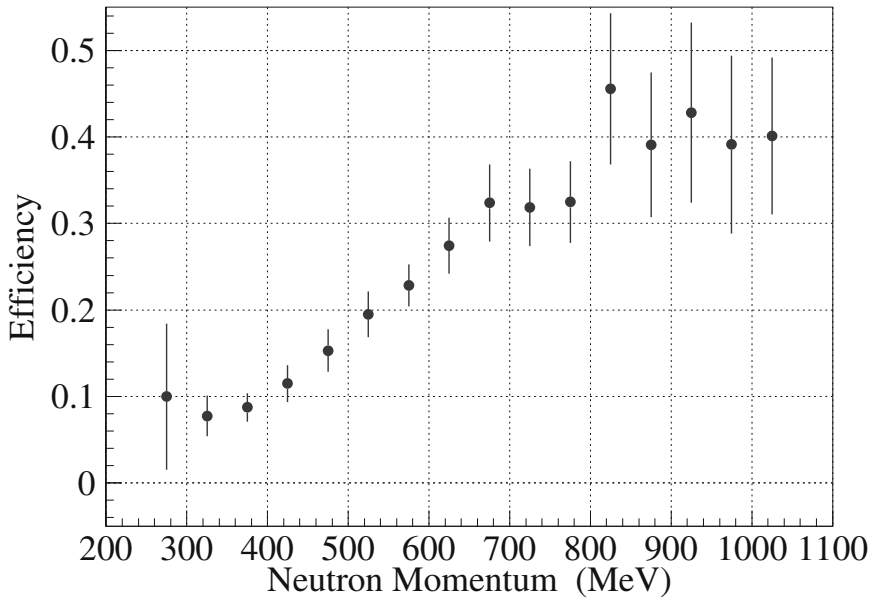

Fig.9. The detection efficiency of SCISSORS III in response to the neutron as a function of the momentum. It increases from 300 MeV/c and reaches 40% at 800 MeV/c.

5.2 Time of flight

The timing calibration of the SPIDER plastic scintillators is made by using electrons and positrons. The reconstructed timing is not good for the proton because the pulse-height time-walk correction is

not appropriate for the proton and because the leading edge of the analog signal might be different for different particles. The reconstructed timing is investigated for the proton generated in the $\gamma p \to \eta p$ reaction. The time of flight determined from the η missing momentum is compared with that from the measured timing with these PS's. Here, the time of flight is calculated as a delayed time from the arrival of the particle having the velocity of the speed of light. The time of flight from the timing measurement is given by the average of the measured timings of the proton arrival with SPIDER PS's t_{Sp} and that between two photons from the η decay detected with BG $t_{\gamma\gamma}$. The η missing momentum and the flight length gives the time of flight of the proton to the SCISSORS III t_p, and the flight length gives that of the particle having the speed of light t_c. Fig. 10 shows the correlation of the time of flights given by the timing measurement $t_{\mathrm{Sp}} - t_{\gamma\gamma}$ and the η missing momentum $t_p - t_c$. The measured timing is earlier than that from the η missing momentum, suggesting the pulse-height time-walk correction is not appropriate for the proton.

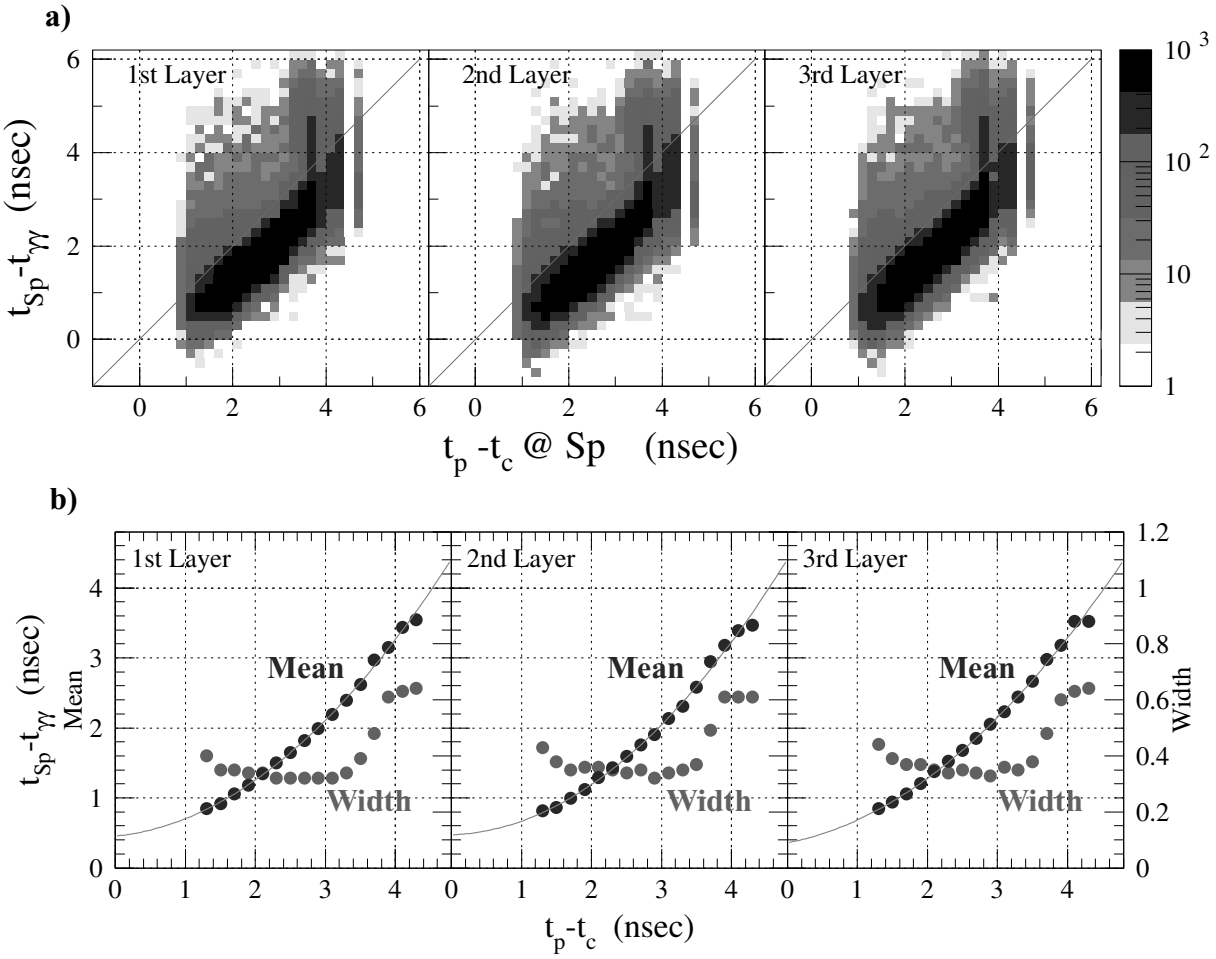

Fig.10. a) Correlation of the time of flights given by the timing measurement $t_{\mathrm{Sp}} - t_{\gamma\gamma}$ and by the η missing momentum $t_p - t_c$. The measured timing is earlier than that from the η missing momentum. b) Mean and width of the time of flight distribution given by the timing measurement as a function of that from the η missing momentum.

The time of flight distribution given by the timing measurement is estimated for every 0.2 nsec of

that from the η missing momentum. The mean and width of the distributions are obtained by fitting with a Gaussian function. Fig. 10b) shows the mean and width of the time of flight distribution given by the timing measurement $t_{\mathrm{Sp}} - t_{\gamma\gamma}$ as a function of that from the η missing momentum $t_p - t_c$. The mean and width behaves similarly for three layers. The mean for the timing measurement μ_{Sp} for each layer is fitted with

$$\mu_{\mathrm{Sp}}(\delta t) = \begin{cases} (0.151 \pm 0.004)\,(\delta t)^2 + (0.098 \pm 0.018)\,\delta t + (0.454 \pm 0.022) & \text{for layer 1,} \\ (0.165 \pm 0.002)\,(\delta t)^2 + (0.028 \pm 0.011)\,\delta t + (0.475 \pm 0.015) & \text{for layer 2, and} \\ (0.136 \pm 0.003)\,(\delta t)^2 + (0.189 \pm 0.015)\,\delta t + (0.360 \pm 0.019) & \text{for layer 3} \end{cases} \quad (2)$$

where $\delta t = t_p - t_c$ is the time of flight determined from the η missing momentum.

Here, we assume that the time of flight determined from the η missing momentum $\delta t = t_p - t_c$ is correct. The precise time of flight of the proton is reconstructed from the difference of measured timings $t_{\mathrm{Sp}} - t_{\gamma\gamma}$ by using the inverse functions of Eq. (2). Fig. 11 shows the timing and momentum resolutions where the time of flight is determined from the timing measurement. The resolutions obtained here is rather the upper limits of them since the time of flight given by the η missing momentum is influenced by the energy and position resolutions of BG.

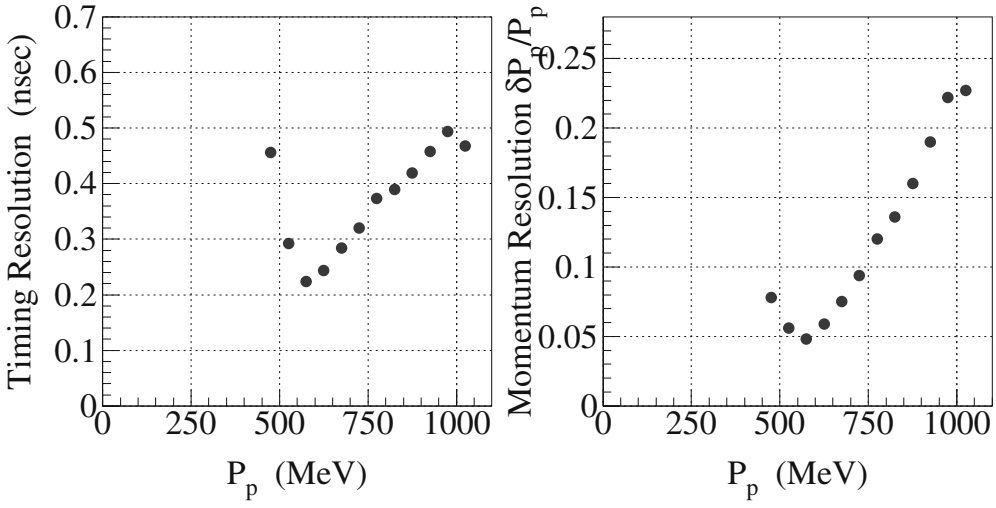

Fig.11. Timing and momentum resolutions where the time of flight is determined from the timing measurement by using the inverse functions of Eq. (2).

The timing calibration of CsI crystals for SCISSORS III is made by using γ's. The reconstructed timing is not also good for the proton because the particles which do not generate the EM shower. The reconstructed timing with SCISSORS III is investigated in the same way for SPIDER. Fig 12 shows the correlation of the time of flights given by the timing measurement $t_{\mathrm{Se}} - t_{\gamma\gamma}$ and the η missing momentum $t_p - t_c$. The measured timing is later than that from the η missing momentum, suggesting the propagation of the scintillation lights are slower than the development of the EM shower.

The mean and width of the time of flight distributions given by the timing measurement are obtained by fitting with a Gaussian function for every 0.2 nsec of that from the η missing momentum. Fig. 10b) shows the mean and width of the time of flight distribution given by the timing measurement

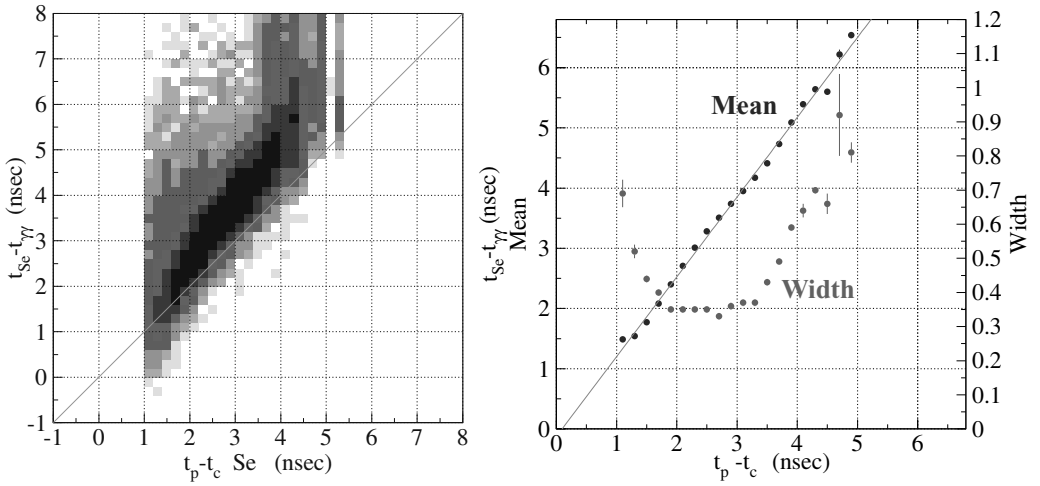

Fig.12. a) a) Correlation of the time of flights given by the timing measurement ($t_{\mathrm{Se}} - t_{\gamma\gamma}$) and by the η missing momentum ($t_p - t_c$). The measured timing is later than that from the η missing momentum. b) Mean and width of the time of flight distribution given by the timing measurement as a function of that from the η missing momentum.

$t_{\mathrm{Se}} - t_{\gamma\gamma}$ as a function of that from the η missing momentum $t_p - t_c$. The mean for the timing measurement μ_{Se} is fitted with

$$\mu_{\mathrm{Se}}(\delta t) = (1.325 \pm 0.003)\,\delta t - (0.124 \pm 0.009) \tag{3}$$

where $\delta t = t_p - t_c$ is the time of flight determined from the η missing momentum.

The precise time of flight can be obtained from that given by the difference of the measured timings $t_{\mathrm{Se}} - t_{\gamma\gamma}$ by using the inverse functions of Eq. (3). Fig. 13 shows the timing and momentum resolutions where the time of flight is determined from the timing measurement of SCISSORS III. The resolutions obtained here is also rather the upper limits of them.

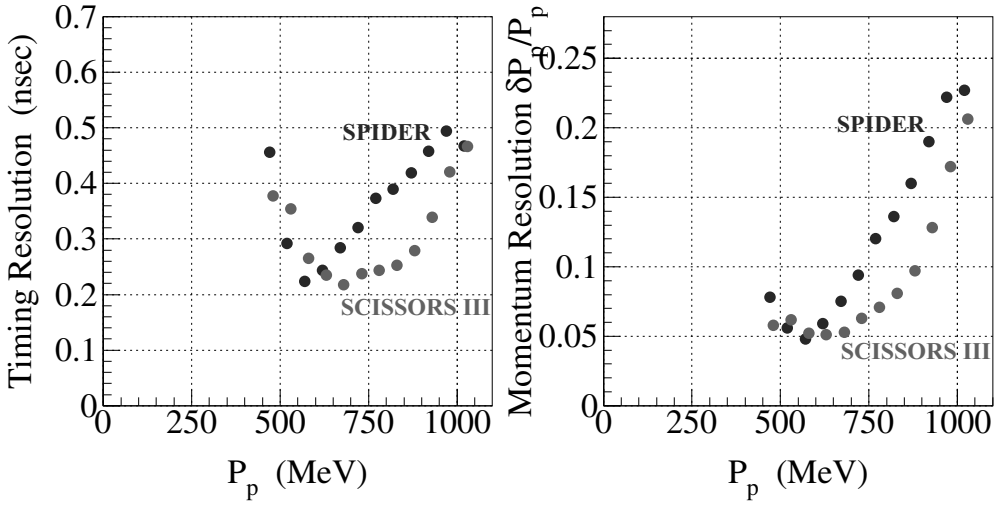

Fig.13. Timing and momentum resolutions where the time of flight is determined from the timing measurement by using the inverse functions of Eq. (3). For comparison, the timing and momentum resolutions from SPIDER information are also plotted.

The time of flight reconstruction for the proton discussed in this subsection works very well. Fig. 14 shows the missing mass M_X distribution for the $\gamma p \to pX$ reaction as a demonstration. Here, the reaction of interest is $\gamma p \to \pi^+\pi^-\pi^0 p$ and the $\pi^0 \to \gamma\gamma$, the proton, and two charged particles detected events are selected. The proton momentum is reconstructed from the time of flight discussed in this subsection. The η and ω meson peaks are clearly observed. The details of the analysis on the precise time of flight determination for the proton are described elsewhere [36].

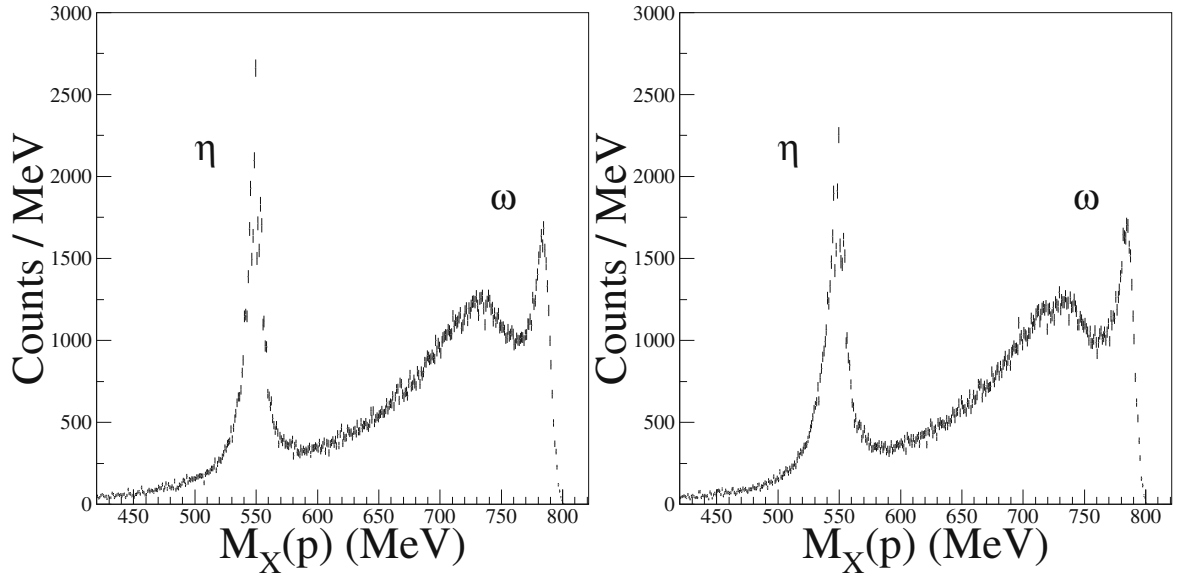

Fig.14. Missing mass M_X for the $\gamma p \to pX$ reaction. The reaction of interest is $\gamma p \to \pi^+\pi^-\pi^0 p$, and the events with the $\pi^0 \to \gamma\gamma$, the proton, and two charged particles are selected. The left and right panels show the missing mass distributions where the four momentum of the proton is reconstructed from the SPIDER and SCISSORS III informations, respectively. The η and ω meson peaks are clearly observed.

To get the precise time of flight for the neutron, the difference of the measured timings with SCISSORS III between the neutron and proton by using the $\gamma N \to \eta N$ reaction events from the data taken for the deuterium target. Fig. 15 shows the mean and width of the time of flight distribution of the nucleons as a function of the momentum. The difference $\delta\mu = \mu_n - \mu_p$ of the means for the neutron and the proton is fitted with

$$\delta\mu(p_X) = (3.78 \pm 0.64)\exp\left(-\frac{p_X^2}{(310.8 \pm 11.2)^2}\right) + \left(\frac{p_X}{1376.2 \pm 31.6}\right)^{(5.0\pm0.3)} \quad (4)$$

as a function of the nucleon momentum p_X given by the η missing momentum.

The difference of the measured timings for the same momentum nucleons is determined. The precise time of flight for the neutron can be obtained from Eqs. (3) and (4). Fig. 16 shows the resolutions of the time of flight and the momentum for the neutron as a function of the momentum. The poor resolutions are thought to come from the ambiguity of the depth of the position that the (n, p) or (n, γ) reactions take a place. The details of the analysis on the precise time of flight determination for the neutron are described elsewhere [37].

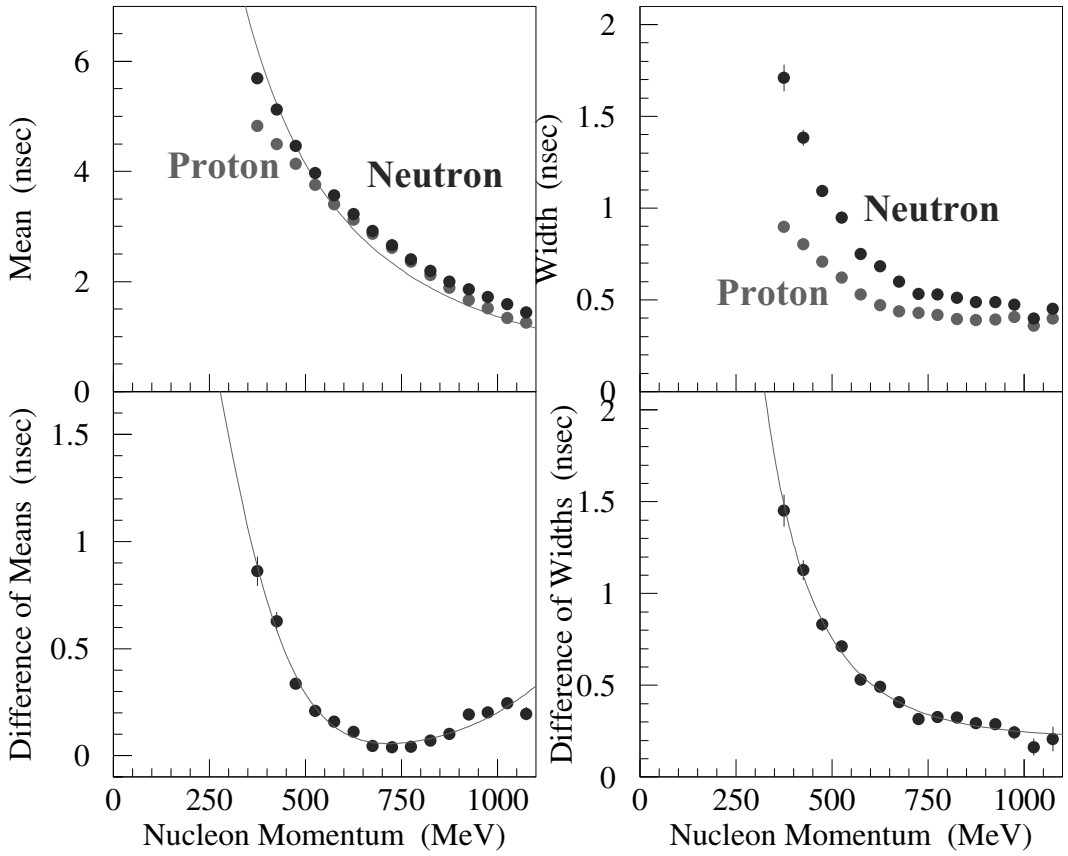

Fig.15. Mean and width of the time of flight distribution of the nucleons as a function of the momentum. The left panel shows the means μ_n and μ_p for the neutron and the proton together with the difference of them $\mu_n - \mu_p$. The right one shows the widths σ_n and σ_p together with the difference of them $\sqrt{\sigma_n^2 - \sigma_p^2}$.

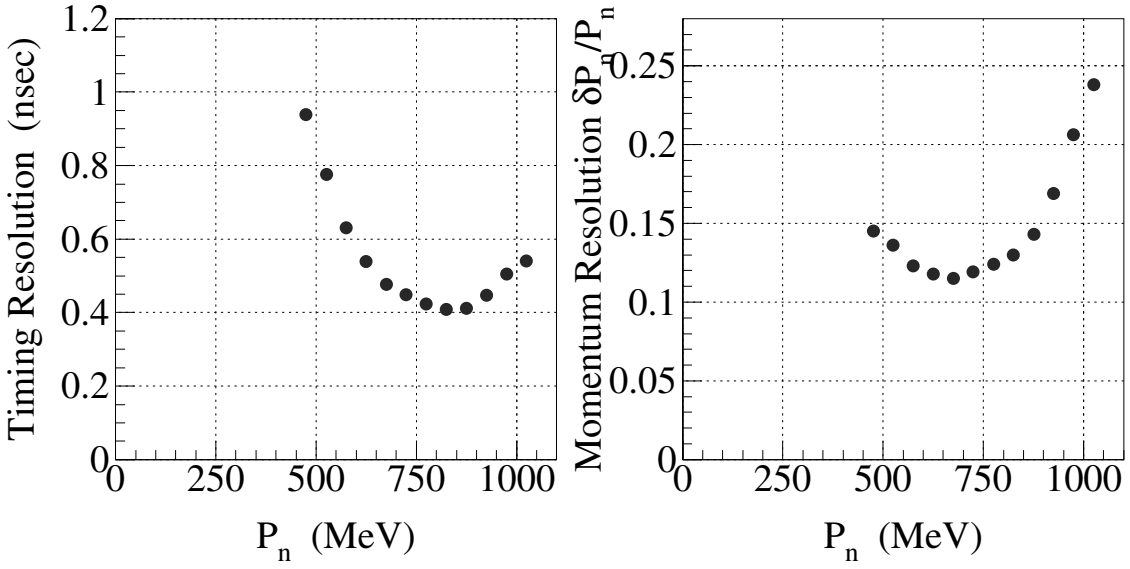

Fig.16. Resolutions of the time of flight and the momentum for the neutron as a function of the momentum.

§6. Summary

The 8 series of meson photoproduction experiments with FOREST has been carried out in 2008 and 2009. The main purpose of the FOREST experiments is to study a nucleon resonance $N^*(1670)$, which is a candidate of antidecuplet pentaquark baryons via η photoproduction on the neutron. A huge amount of the events have been collected at the STB circulating energy of 1200 MeV: 1.88 G for the hydrogen and 2.02 G for the deuterium targets. The energy and timing calibrations of all the detectors are finished. The software alignment of SPIDER and the estimation of the nucleon detection efficiency is completed. The precise determination of the time of flight for the nucleon is also developed. The total and differential cross sections for the $\gamma p \to \eta p$ and $\gamma d \to \eta pn$ reactions will be obtained from these data in the near future.

Acknowledgment

This work was supported in part by Grant-in-Aid for Scientific Research (B) (17340063) and for Specially promoted Research (19002003).

References

[1] M. Karliner and H.J. Lipkin, Phys. Lett. B **575**, 249 (2003) 249; R.L. Jaffe and F. Wilczek, Phys. Rev. Lett. **91**, 232003 (2003).
[2] T. Nakano *et al.*: Phys. Rev. Lett. **91**, 012002 (2003).
[3] D. Diakonov, V. Petrov, M. Polyakov: Z. Phys. A **359**, 305 (1997).
[4] V. Kuznetsov *et al.*: Phys. Lett. B **647**, 23 (2007).
[5] F. Miyahara *et al.*: Prog. Theor. Phys. Suppl. **168**, 90-96 (2007); H. Shimizu: talk at NSTAR2007.
[6] I. Jaegle *et al.*: Phys. Rev. Lett. **100**, 252002 (2008).
[7] T. Nakabayashi *et al.*: Phys. Rev. C **74**, 035202 (2006).
[8] T. Ishikawa *et al.*: Research Report of LNS **40**, Tohoku University, 6 (2008).
[9] T. Ishikawa, H. Fujimura, and H. Shimizu: Internal GeV-γ Analysis Note No. **132** (2009).
[10] T. Ishikawa *et al.*: Nucl. Instr. and Meth. A **622**, 1 (2010).
[11] T. Ishikawa: Internal GeV-γ Analysis Note No. **130$\mathcal{A}$** (2009).
[12] T. Ishikawa *et al.*, Research Report of LNS **39**, Tohoku University, 35 (2007).
[13] T. Ishikawa *et al.*, Research Report of LNS **40**, Tohoku University, 23 (2008).
[14] T. Ishikawa *et al.*, Research Report of LNS **40**, Tohoku University, 19 (2008).
[15] T. Ishikawa *et al.*, Research Report of LNS **41**, Tohoku University, 7 (2009).
[16] R. Hashimoto *et al.*: Research Report of LNS **41**, Tohoku University, 31 (2009).
[17] H. Fujimura *et al.*: Research Report of LNS **41**, Tohoku University, 26 (2009).
[18] T. Ishikawa: Internal GeV-γ Analysis Note No. **36** (2006).
[19] T. Ishikawa: Internal GeV-γ Analysis Note No. **157$\mathcal{F}$** (2009–2010).
[20] T. Ishikawa: Internal GeV-γ Analysis Note No. **150$\mathcal{F}$** (2009–2010).

[21] T. Ishikawa: Internal GeV-γ Analysis Note No. **137**$\mathcal{F}$ (2009).

[22] T. Ishikawa: Internal GeV-γ Analysis Note No. **158**$\mathcal{F}$ (2010).

[23] T. Ishikawa: Internal GeV-γ Analysis Note No. **145**$\mathcal{F}$ (2009).

[24] T. Ishikawa: Internal GeV-γ Analysis Note No. **138**$\mathcal{F}$ (2009).

[25] T. Ishikawa: Internal GeV-γ Analysis Note No. **159**$\mathcal{F}$ (2010).

[26] T. Ishikawa: Internal GeV-γ Analysis Note No. **152**$\mathcal{F}$ (2009–2010).

[27] T. Ishikawa: Internal GeV-γ Analysis Note No. **168**$\mathcal{F}$ (2010).

[28] T. Ishikawa: Internal GeV-γ Analysis Note No. **169**$\mathcal{F}$ (2010).

[29] T. Ishikawa: Internal GeV-γ Analysis Note No. **143**$\mathcal{F}$ (2009).

[30] T. Ishikawa: Internal GeV-γ Analysis Note No. **161**$\mathcal{F}$ (2010).

[31] T. Ishikawa: Internal GeV-γ Analysis Note No. **147**$\mathcal{F}$ (2009).

[32] S. Kaida: Internal GeV-γ Analysis Note No. **193**$\mathcal{F}$ (2010).

[33] T. Ishikawa: Internal GeV-γ Analysis Note No. **167**$\mathcal{F}$ (2010).

[34] T. Ishikawa: Internal GeV-γ Analysis Note No. **174**$\mathcal{F}$ (2010).

[35] T. Ishikawa: Internal GeV-γ Analysis Note No. **175**$\mathcal{F}$ (2010).

[36] T. Ishikawa: Internal GeV-γ Analysis Note No. **172**$\mathcal{F}$ (2010).

[37] T. Ishikawa: Internal GeV-γ Analysis Note No. **173**$\mathcal{F}$ (2010).

(LNS Experiment : #2633, #2638, #2658)

Status of the NKS2 experiment

B. Beckford[1], A. Chiba[1], D. Doi[1], J. Fujibayashi[1], T. Fujii[1], Y.Fujii[1], K. Futatsukawa[1], T. Gogami[1], O. Hashimoto[1], Y.C. Han[2], K. Hirose[3], S. Hirose[1], R. Honda[1], K. Hosomi[1], A. Iguchi[1], T. Ishikawa[3], H. Kanda[1], M. Kaneta[1], Y. Kaneko[1], S.Kato[1], D. Kawama[1], T. Kawasaki[1], S. Kiyokawa[1], T. Koike[1], K. Maeda[1], K.Makabe[1], N.Maruyama[1], M. Matsubara[1], K. Miwa[1], Y. Miyagi[1], S. Nagao[1], S.N. Nakamura[1], A. Okuyama[1], K. Shirotori[1], K. Sugihara[1], K. Suzuki[3], T. Tamae[3], H. Tamura[1], N. Terada[1], K. Tsukada[1], K. Yagi[1], F. Yamamoto[1], T.O. Yamamoto[1], H. Yamazaki[3], and Y. Yonemoto[1]

[1]*Department of Physics, Tohoku University, Sendai, 980-8578, Japan*
[2]*School of Nuclear Science and Technology, Lanzhou University, Lanzhou, 730000, China*
[3]*Laboratory of Nuclear Science, Tohoku University, Sendai, 982-0826, Japan*

We will report the current status of NKS2 experiments. In this report, we focus the results of LNS experiment number 2633, 2638, and 2658. Those are including a commissioning run after upgrading of inner detectors of NKS2 and data taking of physics run.

§1. Introduction

The elementary photo-strangeness production process had been intensively studied based on the high-quality data of the charged kaon channel, $\gamma + p \rightarrow K^+ + \Lambda(\Sigma^0)$. However, there was no reliable data for the neutral kaon channel $\gamma + n \rightarrow K^0_S + \Lambda$ and the theoretical investigations suffer seriously from the lack of the data. In order to have reliable data for the neutral kaon photo-production data, we have been putting an effort to measure the $\gamma + n \rightarrow K^0_S + \Lambda$ process in the $\pi^+\pi^-$ decay channel, using a liquid deuterium target and a tagged photon beam in the threshold region at Laboratory of Nuclear Science, Tohoku University. We have already taken exploratory data quite successfully with use of Neutral Kaon Spectrometer (NKS) at LNS-Tohoku in 2003 and 2004. We intend to extend the previous experiment by considerably upgrading the original neutral kaon spectrometer to a completely new neutral kaon spectrometer (NKS2), fully replacing the spectrometer magnet, tracking detectors and all the trigger counters. The new spectrometer, NKS2, has significantly larger acceptance for neutral kaons compared with NKS, particularly covering forward angles and much better invariant mass resolution. The data taking was done in 2006 and 2007 and its results will be shown in the doctoral thesis of Kenta Futatsukawa.

We started NKS2 upgrade project after we had finished the construction of NKS2 spectrometer. The goal of the experiment is further investigate strangeness photo-production via the neutral channel in the threshold region. In this particular proposal, we aim to measure

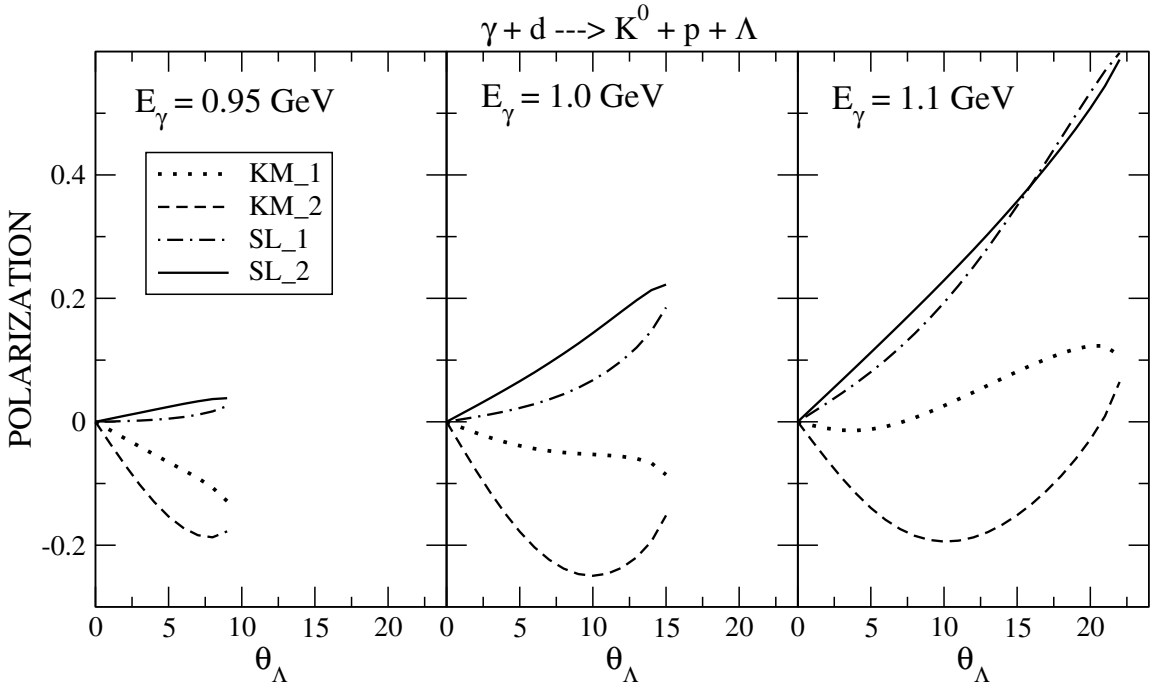

Fig.1. Angular dependence of Λ polarization in Lab. frame in spectator kinematics. The unit of horizontal axis is degree. The calculation is done by P. Bydzovsky.

- $\boldsymbol{K}^0_S + \Lambda$ coincidence events with reasonable statistics, and
- Determine the sign of Λ recoil polarization.

A coincidence measurement of $\boldsymbol{K}^0 + \Lambda$ requires four track re-construction of decay particles, because we will use decay mode of $\boldsymbol{K}^0_S \to \pi^+ + \pi^-$ and $\Lambda \to \boldsymbol{p} + \pi^-$ for the event. In order to maximize the acceptance for the four track events under the NKS2 setup, we had designed and installed a new inner detector package, Vertex Drift Chamber (VDC)and Inner Hodoscope(IH). The VDC allows us to reconstruct 3D trajectories in the target region with its 8-layer stereo-wire configuration. The geometrical acceptance for $\boldsymbol{K}^0$ + Λ coincidence measurements is expected to increase by a factor of about 7 compared to the Neutral Kaon Spectrometer 2 (NKS2) prior to the upgraded since the two out of four tracks can be identified and momentum-analyzed, requiring detection of the two particles only by the inner detector system.

The advantages of measuring Λ and $\boldsymbol{K}^0$ concurrently, in the $\gamma + \boldsymbol{n} \to \boldsymbol{K}^0 + \Lambda$ reaction are as follows: Firstly, it will allow the derivation of the invariant masses of the kaon and lambda hyperon simultaneously and uniquely identify the reaction. The second advantage will be the elimination of a Fermi motion correction of the neutron in deuteron. Also, the reaction plane will be well defined ensuring that the Λ recoil-polarization can be measured. The polarization measurement of single Lambda hyperons, particularly its sign determination, would give us enough information as suggested by recent calculation shown in Fig. 1. Lastly, Λ events from $\gamma + \boldsymbol{p}$ and $\gamma + \boldsymbol{n}$ and reactions can be separated; This shall reduce possible background contamination from incorrectly combined pions.

§2. Experimental Setup

The experimental setup consists of beam line and the NKS2 spectometer. There are tagged photon system to measure photon energy and timing and a sweep magnet which removes background.

The NKS2 consists of an array of detectors centered on a target housed in a vacuum chamber. The target is surrounded by a Vertex Drift Chamber (VDC) and a plastic Inner Hodoscope (IH), which is the start trigger for the time of flight, and both are enclosed in a Cylindrical Drift Chamber (CDC). Those detectors reside within the poles of a dipole magnet with 680 mm gap. An outer plastic scintillator hodoscope (OH), the stop trigger for time of flight measurement, is then placed outside the drift chambers. Lastly, in order to improve trigger efficiency, and reduce the level of background as a result of pair production from the photon beam, scintillator Electron Veto (EV) detectors are installed on a zero degree plane perpendicular to the beam line. The pair produced e^+e^- are only generated in the forward direction. However, only the EV counters setup at the backward angles are used in the trigger to minimize the bias to the acceptance of the NKS2 spectrometer at the forward angles.

§3. Inner Detectors and Its Commissioning

The inner detectors consist from Vertex Drift Chamber (VDC) and Inner Hodoscope (IH). We applied the beam time for NKS2 upgraded including a commissioning of the inner detectors. The proposal was

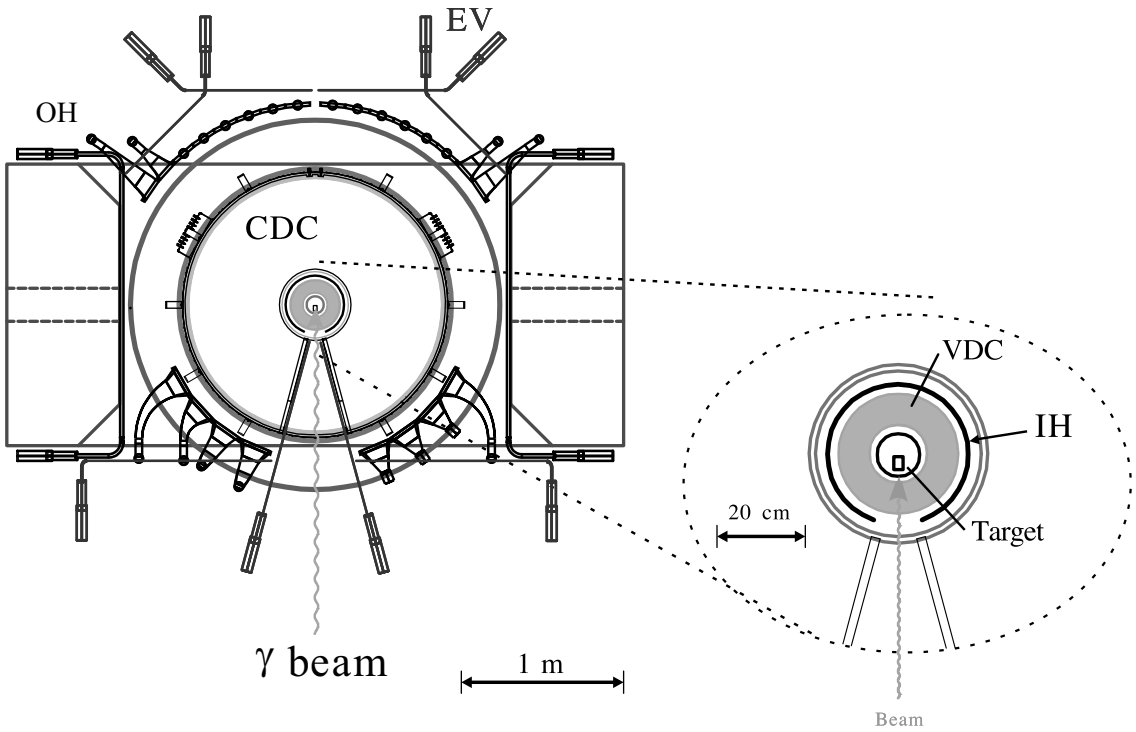

Fig.2. The schematic view of NKS2 after upgrade. This is a slice of the spectrometer on the beam plane. Inner detectors are replaced.

accepted and the experiment is assigned as No. 2633 (test of NKS2 vertex chamber) and No. 2638 (Study of Neutral Kaon Photoproduction on Deuterium Target by NKS2). We found some problems on chambers during the beam time.

- Oscillation on read-out card of chambers
- Strange TDC distribution of chambers

We decided to take an time to study and to fix the problem before starting of physics run. We applied the other beam time for the test (No. 2658). In the following subsections, we describe the inner detectors (VDC and IH) and result of test experiment.

3.1 VDC

The Vertex Drift chamber is an inner detector. It is positioned inside Cylindrical Drift Chamber (CDC) and due to its unique design, will be capable of performing three-dimensional tracking. The diameter of the vertex drift chamber is 330 mm with a height of 506 mm and the solid angle is about three times of CDC. The detector is composed 626 sense wires placed at stereo angles such that they create eight layers in a $U, U', V, V', U, U', V, V'$ structure. The cells are trapezoidal in shape with a half-cell size of approximately 4 mm. Each sense wire was made from gold plated tungsten with a diameter of 20 microns. Figure 3 is a picture of VDC. Table 1 shows the cell size and stereo angle for all of layers.

The choice of drift gas is Ar+Ethane (50:50) which is also the same gas choice of CDC. A cosmic-ray test of the VDC performance yielded a tracking efficiency $\geq 99\%$ for all layers. A position resolution (residual to track) ranging from $150-200$ μm as shown in Fig. 4.

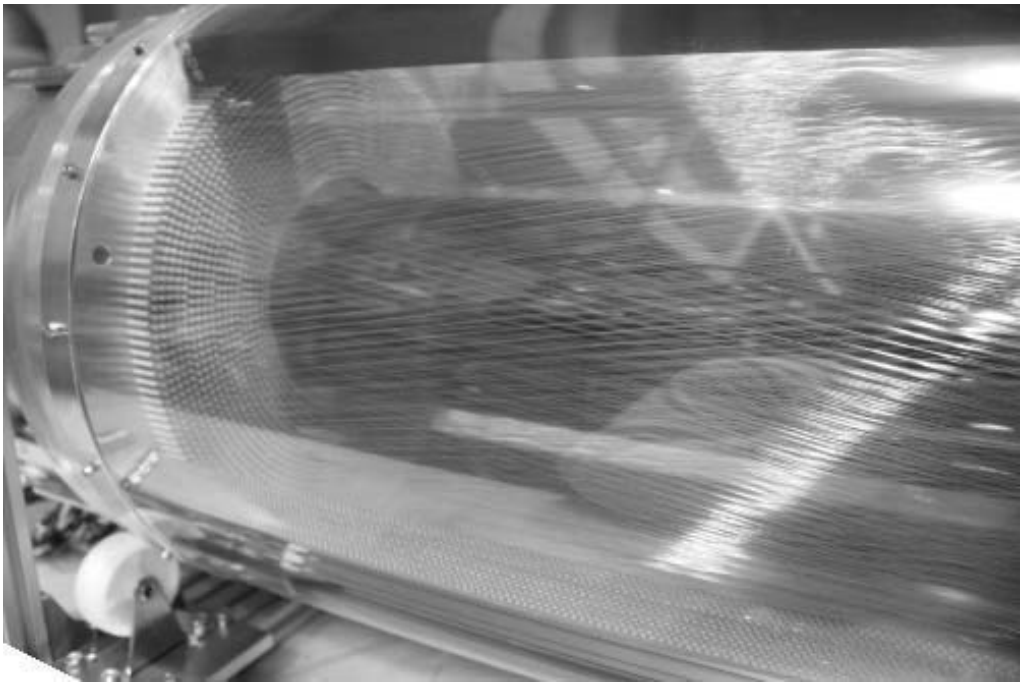

Fig.3. Picture of VDC. It is placed sideways for maintenance.

Table 1. VDC cell size and wire specifications.

group number	layer number	half-cell size radial [mm]	half-cell size azimuthal [mm]	stereo angle [deg]	number of sense wires
1	1 (U)	4	3.89	6.35	59
2	2 (U')	4	4.31	7.03	59
3	4 (V)	4	3.88	7.72	72
4	3 (V')	4	4.23	8.41	72
5	5 (U)	4	3.88	9.09	85
6	6 (U')	4	4.18	9.77	85
7	7 (V)	4	3.92	10.44	97
8	8 (V')	4	4.18	11.12	97
				TOTAL	626

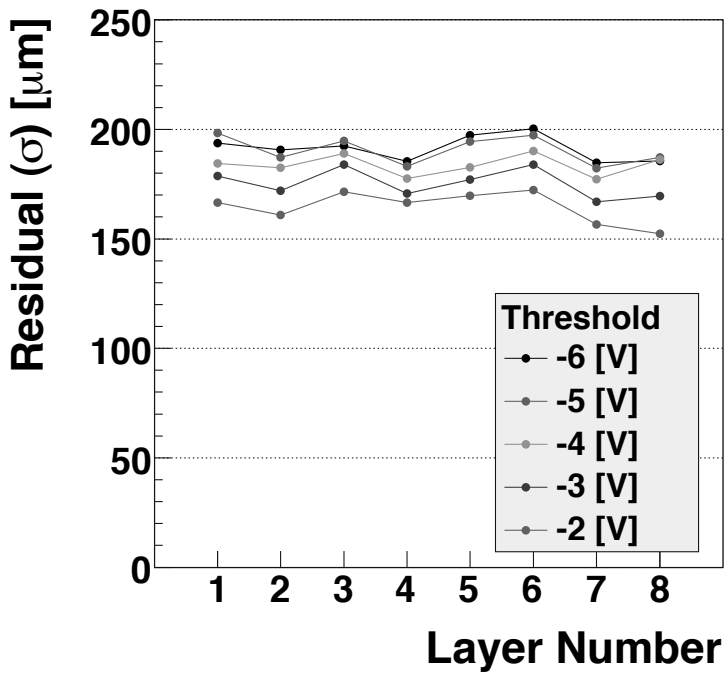

Fig.4. Vertex drift chamber (VDC) position resolution for all layers (1-8), as a function of threshold setting. A position resolution (residual to track) is less than 200 μm.

A read-out card, GNA-220, is designed to fit a space at inner detector region. GNA-220 has 32 channel inputs/digital outputs and used an ASD chip (SONY CXA3183Q). The threshold voltage V_{th} = -1 V corresponds to 8.93×10^{-3} pC in GNA-220. On the other hand, the charge of the VDC signal is estimated about 0.14−0.16 pC. That means that the VDC signal will not be killed even if we set the maximum threshold value -7 V.

We designed symmetric wire alignment in VDC. Therefore, there is the wire material on the beam line in upstream of the target. In order to increase the data acquisition capabilities the wires in the upstream direction along the beam line have been removed. As the result, the order of material in upstream region is similar with before.

3.1.1 Inner Hodoscope (IH)

The inner hodoscope counter has also been re-designed. The size of each segment was specifically designed considering the probability of multiple hits on one segment and the PMT beat operational singles rate. To satisfy the wanted requirement of a less than 2% probability of multi-hits and a singles rates $\leq$ 200 kHz. The reduction of multiple hits on one counter is necessary to avoid discarding $\pi^+\pi^-\pi^-p$ events, where two or more decay particles transverse the same IH segment.

A GEANT4 simulation of the detectors performance was undertaken. The simulation conditions used bremsstrahlung photons is in the energy range of 5MeV to 1.2GeV. The results were a singles rate of 160 kHz at a tagged photon rate of roughly 2MHz. The inner hodoscope is composed of 20 segments consisting of 5 mm thick plastic scintillators with a height of 380 mm, light guides and photomultipliers that are arranged to enclose the VDC. The angle coverage of IH is shown in Table 2. Figure 5 shows the IH counters mounted on VDC body.

It is essential for providing the initial trigger signal for Time-Of-Flight particle identification. We

Fig.5. Picture of IH viewed from downstream side. The counters are mounted on VDC body. The PMT's are connected both edge of the scintillator, excepting 1L and 1R. Those have only one side read-out to avoid hit of photo beam.

Table 2. IH angle coverage.

Segment ID	angle coverage [deg]	Segment ID	angle coverage [deg]
L1	-4 – +4	R1	+4 – -4
L2	4 – 10	R2	-4 – -10
L3	10 – 18	R3	-10 – -18
L4	18 – 30	R4	-18 – -30
L5	30 – 54	R5	-30 – -54
L6	54 – 78	R6	-54 – -78
L7	78 – 102	R7	-78 – -102
L8	102 – 126	R8	-102 – -126
L9	126 – 144	R9	-126 – -144
L10	144 – 162	R10	-144 – -162

require that will be operational within a strong magnetic field. The final design utilizes a fine mesh dynode type photomultiplier, HAMAMATSU H6152-01B, that operates on a negative high voltage setting.

The new IH has two read-out and it makes us better energy deposit information than one side read-out, because we want to make particle identification by dE/dx instead of TOF for charged particles that will not make a hit on OH. Its capability is studied from data and the results shows that it is possible [1].

3.2 Results from the commissioning run

In this sub-section, we will explain what we tried in the commissioning run and its results. The summary of the commissioning run and related works are shown in the following list.

- 2008/Sep

  The first commissioning run of VDC (LNS Exp. No. 2633).
- 2008/Nov and Feb

  Physics data taking with Liq. D2 target (LNS Exp. No. 2638).
- 2009/Jun

  VDC stand-alone-test with changing the gas mixture with ethanol (LNS Exp. No. 2658).
- 2009/Summer shutdown

  Ground toughness modification of the chambers.
- 2009/Sep

  Beam rate study after the ground toughness (LNS Exp. No. 2658).
- 2009/Feb to Mar

  Checking AMT-VME control programs and modification of programs. Test for the effect of modification of AMT-VME with using pulse generator signal.
- 2010/Apr

  Beam rate study after the modification of the AMT-VME DSP program (LNS Exp. No. 2658).
- 2010/Jun and Jul

  Trigger test as a function of beam rate and physic run (LNS Exp. No. 2638).

In 2008, we met two problems of chambers. The first one is the oscillation of read-out card (we call it Amp-Shaper-Discriminator (ASD) card). In the situation of NO BEAM, the oscillation level was low and acceptable. The oscillation of CDC in some channels, however, occurred during data taking. Additionally, we found many channels of VDC has larger number of hit in higher beam rate. Figure 6 shows the hit patter on VDC with different threshold of ASD card. We thought that all of phenomena was due to a oscillation that appeared in high beam rate (more than 1 MHz).

That makes an bad effect to DAQ rate because a large event size makes a rate of trigger accepted lower due to longer read-out time from the TDC module. The worst case of DAQ efficiency was about 10 to 20% with 2 to 3 MHz of beam rate. The second problem is that we see a distribution of TDC in a region of large value. We expect that the TDC distribute only in a rage of 0 to a channel corresponding to a common stop timing. At that time, it was dominant in the collaboration that the unexpected distribution was also due to a oscillation.

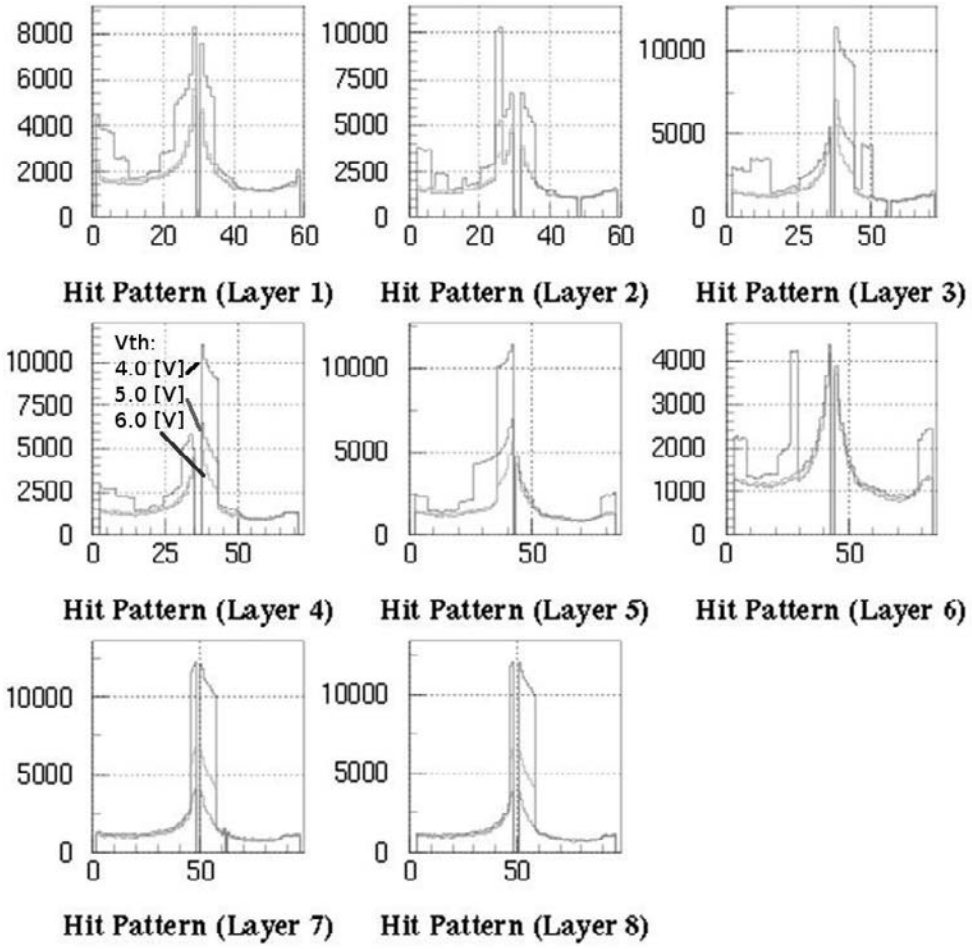

Fig.6. Layer hit patter of VDC from run 2009/Sep. Horizontal axis is the wire number of each layer. The vertical axis is total number of hit in a run. Data from different three setting of threshold are shown. We see the large number of hit around center and edge of histogram (corresponding to beam line). However, layer 6 has a bump around side of chamber (around channel 20 to 30) and its region is expected lower single rate.

In the beam time of 2009/Jul, we tested VDC as a stand-alone system. VDC is mounted to CDC body in the spectrometer. We needed to separate the origin of problem. Because there was a discussion that the VDC had a oscillation and it make CDC something bad with beam. Additionally, we tested an ethanol effect to the oscillation following a suggestion from one of KEK E325 collaborator (They could not operator a small size of drift chamber without ethanol). The results say that VDC itself was quiet with higher beam rate (3 MHz) and we didn't see larger size of background under the TDC peak. However, TDC distribution showed two continuum around 10^5 and 10^6 of channel number.

In the summer shutdown, we exchanged CDC shield plate on the top side and added shield cover for each ASD card to make the ground line more toughness. We didn't see any oscillation around lower limit of the threshold setting of ASD card.

In the beam time of 2009/Sep, we test whole NKS2 system. This is the test for beam rate dependence of DAQ rate. The situation of large event size was not change even if we had made a better ground line connection of ASD card.

We checked number of hit distribution for two TDC region. One is in the expected range, and the other one is in unexpected range. Figures 7 and 8 show the number of hit per event as a function of wire number for each layer. This data is taken with normal trigger for physics run with 3 MHz of beam rate.

The total number of hit (solid circle) shows a bump on not only VDC but also CDC. After TDC range cut, the distribution with a range of TDC channels expected (solid square) show reasonably smooth. It is clear that the unexpected region (solid triangle) made large event size.

The TDC distribution is shown in Fig. 9. The region which we expected hit in TDC channel is 0 (common stop timing) to about 1300 (trigger timing). We see two continuum in the whole TDC distribution (0x10000 to 0x1FFFF and 0xF0000 to 0xFFFFF). We found that those region was corresponding to negative TDC region due to record of hit after common stop. To remove those record in the module, we modified a DSP program in AMT-VME, that set some parameters of the AMT chip, formatted data from the chip, and send to a VME memory. In the original DSP program, the time window was fixed and cover negative time region (about 50 μs!). A new program has a capability of changing a time window by setting values on VME memory. The summary of problem and solution is reported in Ref. [2].

We had test beam time for trigger rate study to check the effect by modification of AMT-VME module in 2010/Apr. Before the modification of AMT-VME, the trigger accepted is saturated about 300 Hz and the DAQ efficiency was singularly bad. After modification, it is achieved to have 90 (80)% of DAQ efficiency at 2 (3) MHz of beam rate (see Fig. 10). The trigger configuration of the test included signal of Electron Veto. When we included electron veto signal in the trigger, we lose an acceptance in forward region and it might make a bias in the data.

Figure 10 shows an effect of Electron Veto (EV) in the trigger after the modification of AMT-VME. We tested two combination of triggers. The first one used all of EV counters (EV1 to EV4). The second one used EV counters of upstream side (EV3 and EV4).

When we used all of EV counters in the trigger, the DAQ efficiency is about 90% at beam rate of 2.0 MHz. However, the charged particle veto in the downstream side will kill pion and proton in the data

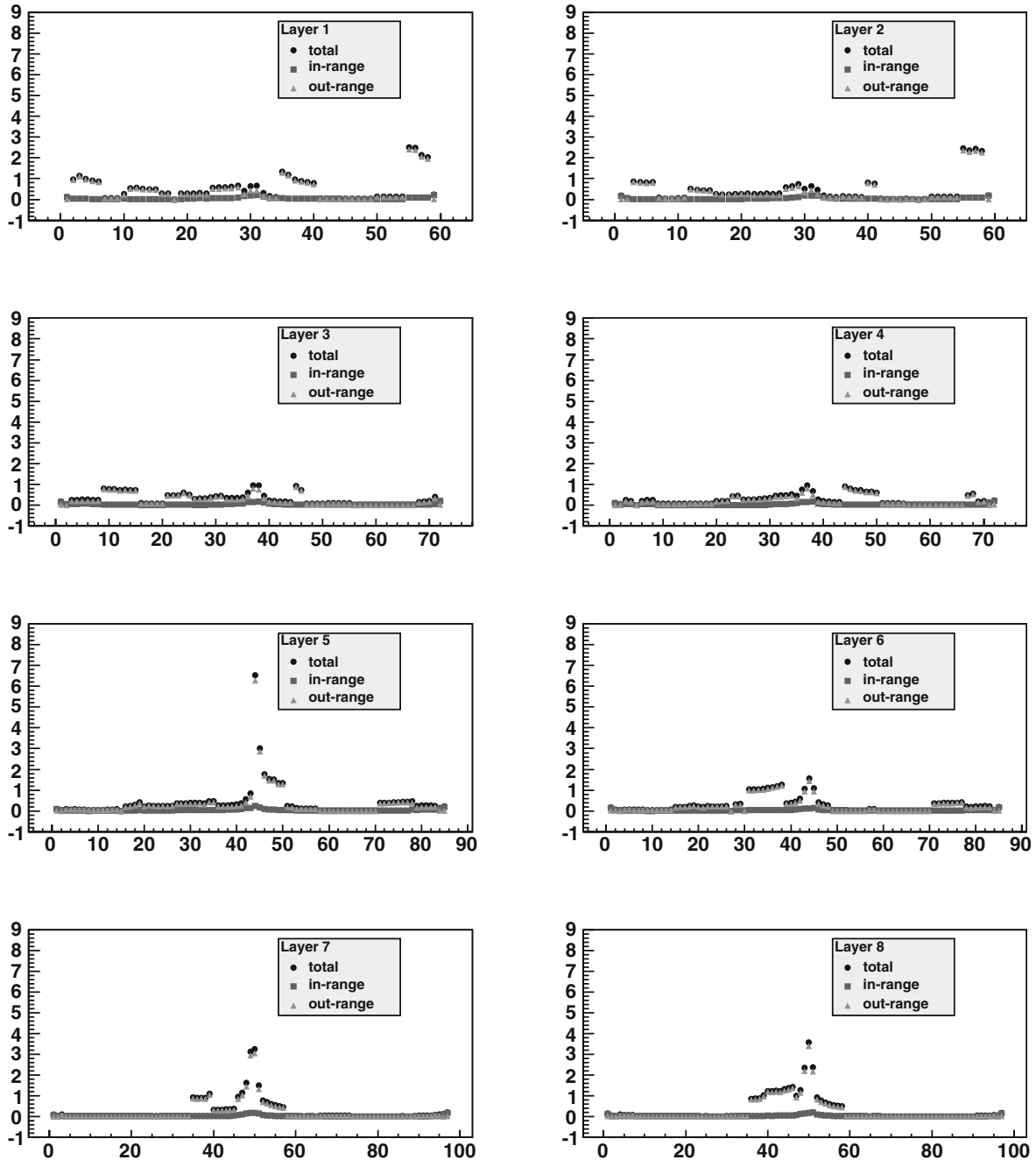

Fig.7. Layer hit patter of VDC. Horizontal axis is the wire number of each layer. The vertical axis is number of hit per event.

and make a significant bias in data. We decided to use only counters in the upstream side.

The use of the upstream electron veto counters EV3 and EV4 at the trigger level shows a saturation for the trigger accepted at 2.5 kHz. This occurs at an requested trigger rate of 4 kHz. A data acquisition efficiency of approximately 70% can be achieved at a tagged photon beam rate of 2.0 MHz. This is a significant improvement. The NKS2 spectrometer prior to DAQ improvements had the same DAQ efficiency at 2.0 MHz.

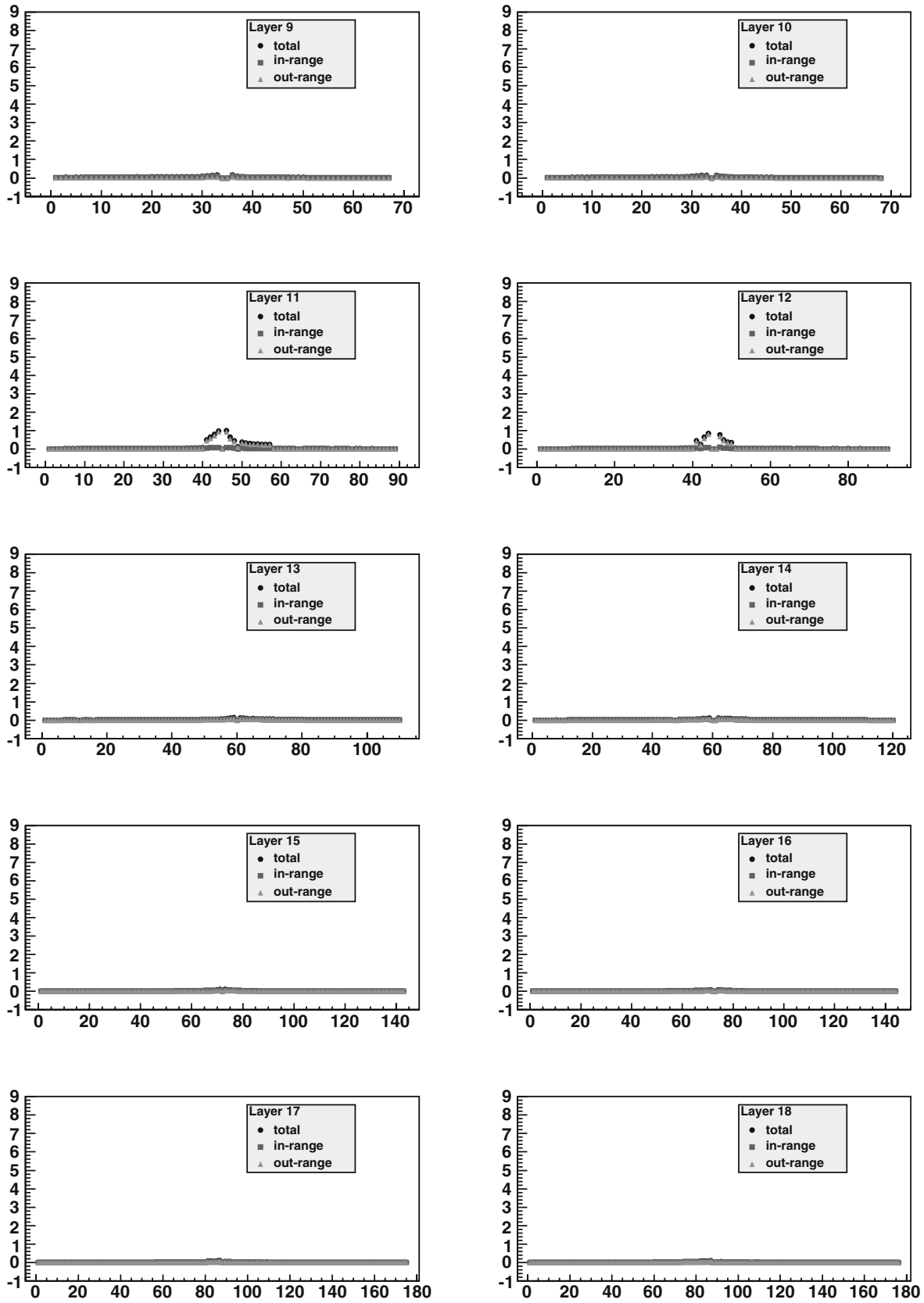

Fig.8. Layer hit patter of CDC. Horizontal axis is the wire number of each layer. The vertical axis is number of hit per event.

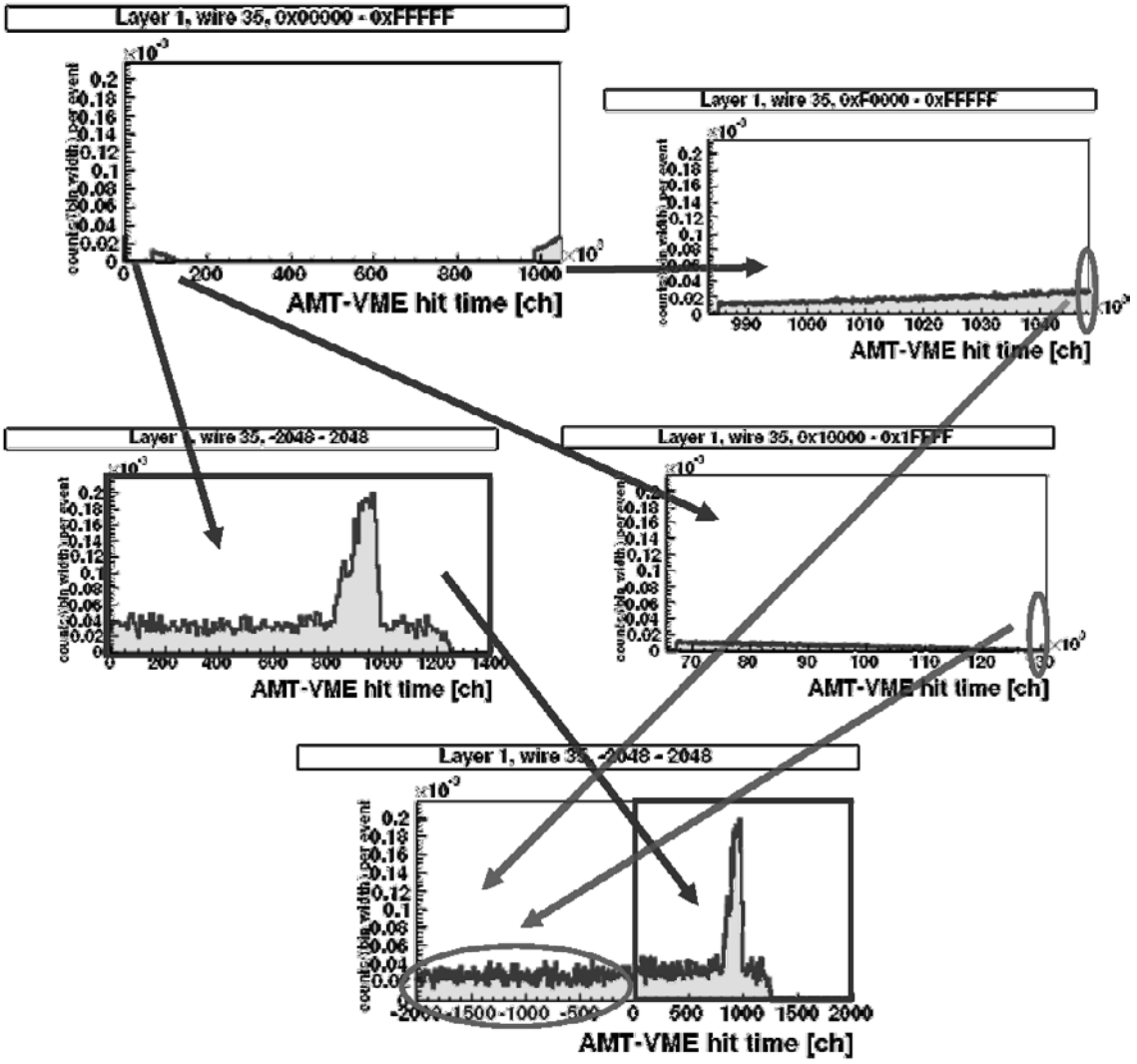

Fig.9. An example of TDC distribution from run 2009/Sep. Top-left plot is from all of TDC range (20 bits). The TDC range expected is in o to 1400 ch of TDC (middle-left). However, we see continuum in a range in 0x10000 to 0x1FFFF (middle-righ) and 0xF0000 to 0xFFFFF (top-right). Those parts are corresponding to the negative TDC region. That means that AMT-VME module recorded some hits after common stop. In the bottom plot, the both negative TDC region is added as negative values.

§4. Data Taking of Physics run

After substantial effort, we fixed two problems related chamber and AMT-VME module. The physics production run data were taken in 2010/Jul, Sep and Oct. The beam time of 2010/Jul was assigned as LNS Exp. No. 2638. The run of 2010/Sep and Oct are as No. 2716 and 2731, that are accepted in FY2010.

In the run of 2010/Jul and Sep, the duty factor of beam cycle is about 50 to 60%. Under strong support of ELPH, we took the data with 80% of the duty factor in 2010/Oct. The summary of number of tagged photon and trigger accepted is shown in Table 3.

Before starting of 2010/Sep and Oct runs, we did quick analysis of a part of 2010/July data to check number of Λ. The number is consistent with expected and shown in PAC meeting in 2010/Aug.

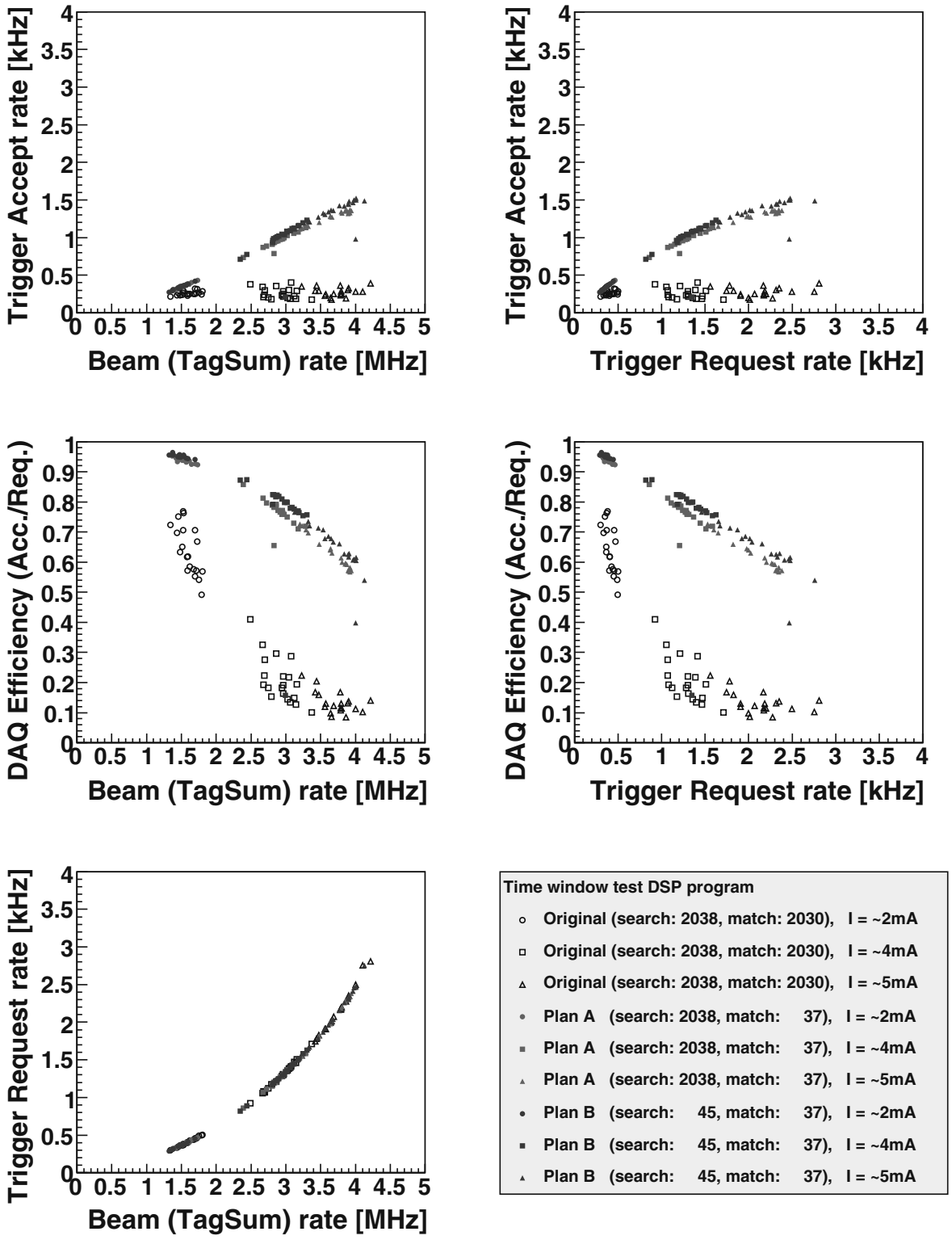

Fig.10. Correlation among rate of trigger accepted, trigger requested, beam rate and DAQ efficiency. DAQ efficiency is defined as number of trigger accepted divided by trigger requested in each beam spill. The open markers are NO modification of time window.

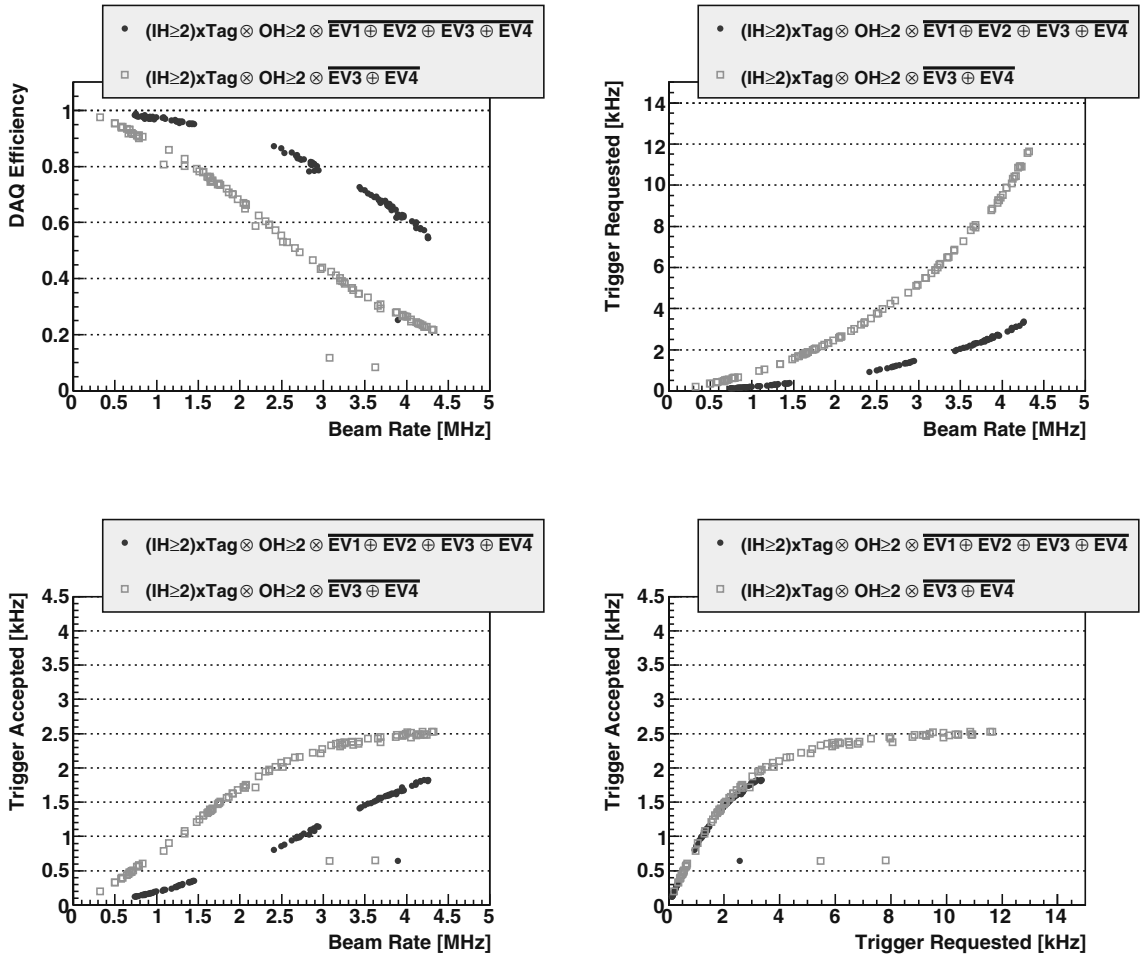

Fig.11. NKS2 data acquisition performance as a function of Tagged photon beam rate. The curves show the different combination of electron veto introduced into the main trigger logic. The data we used all of electron veto counters (EV1 to EV4) are shown by solid circles. The open square are data we used the upstream EV3 and EV4 combination only. The top-left figure is the DAQ efficiency as a function of the tagged photon beam rate. The top-right figure presents the trigger requested rate. The bottom-left shows the trigger accepted rate. The bottom-right illustrates the trigger accepted rate verses the trigger requested rate.

Table 3. Statistics of physics run.

run period	Target	Total number of tagged photon	Total number of trigger accepted
2010/Jul	Liq. D_2	0.12×10^{12}	0.16×10^{9}
2010/Sep	Liq. H_2	0.31×10^{12}	0.31×10^{9}
2010/Sep	Liq. D_2	0.89×10^{12}	0.64×10^{9}
2010/Oct	Liq. D_2	2.77×10^{12}	1.72×10^{9}

Acknowledgment

We thank to the accelerator group providing the stable beam. The program is partly supported by Creative research program (16GS0201) from Japan Society for the Promotion of Science (JSPS).

References

[1] A. Okuyama, Master thesis, Tohoku University (2010)
http://lambda.phys.tohoku.ac.jp/~k0/Thesis/2010Mthesis_Okuyama.pdf.

[2] Report of AMT-VME Problem (written in Japanese)
http://lambda.phys.tohoku.ac.jp/ kaneta/pukiwiki/index.php?AMT-VME

(LNS Experiment : #2660)

Double pion photoproduction on the deuteron in the energy region of $0.67 < E_\gamma < 0.92$ GeV

C. Kimura[1], B. Beckford[1], A. Chiba[1], D. Doi[1], T. Fujibayashi[1], T. Fujii[1], Y. Fujii[1], K. Futatsukawa[1], T. Gogami[1], O. Hashimoto[1], Y. C. Han[2], K. Hirose[3*], R. Honda[1], K. Hosomi[1], T. Ishikawa[3], A. Iguchi[1], H. Kanda[1], M. Kaneta[1], D. Kawama[1], T. Kawasaki[1], S. Kiyokawa[1], T. Koike[1], Y. Ma[1], K. Maeda[1], T. Maruta[1†], N. Maruyama[1], Y. Miyagi[1], K. Miwa[1], S. Nagao[1], S. N. Nakamura[1], A. Okuyama[1], M. Sato[1], A. Shichijo[1], H. Shimizu[3], K. Shirotori[1], K. Suzuki[3], T. Tamae[3], H. Tamura[1], N. Taniya[1], N. Terada[1], K. Tsukada[1‡], K. Yagi[1], T. O. Yamamoto[1], F. Yamamoto[1], H. Yamazaki[3], and Y. Yonemoto[1]

[1]*Department of Physics, Tohoku University, Sendai, 980-8578*
[2]*School of Nuclear Science and Technology, Lanzhou University, Lanzhou, 730000*
[3]*Laboratory of Nuclear Science, Tohoku University, Sendai, 982-0826*

We carried out experiments to investigate the double pion photoproduction on the deuteron using a photon beam in an energy range from 0.67 to 0.92 GeV. Charged particles were detected by use of Neutral Kaon Spectrometer 2 (NKS2). Events that include three charged particles have been selected and their masses were obtained from the measured momenta and velocities. In order to identify the $\gamma d \to \pi^+\pi^- pn$ and $\gamma d \to \pi^+\pi^- d$ events, the data calibration are in progress.

§1. Introduction

Double pion photoproduction on the proton and deuteron had been investigated in the photon energy range from 0.8 to 1.1 GeV at LNS [1]. In that study, the cross-section for the $\gamma d \to \Delta^{++}\Delta^-$ was observed and its contribution was not negligible contribution to the cross section of total photoabsorption. The quasi-free process was found to be smaller than that of the free proton. It suggests that the contribution of the non-quasi-free process is not small for the photon absorption by the bound nucleon.

The experiment performed in lower energy region than previous one will be useful for the extension of our understanding of the photoabsorption on the deuteron as bound nucleons in the wide energy region. We focused on the non-quasi-free process, especially the reaction in which the deuteron remains

*Present address: Division of Nuclear Data and Reactor Engineering, Nuclear Science and Engineering Directorate, Japan Atomic Energy Agency, Tokai, 319-1195

†Present address: J-PARC Center, Japan Atomic Energy Agency, Tokai, 319-1195

‡Present address: Advanced Meson Science Laboratory, RIKEN Nishina Center for Accelerator-Based Science, Wako, 351-0198

in the final state, $\gamma d \to \pi^+\pi^- d$. The cross section was predicted to be $\sim$7 μb at the photon energy of $E_\gamma > 0.5$ GeV [2].

§2. Experiment and Current Status of Analysis

The experiment in a photon energy of $0.67 < E_\gamma < 0.92$ GeV was carried out using a liquid deuterium target. The events with two or more charged particles were measured with the Neutral Kaon Spectrometer2 (NKS2). The total number of the irradiated photon counted by the STB Tagger in the experimental period, lasting approximatly two weeks was 9.15×10^{11}. For this statistics, the expected number of event for $\gamma d \to \pi^+\pi^- d$ reaction is 4×10^3 for the cross-section of 7 μb. The assumed acceptance which included the analysis efficiency was 0.01. Figure 1 shows the distribution of squared mass of observed particles. Mass square regions for $\pi(-0.5$–$0.3[(\mathrm{GeV/c^2})^2])$, p $(0.5$–$1.8[(\mathrm{GeV/c^2})^2])$ and d $(1.8$–$5.5[(\mathrm{GeV/c^2})^2])$ are denoted with arrows in the figure.

We are presently working to improve the quality of detector calibrations and plan to verify our analysis method.

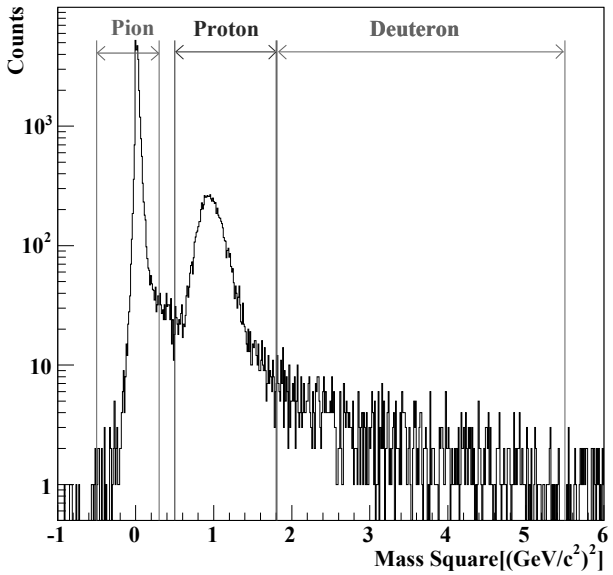

Fig.1. Mass square distribution of measured particles, $\pi(-0.5$–$0.3[(\mathrm{GeV/c^2})^2])$, $p(0.5$–$1.8[(\mathrm{GeV/c^2})^2])$ and $d(1.8$–$5.5[(\mathrm{GeV/c^2})^2])$.

References

[1] K. Hirose *et al.*: Phys. Lett. B**674** (2009) 17-22

[2] A. Fix and H. Arenhövel: Eur. Phys. J. A**25** (2005) 115-135

(LNS Experiment : #2550, #2556)

Development of direction-sensitive positron counters in the muon decay: performance feasibility tests using positron beam

D. Tomono[1], Y. Hirayama[2,1], M. Iio[1], K. Ishida[1], M. Iwasaki[1,2], Y. Matsuda[1], T. Matsuzaki[1], H. Ohnishi[1], H. Outa[1], J. Kasagi[3], H. Yamazaki[3], M. Kawai[4], R. Klein[4], and S.N. Nakamura[4]

[1]*Nishina Center for Accelerator Based Science, RIKEN, Saitama 351-0198*
[2]*Department of Physics, Tokyo Institute of Technology, Meguro, Tokyo 152-8551*
[3]*Laboratory of Nuclear Science, Tohoku University, Sendai 982-0826*
[4]*Department of Physics, Tohoku University, Sendai 980-8587*

We performed feasibility tests for positron counters for the muon decay using the positron beam at GeV-γ beam line. Two types of counters are developed: a Čerenkov counter and a spindle scintillation counter. These counters are designed to be sensitive to the incident positron direction. Each counter is tilted to the beam axis and the number of photon is counted. The angular resolutions of 3.8° and 14° are obtained for the Čerenkov and spindle counters, respectively. Based on these tests, the spindle scintillator is fabricated for new muon spectrometer at RIKEN-RAL.

§1. Introduction

A new detector for muon decay positrons is essential in highly intense pulsed muon beam. Generally in experiments using MeV muons, the muons are stopped at a sample or target and then decay positrons was observed by counters surrounding the sample. A direction-sensitive counter enables us to identify an initial positron direction. The muons that have stopped at the sample can be preferably observed with this counter. However, it is difficult to investigate detector performance using positrons from the muon decay in the pulsed muon source. The positron from the muon decay cannot be identified particle-by-particle due to a high rate beam, in particular, just after the muon injection. The positron has a continuous energy spectrum. It is emitted all around the target. Therefore, a performance feasibility test have been performed with the positron beam at the GeV-γ beam line, LNS-Tohoku.

Two types detectors are developed on the basis of new ideas by improving existing techniques. One is a Čerenkov counter. A picture of this counter is shown in Fig. 1 (a1). They are composed of acrylic block radiator (front 10×10 mm, back 50mm×50 mm, 50 mm length), a focusing mirror and a photomultiplier tube (PMT, Hamamatsu H2150). If a positron is injected perpendicular to the front of the radiator (Fig. 1 (a2)), photons are emitted along with the positron path. Part of these photons are reflected at a side surface of the acrylic radiator, are directed in parallel to the initial beam, and then are reflected by the mirror. They are focused at the PMT position. The focusing spot is squeezed with

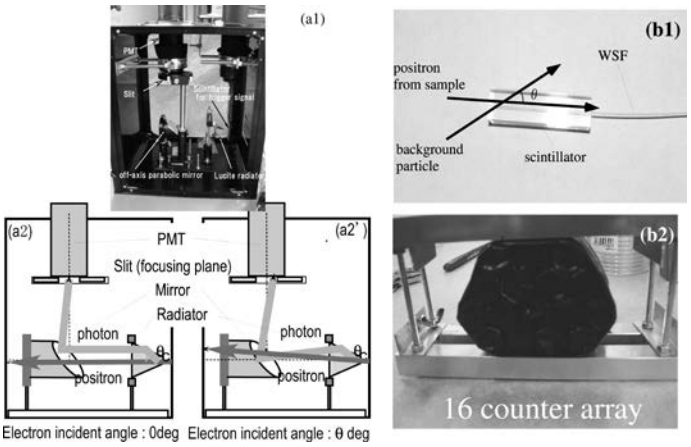

Fig.1. (a1):photograph of Čherenkov counter. (a2):separation mechanism by a positron incident angle in the Čerenkov counter. (b1): photograph of spindle scintillation counter. (b2): photograph of cross section of the spindle counter bundle.

slit. In contrast, if the positron is injected at some angles to the front of the radiator (Fig. 1 (a2')), such photons are reflected with some angles to the initial beam. As a result, all photons are not focused at the PMT position. If these difference is observed, an initial direction of positrons can be identified. Since an output pulse width in these Čerenkov radiation is expected to be shorter than that of a scintillating light, this method can reduce detector dead-time in the high intensity beam.

The other is a spindle scintillation counter. A picture of this counters is shown in Figs. 1 (b1) and (b2). A single wavelength shifter fiber (WSF) and a clear fiber is used as a compact light guide instead of a bulky acrylic light guide. Figure 1 (b1) shows the counter, which is composed of a scintillator ($14\times14\times50$ mm^3), a 75 cm WSF (Kuraray Y-11(200)M-S 1 mm) and a 16ch multianode photomultiplier tube (MAPMT, Hamamatsu H6568-10, UBA type). In this test, 16 scintillators are bundled (Fig. 1 (b2)). The spindle scintillator is pointed at the sample, so that positrons from the sample position penetrate through the longest path and background particles from outside of the target penetrate through a path shorter than the former path. If an appropriate threshold level of output signals from the MAPMT is provided in proportion to the light output, we can preferably observe decay positrons only from the sample direction and reject background particles. In this method, an instantaneous beam rate per counter can be reduced by increasing the number of counters although dead-time of the scintillation counter is not shorter than that of the Čerenkov counter.

§2. Experiment

After a preliminary test at the front of the NKS2 spectrometer, a beam test was performed at the GeV-γ beam line. These counters were tested in parallel. Momentums of p_e=500 MeV/c and p_e=252 MeV/c positrons were used for the Čerenkov counter and spindle counter tests, respectively. A schematic view of the setup is shown in Fig. 2. The 500 MeV/c positron penetrated a beam defining counter array in front of the Čerenkov counter to define the initial position. The Čerenkov counter was tilted to the beam axis from θ_c= -20° to 20°. The number of photon was counted for each angle with PMT.

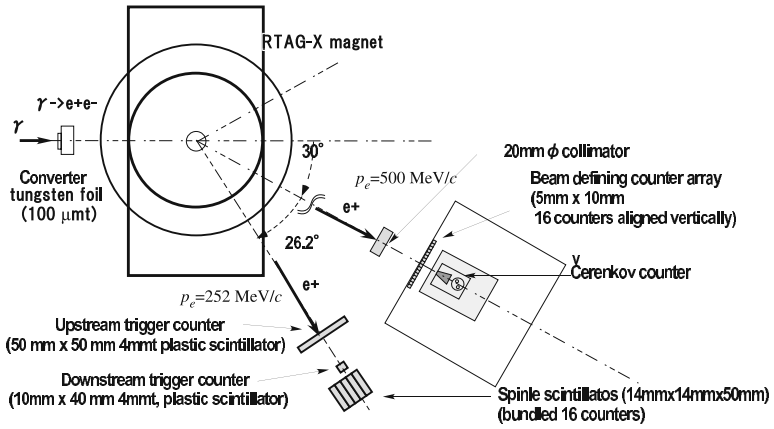

Fig.2. Setup at the GeV-γ beam line. For the Čerenkov counter, the beam defining array counters was installed in front of the Čerenkov counters. The array counter was composed of 10 mm-long and 5 mm-thick plastic scintillators. For the spindle counters, the counter bundle is composed of 16 spindle scintillation counters. Two beam defining were installed: the smaller scintillator is installed for identifying hit position at the spindle counter bundles.

As for the spindle counters, the 252 MeV/c positron penetrated two beam defining counters. A smaller counter was almost the same size as the cross section of spindle counter. The smaller counter was used to identify an incident point of the beam. They were tilted at θ = 0°, 5°, 10°, 17° and 90°. The number of photon was counted by MAPMT.

§3. Results

The angular distribution of the light output is shown for the Čerenkov and the spindle counter. Figure 3 shows the angular distribution of the photon using the Čerenkov counter when the slit is fully opened, opened by half and fully closed. The number of photon rapidly decreases up to 10° and then gradually decreases. The former component is composed of positrons that comes at a incident angle around 0°. By fitting this peak, an angular resolution is estimated to be 3.8° if the slit is fully opened.

Figure 4 (a) shows energy deposit spectrum for each angle. The vertical axis in Fig. 4 (a) is normalized by the average number of photons at 0°.Figure 4 (b) shows angular distribution of the peak energy observed with PMT. Each error was estimated with a FWHM of a peak at each angle. The number of photons calculated from the shape of the scintillator ($14\times14\times50$mm^3) is also shown in Fig. 4 (b) with a dotted line. These indicated that the calculated value ($14\times14\times50$mm^3) is consistent with the experimental value. If the threshold level were set at 0.8, we could observe positrons with the incidence angles below 15° effectively. This results was also reported in Ref. [1].

§4. Summary and Prospects

We successfully measured the angular distribution of the light output for the Čerenkov and the spindle counter. The angular resolutions of 3.8° and 14° are obtained, respectively. The Čerenkov counter is required to be modified around a photon collection component. At present, it is easier to employ the spin-

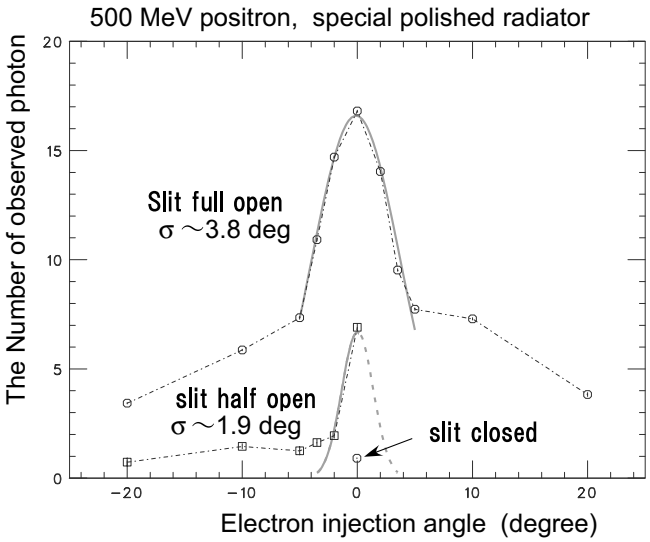

Fig.3. Angular dependence of the light output measured by the Čerenkov counter at p_e=500 MeV/c positron beam. When the slit is fully opened or opened by half, the numbers of photons observed with the PMT are plotted with a solid and dotted line, respectively. The peak at the center was fitted with a Gaussian shown in a bold solid line. the slit half-open data are not completed to the positive angle. Angular resolution is estimated to be 3.8°.

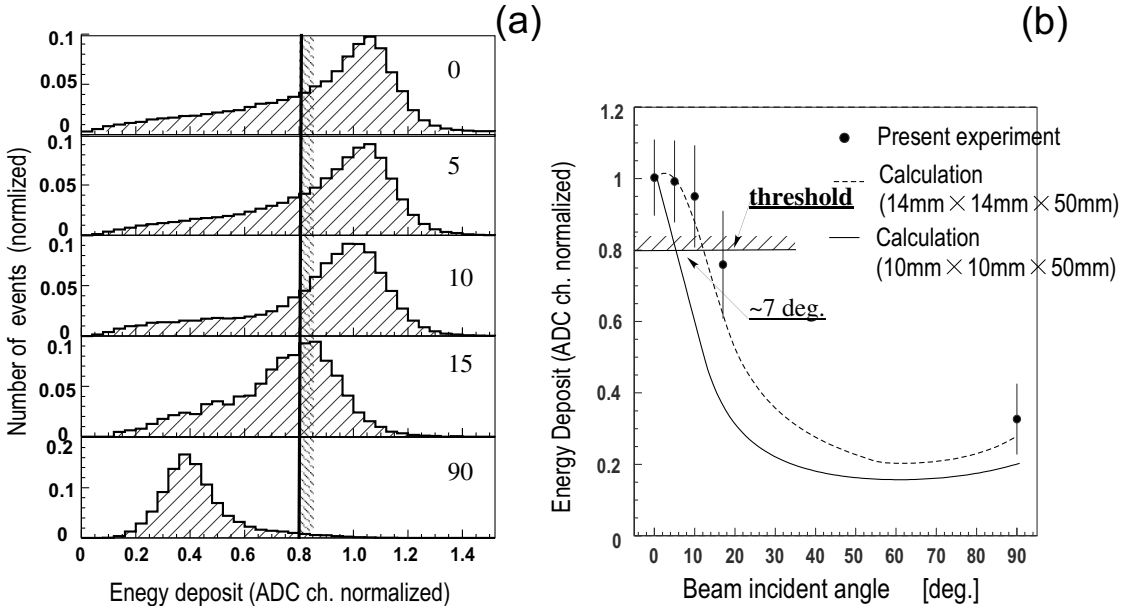

Fig.4. Result for the spindle counters. (a): Positron energy deposits in the scintillator at each angle. A vertical axis is scaled by the number of photons at 0 °. (b) Angular dependence of a peak position in each energy spectrum. Each error in the experiment was estimated with a FWHM of the spectrum at each angle. The relative number of photons is shown for $14\times14\times50\text{mm}^3$ and $10\times10\times50\text{mm}^3$ scintillators with dotted and solid line, respectively.

dle counter for observing a muon decay although the Čerenkov counter has a shorter angular resolution. In practice, this spindle counter is employed for a new spectrometer at RIKEN-RAL [2, 3]. Since a tighter constraint of the incident angle is required for the spectrometer, a thinner scintillator ($10\times10\times50$ mm^3) is employed. The calculated value is also shown in Fig. 4 (b) with a solid line. The angular resolution is expected to be 7° at the same threshold level.

Acknowledgment

The authors would like to thank to all the facility staffs in the LNS-tohoku for their kind supports. Especially, Prof. H. Shimizu, Dr. T. Ishikawa and Dr. K. Tsukada for their kind supports and encouragements. The authors would also like to thank members in NKS experiments for using their beam line.

References

[1] D. Tomono *et al.*: Nucl. Instum. Methods **A600** (2009) 44.

[2] D. Tomono *et al.*: J. Phys. Conf. Ser. **225** (2010) 01256.

[3] D. Tomono *et al.*: Nucl. Instrum Methods **A** (in preparation).

(LNS Experiment : #2591, #2660, #2676, #2691)

Test of the STB Tagger with the electron beam energies of 820 MeV and 1000 MeV

H. Kanda[1], B. Beckford[1], A. Chiba[1], D. Doi[1], T. Fujii[1], Y. Fujii[1], K. Futatsukawa[1], T. Gogami[1], O. Hashimoto[1], Y. C. Han[2], K. Hirose[3*], R. Honda[1], K. Hosomi[1], A. Iguchi[1], T. Ishikawa[3], M. Kaneta[1], Y. Kaneko[1], T. Kawasaki[1], S. Kiyokawa[1], T. Koike[1], Y. Ma[1], K. Maeda[1], T. Maruta[1†], M. Matsubara[1], K. Miwa[1], S. Nagao[1], S. N. Nakamura[1], A. Okuyama[1], M. Sato[1], A. Shichijo[1], H. Shimizu[3], K. Shirotori[1], T. Tamae[3], H. Tamura[1], N. Taniya[1], N. Terada[1], K. Tsukada[1‡], K. Yagi[1], F. Yamamoto[1], T. Yamamoto[1], T. O. Yamamoto[1], H. Yamazaki[3], K. Yokota[1], and Y. Yonemoto[1]

[1]*Department of Physics, Tohoku University, Sendai, 980-8578*
[2]*School of Nuclear Science and Technology, Lanzhou University, Lanzhou, 730000*
[3]*Laboratory of Nuclear Science, Tohoku University, Sendai,982-0826*

We tested photon beams provided by the STB Tagger with STB electron energies of 820 MeV and 1000 MeV. Tagging efficiencies and energy spectra of bremsstrahlung photons were measured with a lead glass counter. The average tagging efficiency was 0.48 for the electron energy of 820 MeV and 0.72 for 1000 MeV. The distributions of the tagging efficiencies with respect to the TagF segment were uniform. They were sufficient property for the production runs of double pion photoproduction. The endpoint energy of the bremsstrahlung photon was estimated by fitting the bremsstrahlung cross section formula to the ADC spectrum of the lead glass counter. The obtained endpoint energies were 814 MeV and 1013 MeV for the electron energy of 820 MeV and 1000 MeV, respectively. The energy calibration used for these measurements are based on the calibration for the electron energy of 1200 MeV using the pion photoproduction events on the deuteron measured with NKS2. The estimated errors are $\sim$ 10 MeV for both electron energies. By considering the errors, the measured endpoint energies were in agreement with the STB electron energies.

§1. Introduction

The deuteron have been used as a target to study reactions on the neutron because it is a loosely bound system of the proton and the neutron. Most experimental data for the pion photoproduction on the deuteron show the validity of the quasi-free view of the reactions. However, there exist some ex-

*Present address: Division of Nuclear Data and Reactor Engineering, Nuclear Science and Engineering Directorate, Japan Atomic Energy Agency, Tokai, 319-1195
†Present address: J-PARC Center, Japan Atomic Energy Agency, Tokai, 319-1195
‡Present address: Advanced Meson Science Laboratory, RIKEN Nishina Center for Accelerator-Based Science, Wako, 351-0198

perimental results in the study of double pion photoproductions which show the difference between the free proton target and the bound proton or bound neutron. We measured the total cross sections for $d(\gamma,\pi^+\pi^-p)n$ and $p(\gamma,\pi^+\pi^-p)$ reactions at Laboratory of Nuclear Science, Tohoku University (LNS-Tohoku), with the Neutral Kaon Spectrometer (NKS) and the tagged photon beam provided by the STB Tagger [5]. The contribution of the quasi-free process was derived by selecting the smaller momentum regions of the undetected neutron in $d(\gamma,\pi^+\pi^-p)n$, and the obtained cross section was roughly 60 % of that for $p(\gamma,\pi^+\pi^-p)$ [1]. We also derived the measurable cross section for the simultaneous $\Delta^{++}\Delta^-$ excitation in the intermediate state of the non-quasi-free process of the $d(\gamma,\pi^+\pi^-p)n$ reaction. Its energy dependence shows a discrepancy from the previous experimental data and the theoretical calculations. It is very interesting to measure these cross sections in the broad energy range.

We proposed experiments to measure the double pion photoproductions with the renewed Neutral Kaon Spectrometer (NKS2), in the lower energy regions by setting the STB electron energy as 820 MeV and 1000 MeV. The energy regions of the tagged photon beam provided by the STB Tagger were $550-750$ MeV, $670-920$ MeV, and $800-1100$ MeV for the STB electron energy of 820 MeV, 1000 MeV and 1200 MeV, respectively. The energy regions were chosen so that they have overlaps with neighboring energy regions. The range of the overlap is the energy which corresponds to roughly 20 tagger segments.

The STB electron energies of 820 MeV and 1000 MeV have not been operated and we performed the study of the tagged photon beam. We have measured the tagging efficiencies and the energies of the radiated photon. We report here the preliminary results of the analysis of the photon beam.

§2. STB Tagger

The STB Tagger is an internal tagging system installed in the BM4, one of the bending magnet of STB. It consists of a position-adjustable radiator target (carbon fiber with the thickness of 11 μmϕ), an analyzing magnet (BM4), and two sets of arrays of scintillation counters (50 TagF counters and 12 TagB counters). The radiator target is located outside the electron beam orbit during the beam injection and acceleration. It is inserted to the center of the electron beam orbit during the flat top period. The insertion speed and position of the radiator target is tuned to obtain the constant photon beam intensity. The coincidence of the suitable TagF and TagB counters selects the true trajectory of the recoil electron from the bremsstrahlung of the circulating electron on the radiator target. The momentum acceptance of one TagF counter is designed to be 6 MeV/c for the STB electron energy (E_0) of 1200 MeV. It corresponds to the span of the photon energy $\Delta E_\gamma = 6$MeV for the one TagF counter. The nominal energy range of the tagged photon is from 800 to 1100 MeV for $E_0 = 1200$ MeV. For lower electron energy, the energy span and the energy range of the tagged photon (from $E_\gamma^{\rm low}$ to $E_\gamma^{\rm high}$) can be obtained by scaling:

$$\Delta E_\gamma = 6 \times E_0/1200,$$
$$E_\gamma^{\rm low} = 800 \times E_0/1200,$$
$$E_\gamma^{\rm high} = 1100 \times E_0/1200,$$

where the unit of the energies for E_0, ΔE_γ, $E_\gamma^{\rm low}$, and $E_\gamma^{\rm high}$ is MeV. The detailed description is found elsewhere [5]. It was developed for providing the tagged photon beam to SCISSORS-I and NKS. Now, NKS2 is settled on the beamline.

§3. Tagging efficiency

Tagging efficiency is the ratio between the number of photons which are irradiated on the target and the number of recoil electrons which are detected with the tagger. We set a lead glass counter with size of $150\times150\times300$ mm^3 made from SF-5 on the photon beam line 9.5 m downstream from the radiator target. It sufficiently covers the size of photon beam for the detection of the photon. We assumed 100 % detection efficiency for it. The tagging efficiency can be obtained as:

$$\epsilon_i = \frac{N_i^{\rm photon}}{N_i^{\rm tag}(ON) - N_i^{\rm tag}(OFF)},$$

where ϵ_i is the tagging efficiency for i-th TagF counter; $N_i^{\rm photon}$, the number of photon detected with the lead glass counter in coincidence with the i-th TagF counter; $N_i^{\rm tag}(ON)$, the number of the hit on the i-th TagF counter with the radiator inserted to the electron beam; and $N_i^{\rm tag}(OFF)$, the number of the hit on the i-th TagF counter with the radiator target not inserted to the electron beam. Tagger OR signal was utilized as the DAQ trigger and a low intensity electron beam (hit rate of the tagger as $\sim 10^3$ Hz) was used for this measurement.

The tagger hit by the electrons scattered on the residual gas inside the accelerator vacuum pipe: Its contribution was measured as $N_i^{\rm tag}(OFF) < 10^{-3} N_i^{\rm tag}(ON)$ for every i and was negligible. The average tagging efficiencies were 0.48, 0.63, 0.72 and 0.79 for electron energies of 820 MeV, 930 MeV, 1000 MeV and 1200 MeV, respectively. Figure 1 shows ϵ_i for each E_0. The tagging efficiencies for all the electron energies show sufficiently high and uniform distributions over all the TagF segment.

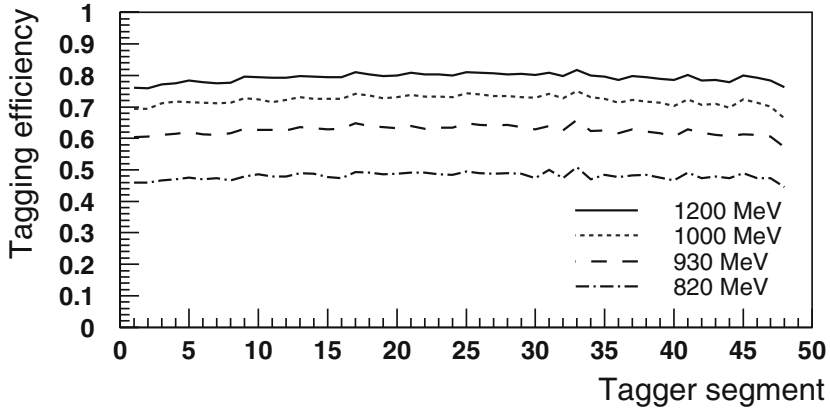

Fig.1. Tagging efficiencies for the collimated photon beam with regard to the TagF hit segments. The dot-dashed curve is for $E_0 = 820$ MeV; the dashed curve, for $E_0 = 930$ MeV; dotted curve, for $E_0 = 1000$ MeV; and the solid curve, for $E_0 = 1200$ MeV.

The most important factor to reduce the tagging efficiency is the loss of the photon beam by a collimator. The collimator consists of five lead blocks of $100 \times 108 \times 50$mm^3 with a hole of 10 mm-

diameter. It serves to suppress the beam halo but it also absorbs some fraction of the bremsstrahlung photon with large emission angle. Because the angular distribution of the bremsstrahlung photon is broader in lower electron energy, the collimated tagging efficiency is supposed to drop in lower electron energy. For the measurement of uncollimated tagging efficiency, we placed another lead glass counter in front of the collimator (2.8m downstream from the radiator target).

Figure 2 shows the tagging efficiencies for the uncollimated photon beam for $E_0 = 930$ MeV and $E_0 = 1000$ MeV. The almost identical efficiencies larger than 0.9 were obtained for both E_0. As can be seen, the collimator significantly reduces the tagging efficiency. The reduction ratio depends on the E_0 not on the photon energy. That is the natural consequence of the angular distribution of the bremsstrahlung photon. Though the low tagging efficiencies for collimated photon beam is qualitatively as our expectation, the further studies with use of a Monte Carlo simulation or an analytic method are needed for the quantitative explanation.

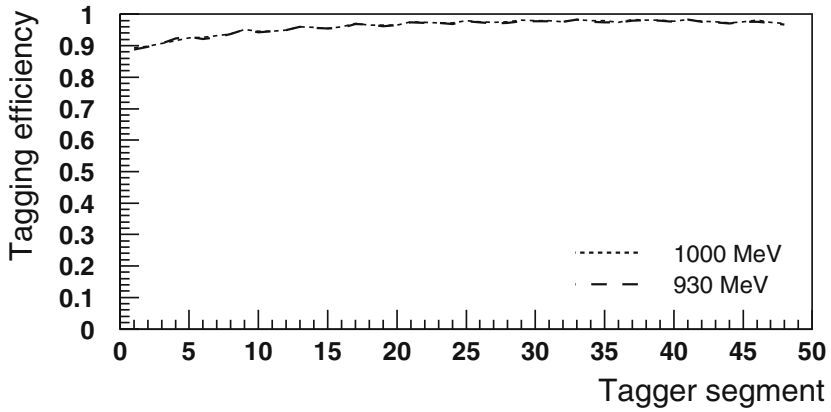

Fig.2. Tagging efficiencies as functions of TagF hit segments for the uncollimated photon beam with regard to the TagF hit segments. The dashed curve is for $E_0 = 920$ MeV; and the dotted curve, for $E_0 = 1000$ MeV.

§4. Photon energy spectrum

The response of the lead glass counter for the incident photon or electron is known to be linear to their energy [2, 3]. We measured the energy of collimated photons in both tagged and untagged regions with the lead glass counter as a DAQ trigger. The energy calibration of the ADC for the lead glass counter was performed with use of the events with hits on the tagger. The peak in the pedestal-subtracted ADC spectrum with hit on the 23rd and 24th TagF counters was set to the scaled energy from the calibrated energy for $E_0 = 1200$ MeV in the analyses for both $E_0 = 820$ MeV and $E_0 = 1000$ MeV data. We adopted a new energy calibration obtained from inclusive analyses of the incident photon energy in the, single, double, and triple pion photoproductions on the deuteron measured with NKS2 for $E_0 = 1200$ MeV. The obtained photon energies for all these reactions for each TagF segment are consistent within the statistic errors. The photon energy of each TagF segment was determined by the error weighted average of the results for these reactions. This analysis contained the smaller statistic errors than our previous energy

calibration performed with use of single pion photoproduction ($\gamma d \rightarrow \pi^- pp$) on the deuteron with the NKS2 [4].

In Fig. 3, the peak positions of lead glass ADC (pedestal not subtracted) fitted with Gaussian with respect to the TagF segment and the result of linear regression are shown. The linearity of the peak position to the TagF segment can be seen. Knowing the linearity of the tagged photon energy to the TagF segment, the linearity of the lead glass response was reassured and the energy calibration between the lead glass ADC and the photon energy was obtained.

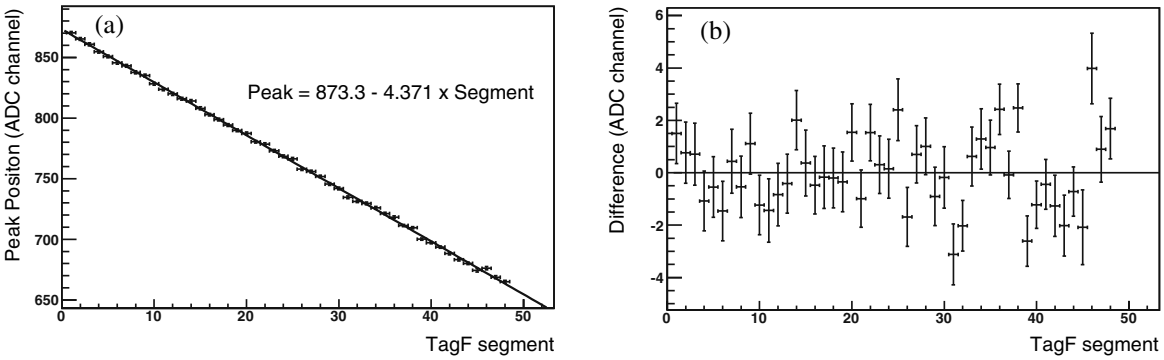

Fig.3. The peak positions of the lead glass ADC with respect to the hit TagF segment is shown in (a) and the difference from the fitted line is shown in (b) for $E_0 = 1000$ MeV. The peak position was obtained by fitting the Gaussian function to the $\pm 2\sigma$ region of the ADC peaks.

Figure 4 shows the energy spectra of the collimated photon beam obtained from the calibrated lead glass ADC spectra for $E_0 = 1000$ MeV As can be seen in the figure, the energy spectrum without TagF hit shows a tail above the endpoint energy of 1000 MeV. The energy spectrum with hit on TagF1 has a similar tail. It is considered as the effect of the response function of the lad glass. It can be well fitted with use of the sum of two Gaussian functions: one for the main peak and the other for the tail. The sum of fitted Gaussian function is used for the simulation of the response function of the lead glass to the high energy photon.

Figure 5(a) and (b) show the energy spectrum for $E_0 = 820$ MeV and $E_0 = 1000$ MeV, respectively. They are fitted with the bremsstrahlung cross section for the carbon nucleus (solid line) and the folded curve of the bremsstrahlung cross section by the above explained response function (dashed line). The nonscreened bremsstrahlung cross section differential in photon energy with Coulomb correction was calculated with Formula 3CN in Ref. [6]. The screened cross section differential in photon energy with Coulomb correction was calculated with Formula 3CS in Ref. [6]. We referred to Ref. [7] for the screening functions $\phi_1(\gamma)$ and $\phi_2(\gamma)$ required in Formula 3CS. The γ is the screening parameter of the bremsstrahlung. The screening has to be considered for the region with $\gamma \leq 15$; can be ignored for the region with $\gamma > 15$. The nonscreened region with the carbon target is only from $998.1 < k < 1000$ MeV for $E_0 = 1000$ MeV where k is the energy of the radiated photon. The spectra from the detection threshold to $0.9E_0$ were well fitted with the bremsstrahlung cross section. The tails of the spectra in the energy region higher than the endpoint energy are were reproduced by the folded curves. The folded

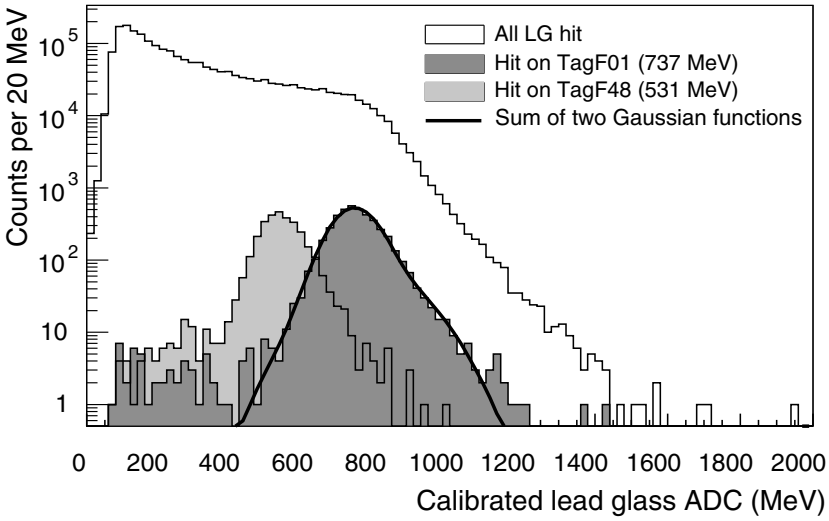

Fig.4. The total calibrated lead glass ADC spectrum shown together with the ADC spectrum with TagF1 hit (pale hatched histogram) and TagF48 hit (dark hatched histogram). The ADC spectrum with TagF hit was fitted with the sum of two Gaussian functions as a simulated response function.

curve slightly overestimates the photon yield in the lower energy region. The fitting parameters for the function fitting was a scaling factor, an endpoint energy, a detection threshold and an energy spread of the threshold. The threshold was expressed with use of normal frequency function (TMath::Freq(x) in ROOT [8]). The fitting results with the folded bremsstrahlung cross section were much affected by the shape of the response function. Because our response function is very preliminary, the fitting results are not reliable. The obtained endpoint energy by the fitting with the bremsstrahlung cross section was 813.85 ± 0.09 MeV and 1012.59 ± 0.07 MeV for $E_0 = 820$ MeV and $E_0 = 1000$ MeV, respectively. The very small errors on these values are the only fitting errors. They are only reflected in the data points with high statistics in the low energy region. The errors on the endpoint which come from the energy calibration were ± 1.9 MeV for $E_0 = 820$ MeV and ± 1.7 MeV for $E_0 = 1000$ MeV. They may originate from the statistic errors in finding the ADC peaks with Gaussian fitting. The systematic error in the energy calibration for $E_0 = 1200$ MeV was estimated to be less than 10 MeV. The scaled errors, 6.8 MeV for $E_0 = 820$ MeV and 8.3 MeV for $E_0 = 1000$ MeV are also expected. Another energy calibration using the result of the linear regression for the peak positions of the lead glass ADC was also tested. By adopting the calibration, the endpoint energy shifted by -3 MeV and -6 MeV for $E_0 = 820$ MeV and $E_0 = 1000$ MeV, respectively. These can be considered as ones of the systematic errors in this measurement. The obtained endpoint energies were in agreement with the energy of the electron beam within errors.

The formulas 3CN and 3CS were obtained by integrating the differential cross section with respect to the emission angles of the photon and the electron over the whole emission directions of them. However our measurement showed that the collimate limited the angular distributions of the photon, the formula 3CS well reproduced theenergy spectra in the broad energy region. A detailed analysis of the bremsstrahlung cross section and the Monte Carlo simulation will resolve this inconsistency.

We have also tried the measurement of photon energy by the use of the TOF of the proton in

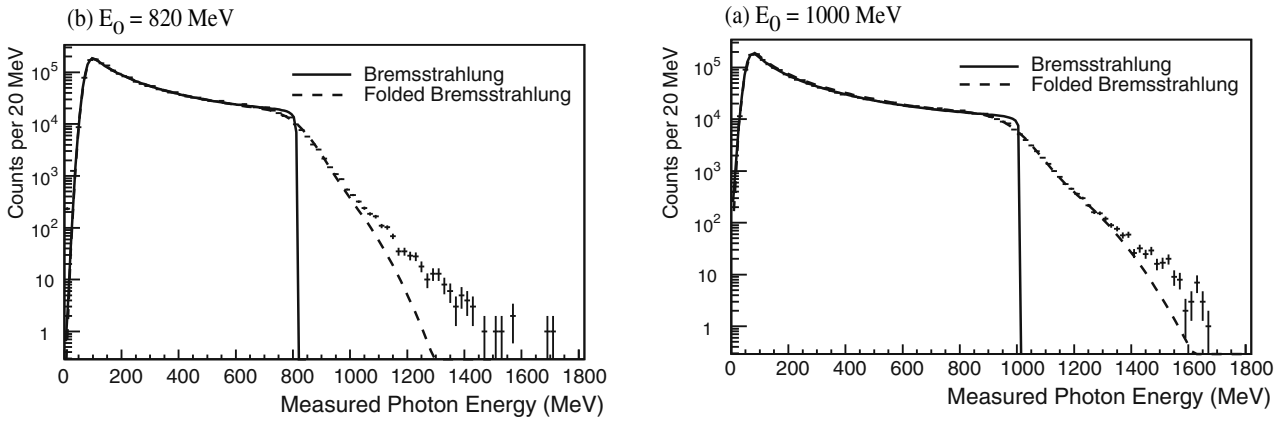

Fig.5. The calibrated lead glass ADC spectrum fitted with the bremsstrahlung cross section formula (solid curve) and the bremsstrahlung cross section formula folded by the simulated response function of the lead glass counter (dashed curve) for $E_0 = 1000$ MeV (a) and $E_0 = 820$ MeV (b).

$p(\gamma, p)\pi^0$ reaction and the neutron in $n(\gamma, \pi^+ n)$ reaction. The analyses of the photon energy from the obtained data are still underway. This method with TOF measurement does not depend on the momentum measurement with NKS2 which suffers the difficulty and ambiguity from the determination of the magnetic field. It will give the photon energy data with other kind of systematics and be important information for our knowledge of the STB-Tagger.

Acknowledgment

We should like to thank the accelerator group of LNS-Tohoku for providing a high-quality beam by frequent monitoring and tuning of the status of the accelerators. We also should like to thank the supporting staffs of LNS-Tohoku for their sincere assistance during our experiment. This program was partly supported by Special promoted program (12002001), Creative research program (16GS0201) and Scientific research on Priority Areas (08239102) from Japan Society for the Promotion of Science (JSPS).

References

[1] K. Hirose *et al.*: Phys. Lett. **B674** (2009) 17.

[2] A. Ando *et al.*: KEK Report, KEK-79-21 (1979).

[3] T. Ishikawa: Internal GeV-γ Analysis Note, No. **125**$\mathcal{T}$ (2009).

[4] Y. C. Han *et al.*: Chinese Phys. **C34** (2010) 35.

[5] H. Yamazaki *et al.*: Nucl. Instrum. Methods **A536** (2005) 70.

[6] H. W. Koch and J. W. Motz: Rev. Mod. Phys **31** (1959) 920.

[7] J. L. Matthews and R. O. Owens: Nucl. Instrum. Methods **111** (1973) 157.

[8] Description of MathCore library: `http://root.cern.ch/root/html/MATH_MATHCORE_Index.html`.

(LNS Experiment : #2592, #2621)

Beam Test of J-PARC K1.8 Beam Line Chambers

T.Takahashi[1], T.N.Takahashi[2], A.O.Tokiyasu[3], S.Adachi[3], M.Endo[4], P.Evtoukhovitch[5], H.Fujioka[3], T.Hiraiwa[3], K.Hosomi[6], T.Ishikawa[7], Y.Igarashi[1], K.Itahashi[8], R.Kiuchi[1*], K.Matsuda[4], K.Miwa[6], D.Mzhavia[5], D.Nakajima[2], M.Naruki[1], T.Ohtani[6], V.Samoilov[5], K.Shirotori[6], H.Sugimura[3], Z.Tsamalaide[5], and K.Tsukada[6†]

[1]*Institute of Particle and Nuclear Study (IPNS), High Energy Accelerator Research Organization (KEK), Tsukuba, 305-0801*
[2]*Department of Physics, University of Tokyo Tokyo, 111-0033*
[3]*Department of Physics, Kyoto University, Kyoto, 606-8502*
[4]*Department of Physics, Osaka University, Toyonaka, 560-0043*
[5]*Joint Institute for Nuclear Research (JINR), Dubuna, 141980, Russia*
[6]*Department of Physics, Tohoku University, Sendai, 980-8578*
[7]*Laboratory of Nuclear Science, Tohoku University, Sendai, 982-0826*
[8]*Advanced Meson Science Laboratory, RIKEN, Wako, 351-0198*

A 1 mm anode spacing MWPC and a 3 mm anode-anode spacing MWDC were developed for the K1.8 beam line tracking detectors at J-PARC Hadron Facility. These detector were designed to measure the beam trajectories with the accuracy of 0.2 mm (RMS) under the counting rates of $\sim$10 MHz. The detectors and their readout system were tested at test beam line of LNS. In this report, however, the detectors and their readout system are described as well as the operation results at J-PARC beam line in 2009.

§1. Introduction

In the Hadron Facility of J-PARC, particle and nuclear physics experiments using high intensity secondary kaon beam, produced by 30 GeV primary protons with high intensity from Main Ring. Hypernuclear physics is one of main subjects at Hadron Facility. K1.8 beam line can deliver mass-separated charged particle beam such as kaon up to 2 GeV/c. A high-resolution beam spectrometer (K1.8BS) and SKS spectrometer [1] with a large acceptance of 100 msr and high resolution of $\Delta p/p$=0.1%(FWHM) are equipped in the beam line. Therefore studies on hypernuclei of both S=-1 and -2, especially the spectroscopy experiments, will be performed in this beam line.

To achieve the momentum resolution of better than 10^{-3} at K1.8BS, beam trajectories should be measured with 0.2 mm accuracy at upstream and downstream of K1.8BS. To avoid multiple scattering

*Present address: Department of Physics and Astronomy, Seoul National University, Seoul, 151-747, Korea

†Present address:Advanced Meson Science Laboratory, RIKEN, Wako, 351-0198

Table 1. Parameters of the K1.8 beam line MWPC (left) and MWDC (right).

MWPC	
anode diameter	15 μm
anode spacing	1.0 mm
anode-cathode gap	3.0 mm
effective area	$250^{H}\times80^{V}$ mm^2
(window size)	$305^{H}\times100^{V}$ mm^2
gas	Ar(80):iso-C_4H_{10}(20)
operation voltage	
cathode	-2.55 kV
threshold of ASD	20 mV

MWDC	
anode(a) diameter	12.5 μm
potential(p) diameter	75 μm
a-p spacing	1.5 mm
a(p)-cathode gap	2.0 mm
effective area	$190^{H}\times80^{V}$ mm^2
(window size)	$240^{H}\times100^{V}$ mm^2
gas	Ar(80):iso-C_4H_{10}(20)
operation voltage	
cathode	-1.20 kV
potential	-1.25 kV
threshold of ASD	40 mV

and energy loss straggling which degrade the resolution, these tracking detectors should be as thin as possible. Intensity of K^- at 1.8 GeV/c is expected to be 1.4×10^6/spill, where spill length (flat top) is 0.7sec., in the Phase-1 goal. Taking into account kaon purity and kaon decays, particle's rates are expected to be about 10 MHz and a few MHz at the upstream and downstream of K1.8BS, respectively. Considered that the maximum rate is 200 kHz/wire from our experience at Tsukuba, we adopted a 1 mm anode spacing multi-wire proportional chamber (MWPC) for the upstream detectors and 3 mm anode-anode spacing multi-wire drift chamber (MWDC) for downstream ones. Readout electronics for these detectors has been also developed.

These detectors and their readout system were tested at LNS using positron beams at the test beam line in July 2007 and May 2008. These beam tests were helpful for the modification and updating the original design of these detectors and readout system. In this report developed MWPC, MWDC and their readout system are described as well as the operation results at J-PARC in 2009.

§2. K1.8 beam line chambers and their readout system

2.1 1mm spacing MWPC

Geometrical and operation parameters are listed in Table.1 left. We choose gold-plated Tungsten wire with Rhenium, whose diameter is 15 μm and a gap of 3 mm between the anode-wire plane and cathode plane. This gap is made by using G10 frame with 3 mm thickness both for anode and cathode frames. Cathode plane is made of the carbon-pasted aramid film, in which carbon ink is pasted with 20 μm thickness on the anode side of the base film of 12 μm. This carbon-pasted film cathode is strong against the spark. In sprite of the continuous spark during 1 day, the conductivity was kept, although the trace of the sparks were seen along the anode wire position. Number of the readout anode channels is 256/plane. Since a surface field of the anode becomes higher in the edge region, anode dummy wires are spread out of the window, in order that such anode wires are covered by the G10 insulator.

Amplifier-Shaper-Discriminator (ASD) cards with half-pitch connectors are installed both up and down sides of the anode frame because of high density readout channels. Therefore the distance to the next layer is chosen to be 20 mm. The MWPC comprises 6 readout layers with X-U-V-X-U-V configuration, where X layer measures horizontal position, U and V are tilted by $\pm15^\circ$ to X. The structure of the

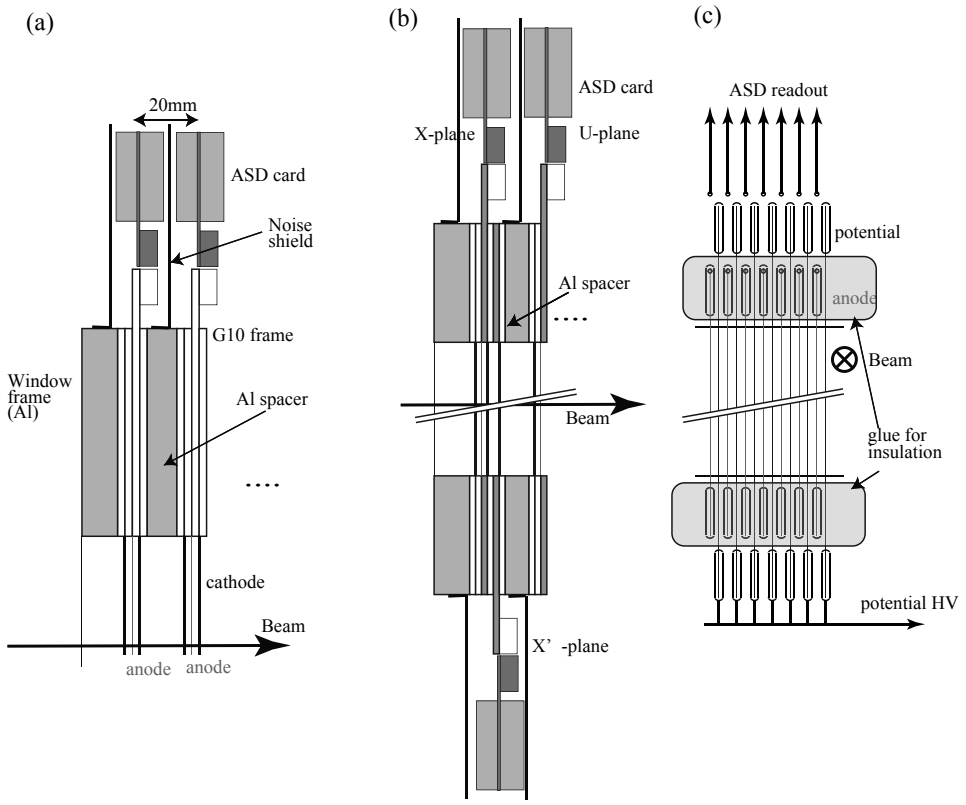

Fig.1. (a) Layer structure of the 1 mm MWPC. (b) Layer structure of the 3 mm MWDC. (c) Structure of anode and potential wires on the wire plane of 3 mm MWDC.

MWPC and ASD cards are shown in Fig.1 (a). In the operation, negative high voltage is applied to the cathode side, while the anode wire is set to the 0V.

2.2 3 mm spacing MWDC

The geometrical and operation parameters are listed in Table.1 right, while the structure are shown in Fig.1 (b) and (c). The MWDC comprises 6 layers with the configuration of X-X'-U-U'-V-V'. The prime means pair plane, in which wire position is sifted by half of the cell size, namely, 1.5 mm in order to solve the L/R ambiguity. A number of the readout channels is 96(95)/layer, thus, three ASD cards can be installed in one side of anode(wire) frame. Therefore the distance between the pair planes is 4 mm. Cathode planes are made of the carbon-pasted film similar to MWPC, but carbon ink is pasted on the both size of the base film, since the common cathode plane is used between the pair planes. Between very narrow distance of 1.5 mm between anode and potential wires, high voltage is applied. Therefore these wires near the soldering pads are insulated by the epoxy grue to prevent the spark as shown in Fig.1 (c).

2.3 32channel ASD card

Anode signals are amplified, shaped, and discriminated by the ASD cards which are connected to the MWPC or MWDC with the half-patch connectors of 68 pins as described in the previous section. 8

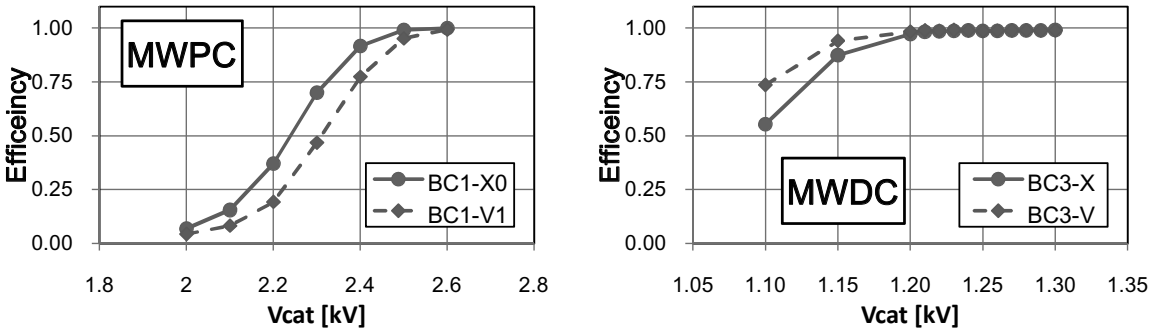

Fig.2. Efficiency .vs. operation voltage measured with the low-intensity pion beams at K1.8 beam line. Left one is for 1 mm MWPC and right one for 3 mm MWDC.

ASD IC's, which were originally developed for ATLAS Thin Gap Chamber with the time constant of 16 ns [2], are mounted on the both sides of the card (32channels/card). The LVDS logic signals are output through an another type of half-pitch connectors. 4 power lines of $+3.3$V(0.82A), -3.0V(0.11A), threshold (Vth) and GND are connected by the different connector. TEST Input of NIM signal can be sent to the card for the test of the downstream module and time zero calibration.

2.4 MWPC Encoder – Encoder FINNESE on COPPER –

A DAQ front end module for MWPC readout was developed as a FINNESE board on COPPER system [3], which was developed in KEK. This MWPC encoder accepts 32 channels LVDS or ECL inputs from the same half pitch connector as a ASD card output one and trigger signal from the connector on board (NIM) or Trigger-Card on COPPER system. The input logic level is latched by synchronizing with 100 MHz interal clock and sent to FIFO. By the trigger signal, data which match the selected time range are sent to the readout buffer. Maximum delay time is 2.55μsec, which is determined by the FIFO size. These functions are realized by firm-ware of on-board FPGA (XILINX, Spartan3 XC3S400). It works like a multihit TDC with 10 ns LSB and 2.55 μsec maximum range or a 1 bit flash ADC with 100 MHz.

Since no data compression is implemented, data size is proportional to the number of channels and time window. In the production runs, we set the time window of 300 ns (30 records).

§3. Operation at J-PARC

Beam commissioning at K1.8 beam line was done from October 2009 to February 2010. A part of the results on the beam line chambers are reported here. Figure.2 shows the efficiencies measured by changing the cathode voltage using low-intensity pion beams. From this results we decided the operation voltages as listed in Table.1.

MWPC data and the analysis method are described. Figure.3 shows MWPC encoder data of 1 layer in an event. The horizontal axis means a record number of the encoder data, 1 record corresponding to 10 ns. The vertical one is a wire number, namely, position. The hits around the record number of 110 are associated with the trigger of the event. These hits spread in 50–80 ns and 1–3 wires. These neighboring

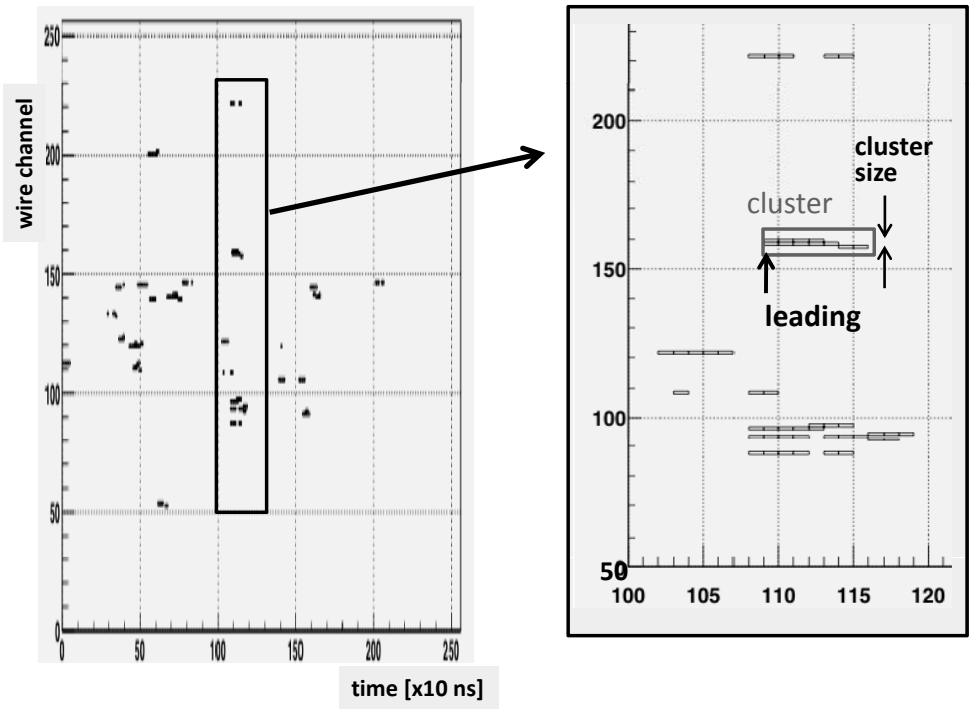

Fig.3. Encoder data of 1 layers for one event.

hits are called a cluster. A leading time and center position of the cluster are inputs of the track-finding algorithm described later.

Distributions of the leading time (of the hit before clustering) at the different operation voltages are shown in Fig.4. At -2.3 kV, where an efficiency is not sufficient, peak position is slightly delayed and a width is larger than that for others. However, at -2.5 and -2.6 kV, where an efficiency is almost 100%, the width is $\sim$20 ns (FWHM). This width is well understood from the time constant of ASD (16 ns) and the spread of the initial ionization. A board peak exists at $\sim$60 ns later of the narrow one. As higher voltage, a count of the broad peak increases. The wire which gives the broad peak is next to the wire which makes the narrow one. Thus, this broad peak may be caused by the UV photon from the initial avalanche.

Since two sets of the MWPC/MWDC are installed at the upstream and downstream of the K1.8BS, there are 12 layers in each straight track regions of the upstream and downstream parts of K1.8BS. Track-finding algorithm requires $\geq$4 hits in U and V layers and $\geq$8 hits in total out of 12 layers, and fits these positions by a straight track with 4 parameters.

As the beam rate increases, a number of hits also increases. Accordingly a number of the combinations to be fitted increases exponentially. At present this limits practically acceptable rate. The track finding efficiency in the upstream part of K1.8BS (MWPC) was 80% in the highest rate condition in the commisioning. Instantaneous rate was estimated from the accidental rates of MWPC. Due to the beam profile, the rate depends both on the wire position and layer. The maximum rate was 130 kHz/wire at

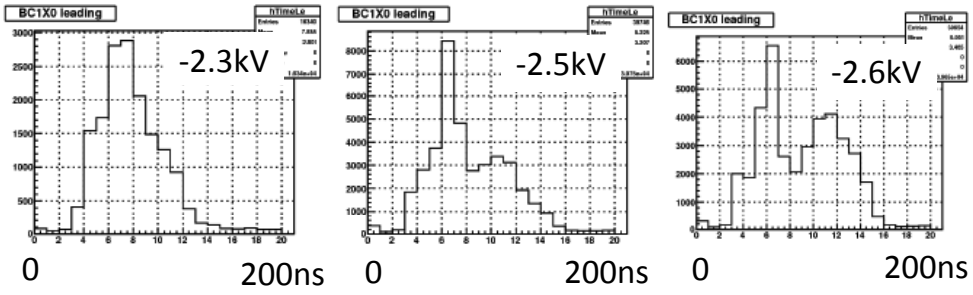

Fig.4. Distribution of the leading edge time. The operation voltages are displayed in the histograms.

the first layer of the MWPCs. Total rate, integrated over the wires in the layer, was 8 MHz.

In summary, we have developed 1 mm spacing MWPC and 3 mm spacing MWDC for the K1.8 beam line tracking detectors as well as their readout system. In the developments, beam tests were performed twice at the test beam line in LNS. These detectors and readout system are in operation at K1.8 beam line of J-PARC.

Acknowledgment

The authors thank the staffs at LNS for their kind supports for the beam operation. They also acknowledge the members of electronics group at KEK for their efforts to develop the readout system. These detectors and readout system were constructed by Grant-In-Aid for Scientific Research on Priority Area, ”Multi-Quark System with Strangeness”.

References

[1] T.Fukuda *et al.*: Nucl. Inst. Meth. **A361** (1995) 485.

[2] O.Sakaki and M.Yoshida: IEEE Trans. Nucl. Sci., vol 46 (1999) 1873.

[3] Y.Igarashi, *et al.*: IEEE Trans. Nucl. Sci. vol 52 (2005) 2866.

(LNS Experiment : #2601, #2626)

国際宇宙ステーション搭載用電子，ガンマ線観測装置 (CALET) の基礎開発

鳥居祥二 [1], 小澤俊介 [1*], 清水雄輝 [1], 田村忠久 [2], 赤池陽水 [1], 植山良貴 [1]

[1] 早稲田大学理工学術院総合研究所 (169-8555 新宿区下大久保 3-4-1)
[2] 神奈川大学工学部（221-8686　横浜市神奈川区六角橋 3-27-1）

The basic development of Calorimetric Electron Telescope (CALET) for the observation on ISS

TORII, Shouji[1], OZAWA, Shunsuke[1*], SHIMIZU, Yuki[1],
TAMURA, Tadahisa[2], AKAIKE, Yosui[1], and UEYAMA, Yoshitaka[1]

[1]*Research Institute for Science and Engineering, Waseda University, Shinjuku, 169-8555*
[2]*Institute of Physics, Kanagawa University, Yokohama 221-8686*

The CALET project aims the investigation of high energy universe by observing cosmic-rays, which will be carried out onboard the Japanese Experiment Module of the International Space Station. In this experiment, we tested the detector performance of the γ ray observation in the GeV region. A prototype detector of CALET was irradiated to the GeV*gamma* beam from STB ring at LNB. We confirmed the capabilty of detecting gamma-rayswe , and clarified that the experiment results are compatible with simulations in the angular resolution and the energy resolution.

CALET 計画は，国際宇宙ステーション日本実験モジュールに搭載し，宇宙線の総合的な観測を行うことで高エネルギー宇宙の解明を目指している．本実験では，GeV 領域での γ 線の検出性能を検証するため，CALET のプロトタイプ検出器を用い，核理研 STB リングからの GeVγ 線の照射を行った．この結果，CALET は γ 線の検出に十分な性能を有することが確認され，角度決定精度及びエネルギー分解能において，シミュレーションと矛盾のない性能が実現できていることが明らかになった.

§1．宇宙線電子線望遠鏡（CALET) 計画

高エネルギー天体現象を起源とすると考えられる宇宙線の加速や伝播の機構は，まだ未解決な重要な宇宙科学の課題となっている．その理由の一つとして，宇宙線はエネルギーの増大とともに急速に現象するため，粒子種別の決定が可能な直接測定を高エネルギー領域で行うためには，大型装置による長期間のスペース実験が必要となるためである．我々はこのような困難を克服するため国際宇宙ステーションにおいて，CALET による観測を提案し JAXA によって日本実験棟「きぼう」の船外実験プラットフォームへの

*Present address: Research Institute for Science and Engineering, Waseda University, Shinjuku, 169-8555

2013 年の打ち上げが承認されている.

検出器部分の主な構成は，入射粒子のトリガーとシャワー初期発達段階の粒子飛跡検出を行ない，入射粒子の電荷の有無や到来方向を決定するシンチファイバーを利用した撮像型カロリーメータ (IMC) と，エネルギー測定を行う無機シンチレータを使った全吸収型カロリーメータ (TASC) によって構成されている. 力ロリーメータに加え，原子核成分の弁別を行うために，セグメント化したプラスチックシンチレータを用いた電荷測定装置 (CHD) を搭載する．検出器の概要図を第 1 図に示す．宇宙空間で最長 5 年間という長期間にわたり行うことで，宇宙線や γ 線の直接観測を実施し，高エネルギー宇宙線の加速・伝播機構の解明や，暗黒物質の探索を実施する.

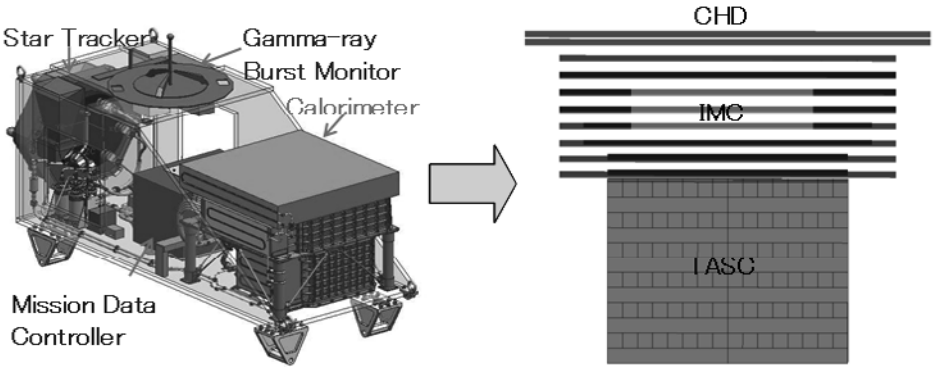

第 1 図　CALET の概要図．左はカロリーメータ部の構造図

§2．実験の概要

本実験では，観測対象の一つである GeV 領域のガンマ線の検出能力を検証するため，ビーム実験用に製作した CALET プロトタイプ検出器に核理研 STB リング加速器によるガンマ線照射試験を行なった．第 2 図にプロトタイプ検出器の構造図を示す.

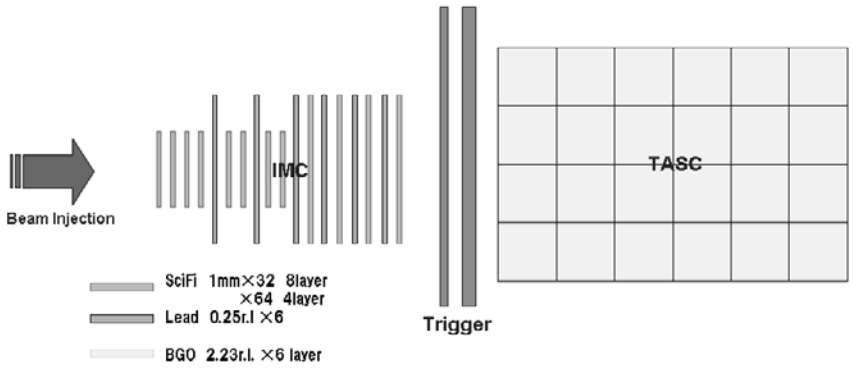

第 2 図　試験に用いた検出器の構造図.

プロトタイプ検出器の IMC 部分は 1mm 角のシンチファイバー (SciFi)32 本からなる層が 4 層，64 本からなる層が 8 層と，0.25r.l. の鉛プレート 6 層で構成されている．各 SciFi は 64 チャンネルマルチアノード光電子増倍管 (MaPMT) によって，独立に読み出される．また，各 MaPMT の出力信号は，ASIC を用いた前置回路システム (FEC) によって AD 変換される．

TASC 部分は 25mm×25mm×320mm の無機シンチレータ BGO を 4×6 本積層した構造である．各 BGO からの信号は PIN フォトダイオードで読み出され，Peak hold 型の ADC で AD 変換される．

トリガーにはプラスチックシンチレータからの出力と，ビームラインからのエネルギータグ信号との同期信号によって生成した．エネルギータグ信号は 0.75GeV∼1.1GeV の 6 種類の信号の論理和を用いた．

1 回目の照射試験は平成 19 年 9 月に行われ，主に，ビーム測定のための基礎データ収集を行った．その結果を参考にして，２回目の照射実験を平成 20 年 9 月に行い，ガンマ線に対する性能テストを実施した．最初の試験の結果から，イベントのパイルアップを避けるため，ビーム強度は 30∼50Hz と低く設定した．特にエネルギータグの付いたイベントに対しては，複数のイベントの同時入射を除去するために，回路系で VETO 信号を用いた．収集イベントは，エネルギータグの付いたものを 180 万イベント，タグ無しのイベントを 50 万イベントをそれぞれ取得した．第 3 図に取得したイベントの例を示す．

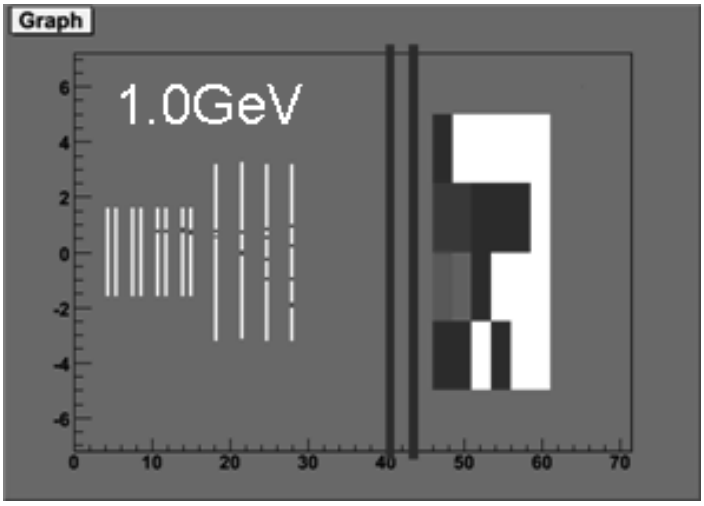

第 3 図　1GeV のときのイベント例．初めのほうの層（上層）では飛跡が検出されていないことから，γ 線であることがわかる

§3．角度分解能及びエネルギー分解能の評価

γ 線が IMC に入射した場合，4 層目までにはコンバータとなる鉛を設置していないため，下層 4 層の SciFi からのデータを用いて飛跡再構成を行った．この再構成された飛跡の角度分布をとり，ここでは正規分布へのあてはめを行って標準偏差を角度分解能としている．また，これら測定結果との比較のため，モンテカルロシミュレーションを用いて検出器を構成し，検証を行った．検証の結果，角度分解能は第 4 図のようになり，1GeV で 1.2° と，シミュレーションと矛盾しない結果となった．

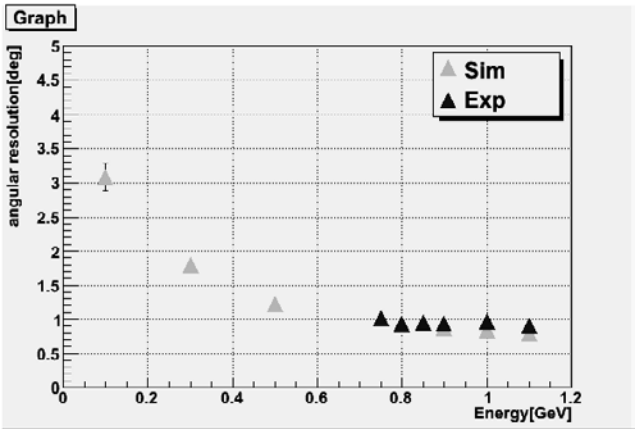

第 4 図　各エネルギーごとの角度分解能

同様に，1GeV における TASC でのエネルギー損失の分布のモンテカルロシミュレーションとの比較を第 5 図に，また，エネルギーごとに比較した場合を第 6 図に示した．

シミュレーションと比較した場合，実験データでは，エネルギー分解能が ∼2% 程度落ちている．これは，イベントのパイルアップとシャワーの漏れ出しによって起こると推定される．また，低エネルギーで分解能が悪くなる傾向があるが，これは，タギングされたイベントに，0.5GeV 程度のバックグラウンドが存在しているためである [4].

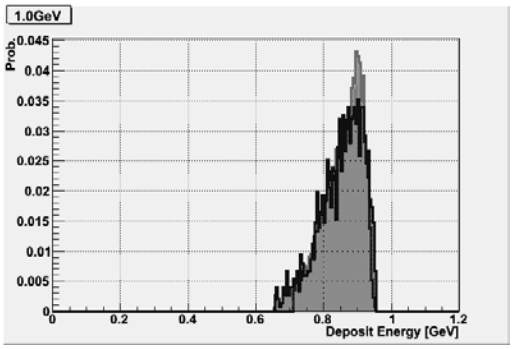

第 5 図　1.0GeV での TASC における吸収エネルギー分布．グレーがシミュレーション，黒が実験によるもの．

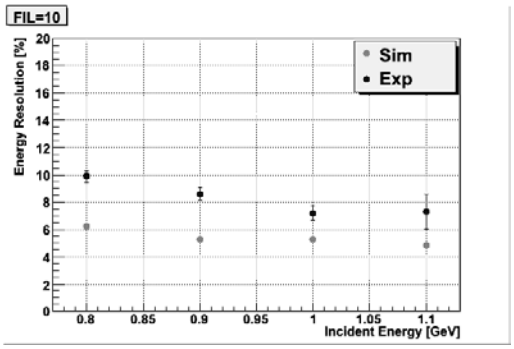

第 6 図　各エネルギーごとのエネルギー分解能の比較．

§4．ま と め

東北大学核理研 GeVγ 線ビームラインにおいて，CALET の構成検出器である IMC 及び TASC の γ 線検出における性能実証実験を行った．

IMC の角度分解能に関して，1.0GeV で 1.2° とシミュレーションと矛盾のない結果が得られた．また，TASC のエネルギー分解能に関してもイベントのパイルアップやコンタミで予想できる範囲内で矛盾しない結果が得られた．

現行の検出装置では，搭載重量の制限をクリアするため検出器本体のダウンサイジングがなされた．この際，γ 線照射実験の結果も踏まえ，基礎的な検出器構成にも更新がなされており，ペイロードに対する厳し

い制限のある飛翔体観測において，少ない体積，重量で，より効率的にエネルギー測定が行えるよう検討したものである．変更点としては，IMC のターゲットにはタングステンを採用し，厚さの比率を上層では 0.1r.l.，下層 2 層は 1r.l. とした．また，TASC に使用するシンチレータには，BGO に代わり PWO を採用した．このことにより，IMC での角度決定精度と TASC でのエネルギー分解能の向上が見込める．これらの性能評価には，本実験で較正されたシミュレーションを用いている．

現在，CALET は平成 25 年の打ち上げを目指し，開発作業を進めている．今後は，加速器による試験も含め，CALET 本体の試作品，実際のフライトモデルでの実証・較正試験を予定しており，更なる性能向上と高精度観測を目指す．

謝　辞

東北大学電子光理学研究センター 清水 肇センター長，山崎 寛仁助教には，実験の実施に際してサポートをいただきました．この実験が所期の目的を達成できたのは，両氏のサポートによるものであり，深く感謝いたします．

参　考　文　献

[1] Kobayashi *et al.*: ApJ **601**, (2004) 340.
[2] J. Chang *et al.*: Nature, **456**, 7220, (2008) 362.
[3] S. Torii *et al.*: SPIE **7021** (2008) 702114
[4] T. Ishikawa *et al.*:Nucl. Instr. and Meth. A**622** 1 (2010) 1

(LNS Experiment : #2602)

Beam test of an improved PWO crystal

S. Kuwasaki[1], T. Ishikawa[1], Y.C. Han[2], R. Hashimoto[1], J. Kasagi[1], K. Nawa[1], Y. Okada[1], M. Sato[1], H. Shimizu[1], K. Suzuki[1], H. Yamazaki[1], and T.S. Wang[2]

[1]*Laboratory of Nuclear Science (LNS), Tohoku University, Sendai 982-0826, Japan*
[2]*Department of Nuclear Science, Lanzhou University, Lanzhou 730000, China*

Meson photoproduction experiments are planed to study nucleon resonances with a large solid angle electro-magnetic (EM) calorimeter complex FOREST at Laboratory of Nuclear Science, Tohoku University. Three types of EM calorimeters are employed in FOREST: pure CsI crystals, lead scintillating fiber modules (Lead/SciFi), and lead glasses. The energy resolutions of the Lead/SciFi and Lead/Glass calorimeters are not so high, and the gaps of EM calorimeters lose the acceptance for the reactions of interest. Thus, the replacement of FOREST with a homogeneous inorganic scintillators is desired.

A $PbWO_4$ (PWO) crystal is a candidate of a new EM calorimter. Although PWO has a good energy resolution at high energies, it has a relatively small light output. Recently, we obtain an improved PWO crystal which impurities are doped to increase the light output. The improved PWO crystal is expected to have the better energy resolution due to the larger light output. In this report, the performance of an improved PWO crystal was investigated by using momentum-analyzed 200–800 MeV/c positrons.

§1. Introduction

Meson photoproduction experiments are planed to study nucleon resonances with an EM calorimeter complex FOREST at Laboratory of Nuclear Science (LNS), Tohoku University. FOREST consists of three types of EM calorimeters: pure CsI crystals, lead scintillating fiber modules (Lead/SciFi), and lead glass Čerenkov counters. Although the pure CsI crystal is an inorganic scintillator and it has the better energy resolution for several hundred MeV photons, the Lead/SciFi and a lead glass calorimeters have poor energy resolutions. A 4π homogeneous inorganic scintillator calorimeter is desired for the precise measurement of photoproduction reactions.

A lead tungstate $PbWO_4$ (PWO) is one of the widely used inorganic scintillators. Compared to other scintillating crystals, PWO has several superior characteristics [1]: a high density of $\rho = 8.2$ g/cm^3, a short radiation length of $X_0 = 0.92$ cm, and a fast decay time ($\tau = 10$ ns). Although PWO has a good energy resolution at high energies, the energy resolution is not so high for several hundred MeV photons [2] due to the small light output. The light output of PWO is only 4%–5% of that of BGO [3]. Recently, we obtain an improved PWO crystal which impurities are doped to increase the light output. The improved PWO crystal is expected to have the better energy resolution due to the larger light output. The beam test of an improved PWO crystal has been carried out with 200–800 MeV/c positron beams.

§2. Experimental Setup

The energy resolution of an improved PWO crystal with a size of $22 \times 22 \times 180$ mm^3 was measured at the positron beamline for testing detectors. The momentum of the positron beam ranges from 200 to 800 MeV/c. Since we have obtained one improved PWO crystal, a prototype calorimeter was constructed being surrounded by 8 $Bi_4Si_3O_{12}$ (BSO) crystals with the same size of the PWO one. Each crystal was connected to a 3/4-inch photo-multiplier tube Hamamatsu R4125GMOD. In order to compare the performance of the improved PWO crystal to other one, the calorimeters which the central crystal is replaced with a nominal PWO and BSO crystals with the same size of the improved PWO one were also tested. Fig 1 shows the photo of tested three crystals.

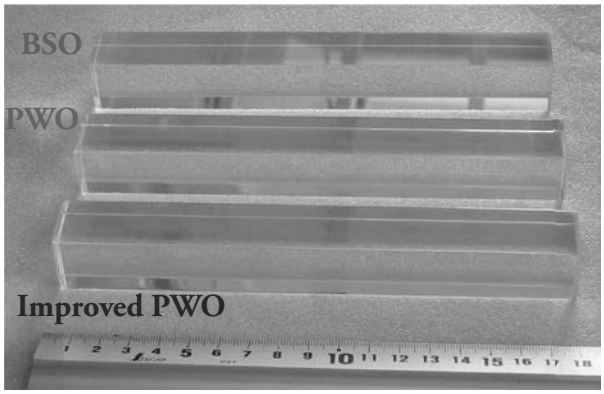

Fig.1. Photo of tested three crystals: BSO, PWO, and improved PWO. The size of each is $22 \times 22 \times 180$ mm^3.

Positrons with energies ranging from 200 to 800 MeV/c were used as incident beams. To determine the incident position of the positrons, a beam profile monitor (BPM) was used. The BPM consists of two layers of scintillating fiber (SciFi) hodoscopes and 16 SciFi's with a cross section of 3×3 mm^2 were aligned in each hodoscope. The upstream and downstream layers determine x and y positions from responding fibers, respectively. Fig. 2 shows the experimental setup for the energy resolution measurement of the calorimeters.

The trigger condition of the data taking system was described as

$$[x \text{ fiber OR}] \otimes [y \text{ fiber OR}], \tag{1}$$

where $\otimes$ stands for the coincidence of signals. The maximum trigger rate was 3 kHz and a fraction of accidental coincidence events was negligibly small.

§3. Waveform

The waveform was measured with a digital phosphor oscilloscope DPO-4104 by using 589, 673, 744, and 800 MeV/c positrons injected onto the central region (33 mm^2) of each crystal. The photomultiplier tube (PMT) used is the same for three crystals, and the same high voltage (-1169 V) is supplied to it. Fig. 3 shows the measured waveform of three crystals by using 589 MeV/c positrons.

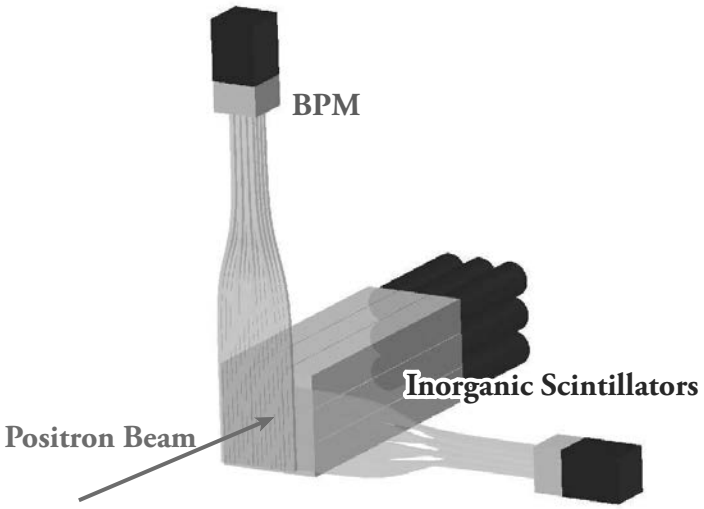

Fig.2. Experimental setup for the performance measurement of an improved PWO crystal. It is surrounded by 8 BSO crystals with the same size of the improved PWO one. The 16×16 scintillating fiber hodoscopes are placed in front of a calorimeter to determine incident positions of positrons.

The light output was estimated by integrating the pulse height form -200 to $+600$ ns. Table 1 summarizes the relative light outputs of the improved PWO and BSO crystals to the PWO one. Since the waveform of each crystal was taken once at every incident momentum, the deduced light output has a fluctuation coming from the energy resolution discussed in §4. The improved PWO crystal has a three times larger light output as compared with the nominal PWO one.

Table 1. Relative light outputs of the improved PWO and BSO crystals to the PWO one.

Momentum (MeV/c)	Improved PWO	BSO
589	2.4	12.2
673	3.1	14.1
744	3.4	13.4
800	3.2	12.2

The decay times of three crystals were roughly estimated by fitting the waveform with an exponential function from 20 to 500 ns. The decay times obtained were 14.5 ± 0.2, 20.1 ± 0.1, and 112.8 ± 0.9 ns for the PWO, improver PWO, and BSO crystals, respectively. The improved PWO has a longer decay time as compared with the nominal PWO.

§4. Energy Resolution

The energy resolution of three crystals was measured by using 200, 457, 673, and 800 MeV/c positrons injected onto the central region (3×3 mm^2) of each crystal. Fig. 4 shows the ADC distributions for three crystals. The ADC distributions are asymmetric due to the energy leakage in the lateral direction. Thus, the ADC distribution in each measurement was fitted with a logarithmic Gaussian [4], and

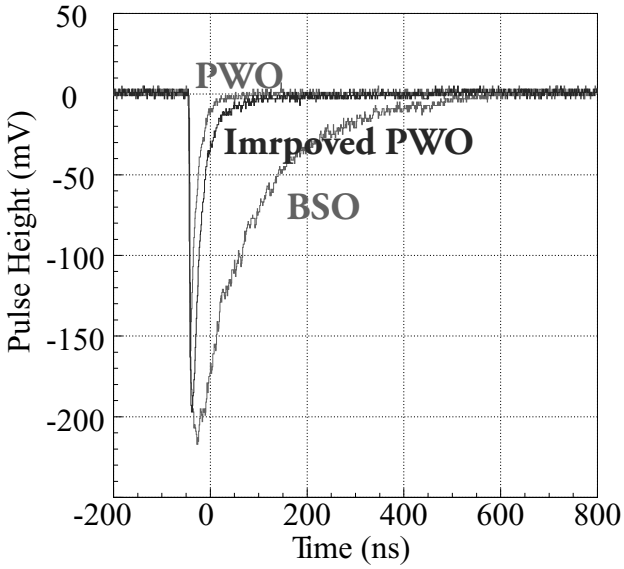

Fig.3. Measured waveform of three crystals by using 589 MeV/c positrons.

the mean μ_c and width σ_c were determined.

The pedestal distribution was measured with a 100 Hz clock signal trigger in each measurement, and the mean μ_p and width σ_p of which were determined by fitting with a nominal Gaussian. The energy resolution of each crystal σ_E/E is calculated by

$$\left(\frac{\sigma_E}{E}\right)^2 = \left(\frac{\sigma_c}{\mu-\mu_p}\right)^2 - \left(\frac{\sigma_b}{\mu_b}\right)^2 - \left(\frac{\sigma_0}{\mu-\mu_p}\right)^2, \tag{2}$$

where σ_b/μ_b stands for the beam energy spread given in Ref. [5]. Since the energy leakage in the lateral direction exists, the obtained energy resolution with one crystal is not so high. Fig. 5a) shows the energy resolution of three crystals as a function of the incident positron energy.

The energy resolutions obtained were fitted with a function

$$\left(\frac{\sigma_E}{E}\right)^2 = \left(\frac{a_1}{\sqrt{E}}\right)^2 + (a_0)^2. \tag{3}$$

The a_0 and a_1 parameters are the coefficients for the constant and statistical terms. Table 2 shows the fitted parameters of the function (3) to the energy resolution.

Table 2. Fitted parameters of the function (3) to the energy resolution.

Crystal	a_0	a_1
PWO	0.0000±00.0045	0.0551±0.0003
Improved PWO	0.0000±00.0137	0.0539±0.0003
BSO	0.0000±00.0056	0.0609±0.0004

The coefficient a_0 for the constant term is zero for all the crystals, suggesting that the number of detected photoelectrons with PMT is very small. To compare the energy resolutions of the improved PWO crystal to the PWO one directly, the difference of the energy resolution square was obtained. Fig. 5b) shows the difference of the energy resolution squares between the PWO and improved PWO crystals as

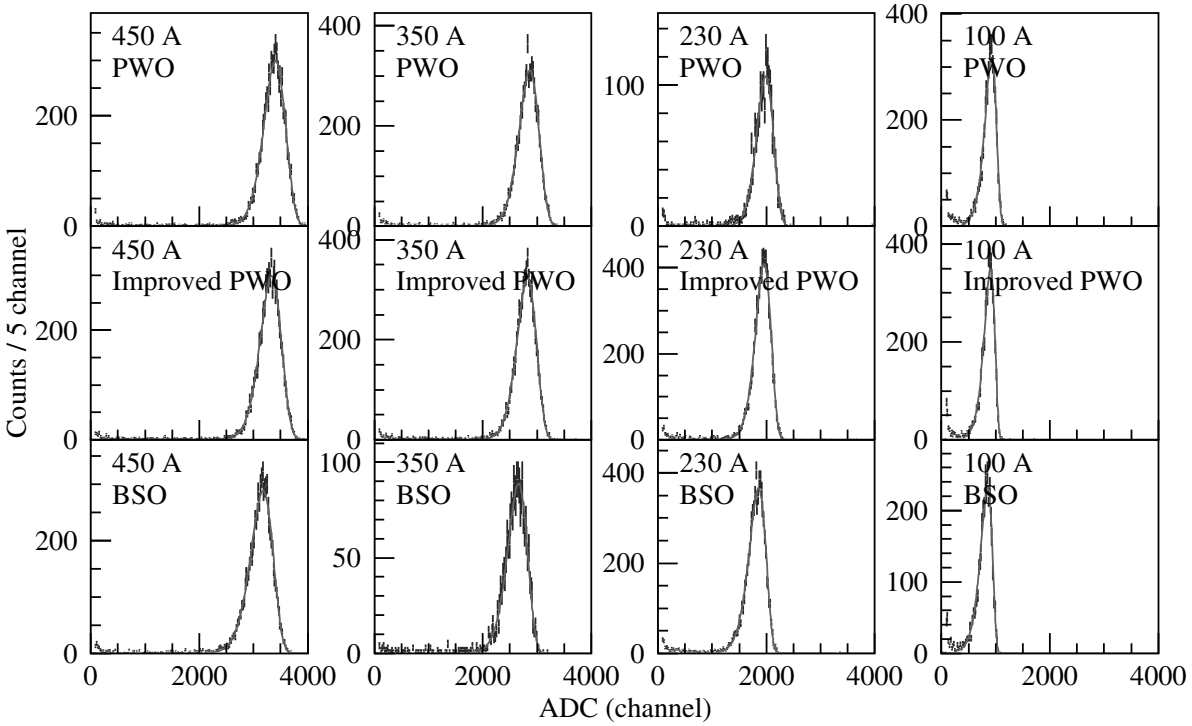

Fig.4. ADC distributions for three crystals. The crystal and the $\mathcal{R}$TAGX current which determines the momentum of the positron beam are described in each panel. The solid curve shows the fitted logarithmic Gaussian.

a function of the incident positron energy.

Ideally, the improved PWO differs only in the light output from the PWO. Thus, the difference of the energy resolution squares are expressed only by the a_1 coefficients for two crystals:

$$\left(\frac{\sigma_E}{E}\right)^2_{\text{PWO}} - \left(\frac{\sigma_E}{E}\right)^2_{\text{Improved PWO}} = \frac{a^2_{1(\text{PWO})} - a^2_{1(\text{Improved PWO})}}{E} \tag{4}$$

because the other terms are common for both the PWO crystals. The difference was fitted with a function being proportional to $1/E$, and

$$a^2_{1(\text{PWO})} - a^2_{1(\text{Improved PWO})} = (1.25 \pm 0.05) \times 10^{-2} \tag{5}$$

was obtained. The obtained $a^2_{1(\text{PWO})} - a^2_{1(\text{Improved PWO})}$ was consistent with the value given by the individual fitting results of the energy resolution as a function of the incident energy.

Since the light output of the improved PWO is about three times as large as that of the nominal PWO, the coefficient for the statistical term a_1 for the improved one is expected to be $1/\sqrt{3}$ of that for the nominal one. The difference of a_1 between two PWO's is not as large as expected. There might be a problem of the light output uniformity in the improved PWO crysyal. The details of the analysis and discussion are described elsewhere [6, 7].

§5. Summary

We obtain an improved PWO crystal which impurities are doped to increase the light output. The light output of the improved PWO crystal is about three times as large as that of the nominal PWO one.

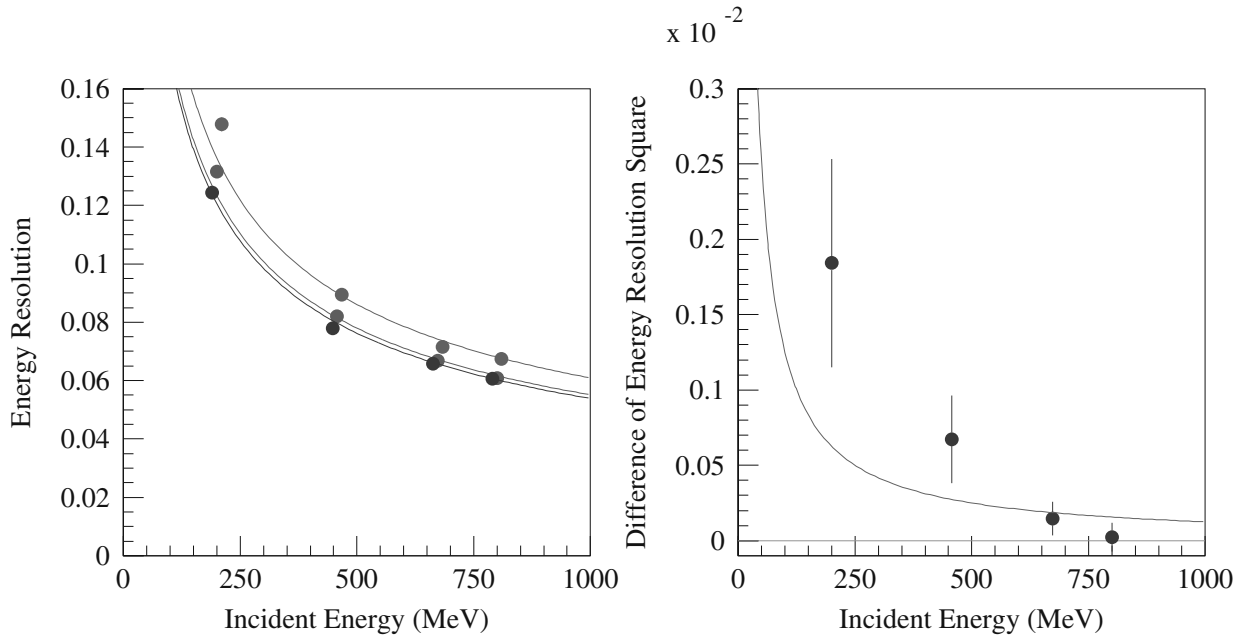

Fig.5. a) Energy resolution of three crystals as a function of the incident positron energy. The solid curves show fitted function (3). b) Difference of energy resolution squares between the PWO and improved PWO crystals as a function of the incident positron energy. The data are compared with $0.0125/E$ where E is given in GeV.

The energy resolution of the improved PWO was measured by using 200–800 MeV/c positrons, and it is higher than that of the nominal one. Yet, it is not as good as we expected from the increase of the light output.

Acknowledgement

This work was supported in part by Grant-in-Aid for Scientific Research (B) (15340069) and for Specially promoted Research (19002003).

References

[1] M. Ishii and M. Kobayashi: Prog. Crystal Growth Charact. **23**, 245 (1991).

[2] H. Shimizu *et al.*: Nucl. Instr. and Meth. A **447**, 467 (2000).

[3] M. Kobayashi *et al.*: Nucl. Instr. and Meth. A **333**, 429 (1993).

[4] H. Ikeda, et al: Nucl. Instr. and Meth. A **441**, 401 (2000).

[5] T. Ishikawa *et al.*: Research Report of LNS **40**, Tohoku University, 6 (2008).

[6] S. Kuwasaki: Internal GeV-γ Analysis Note No. **80** (2007).

[7] T. Ishikawa: Internal GeV-γ Analysis Note No. **200$\mathcal{D}$** (2011).

(LNS Experiment : #2603)

J-PARC E15 実験のためのビーム VETO カウンターの開発

大西宏明[1], 岡田信二[1†], 佐久間史典[1], 藤原裕也[1*]

[1] 理化学研究所　先端中間子研究室 （351-0198　和光市広沢２－１）

Development for Kaon Decay Veto counter for J-PARC E15 experiment

Hiroaki Ohnishi[1], Shinji Okada[1†], Fuminori Sakuma[1], and Yuya Fujiwara[1*]

[1]*Advanced meson science Laboratory, RIKEN, Wako, Saitama, 351-0198*

The J-PARC E15 experiment is designed to be performed its measurement under high intensity Kaon beam condition (0.8 M K^-/spill(0.7s)) which will be available J-PARC very soon. The main issue for the E15 is the high level background trigger level, especially Kaon decay in flight easily fired our trigger condition. Therefore we need to install new trigger counter to reject fake trigger which is mainly comming from Kaon decay. Therefore we are developing new counter, Kaon Decay Veto counter. In this report, we are presenting conceptual design of KDV and first test results which carried out using positron beam at LNS, Tohoku Univ.

§1. Introduction

1997 年に行われた KEK-E228 実験 (KpX) の結果 [1]は現在、反K中間子ー核子間に強い引力が働いていると理解されている。この結果をもとに、赤石ー山崎は、それまでにも議論されていた“反K中間子ー核子のエネルギー閾値すぐ下に存在するバリオン Λ(1405) はK中間子ー陽子の束縛状態である”という考え方をさらに推し進め、その自然な拡張として、K中間子原子核の存在を予言した [2]。この考えの非常に興味深い点は、非常に強い引力により系内の核子がその斥力芯を超えるほどの高密度の状態を形成する事が示唆される事に在り、そのような状態が見つかればカイラル対称性の理解に大きく貢献する事が期待される。我々は、まず「最も基本的なK中間子原子核」である K^-pp 状態を ^{3}He 標的を使い　In-flight (K-,n) 反応において、直接生成、生成反応に伴う中性子をつかったミッシングマス測定と K-pp 崩壊粒子（Λ+p）の同時計測を行う完全実験を目指した、J-PARC　E15 実験を実施する。

E15 実験の検出器セットアップ、特に Cylindrical Detector Sysytem (CDS) 近傍　を Figure 1 として示す。実験現場である K1.8BR ビームラインスペクトロメータにより ID された入射ビームは、Aerogel counter(AC) によりトリガーレベルで K 中間子として同定、その後、 約８０ｃｍ　下流の ^{3}He 標的にて

*Present address: Univ. of Tokyo

†Present address: INFN-Frascati

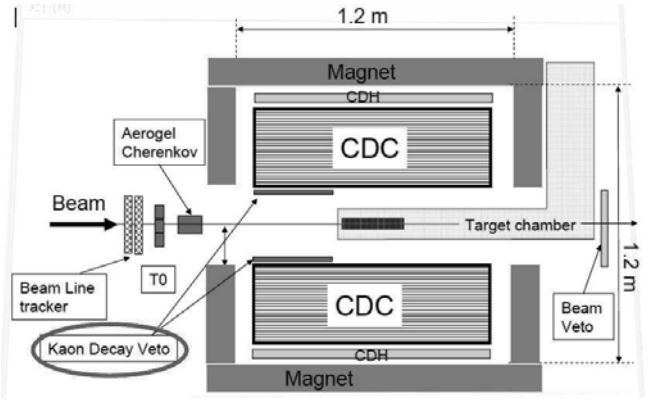

第 1 図　Configuration of the E15 CDS

原子核反応を起こす。目的となる　(K^-,n) 反応で生成される　中性子は 0 度方向に設置する中性子カウンターで検出、反応により生成される 2 次荷電粒子は CDS にて測定する。本実験では、（1）Aerogel によるビーム粒子が K 中間子であることの識別,　（2）前方（0 度方向）に荷電粒子が放出されていないこと、（3）CDS 中に最低 1 つ以上の荷電粒子が検出されることの 3 つをトリガー条件として課し実験を行う。トリガーレベルで予想されるバックグラウンドは最後の AC での Kaon 同定から標的まで、その距離約８０ｃｍの間に崩壊する K 中間子の崩壊、$K^- \to \pi^0\pi^- or \pi^-\nu$　イベントである。E15 実験では、J-PARC 達成できる最高 K 中間子ビーム強度、０．８ M ／ spill(0.7s) での実験実施を想定、トリガー条件を満たす K 中間子崩壊イベントは８０ k/spill(0.7s) に達すると予想される。そこで、このトリガーレベルでのバックグラウンドを効率よく排除するため、われわれは、AC －標的直前の空間を覆うようにシンチレーションカウンター、Kaon Decay Veto Counter (KDV) を設置する。

KDV はソレノイド電磁石内部という非常に限られた空間、さらに磁場中に設置するため、その読み出し方法を工夫する必要がある。そこでわれわれはシンチレーターの板に溝つけ、波長変換ファイバー（WLSF）を埋め込み、WLSF をライトガイドとして使うことで比較的容易に信号をソレノイド外部まで誘導することを考え、検出器の試作を行った。本報告では、この E15 実験に必要不可欠なトリガーカウンターのひとつ、KDV　の性能評価について報告するものである。

§２．テストカウンター概要

テストカウンターは厚さ１ｃｍのプラスチックシンチレーター（EJ-200） と波長変換ファイバー（WLS ファイバー）kuraray Y-11 $\Phi = 1$、光検出器として光電子増倍管　Hamamatsu － R7400 もしくは MPPC から構成される。今回製作した 6 基のテストカウンターは、シンチレーター表面に、長辺方向に沿って彫った溝（深さ 1 mm）にＷＬＳファイバーを渡したもの（surface type）と、2 枚のシンチレーターにそれぞれ 0.5 mmの深さの溝を掘り、ＷＬＳファイバーをそれらで挟み込むもの（sand type）の２つに分けられる。Surface type のカウンターはファイバー数が 1，3，5，7 の 4 種、sand type のカウンターはファイバー数 1,7 の 2 種類である。またファイバーとシンチレーター間は Air couple である。ファイバーと光電子増倍管の間はオプティカル・グリスで埋められており、取り外し可能な構造とした。テストカウンター構成を Figure 2 として示す。

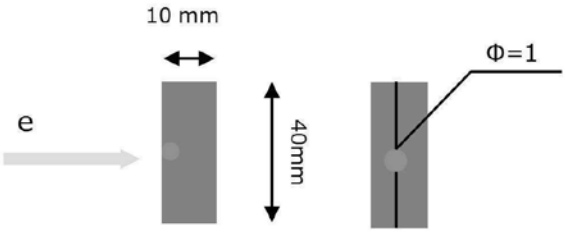

左　surface type；beam はファイバー側から入射する。
右　sand type；5mm 厚のシンチレーターでファイバーを挟んでいる

第 2 図　KDV element 構成

§3．テスト実験セットアップ

テスト実験は東北大学　核理学研究所、400MeV の陽電子ビームを用いて実施した。テスト実験セットアップを Figure 3 として示す。陽電子ビームは Trigger カウンター　T0、T1　で ID し、トリガーとの

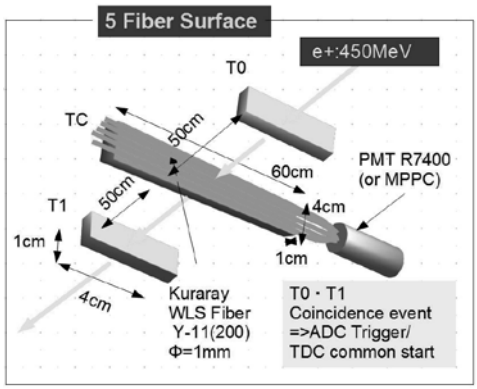

第 3 図　Beam Test setup

コインシデンス条件の下、テストカウンターの pulse hight distribution から検出された光子の数を評価した。ビームタイムにおいては、シンチレータに埋め込むファイバーの数と光子数の関係、粒子入射角度と光子数の関係の測定を行なった。

§4．実験結果

4.1　photon 数とファイバー数の関係

surface type、1，3，5，7 のテストカウンターに対して、400MeV の電子ビームを入射し、放出される光子数をそれぞれ測定した。Figure 4-(a) として、ビームはカウンターの表面中央に対して垂直に入射したときの典型的なアナログ信号を、Figure 4-(b) として　算出した光子数と埋め込んだファイバーの数の関係を示す。結果は予想どおり、ファイバーの本数と光子数は比例関係にあり、ファイバーを 7 本埋め込んだ状態で、３０程度の光子数が見込める。

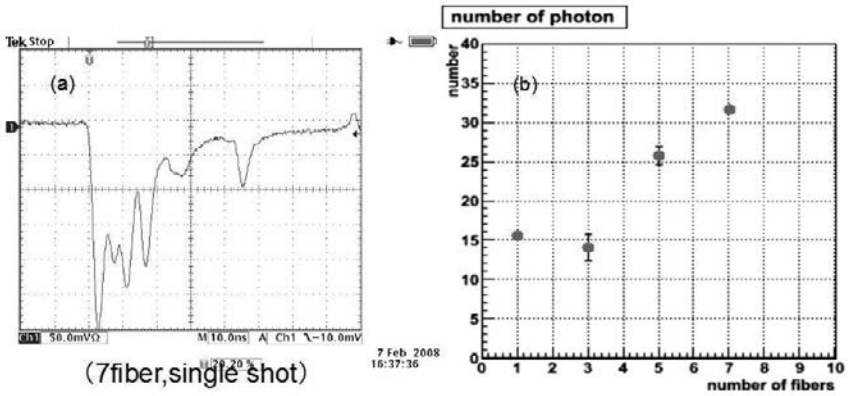

第 4 図　(a) ビームはカウンターの表面中央に対して垂直に入射したときの典型的なアナログ信号,(b) 算出した光子数と埋め込んだファイバーの数

4.2 photon 数とビーム入射位置および角度に対する関係

まず、photon 数とビーム入射位置に関する結果を　Figure 5(a) として示す。カウンターから出てくる光子量をファイバーの Attenuation length $>$ 3.0m より計算すると、55cm の時で 5cm の場合の 86%になるはずである。1 本ファイバーのときは正しいが、5 本ファイバーが入ったカウンターの場合 66%まで落ちていることがわかる。この結果の意味することについては現在検討中である。　ビーム入射角度と得られた光子数に関する結果を　Figure 5(b) として示す。図上のラインは $1/\cos(\theta)$ でフイッティングを行った結果である。結果は予想通りではあるが、光子数は $1/\cos\theta$ に比例していることがわかる。

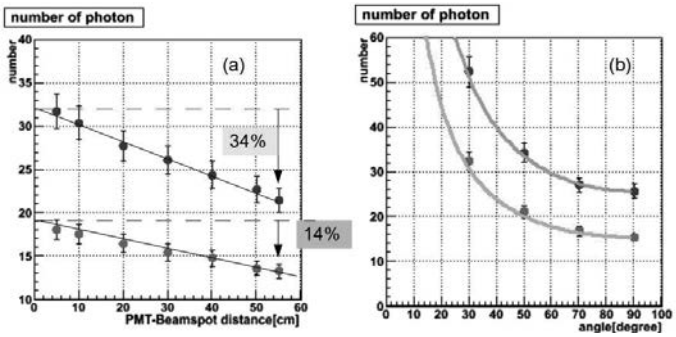

第 5 図　(a)photon 数とビーム入射位置 ,(b) ビーム入射角度と得られた光子数

§5. ま と め

今回、J-PARC　E15 実験用　トリガーカウンターとして、シンチレータ＋ Wave length shifting fiber というカウンターを試作、東北大学　核物理研究所、４００ MeV/c　陽電子ビームを用いその性能評価を行った。基本的な特性を評価した。この結果をもとに、今後実機製作に向けた最終試作機の製作を準備している。

謝　辞

良質な電子ビームを供給していただいた核理研加速器グループの皆様と、実験準備および実施期間中に協力していただいた山崎寛仁博士に感謝いたします。

参　考　文　献

[1] M. Iwasaki et al., Phys. Rev. Lett. **78** (1997) 3067

[2] Y.Akaishi and T.Yamazaki, Phys. Rev.C **65** (2002) 044005, Phys. Lett. B535 **70** (2002) 76

(LNS Experiment : #2604)

Avalanche photo-diode (APD) readout of the CsI(Tl) electro-magnetic calorimeter for J-Parc E06 experiment

J. Imazato[1], M. Hasinoff[2], Y. Igarashi[1], A.P. Ivashkin[3], S. Shimizu[4], and H. Yamazaki[5]

[1]*IPNS, High Energy Accelerator Research Organization (KEK), Tsukuba 305-0801, Japan*
[2]*Department of Physics and Astronomy, University of British Columbia, Vancouver, BC, Canada*
[3]*Institute for Nuclear Research, Russian Academy of Sciences, Moscow 117312, Russia*
[4]*Department of Physics, Osaka University, Osaka 560-0043, Japan*
[5]*Laboratory of Nuclear Science, Tohoku University, Sendai 982-0826, Japan*

The test experiment for the APD readout of the CsI(Tl) electro-magnetic calorimeter for J-Parc E06 (TREK) experiment have been carried out with a single CsI(Tl) module. The necessity of the development of the new current amplifier was confirmed.

§1. TREK experiment

The J-Parc E06 (TREK) experiment aims to search the time reversal violation by measuring the transverse muon polarization (P_T) in the $K^+ \to \pi^0 \mu^+ \nu$ ($K_{\mu 3}$) decay of stopped K^+ meson at the K1.1BR beam line in the J-Parc Hadron hall [1]. P_T is T-odd observable and expected to be little affected by final state interactions between the decaying particles and therefore the non-zero value of the P_T is a signature of the time reversal violation. The world record of the upper bound is $|P_T| < 0.0050$ (90% C.L.) measured by the KEK-PS E246 collaboration, which is mainly limited by the statistics [2]. The K^+ beam intensity at J-Parc is expected to be about ten times larger than KEK-PS, thus the TREK experiment was proposed as a natural extension of E246 experiment. This proposal ware approved as Stage-1 (Scientific approval) by the PAC1 for Nuclear and Particle Physics Experiments at the J-Parc.

The detector system is an upgraded version of the KEK-PS E246 experiment [3]. The momentum of the decaying muons are analysed by the super-conducting Toroidal magnet spectrometer, and the transverse polarizations of the decaying muons are measured by the polarimeters which are installed behind the spectrometer gaps. The direction of the decay plane is determined by the momentum vector of the decaying neutral pion which is detected by the CsI(Tl) barrel counter.

§2. CsI(Tl) barrel counter

Photons from the decaying π^0 mesons are detected by the photon calorimeter: a barrel of 768 CsI(Tl) crystals (Fig. 1) surrounding a kaon stopping target. There are the two beam entrance and exit holes and 12 so-called muon holes that positrons and muons pass into the spectrometer gaps through at the side face. The geometrical acceptance of the CsI(Tl) barrel is 75% of 4π. The thickness of each CsI(Tl)

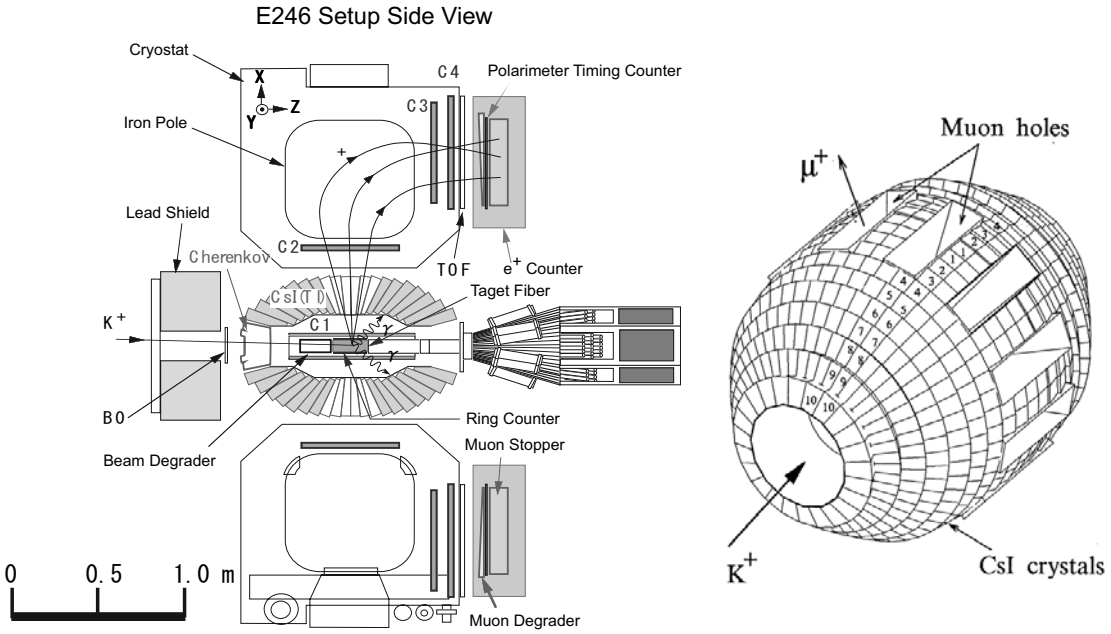

Fig.1. The side view of the E246 detector system and the photon calorimeter with 768 CsI(Tl) crystals.

crystal is 25 cm which corresponds to a radiation length of 13.5 X_0. Each crystal covers 7.5° in both polar and azimuthal angles except for the nearest region to the beam axis, where the azimuthal angle is doubled to 10°. The shapes of the crystals are trapezoidal basis pyramidal sectors. There are 10 different dimensions; the average transverse dimensions are 3×3 cm for the front end and 6×6 cm for the rear end. The light output had been read via PIN photo diodes. The average light yields are 10^4 p.e./MeV with S3204-03 (Hamamatsu,18×18 mm^2). The equivalent noise level is about 70 keV with the shaping time of 1 μsec. The energy of the incident photon is determined by the sum of the light yields of the central crystal and its peripherals. The performance of the CsI(Tl) calorimeter in E246 experiment has been reported in the reference [4] .

§3. APD readout of CsI(Tl)

The APD readout of the CsI(Tl) calorimeter have been developed for the J-Parc E06 experiment in which the very high counting rates is expected. The width of the output signal from the shaping amplifier almost reached 10 μsec with the PIN diode-shaping amplifier readout scheme. Thus the maximum counting rate of the each CsI(Tl) module is limited upto a few 10's kHz. The counting rate at the TREK experiment is expected to be about 20 times larger than the E246 experiment, which corresponds to about a few hundreds kHz. Considering these conditions, we planed the replacement of the PIN diode to the avalanche photo-diode (APD). The APD is a photo-sensor device which has the self-amplification mechanism. The internal gain of some 50 for the output charge makes the pre-amplifier system simpler and faster. The development of the pre-amplifier have been done by Russian group led by A.P. Ivashkin

at the Institute of Nuclear Research, Russian Academy of Science, Moscow.

3.1 Prototype test with positron beam

In order to check the performance of the APD read out of CsI(Tl), the test experiment with the positron beam have been carried out in 4th, Dec. 2007 at Laboratory of Nuclear Science(LNS), Tohoku University. The GeV-γ beam line at LNS provides the positron beam with its energy from 100 MeV/c to 750 MeV/c and its resolution of less than few %.

A positron beams with their momentum of 100, 150, 250, 300, 350, 399, and 458 MeV/c bomberded a single CsI(Tl) cryatal and a beam profiling counter which was installed in front of a crystal. It consists of two layers of a scintillating fiber hodoscope. Each layers which comprises 16 fibers with their cross setions of 3×3 mm^2 determined the vertical and the horizontal position. Four central filbers of both layers were used as the DaQ trigger. One of the CsI(Tl) crystal of the the barrel calorimeter was selected as a test module. We used two types of APD chip to decide which is better for our experiment: 5×5 or 10×10 mm^2. Both APD chips are made by Hamamatsu photonics (HPK), and their products number are S8148-0505 and S8148-1010 for 5×5, 10×10 cm^2 APD's, respectively. Although both APD chips were bombarded by positrons in this experiments, it is easier to control the noise level and the gain parameter for 5×5 APD chip. The following discussions are the result of the experiments with the 5×5 mm^2 APD chip. The signal from the APD chip was fed to the amplifier. The shapes of the output signal from the amplifier were recorded by the FADC, FINESSE on the COPPER system, which was driven by the 50 MHz clock generator.

3.2 Linearity and energy resolution

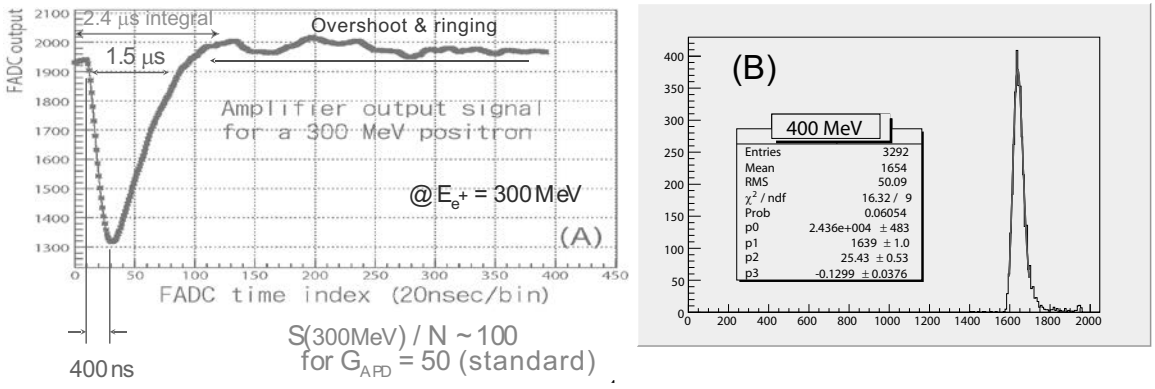

Fig.2. (A) The output signal from the APD-amplifier of the CsI(Tl) crystal., (B) The charge distribution for the 300 MeV positron beam.

In the Fig. 2(A), the wave form of the APD which was optically connected with the CsI(Tl) crystal is plotted for the positron with its energy of 300 MeV. The rise time of the raw signal was about 400 nsec and the full width was about 1.8 μsec. It was about ten times shorter than the width of the PIN diode readout. There was a overshoot and ringing of the signal after 1.8 μsec. The charge distributions of

the APD output for all bombardment energies were deduced by integrating the measured data points from the first to the 120th clock which correspond to the gate width of 2.4 μsec. The charge distribution for each beam energy was fitted by the logarithmic Gaussian [5]. The mean (μ) and the width (σ) ware determined by fitting. The pedestal distribution was measured by the 'off-timing run' in which the timing gate was delayed by 300 μsec from the normal timing with the same condition as the normal run except the gate timing. The mean (μ_p) and the width (σ_p) of the pedestal distribution were determined by the Gaussian fitting. μ_p corresponded to the ground line (no signal) and its value was 1929ch. σ_p was negligible small compared with the σ. The difference between μ and μ_p, and σ for each measurement were regarded as the measured charge integral and its resolution, respectively. In Fig. 2(B), the charge distribution is shown for the 400 MeV positron beam with a fitted result. Fig. 3(A) shows the ratio of the charge integral to an incident positron energy as a function of the beam energies. The error bar corresponds to the fitted error for the mean value of a logarithmic Gaussian. The ratios have almost constant values of 0.79. It means that the output signals have the good linearity in whole energy region. No signature of the saturation on both the APD and the amplifier can be found. The energy resolutions for all measurements as a function of the incident beam energies are plotted in Fig. 3(B). The energy resolutions were well reproduced by the fitting result,

$$(\frac{\sigma}{E})^2 = (0.047 \pm 0.003)^2 + (\frac{0.026 \pm 0.001}{E}^2),$$

where E is the incident beam energy in GeV. The leakage of the EM shower from the lateral surface of a CsI(Tl) crystal caused the higher channel tail of the charge distribution and the large first coefficient of the fitting result. And thus a statistical term could not be fixed by the fitting. The large value of the second coefficient was partly caused by the bad signal to noise ratio of the amplifier.

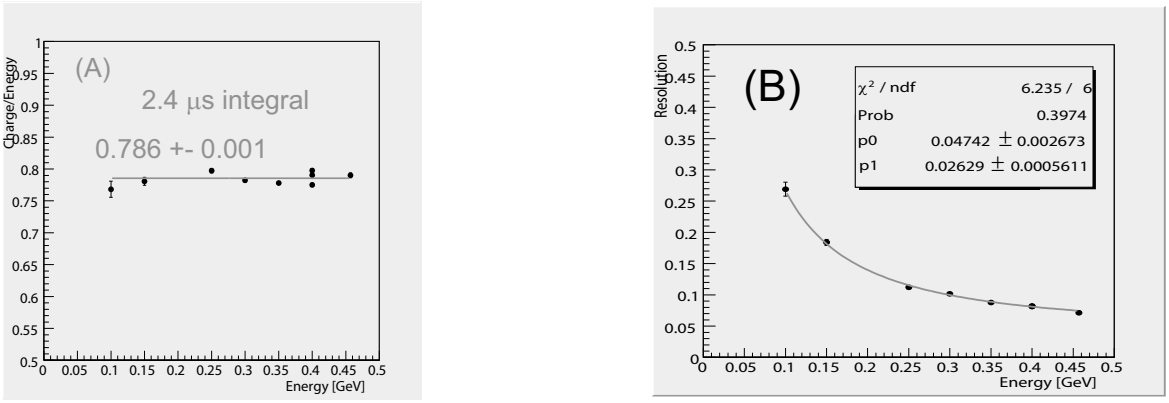

Fig.3. (A) The ratio of charge integral to E_e, (B) the energy resolution measured by CsI(Tl).

3.3 Pile-up analysis

The counting rate of the CsI(Tl) calorimeter is expected to be about a hundred kHz because of the intense K^+ beam at J-Parc. The FADC read out of the APD signal makes possible the off-line analysis of the pile-up event. The capability study of the pile-up analysis have been carried out by the INR

group. About 40,000 pile-up events were accumulated with the intense positron beam of which energy was 200 MeV. Fig. 4 shows the typical examples of the waveform of the pile-up event. The function of

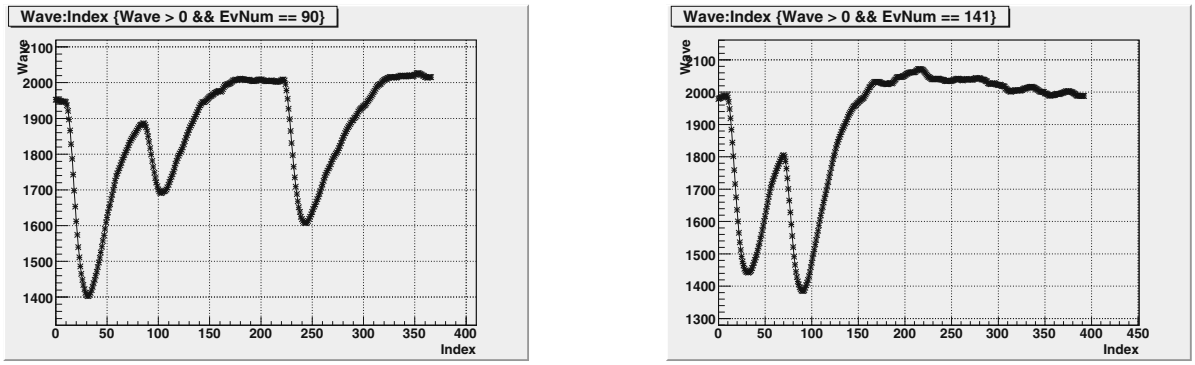

Fig.4. Typical examples of the pile-up events.

the single waveform ($F(x)$) are expressed as,

$$F(x) = p_0 - p_1 e^{p_2 x}(p_3 \cdot \mathrm{erf}(p_4 x - p_5) + p_6),$$

$$\mathrm{erf}(x) = \frac{2}{\sqrt{\pi}} \int_0^x e{-t^2} dt,$$

where $p_0 \sim p_6$ were determined by the fitting of a non-pileup waveform with the low intensity beam. The pile-up signal was fitted by the combination of two waveform functions. The trial function ($f(x)$) is expressed as,

$$f(x) = a_1 F(x) + a_2 F(x + \Delta x),$$

where, a_1, a_2, and Δx are the signal heights for the first and the second signals respectively, and the time difference of the two signals, respectively. Fig. 5(A), (B), and (C) are the pulse height distributions for non-pileup pulse, first (B) and second (C) pulse of the pile-up events, respectively. The shape and the peak position of the first pulse height are almost same as the non-pileup pulse, but the distribution of the second pulse height is completely different. Fig. 5(D) and (E) show the peak positions as a function of FADC clock for the first and second decomposed pulses, respectively. Peak positions for first pulses are almost constant above 60ch corresponding to 1.2 μsec of the time difference between first and second one. It means that we can estimate the correct energy for the first pulse with the time resolution of 1.2 μsec. On the other hand, there seems no constant region in the Fig. 5(E). The overshoot and ringing of the first pulse deteriorate the pulse height information and make troubles in the off-line analysis.

§4. Summary

The test experiment for the APD readout of a CsI(Tl) crystal have been carried out at LNS, Tohoku University, aiming at an establishment of the readout scheme for the TREK experiment at J-Parc. The output signal shape of the APD was very clean for the several hundred's MeV positron beam. But the overshoot and ringing were clearly seen on the output signal from the amplifier. The integral/differential chain in the amplifier circuit is considered as the trouble source. An ideal current amplifier is one of the

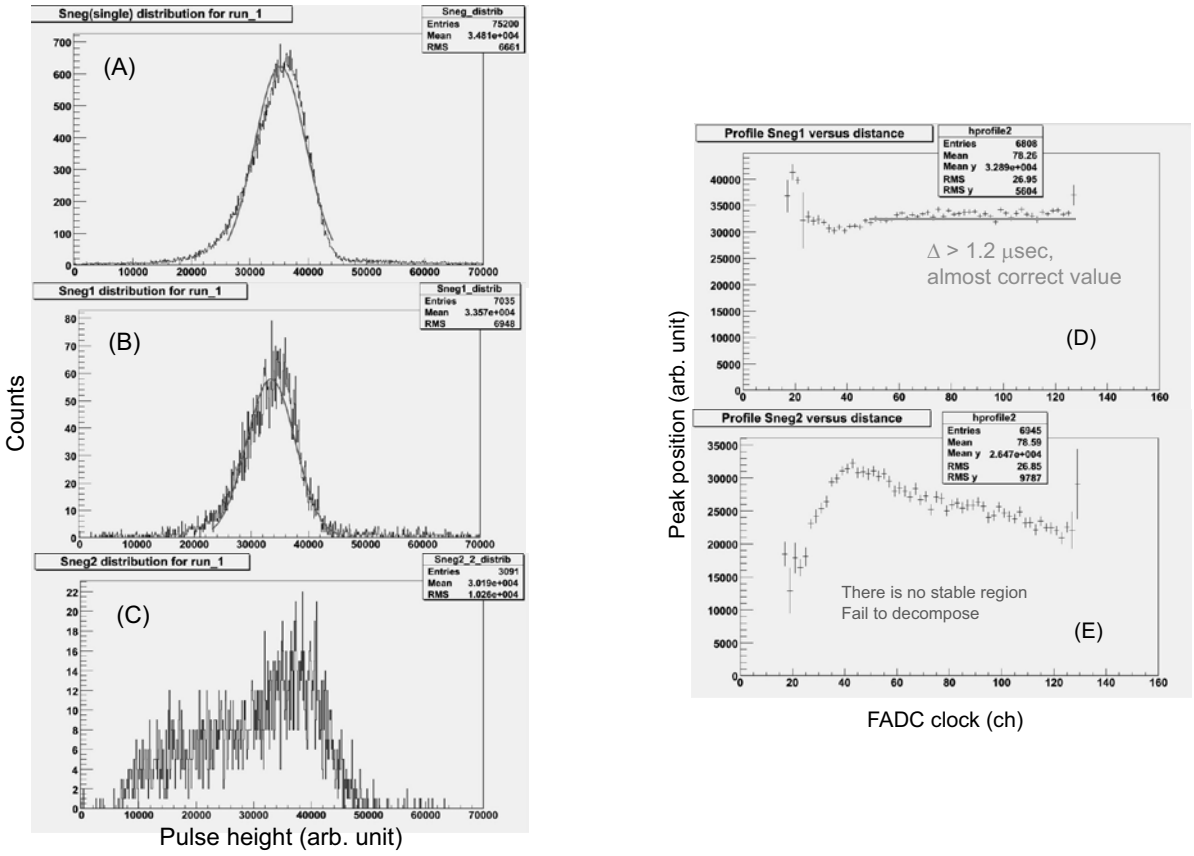

Fig.5. The signal height distributions (left) for non-pileup pulse (A), first pulse (B), and second pulse (C). The peak positions (right) as a function of the FADC clock for first (D) and second (E) pulse.

candidate for the present purpose to meet the requirement of the TREK experiment. The development of the new prototype current amplifier have been completed at INR. The result of the beam test for new amplifier will be appeared soon.

References

[1] J-Parc proposal, http://j-parc.jp/NuclPart/pac_0606/pdf/p06-Imazato_2.pdf.

[2] M. Abe *et al.*: Phys. Rev. **D73** (2006) 072005(1–34).

[3] J.A. Macdonald *et al.*: Nucl. Instrum. and Meath. Phys. Res. Sec. **A506** (2003) 60.

[4] D.V. Dementyev *et al.*, Nucl. Instrum. and Meath. Phys. Res. Sec. **A440** (2000) 15.

[5] H. Ikeda *et al.*: Nucl. Instrum. and Meath. Phys. Res. Sec. **A441** (2000) 401.

(LNS Experiment : #2624)

Energy resolution of a test LNS-type pure CsI crystal calorimeter

A. Nakamura[1], T. Ishikawa[1], H. Fujimura[1], R. Hashimoto[1], S. Kaida[1], H. Shimizu[1], K. Suzuki[1], S. Takahashi[1], and H. Yamazaki[1]

[1]*Laboratory of Nuclear Science (LNS), Tohoku University, Sendai 982-0826, Japan*

Meson photoproduction experiments are carried out to study nucleon resonances with an electromagnetic (EM) calorimeter complex FOREST at Laboratory of Nuclear Science, Tohoku University. FOREST consists of three EM calorimeters, covering a solid angle of about 90% in total. The forward calorimeter is SCISSORS III which consists of 192 pure CsI crystals. Two shapes of crystals are used in SCISSORS III, and 144 of LNS type ones are placed in the central region. The energy resolution of a test calorimeter made up with 4 LNS type CsI crystals has been measured by using a 100–800 MeV/c positron beam.

§1. Introduction

Study of exotic hadrons has been a subject of great interest in nuclear phyiscs. A nucleon resonance $N^*(1670)$ is a candidate of an adjacent member to Θ^+ among the anti-decuplet pentaquark baryons [1]. The relevenat resonance is studied via η photoproduction on the neutron by using an EM calorimeter complex FOREST in the GeV-γ experimental hall. FOREST comprises three calorimeters and covers a solid angle of about 90% in total. SCISSORS III is the forward calorimeter of FOREST, and consists of 144 LNS and 48 INS type pure CsI crystals which had composed the previous calorimeter SCISSORS II in the hall [2]. Fig. 1 shows SCISSORS III and the geometry of the LNS type CsI crystal.

Although the energy resolution of a prototype EM calorimeter made up with INS type crystals were measured thrice [3], that of an LNS type CsI calorimeter had not been measured yet. Thus, the energy resolution of a test calorimeter made up with 4 reserved LNS CsI crystals was measured.

§2. Experimental Setup

The energy resolution of a test LNS CsI calorimeter was measured at the positron beamline for testing detectors at Laboratory of Nuclear Science (LNS), Tohoku University. The test calorimeter is made up with 4 LNS type pure CsI crystals. Momentum-analyzed positrons were used as an incident beam, and the momentum of the beam ranges from 100 to 800 MeV/c. A beam profile monitor (BPM) was used to specify the position of the incident positrons and to make a trigger for the data acquisition. BPM consists of two layers of scintillating fiber (SciFi) hodoscopes. Each hodoscope consists of 16 SciFi's with a cross section of 3×3 mm^2. The upstream and downstream layers determine the y and x positions

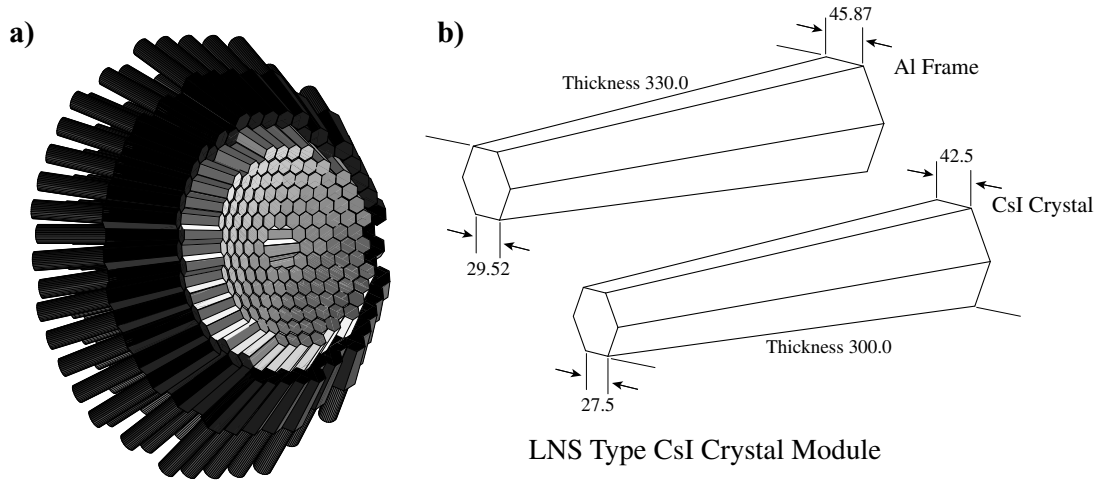

Fig.1. a) Schematic view of SCISSORS III. The central units (gray) are the LNS type, and the peripheral ones (black) are the INS type. b) Geometry of the LNS type CsI crystal.

of the incident positron, respectively. Fig. 2 shows the experimental setup for the energy resolution measurement of the calorimeter.

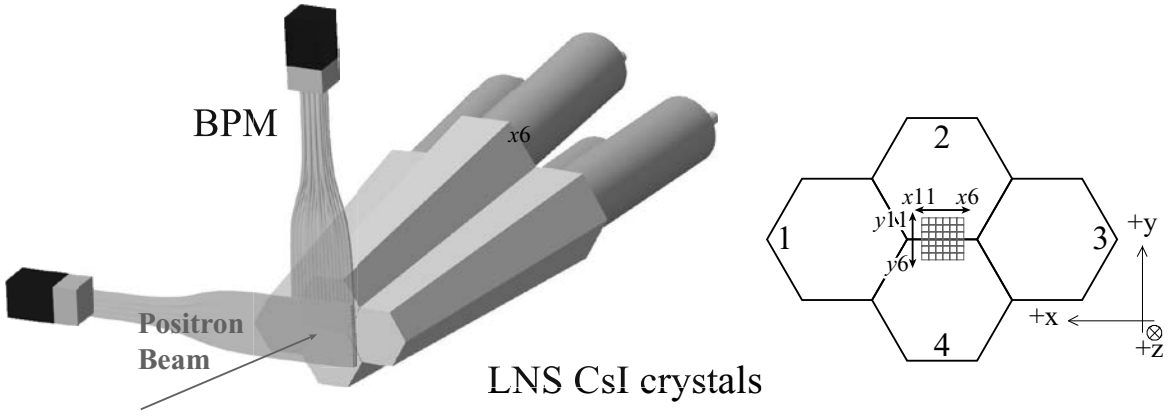

Fig.2. Experimental setup for energy resolution measurement of the test calorimeter comprised of 4 LNS type CsI crystals. The 16×16 scintillating fiber hodoscopes are placed in front of the calorimeter to determine the position of incident positions.

The trigger condition for the data acquisition was described as

$$[x \text{ fiber OR}] \otimes [y \text{ fiber OR}], \tag{1}$$

where $\otimes$ means coincidence of signals. The maximum trigger rate was 2 kHz and a fraction of accidental coincidence events was negligibly small. The energy calibration for the CsI crystals was made by using 200, 300, 458, 589 and 744 MeV positrons injected onto the central region (6×6 mm^2) of each crystal one by one. The LNS type CsI crystal has the shape of a truncated regular hexagonal pyramid. Therefore, the position and the tilted angle of the calorimeter were set so that the beam axis was perpendicular to the front face of the module of interest. Then, the gain of each detector module was roughly adjusted.

§3. Energy Calibration

The energy calibration for 4 crystals was made by using 200, 300, 458, 589 and 744 MeV/c positrons injected onto the central region (6×6 mm^2) of each crystal one by one. The ADC distribution in each measurement was fitted with a logarithmic Gaussian [4], and the mean μ_c and width σ_c were determined. Fig. 3 shows the typical ADC distributions that the positrons are incident on the central region of No. 3 crystal.

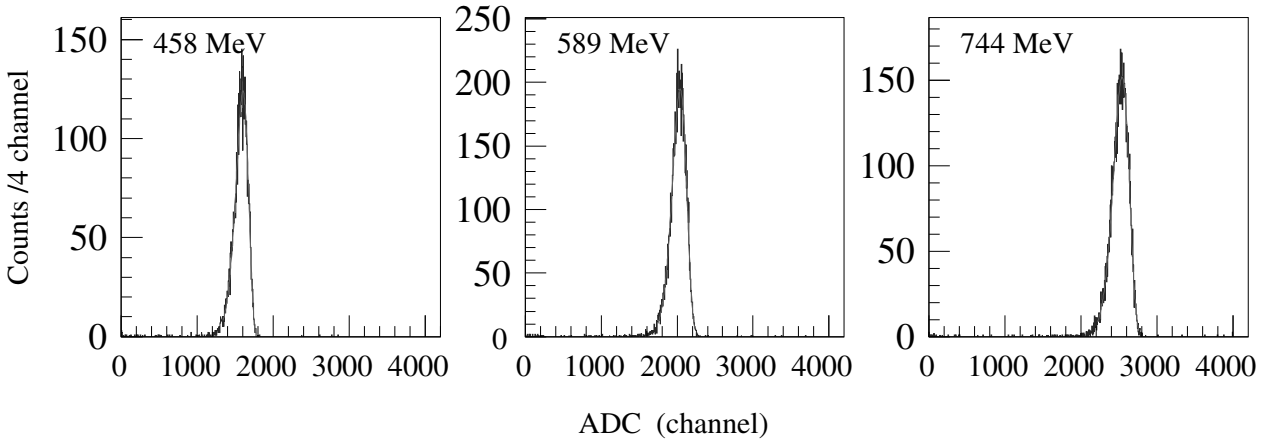

Fig.3. Typical ADC distributions that the positrons are incident on the central region of No. 3 crystal. The incident positron momentum are described in each panel. The solid line shows the fitted logarithmic Gaussians.

The pedestal distribution was measured with a 1 kHz clock signal trigger in each measurement, and the mean μ_p and width σ_p of which were determined by fitting with a nominal Gaussian. Since the energy leakage in the lateral direction exists, the ratios μ/E_e are different for different incident energies E_e where $\mu = \mu_c - \mu_p$. Fig. 4 shows the ratio μ/E_e as a function of the incident energy E_e.

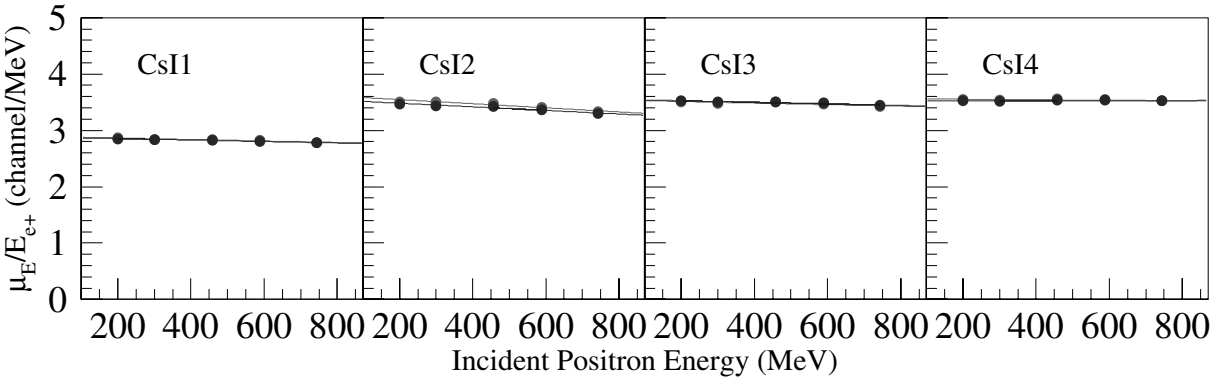

Fig.4. Ratio μ/E_e as a function of the incident energy E_e. The μ/E_e is not constant due to the energy leakage in the lateral direction. The solid line shows the fitted linear function.

The ratio E/μ as a function of the incident energy E_e is different between 4 crystals. Although all the slopes are negative, the slope for No. 2 crystal is larger than that for another one. This behavior cannot be explained only with the energy leakage in the lateral direction. The μ/E_e was well fitted with

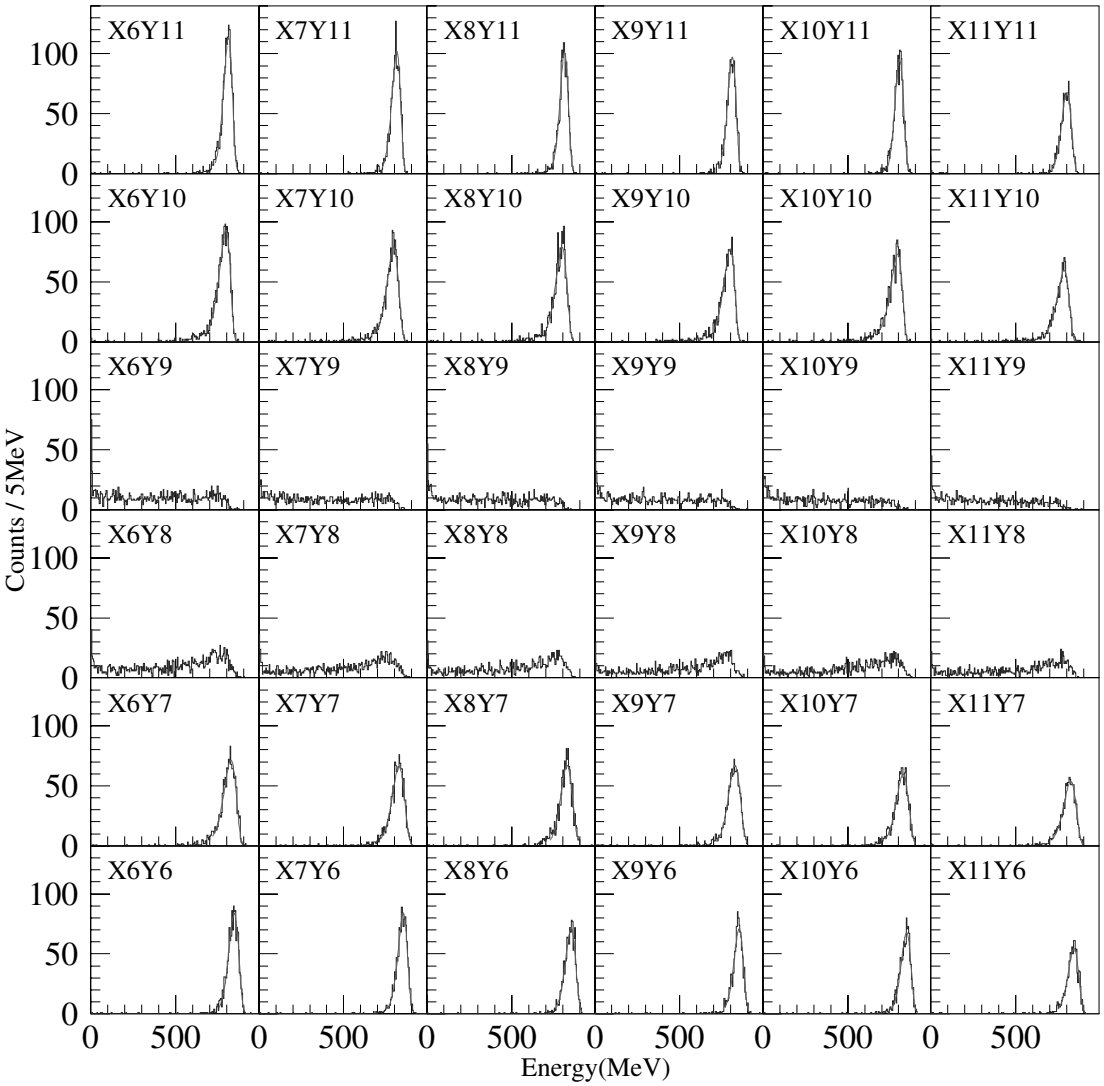

Fig.5. Energy distributions of the calorimeter at the incident energy of 800 MeV for all BPM fiber combinations together with the fitted logarithmic Gaussians. The combination of x and y BPM fibers which corresponds to the incident position is described in each panel.

a linear function for all the crystals. The gain of each crystal was adjusted so that the limit of μ/E_e at $E_e = 0$ should be the same. The energy of each crystal E_i was given by

$$E_i = \alpha\,(A - \mu_p)\,, \tag{2}$$

where A is a measured ADC value and α is the limit of E/μ at $E = 0$.

§4. Energy Resolution

The energy of the calorimeter E was reconstructed by the sum of 4 crystal energies E_i as

$$E = \sum_{i=1}^{4} E_i. \tag{3}$$

The events that positrons were injected onto the central 24×24 mm^3 region of the EM calorimeter were selected to suppress the energy leakage in the lateral direction. The energy distribution is estimated for

each combination of x and y BPM fibers. Fig. 5 shows the energy distributions of the calorimeter at the incident energy of 800 MeV for all the BPM fiber combinations.

When positrons are injected on the $Y9$ and $Y10$ BPM fibers, the reconstructed energy spreads in a wide range. This is because there is a gap between Nos. 2 and 4 crystals in the calorimeter, and because many EM shower particles go through the gap. Fig. 6 shows the photo of the calorimeter front face.

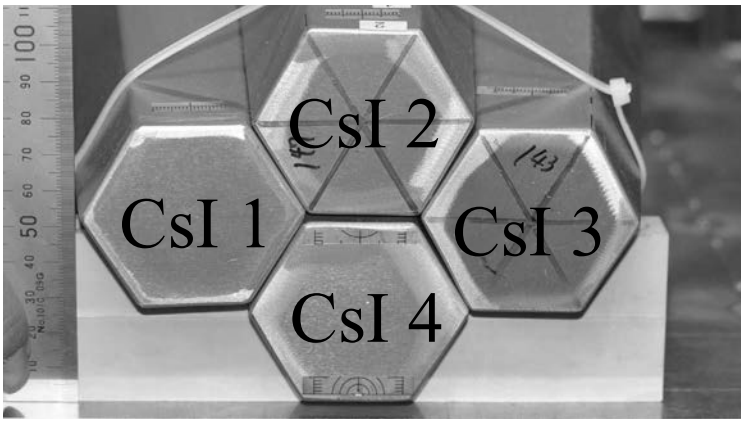

Fig.6. Photo of the calorimeter front face. A 2 mm gap between Nos. 2 and 4 crystals in the calorimeter is observed.

The energy resolution σ_E/E was estimated for each x and y BPM fiber combination as

$$\left(\frac{\sigma_E}{E}\right)^2 = \left(\frac{\sigma}{\mu}\right)^2 - \left(\frac{\sigma_b}{\mu_b}\right)^2 - \left(\frac{\sigma_p}{\mu}\right)^2 \tag{4}$$

from the mean μ and width σ of the reconstructed energy distribution, the beam energy spread σ_b/μ_b given in Ref. [5], and the width σ_p of the energy distribution for the clock trigger (pedestal distribution). Since the events that the positron inject on the $Y8$ and $Y9$ BPM BPM fibers do not form a peak in the energy distribution, the energy resolution for them are not estimated. Fig. 7 shows the energy resolution as a function of the incident energy.

The energy resolutions obtained were fitted with

$$\left(\frac{\sigma_E}{E}\right)^2 = \left(\frac{a_1}{\sqrt{E}}\right)^2 + (a_0)^2, \tag{5}$$

where the incident energy is given in GeV. The a_0 and a_1 parameters are the coefficients for the constant and statistical terms. Table 1 summarizes the fitted parameters.

The energy resolution is about $3.0\% \pm 0.3\%$ at 1 GeV when the positrons are incident on the $Y6$ and $Y11$ BPM fibers, and that is about $4.1\% \pm 0.3\%$ when they are incident on the $Y7$ and $Y10$ ones. In the case that the positrons are incident on the calorimter closely to the crystal boundaries, the energy resolution becomes worse due to the gap between the crystals. In that case, many EM shower particles go through the gap and do not deposit energies in crystals. Although this kind of gaps also exist in SCISSORS III, the target point does not lie on any of the gap planes, and the generated particles in the target material do not go through a gap in SCISSORS III The details of the analysis for the energy resolution are described elsewhere [6].

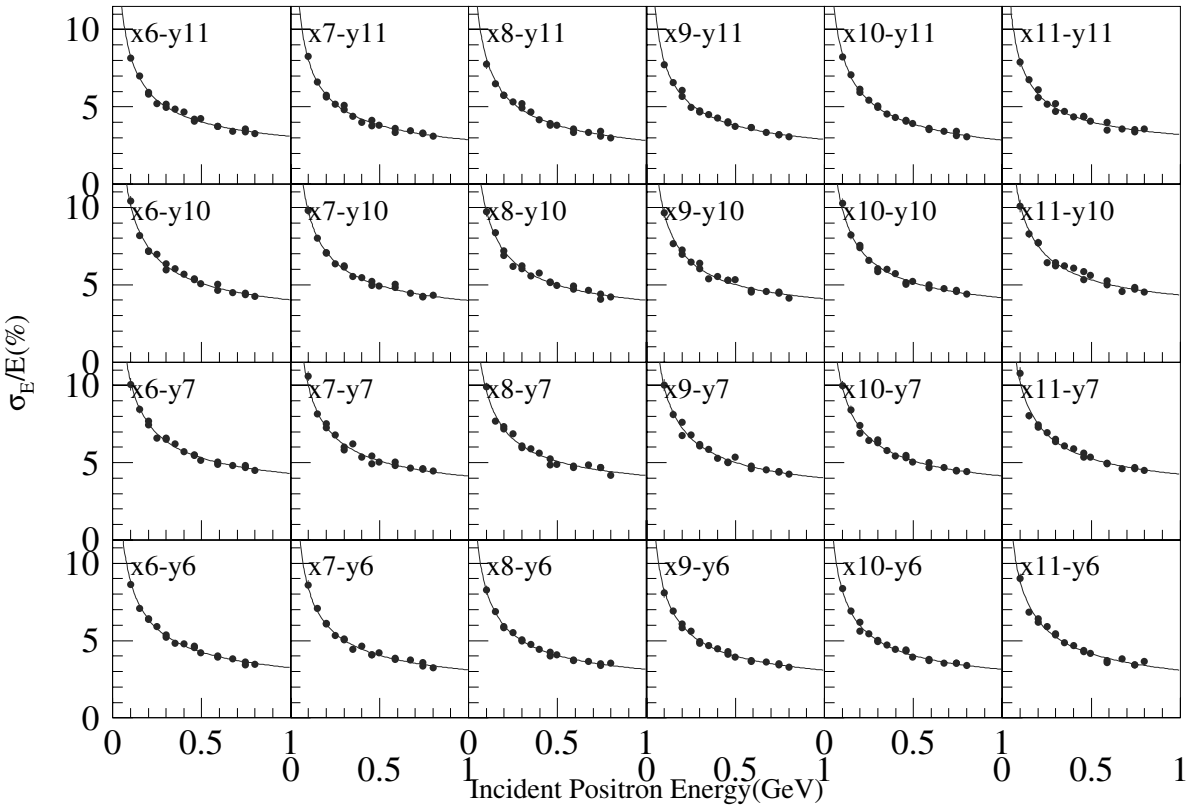

Fig.7. Energy resolution of the LNS CsI calorimeter as a function of the incident positron energy. The incident position is described in each panel and the solid curves show the fitted functions (5).

§5. Summary

The energy of a test calorimeter made up with 4 LNS type CsI crystals has been studied by using a positron beam with energies up to 800 MeV. The energy resolution for 1 GeV positrons obtained is $3.0\% \pm 0.3\%$ for $\boldsymbol{Y}6$ and $\boldsymbol{Y}11$ BPM fibers, and that is $4.1\% \pm 0.3\%$ for $\boldsymbol{Y}7$ and $\boldsymbol{Y}10$ ones, When the positrons are incident on the calorimter closely to the crystal boundaries, the energy resolution becomes worse due to the gap between the crystals.

Acknowledgement

This work was supported in part by Grant-in-Aid for Specially promoted Research (19002003).

Table 1. Fitted parameters in Eq. 5 with measured energy resolutions for each combination of x and y BPM fibers. The a_0 and a_1 parameters are the coefficients for the constant and statistical terms. The energy resolution is give in %.

BPM	a_0	a_1	$\sigma_E/E\|_{1\ \mathrm{GeV}}$	BPM	a_0	a_1	$\sigma_E/E\|_{1\ \mathrm{GeV}}$
6-6	1.748±0.148	2.741±0.041	3.251±0.087	6-10	2.550±0.142	3.108±0.052	4.020±0.099
7-6	1.715±0.140	2.591±0.042	3.107±0.085	7-10	2.685±0.135	2.946±0.053	3.986±0.099
8-6	1.859±0.134	2.537±0.043	3.145±0.086	8-10	2.668±0.146	2.973±0.055	3.995±0.106
9-6	1.736±0.144	2.551±0.043	3.086±0.088	9-10	2.891±0.135	2.894±0.057	4.091±0.104
10-6	1.844±0.108	2.544±0.035	3.142±0.069	10-10	2.878±0.151	3.004±0.059	4.160±0.113
11-6	1.393±0.203	2.762±0.048	3.093±0.101	11-10	3.064±0.161	3.071±0.070	4.338±0.124
6-7	2.989±0.141	3.095±0.060	4.303±0.107	6-11	1.722±0.132	2.569±0.040	3.093±0.081
7-7	2.828±0.134	3.014±0.051	4.133±0.099	7-11	1.419±0.136	2.499±0.037	2.874±0.074
8-7	2.999±0.132	2.901±0.056	4.173±0.103	8-11	1.232±0.125	2.544±0.032	2.827±0.062
9-7	2.649±0.145	3.012±0.058	4.011±0.105	9-11	1.522±0.141	2.461±0.041	2.894±0.082
10-7	2.869±0.144	2.993±0.057	4.146±0.108	10-11	1.016±0.205	2.653±0.039	2.841±0.082
11-7	2.933±0.162	3.089±0.063	4.260±0.121	11-11	2.086±0.132	2.435±0.049	3.206±0.094

References

[1] T. Nakano *et al.*: Phys. Rev. Lett. **91**, 012002 (2003); D. Diakonov, V. Petrov, M. Polyakov: Z. Phys. A **359**, 305 (1997); V. Kuznetsov *et al.*: Phys. Lett. B **647**, 23 (2007); F. Miyahara *et al.*: Prog. Theor. Phys. Suppl. **168**, 90-96 (2007); H. Shimizu: talk at NSTAR2007; I. Jaegle *et al.*: Phys. Rev. Lett. **100**, 252002 (2008).

[2] T. Ishikawa *et al.*: Research Report of LNS **39**, Tohoku University, 35 (2007).

[3] H. Okuno *et al.*: Nucl. Instr. Meth. A **365**, 352 (1995); H. Yamazaki *et al.*: Nucl. Instr. Meth. A **391**, 427 (1997); H. Sugai, T. Ishikawa *et al.*: in this Research Report of LNS, Tohoku University.

[4] H. Ikeda, et al: Nucl. Instr. and Meth. A **441**, 401 (2000).

[5] T. Ishikawa *et al.*: Research Report of LNS **40**, Tohoku University, 6 (2008).

[6] A. Nakamura: Internal GeV-γ Analysis Note No. **180$\mathcal{D}$** (2010).

(LNS Experiment : #2620)

Energy resolution of a SF6 lead glass Čerenkov calorimeter in response to several hundred MeV positrons

T. Ishikawa[1], M. Sato[1], H. Fujimura[1], R. Hashimoto[1], H. Shimizu[1], K. Suzuki[1], and H. Yamazaki[1]

[1]*Laboratory of Nuclear Science (LNS), Tohoku University, Sendai 982-0826, Japan*

Meson photoproduction experiments are carried out to study nucleon resonances with an electromagnetic (EM) calorimeter complex FOREST in the GeV-γ experimental hall. FOREST consists of three EM calorimeters, covering a solid angle of about 90% in total. The backward calorimeter is Rafflesia II which is made up with two types of lead glass Čerenkov counters: 10 SF5 and 52 SF6 lead glasses. The energy resolution of a prototype calorimeter comprised of a 3×3 SF6 lead glass array has been measured by using 100–800 MeV/c positron beams.

§1. Introduction

Nucleon resonances are studied via π^0, η, and ω photoproduction by using an EM calorimeter complex FOREST in the GeV-γ experimental hall. FOREST comprises three calorimeters and covers a solid angle of about 90% in total. Rafflesia II is the backward calorimeter of FOREST, and consists of 10 SF5 and 52 SF6 lead glass Čerenkov counters [1].

Rafflesia II consisted of 36 SF5 courters in the original design of FOREST [2]. The size of the SF5 counter is 150 mm (W) $\times$ 150 mm (H) $\times$ 300 mm (T), and its density is 4.075 g/cm^3. The energy resolution of the SF5 counter measured at the positron beamline for testing detectors corresponded to 4.9% for 1 GeV/c positrons [3]. Since we failed many times in making a solid hydrogen target fitted to FOREST, we decided to make a distance shorter between a target holder and a vacuum chamber for a refrigerator of the target system [4]. The chamber occupied some space reserved for the SF5 counters.

The SF6 lead glass Čerenkov counters were adopted for a large part of Rafflesia II instead of SF5 ones. The size of the SF6 courter is 75 mm (W) $\times$ 75 mm (H) $\times$ 250 mm (T), and its density is 5.20 g/cm^3. Since the density of SF6 is higher than that of SF5, the SF6 counter is thicker in a radiation length unit ($14.7X_0$) than the SF5 one ($11.8X_0$). The higher position resolution will be obtained by adopting the smaller modules. The energy resolution of a prototype calorimeter made up with 9 SF6 counters was measured.

§2. Experimental Setup

The performance study of a test calorimeter was made at the positron beamline for testing detectors. The test calorimeter is comprised of a 3 $\times$ 3 lead glass Čerenkov counter array. Momentum-analyzed

positrons were used as an incident beam. The positron beam with the momentum from 100 to 800 MeV/c irradiated the calorimter. A beam profile monitor (BPM) was used to specify the position of incident positrons and make a trigger for the data acquisition. BPM consists of two layers of scintillating fiber (SciFi) hodoscopes. Each hodoscope consists of 16 SciFi's with a cross section of 3×3 mm^2. The upstream and downstream layers determine the y and x positions of the incident positron, respectively. Fig. 1 shows the experimental setup for the performance study of the calorimeter.

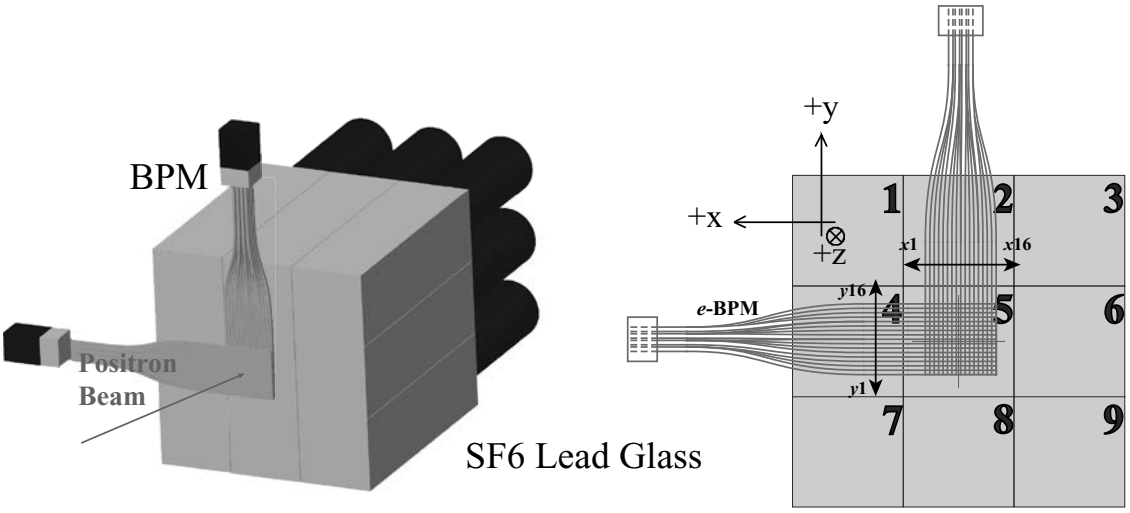

Fig.1. Experimental setup for the performance study of a test calorimeter comprised of 9 SF6 lead glasses. The 16×16 scintillating fiber hodoscopes are placed in front of the calorimeter to determine the position of incident positions.

The trigger condition for the data acquisition was described as

$$[x \text{ fiber OR}] \otimes [y \text{ fiber OR}], \tag{1}$$

where $\otimes$ means coincidence of signals. The maximum trigger rate was 2 kHz and a fraction of accidental coincidence events was negligibly small. The energy calibration for the SF6 counters was made by using 200, 300, 399, 458, 589 and 744 MeV/c positrons injected on to the central region (9×9 mm^2) of each counter one by one. Then, the supplied high voltage to the photo-multiplier tube of each counter was determined so that the gain of each counter became roughly the same.

§3. Energy Calibration

The energy calibration for 9 SF6 counters was made by using 200, 300, 399, 458, 589 and 744 MeV/c positrons injected onto the central region (9×9 mm^2) of each counter one by one. The ADC distribution in each measurement was fitted with a Gaussian, and the mean μ_c and width σ_c were determined. Fig. 2 shows the ADC distributions that the positrons are incident on the central region of No. 5 counter. The obtained ADC distributions were symmetric for all the incident energies, suggesting the energy resolution of the SF6 calorimeter is poor.

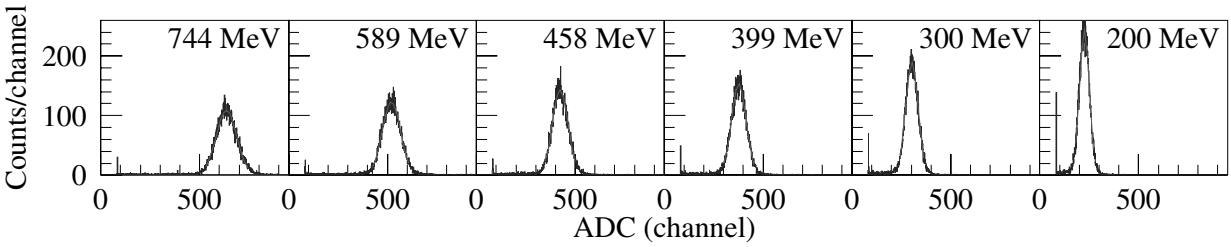

Fig.2. ADC distributions that the positrons are incident on the central region (9×9 mm^2) of No. 5 counter. The incident positron momentum are described in each panel. The solid line shows the fitted Gaussian.

The pedestal distribution was measured with a 1 kHz clock signal trigger in each measurement, and the mean μ_p and width σ_p of which were determined by fitting with a Gaussian. Since the energy leakage in the lateral direction exists, the ratio μ/E_e is not constant for different incident energies E_e where $\mu = \mu_c - \mu_p$. Fig. 3 shows the ratio μ/E_e as a function of the incident energy E_e.

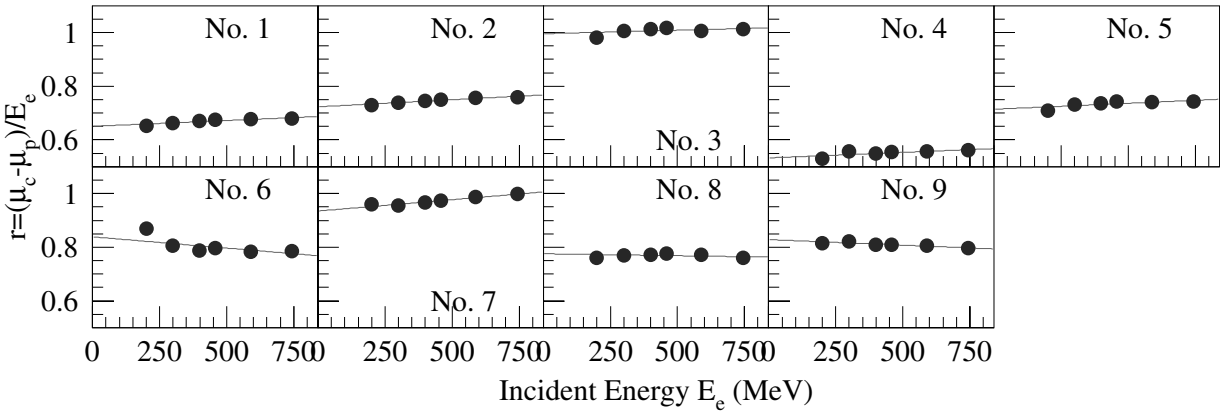

Fig.3. Ratio μ/E_e as a function of the incident energy E_e. The μ/E_e is not constant due to the energy leakage in the lateral direction. The solid line shows the fitted linear function.

The behavior of the ratio μ/E_e as a function of the incident energy E_e is different between 9 counters. Some of the ratios has a positive slope, and this cannot be explained only with the energy leakage in the lateral direction. The μ/E_e was well fitted with a linear function for all the counters. The gain of each counter was adjusted so that the limit of μ/E_e at $E_e = 0$ should be the same. The energy of each counter E_i was given by

$$E_i = \alpha\,(A - \mu_p)\,, \tag{2}$$

where A is a measured ADC value and α is the limit of E_e/μ at $E_e = 0$.

§4. Energy Resolution

The energy of the calorimeter E was reconstructed by the sum of 9 SF6 counter energies E_i as

$$E = \sum_{i=1}^{9} E_i. \tag{3}$$

The events that positrons were injected onto the central 9×9 mm^3 region of the EM calorimeter were selected to suppress the energy leakage in the lateral direction. Fig. 4 shows the energy distributions of the calorimeter for all the incident positron energies.

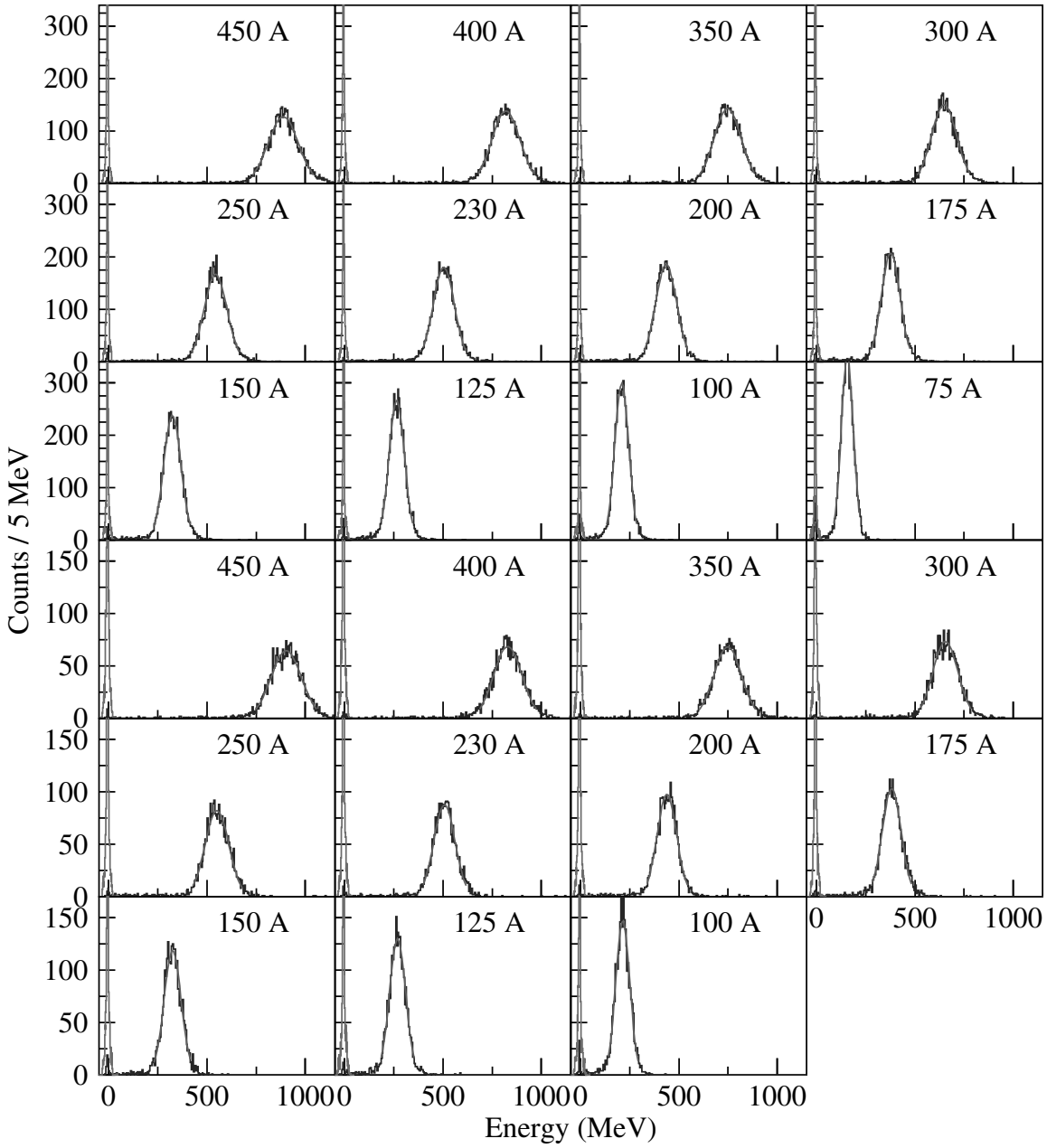

Fig.4. Energy distributions of the calorimeter for all the incident positron energies together with the fitted Gaussians. The lower peak shows the pedestal energy distribution corresponding to the zero energy. The incident energy is described in each panel. Two series of the energy resolution measurement were made.

The energy resolution σ_E/E was estimated for all the incident energies as

$$\left(\frac{\sigma_E}{E}\right)^2 = \left(\frac{\sigma}{\mu}\right)^2 - \left(\frac{\sigma_b}{\mu_b}\right)^2 - \left(\frac{\sigma_p}{\mu}\right)^2 \qquad (4)$$

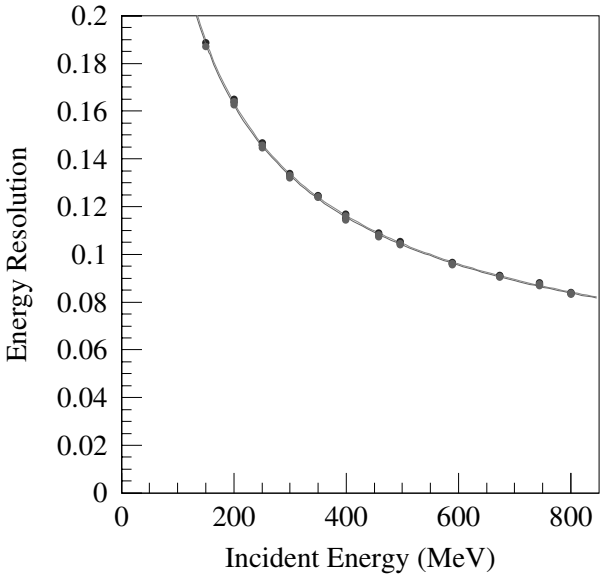

Fig.5. Energy resolution of the SF6 calorimeter as a function of the incident positron energy. The solid curve shows the fitted function (5).

from the mean μ and width σ of the reconstructed energy distribution, the beam energy spread σ_b/μ_b given in Ref. [5], and the width σ_p of the energy distribution for the clock trigger (pedestal distribution). Fig. 5 shows the energy resolution as a function of the incident energy.

The energy resolutions obtained were fitted with

$$\left(\frac{\sigma_E}{E}\right)^2 = \left(\frac{0.0063 \pm 0.0012}{E}\right)^2 + \left(\frac{0.0702 \pm 0.0006}{\sqrt{E}}\right)^2 + (0.0283 \pm 0.0019)^2\,, \qquad (5)$$

where the incident energy is given in GeV. The energy resolution for 1 GeV positrons corresponds to 7.6%. Since the coefficient for the statistical term is dominant in the energy dependence of the energy resolution, the better energy resolution can be obtained by using photomultiplier tubes with a UV window to detect Čerekov lights. The details of the analysis for the energy resolution are described elsewhere [6]. The estimation of the position resolution is in progress.

§5. Summary

The energy resolution of a test calorimeter made up with 9 SF6 lead glass Čerenkov counters has been studied by using a positron beam with energies up to 800 MeV. The obtained energy distributions with the calorimeter were symmetric for all the incident energies due to the poor energy resolution of the calorimeter (suggesting small number of detected photoelectrons with photomultiplier tubes). The energy resolution obtained is 7.6% for 1 GeV positrons. The energy resolution is expected to be better by using photomultiplier tubes with a UV window to detect Čerekov lights.

Acknowledgement

This work was supported in part by Grant-in-Aid for Specially promoted Research (19002003).

References

[1] T. Ishikawa *et al.*: Research Report of LNS **41**, Tohoku University, 7 (2008).

[2] T. Ishikawa *et al.*: Research Report of LNS **39**, Tohoku University, 35 (2007).

[3] M. Sato, T. Ishikawa *et al.*: Research Report of LNS **41**, Tohoku University, 22 (2009).

[4] R. Hashimoto *et al.*: Research Report of LNS **41**, Tohoku University, 31 (2009).

[5] T. Ishikawa *et al.*: Research Report of LNS **40**, Tohoku University, 6 (2008).

[6] T. Ishikawa: Internal GeV-γ Analysis Note No. **189$\mathcal{D}$** (2010).

(LNS Experiment : #2624)

Performance of a test electro-magnetic calorimeter made up with INS type pure CsI crystals

H. Sugai[1], T. Ishikawa[1], H. Fujimura[1], R. Hashimoto[1], S. Ogushi[1], H. Shimizu[1], K. Suzuki[1], and H. Yamazaki[1]

[1]*Laboratory of Nuclear Science (LNS), Tohoku University, Sendai 982-0826, Japan*

Photoproduction experiments are conducted to study nucleon resonances with an electro-magnetic (EM) calorimeter complex FOREST at Laboratory of Nuclear Science, Tohoku University. FOREST consists of three independent calorimeters, covering a solid angle of about 90% in total. SCISSORS III is comprised of pure CsI crystals, and covers the forward part of FOREST. Two shapes of crystals are used in SCISSORS III, and 48 of INS type ones are placed in the peripheral region. The performance of a test calorimeter made up with 7 INS type CsI crystals has been studied by using a positron beam with energies up to 800 MeV.

§1. Introduction

Nucleon resonances are studied via π^0, η, and ω photoproduction by using an EM calorimeter complex FOREST in the GeV-γ experimental hall. FOREST comprises three calorimeters and covers a solid angle of about 90% in total. SCISSORS III is the forward calorimeter of FOREST, and consists of 144 LNS and 48 INS type pure CsI crystals which had composed the previous calorimeter SCISSORS II in the hall [1]. Fig. 1 shows SCISSORS III and the geometry of the INS type CsI crystals.

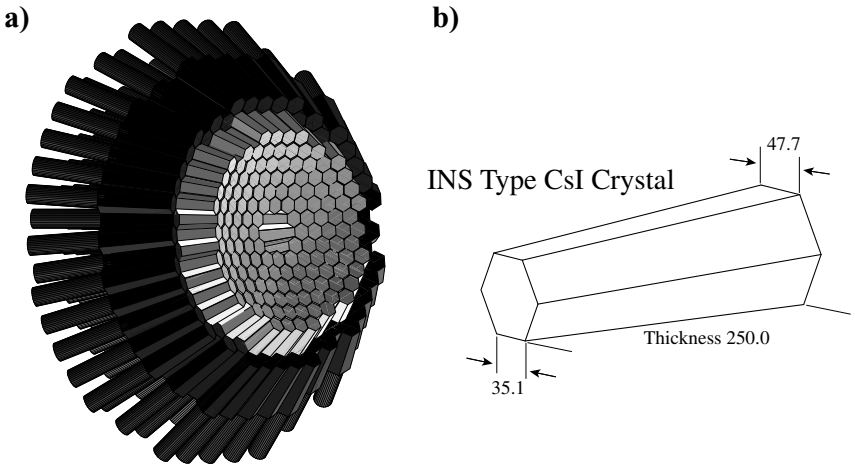

Fig.1. a) Schematic view of SCISSORS III. The central units (gray) are the LNS type, and the peripheral ones (black) are the INS type. b) Geometry of the INS type CsI crystals.

The energy resolution of a prototype EM calorimeter made up with 7 INS crystals were measured

twice. The first measurement was carried out at the 1.3 GeV electron synchrotron in Institute for Nuclear Study (INS), University of Tokyo. The momentum-analyzed electrons converted from the photon beam irradiated the calorimeter. The energy resolution obtained for 1 GeV electrons was 2.12%. The second one was performed at the 12 GeV proton synchrotron in High Energy Accelerator Research Organization (KEK). The momentum-analyzed secondary electrons generated at the production target are used as a beam. The energy resolutions were found to be 3.64%$\pm$0.19% and 3.65%$\pm$0.24% for 1 GeV positrons and electrons, respectively. The difference of the energy resolutions suggests the deterioration due to the hygroscopicity of the CsI material. The 10 of 58 INS CsI crystals which had composed SCISSORS II are not used in SCISSORS III. Thus, the energy resolution of a test calorimeter consisting of 7 reserved INS CsI crystals was measured again.

§2. Experimental Setup

The performance study of a test calorimeter was made at the positron beamline for testing detectors at Laboratory of Nuclear Science (LNS), Tohoku University. The test calorimeter is made up with 7 INS type pure CsI crystals. Momentum-analyzed positrons were used as an incident beam with the energy ranging from 100 to 800 MeV/c. A beam profile monitor (BPM) was used to specify the position of the incident positrons and make a trigger for the data acquisition. BPM consists of two layers of scintillating fiber (SciFi) hodoscopes. Each hodoscope consists of 16 SciFi's with a cross section of 3×3 mm^2. The upstream and downstream layers determine the y and x positions of the incident positron, respectively. Fig. 2 shows the experimental setup for the performance study of the calorimeter.

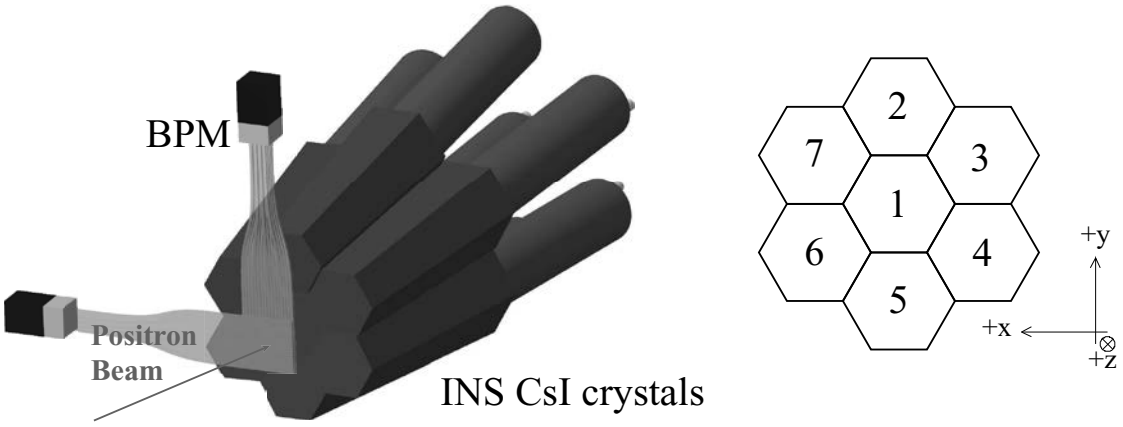

Fig.2. Experimental setup for the performance study of a test calorimeter comprised of 7 INS type CsI crystals. The 16×16 scintillating fiber hodoscopes are placed in front of the calorimeter to determine the position of incident positions.

The trigger condition for the data acquisition was described as

$$[x \text{ fiber OR}] \otimes [y \text{ fiber OR}], \tag{1}$$

where $\otimes$ means coincidence of signals. The maximum trigger rate was 2 kHz and a fraction of accidental coincidence events was negligibly small. The energy calibration for the CsI crystals was made by using

300, 460, 590, and 800 MeV positrons injected onto the central region (9×9 mm^2) of each crystal one by one. The INS type CsI crystal has the shape of a truncated regular hexagonal pyramid. Therefore the position and the tilted angle of the calorimeter were set so that the beam axis was perpendicular to the front face of the module of interest. Then, the gain of each detector module was roughly adjusted.

§3. Energy Calibration

The energy calibration for 7 crystals was made by using 200, 300, 399, 458, 589, and 744 MeV/c positrons injected onto the central region (9×9 mm^2) of each crystal one by one. The ADC distribution in each measurement was fitted with a logarithmic Gaussian [4], and the mean μ_c and width σ_c were determined. Fig. 3 shows the ADC distributions that the positrons are incident on the central region of No. 1 crystal.

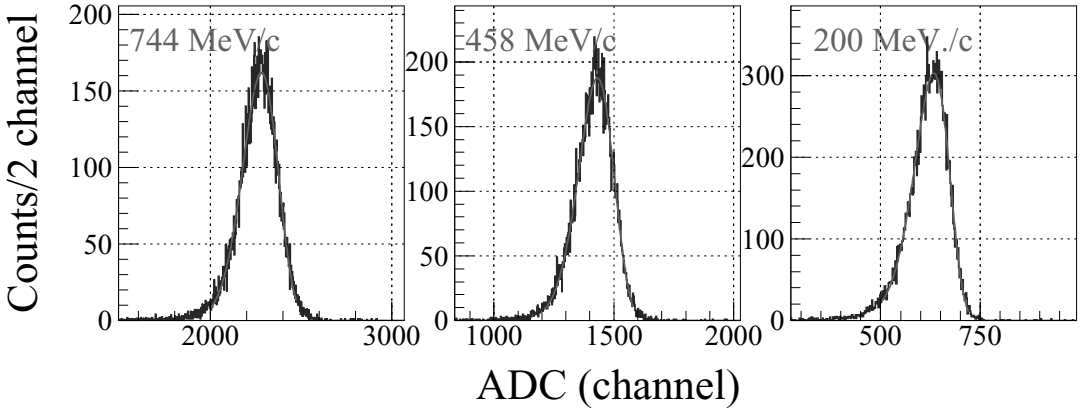

Fig.3. ADC distributions that the positrons are incident on the central region of No. 1 crystal. The incident positron momentum is described in each panel. The solid line shows the fitted logarithmic Gaussian.

The pedestal distribution was measured with a 1 kHz clock signal trigger in each measurement, and the mean μ_p and width σ_p of which were determined by fitting with a nominal Gaussian. Since the energy leakage in the lateral direction exists, the ratios μ/E_e are different for different incident energies E_e where $\mu = \mu_c - \mu_p$. Fig. 4 shows the ratio μ/E_e as a function of the incident energy E_E.

The ratio μ/E_e as a function of the incident energy E_e is different between 7 crystals, and the slope is negative for Nos. 2, 3, 4, and 7, it is positive for Nos. 5 and 6, and it is almost constant for No. 1. This behavior cannot be explained only with the energy leakage in the lateral direction. The μ/E_e was well fitted with a linear function for all the crystals. The gain of each crystal was adjusted so that the limit of μ/E_e at $E = 0$ should be the same. The energy of each crystal E_i was given by

$$E_i = \alpha\,(A - \mu_p)\,, \tag{2}$$

where A is a measured ADC value and α is the limit of $(\mu/E_e)^{-1}$ at $E_e = 0$.

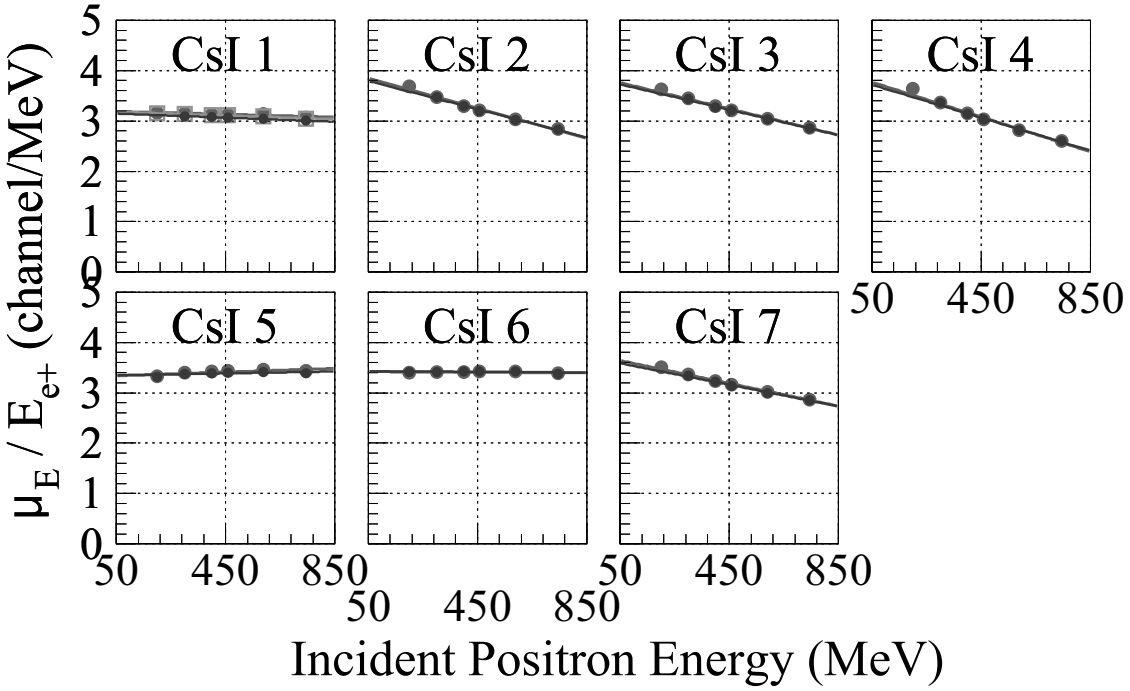

Fig.4. Ratio μ/E_e as a function of the incident energy E_e. The μ/E_e is not constant due to the energy leakage in the lateral direction. The solid line shows the fitted linear function.

§4. Energy Resolution

The energy of the calorimeter E was reconstructed by the sum of 7 crystal energies E_i as

$$E = \sum_{i=1}^{7} E_i. \tag{3}$$

The events that positrons were injected onto the central 9×9 mm^2 region of the EM calorimeter were selected to suppress the energy leakage in the lateral direction. Fig. 5 show the energy distributions of the calorimeter for all the incident positron energies. The energy distributions were also fitted with a logarithmic Gaussian and the mean μ, width σ, and asymmetry parameter η were obtained for each incident positron energy for each incident position.

The energy resolution σ_E/E was estimated as

$$\left(\frac{\sigma_E}{E}\right)^2 = \left(\frac{\sigma}{\mu}\right)^2 - \left(\frac{\sigma_b}{\mu_b}\right)^2 - \left(\frac{\sigma_p}{\mu}\right)^2 \tag{4}$$

from the mean μ and width σ of the reconstructed energy distribution, the beam energy spread σ_b/μ_b given in Ref. [5], and the width σ_p of the energy distribution for the clock trigger (pedestal distribution). Fig. 5 shows the energy resolution as a function of the incident energy. The energy resolutions obtained were

$$\left(\frac{\sigma_E}{E}\right)^2 = \left(\frac{0.157 \pm 0.032}{E}\right)^2 + \left(\frac{1.584 \pm 0.024}{\sqrt{E}}\right)^2 + (2.803 \pm 0.018)^2, \tag{5}$$

where the incident energy is given in GeV.

The energy resolution for 1 GeV positrons corresponds to $3.22\% \pm 0.02\%$, and the behavior of the energy resolution is similar to that measured at KEK for positrons. The energy resolution measured at

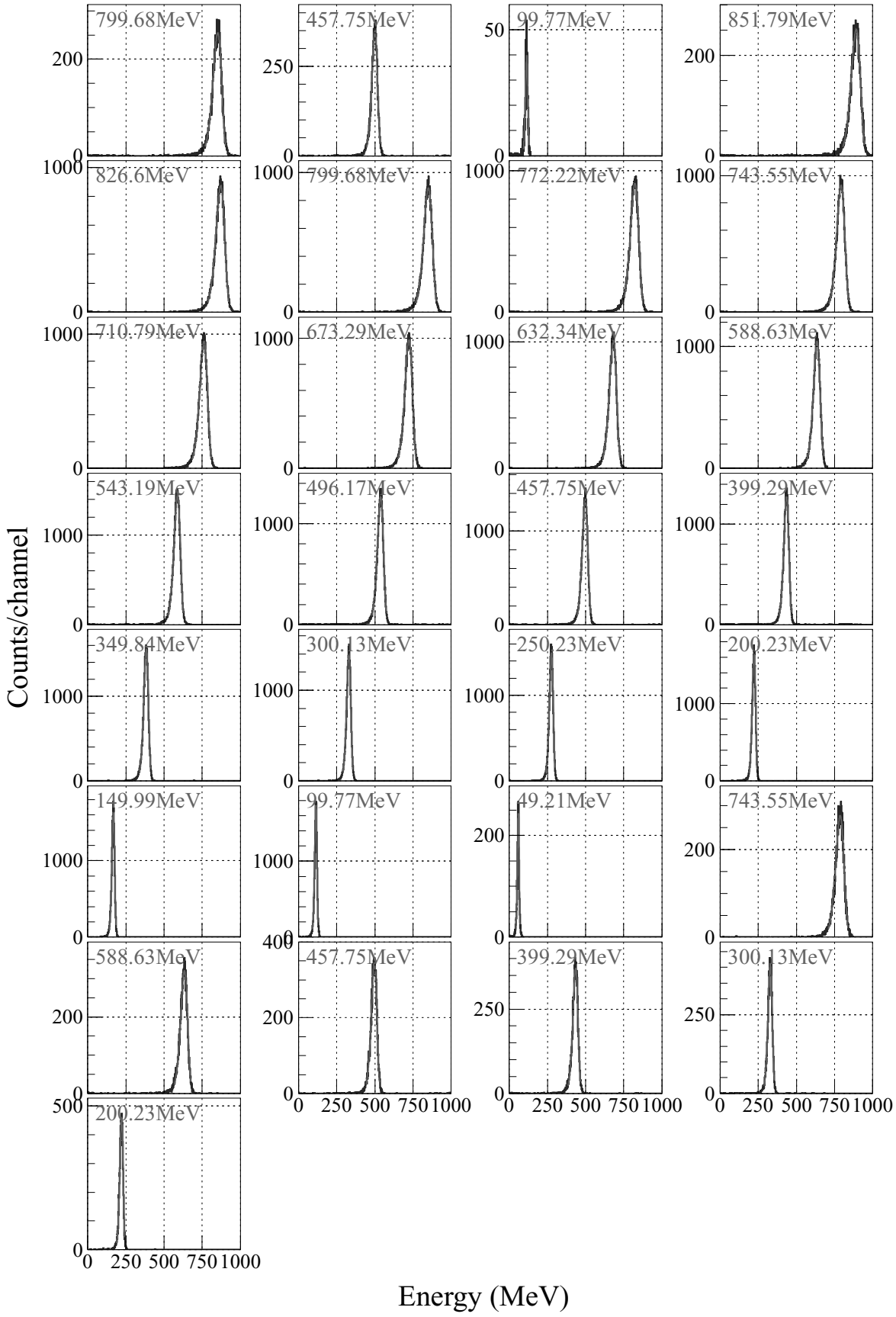

Fig.5. Energy distributions of the INS type CsI calorimeter for all the incident positron energies together with the fitted logarithmic Gaussians. The positrons are incident on the central 9×9 mm^3 region. The incident energy is described in each panel.

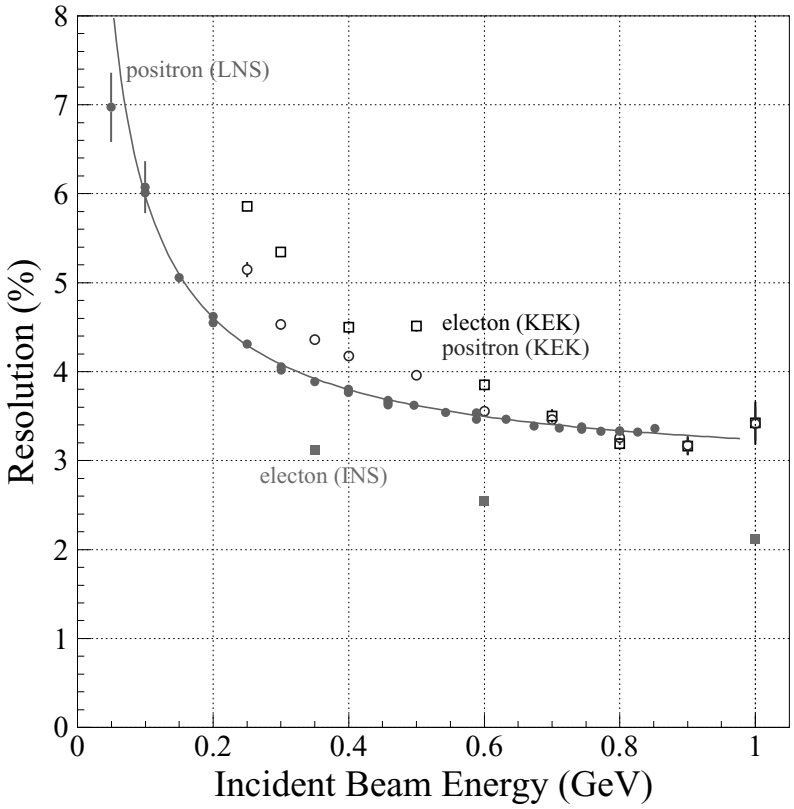

Fig.6. The energy resolutions of the INS CsI calorimeter as a function of the incident positron energy. The filled and open circles show those measured for positrons at LNS and KEK, respectively. The filled and open boxes show those measured for electrons at INS and KEK, respectively. The solid curve shows the fitted function (5) to the LNS measurement.

INS (the first measurement) is extremely high, suggesting the deterioration due to the hygroscopicity of the CsI crystal. The difference of the energy resolutions measured for positrons and electrons probably comes from the ambiguity of the knowledge on the energy spread of the secondary electron and positron beams at KEK. The difference between the LNS and KEK measurements may be caused by the same ambiguity. The details of the analysis for the energy resolution are described elsewhere [6].

§5. Position Resolution

The incident position of positrons on the calorimeter was reconstructed by an energy weighted average of the position vectors $\vec{x}_i$ of 7 crystals as

$$\vec{R}_c = \left(\sum_{i=1}^{7} w_i(E_i)\vec{r}_i \right) \Big/ \left(\sum_{i=1}^{7} w_i(E_i) \right), \tag{6}$$

where the origin of the position vectors was the common center of a circumscribed sphere for front faces of the modules. The normalization was made in such a way that the length of the reconstructed position vector should be the radius of the sphere (700 mm). Since the energy deposit to the central crystal was much larger than that to the peripheral ones, the weight for the signal from the central crystal was set

to be smaller by using an extra factor r_c. And the weight in Eq. (6) becomes

$$w_i(E_i) = \begin{cases} r_c E_i & \text{for central CsI } (i = 1), \textit{ and} \\ E_i & \text{for peripheral CsI.} \end{cases} \tag{7}$$

The factor r_c was determined for each incident energy so that the mean of the difference between the reconstructed position and the incident position determined by BPM should be 0. Fig. 7 shows the optimum factor r_c as a function of the incident positron energy E_e.

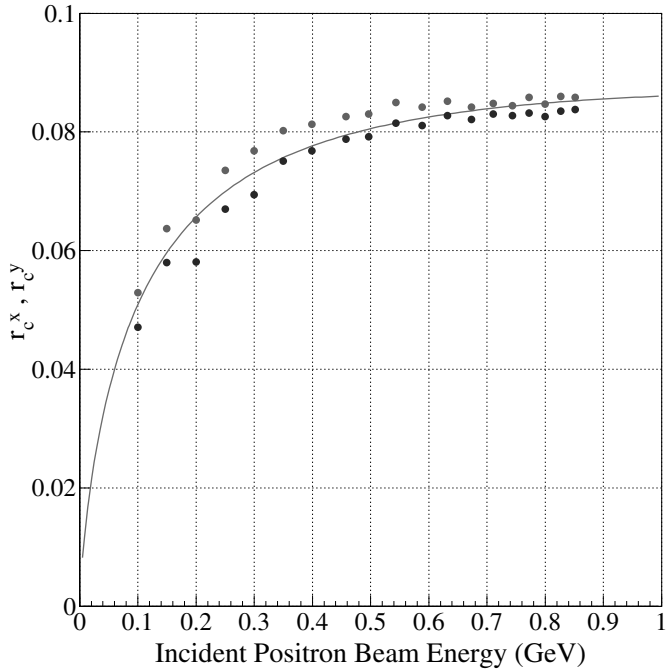

Fig.7. Optimum factor r_c as a function of the incident positron energy E_e. The solid line shows the fitted function (8).

The determined values of r_c are well fitted with

$$r_c(E) = (39.071 \pm 0.263) \log\{1 + (9.360 \pm 0.020)\, E\} \exp\left\{(-6.968 \pm 0.007)\, E^{(0.049 \pm 0.000)}\right\}. \tag{8}$$

The $x(y)$ position resolution is estimated with the width σ_x (σ_y) which is obtained by fitting a Gaussian function. Fig. 8 shows the position resolution as a function of the incident energy.

The position resolution σ_x and σ_y may also be represented with a similar function to Eq. (5). The fitted result are

$$\begin{cases} \sigma_x(E) = \sqrt{\left(\dfrac{5.76 \pm 0.00}{\sqrt{E}}\right)^2 + (12.78 \pm 0.00)^2} \\ \sigma_y(E) = \sqrt{\left(\dfrac{6.48 \pm 0.00}{\sqrt{E}}\right)^2 + (10.90 \pm 0.00)^2} \end{cases}, \tag{9}$$

where the position resolution σ_x (σ_y) and E are given in mm and GeV, respectively. The x and y position resolutions for 1 GeV positrons correspond to 14.0 mm and 12.7 mm, respectively. The details of the analysis for the position resolution are described elsewhere [7]. In Ref. [7], several weight functions are tested to reconstruct the incident positions.

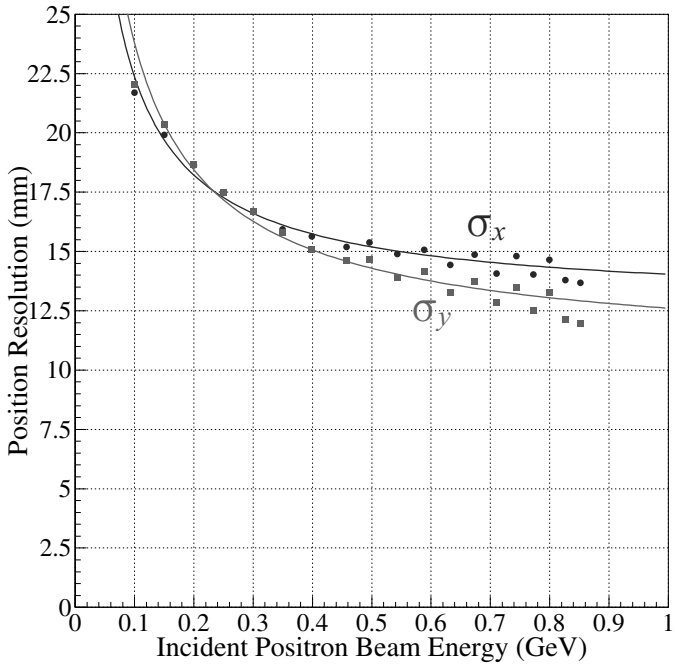

Fig.8. The position resolution as a function of the incident energy. The circles and boxes show the x and y position resolutions, respectively. The data are fitted with the form (9).

§6. Summary

The performance of a test calorimeter made up with 7 INS type CsI crystals has been studied by using a positron beam with energies up to 800 MeV. The energy resolution for 1 GeV positrons obtained is $3.22\% \pm 0.02\%$, and the deterioration due to the hygroscopicity is observed. The x and y position resolutions for 1 GeV positrons obtained are 14.0 and 12.7 mm, respectively.

Acknowledgement

This work was supported in part by Grant-in-Aid for Specially promoted Research (19002003).

References

[1] T. Ishikawa *et al.*: Research Report of LNS **39**, Tohoku University, 35 (2007).

[2] H. Okuno *et al.*: Nucl. Instr. Meth. A **365**, 352 (1995).

[3] H. Yamazaki *et al.*: Nucl. Instr. Meth. A **391**, 427 (1997).

[4] H. Ikeda, et al: Nucl. Instr. and Meth. A **441**, 401 (2000).

[5] T. Ishikawa *et al.*: Research Report of LNS **40**, Tohoku University, 6 (2008).

[6] H. Sugai: Internal GeV-γ Analysis Note No. **153$\mathcal{D}$** (2009).

[7] H. Sugai: Internal GeV-γ Analysis Note No. **160$\mathcal{D}$** (2010).

(LNS Experiment : #2625)

Comparison of the energy resolutions between a BSO and a BGO electro-magnetic calorimeters

M. Sato[1], T. Ishikawa[1], H. Fujimura[1], R. Hashimoto[1], H. Shimizu[1], K. Suzuki[1], and H. Yamazaki[1]

[1]*Laboratory of Nuclear Science (LNS), Tohoku University, Sendai 982-0826, Japan*

Meson photoproduction experiments are being carried out to study nucleon resonances with a large solid angle electro-magnetic (EM) calorimeter complex FOREST at Laboratory of Nuclear Science, Tohoku University. Three types of EM calorimeters are employed in FOREST: pure CsI crystals, lead scintillating fiber modules (Lead/SciFi), and lead glasses. Since Lead/SciFi is a sampling calorimeter, its energy resolution is not so high and the efficiency for charged hadrons is not 100%. The lead glass cannot measure the energy of charged hadrons because they do not generate EM showers and do not emit Čerenkov lights when their energies are low. In addition, the gaps of EM calorimeters lose the acceptance for the reactions of interest. Thus, the replacement of FOREST with a homogeneous inorganic scintillators is desired.

The BSO and BGO crystals are the candidates of new EM calorimeter modules. In this report, the energy resolutions of the prototype calorimeters with these crystals are compared in response to 100–800 MeV/c electrons.

§1. EM calorimeter complex FOREST

Meson photoproduction experiments are being carried out to study nucleon resonances with an EM calorimeter complex FOREST at Laboratory of Nuclear Science (LNS), Tohoku University. Three types of EM calorimeters are employed in FOREST: pure CsI crystals, lead scintillating fiber modules (Lead/SciFi), and lead glass Čerenkov counters. Although the pure CsI crystal is an inorganic scintillator and it has the better energy resolutions at high energies, the energy resolutions of the Lead/SciFi and a lead glass calorimeters are poor.

Lead/SciFi is a sandwich calorimeter made up of a heavy material (lead) and sensitive detector (scintillating fiber), and it is one of the cheapest calorimeter module. The energy resolution of the Lead/SciFi calorimeter in response to 200-800 MeV/c was measured at LNS. It is found to be 7.2% for 1 GeV/c electrons [1]. Since Lead/SciFi is a sampling calorimeter, the detection efficiency for the charged hadrons may depend on the incident position.

A lead glass Čerenkov counter has the higher energy resolution for electrons, positrons, and photons. The energy resolution of an SF5 lead glass calorimeter obtained is 4.9% for for 1 GeV positrons [2], and that of an SF6 one is 7.6% [3]. It is however insensitive to the low energy charged particles that do

not generate the EM shower since Čerenkov photons are not emitted from them.

Although the solid angle of FOREST is larger than that of the previous calorimeter SCISSORS II (2002–2005), there are gaps between different calorimeters. The gaps lose the acceptance for the reactions of interest. Thus, the replacement of FOREST with a 4π homogeneous inorganic scintillators is planed. At this moment, BSO and BGO crystals are the candidates of new EM calorimeter modules.

§2. Experimental Setup

The energy resolutions of the prototype calorimeters with BSO and BGO crystals are measured by using 200–800 MeV/c positron beams for testing detectors at LNS. The prototype EM calorimeters are constructed with a 2×2 array of BSO or BGO crystals. Each crystal was 210 mm long with a cross section of 40×40 mm^2, and was connected to a 1-inch photo-multiplier tube Hamamatsu H7415MOD. The four PMT's used for the BSO calorimeter are exactly the same as the BGO one. Positrons with energies ranging from 100 to 800 MeV/c were used as incident beams. To determine the incident position of the positrons, a beam profile monitor (BPM) was used. The BPM consists of two layers of scintillating fiber (SciFi) hodoscopes and 16 SciFi's with a cross section of 3×3 mm^2 were aligned in each hodoscope. The upstream and downstream layers determine x and y positions from responding fibers, respectively. Fig. 1 shows the experimental setup for the energy resolution measurement of the calorimeters.

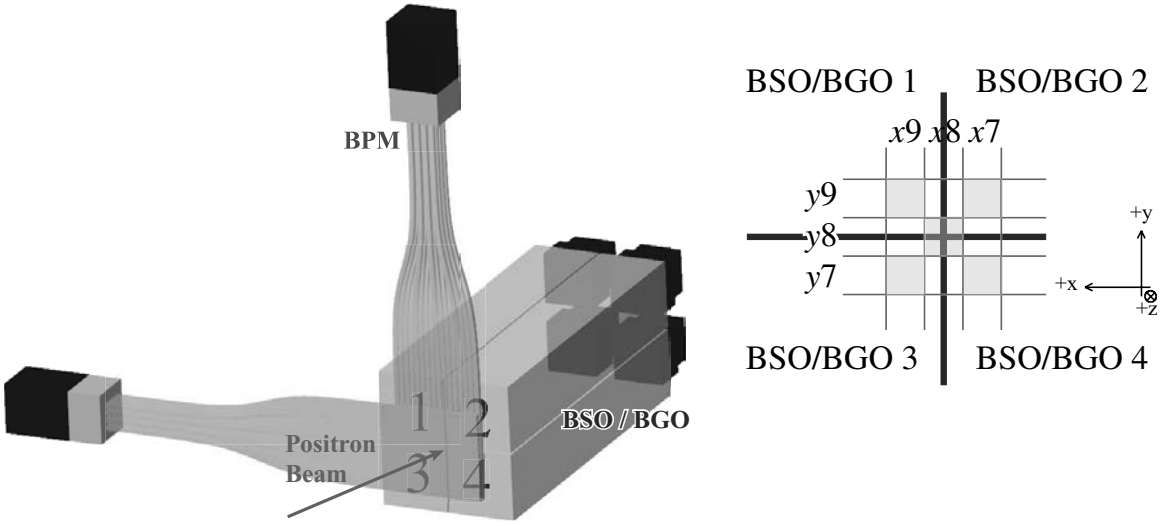

Fig.1. Experimental setup for the performance measurement of prototype BSO and BGO EM calorimeters. The 16×16 scintillating fiber hodoscopes are placed in front of a calorimeter to determine incident positions of positrons.

The trigger condition of the data taking system was described as

$$[x \text{ fiber OR}] \otimes [y \text{ fiber OR}], \tag{1}$$

where $\otimes$ stands for the coincidence of signals. The maximum trigger rate was 3 kHz and a fraction of accidental coincidence events was negligibly small.

§3. Energy Calibration

The energy calibrations for the BSO and BGO modules were made by using 200, 299, 399, 457, 588, and 743 MeV/c positrons injected onto the central region (3×3 mm^2) of each crystal one by one. The ADC distribution in each measurement was fitted with a logarithmic Gaussian [4] to deretermine the mean μ_c and width σ_c. Fig. 2 shows the ADC distributions that the positrons are incident on the central region of No. 1 BGO crystal.

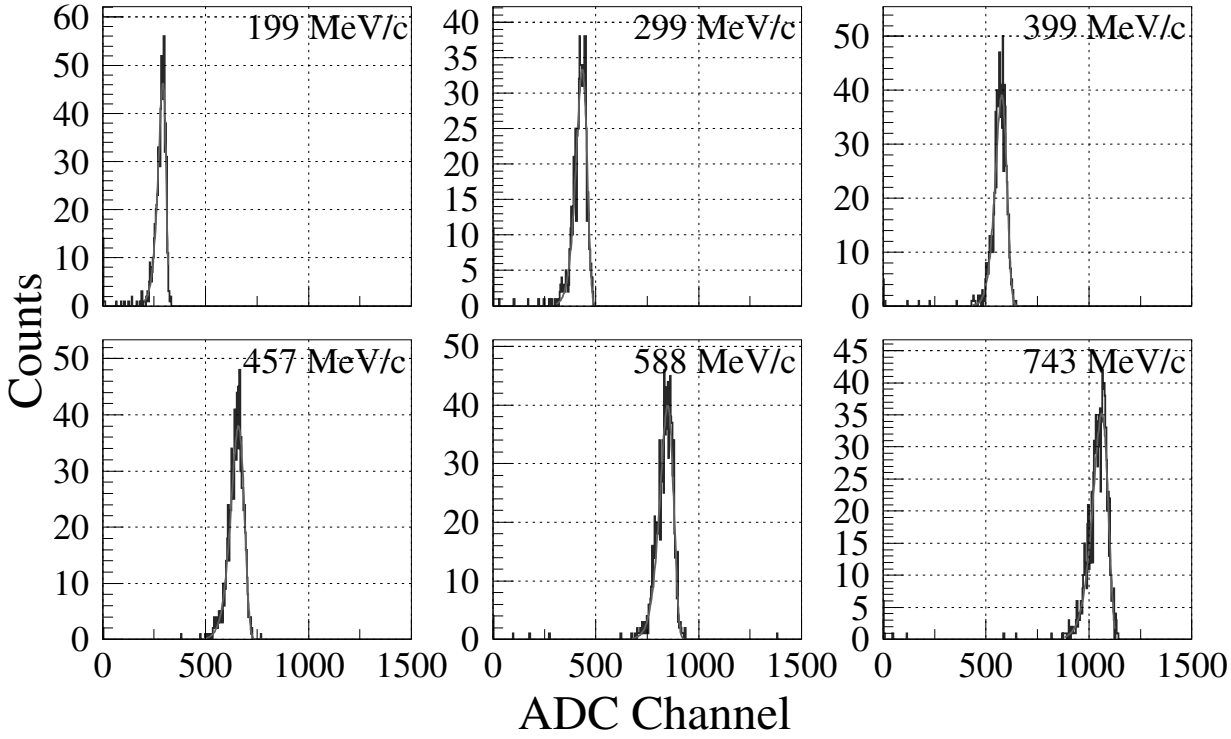

Fig.2. ADC distributions that the positrons are incident on the central region of No. 1 BGO crystal. The incident positron momentum are described in each panel. The solid line shows the fitted logarithmic Gaussians.

The pedestal distribution was measured with a 1 kHz clock signal trigger in each measurement, and the mean μ_p and width σ_p of which were determined by fitting with a nominal Gaussian. Since the energy leakage in the lateral direction exists, the ratios E_e/μ are different for different incident energies E_e where $\mu = \mu_c - \mu_p$. Fig. 3 shows the ratio E_e/μ as a function of the incident energy E_e.

The E_e/μ was well fitted with a linear function for all the crystals. The gain of each crystal was adjusted so that the limit of E_e/μ at $E_e = 0$ should be the same. The energy of each crystal E_i was given by

$$E_i = \alpha\,(A - \mu_p)\,, \tag{2}$$

where A is a measured ADC value and α is the limit of E_e/μ at $E = 0$.

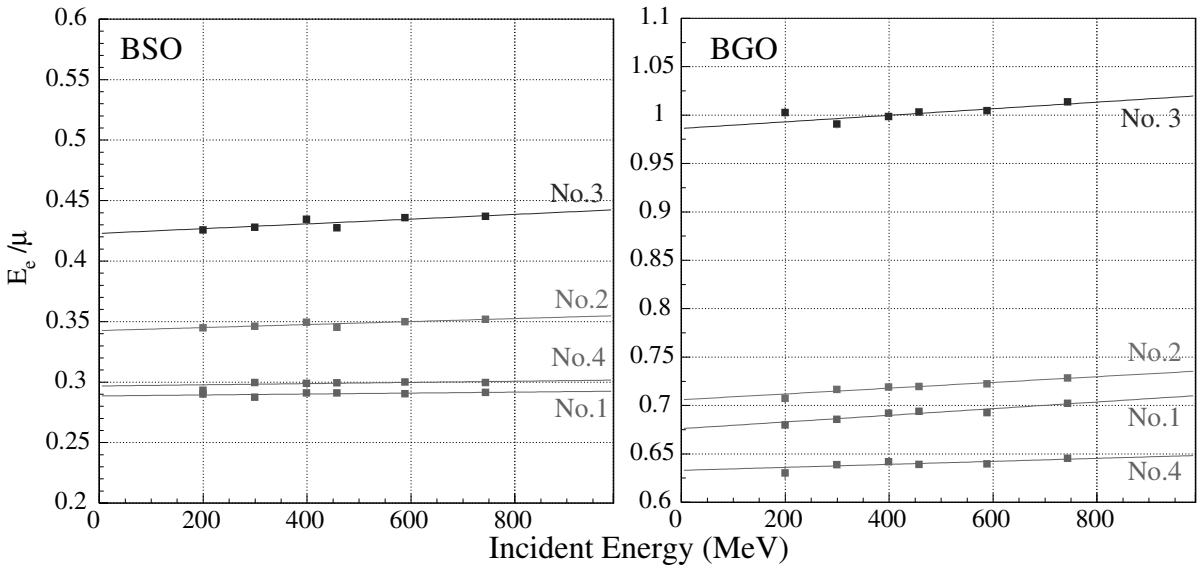

Fig.3. Ratio E_e/μ as a function of the incident energy E_e. The E_e/μ is not constant due to the energy leakage in the lateral direction. The solid line shows the fitted linear function.

§4. Energy Resolution

The energy of the calorimeter E was reconstructed by the sum of 4 crystal energies E_i as

$$E = \sum_{i=1}^{4} E_i. \tag{3}$$

The events that positrons were injected onto the central $x7$-$y7$, $x7$-$y9$, $x9$-$y7$, and $x9$-$y9$ regions of the EM calorimeter depicted in Fig. 1, which did not include the crystal boundaries, were selected to suppress the energy leakage in the lateral direction. Fig. 4 and 5 show the energy distributions of the BSO and BGO calorimeters for all the incident positron energies, respectively. The energy distributions were also fitted with a logarithmic Gaussian and the mean μ, width σ, and asymmetry parameter η were obtained for each incident positron energy for each incident position.

The energy resolution σ_E/E was estimated as

$$\left(\frac{\sigma_E}{E}\right)^2 = \left(\frac{\sigma}{\mu}\right)^2 - \left(\frac{\sigma_b}{\mu_b}\right)^2 - \left(\frac{\sigma_p}{\mu}\right)^2 \tag{4}$$

from the mean μ and width σ of the reconstructed energy distribution, the beam energy spread σ_b/μ_b given in Ref. [5], and the width σ_p of the energy distribution for the clock trigger (pedestal distribution). Fig. 6 shows the energy resolution as a function of the incident energy. The energy resolutions obtained were

$$\left(\frac{\sigma_E}{E}\right)^2 = \left(\frac{0.0205 \pm 0.0001}{\sqrt{E}}\right)^2 + (0.0114 \pm 0.0004)^2 \tag{5}$$

for the BSO calorimeter, and

$$\left(\frac{\sigma_E}{E}\right)^2 = \left(\frac{0.0190 \pm 0.0004}{\sqrt{E}}\right)^2 + (0.0094 \pm 0.0009)^2 \tag{6}$$

for the BGO one, where the incident energy is given in GeV. The energy resolutions at 1 GeV positrons corresponded to $2.35\% \pm 0.02\%$ and $2.12\% \pm 0.05\%$ for the BSO and BGO calorimeters with R8900U

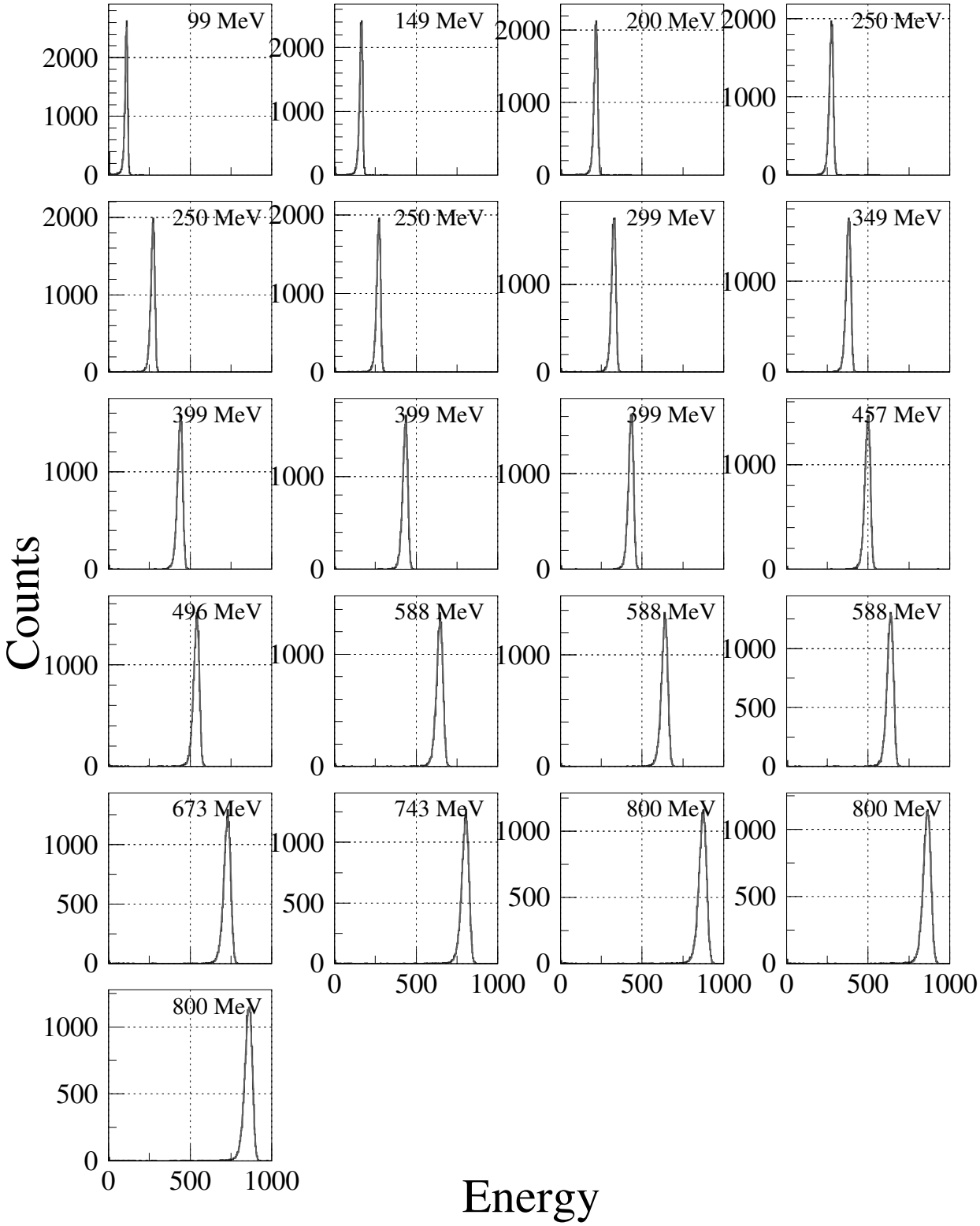

Fig.4. Energy distributions of the BSO calorimeter for all the incident positron energies together with the fitted logarithmic Gaussians. The positrons are incident on the central $x7$-$y7$, $x7$-$y9$, $x9$-$y7$, and $x9$-$y9$ regions. The incident momentum is described in each panel. The measurements are carried out thrice at several positron momenta.

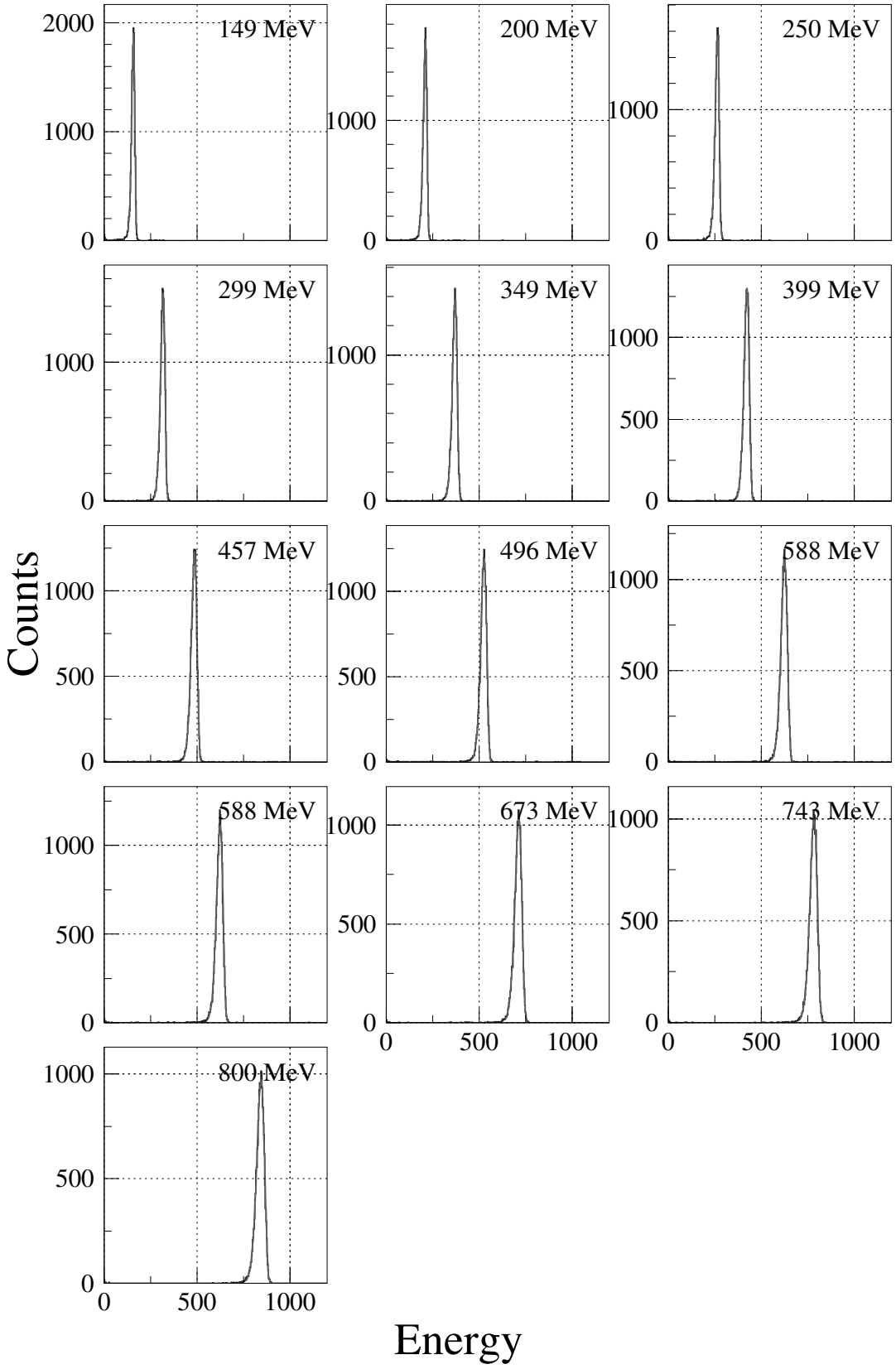

Fig.5. Energy distributions of the BGO calorimeter for all the incident positron energies together with the fitted logarithmic Gaussians. The positrons are incident on the central $x7$-$y7$, $x7$-$y9$, $x9$-$y7$, and $x9$-$y9$ regions. The incident momentum is described in each panel.

PMT's, respectively. The energy resolution of the BSO calorimeter was slightly worse than that of the BGO one.

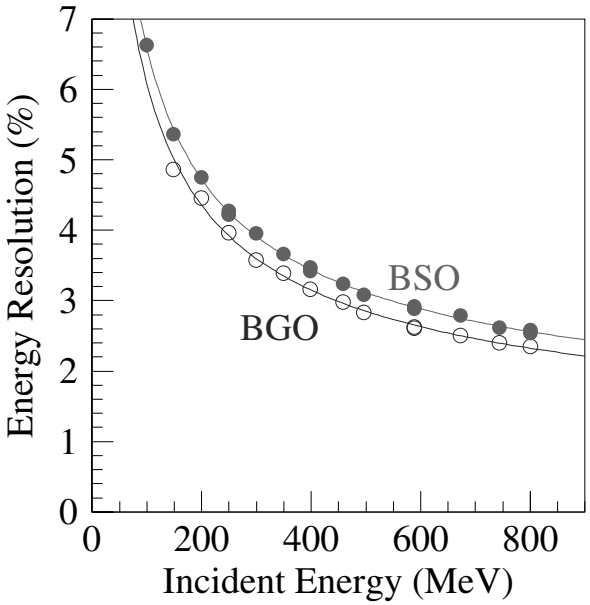

Fig.6. The energy resolutions of the BSO and BGO calorimeter with the R8900U PMT's as a function of the incident positron energy. The filled and open circles show the energy resolutions of the BSO and BGO calorimeters, respectively. The solid curves show the fitted functions (5) and (6).

The energy resolution of a BSO calorimeter with Hamamatsu H7415MOD reported is 2.04%±0.01% for 1 GeV positrons [6]. Although the effective area of the photo-cathode in R8900U (23×230 mm^2) is much larger than that in H7415MOD (25 mmϕ), the energy resolution for the BSO calorimter with R8900U is lower. This suggests that R8900U may have a problem in the focusing of the photoelectrons.

§5. Summary

The BSO and BGO crystals are candidates of new EM calorimeter modules. The energy resolutions of the prototype calorimeters with these crystals are compared in response to 100–800 MeV/c electrons. The energy resolutions for 1 GeV positrons are $2.35\% \pm 0.02\%$ and $2.12\% \pm 0.05\%$ for the BSO and BGO calorimeters, respectively. The energy resolution of the BSO calorimeter was slightly worse than that of the BGO one.

Acknowledgement

This work was supported in part by Grant-in-Aid for Scientific Research (B) (17340063) and for Specially promoted Research (19002003).

References

[1] K. Mochizuki, T. Ishikawa *et al.*: Research Report of LNS **40**, Tohoku University, 15 (2008).

[2] M. Sato, T. Ishikawa *et al.*: Research Report of LNS **41**, Tohoku University, 22 (2009).

[3] T. Ishikawa *et al.*: in this Research Report of LNS, Tohoku University.

[4] H. Ikeda, et al: Nucl. Instr. and Meth. A **441**, 401 (2000).

[5] T. Ishikawa *et al.*: Research Report of LNS **40**, Tohoku University, 6 (2008).

[6] S. Kuwasaki, T. Ishikawa *et al.*: Research Report of LNS **41**, Tohoku University, 11 (2009); S. Kuwasaki, T. Ishikawa *et al.*: Erratum in this Research Report of LNS, Tohoku University.

(LNS Experiment : #2634)

J-PARC ハイパー核γ線実験のためのπ^0同定カウンターの性能評価実験

大谷友和[1], 細見健二[1], 小池武志[1], 馬越[1*], 三輪浩司[1], 佐藤美沙子[1], 白鳥昂太郎[1], 田村裕和[1], 山本剛史[1]

[1] 東北大学大学院理学研究科 （980-8578 仙台市青葉区荒巻字青葉）

Study of a π^0 detection counter for the hypernuclear γ-ray spectroscopy at J-PARC

T. Otani[1], K. Hosomi[1], T. Koike[1], Y. Ma[1*], K. Miwa[1], M. Sato[1], K. Shirotori[1], H. Tamura[1], and T.O. Yamamoto[1]

[1]*Department of Physics, Tohoku University, Sendai, 980-8578*

We have studied a π^0 detection counter (SP0) which is used for a hypernuclear γ-ray spectroscopy experiment E13 at J-PARC. The SP0 is a key detector to separate hypernuclear producton events from many background events due to decays of K^- beam particles. Positoron beams of three different energies were irradiated to a prototype of the SP0 counter at LNS-Tohoku. A response to the positoron beams was compared with a Monte Carlo simulation and good agreement was obtained between the real data and the simulation. The detection efficiency of the SP0 for the $K^- \to \pi^-\pi^0$ event was obtained to be 78.7 $\pm$ 1.5(sys.) % including the systematic error of 1.5% estimated from the present experiment.

§1. ハイパー核γ線分光実験 J-PARC E13 実験とπ^0同定カウンター SP0

我々は J-PARC K1.8 ビームラインにてハイパー核の γ 線分光実験 E13 を計画している [1, 2]。ハイパー核のエネルギー順位を高精度で測定することによりハイペロン核子相互作用を究明し、またバリオンの原子核媒質中での性質の変化を調べることを目的としている。ハイパー核からの γ 線を検出のための大立体角ゲルマニウム検出器群 Hyperball-J、およびハイパー核生成を同定するためのスペクロメーターシステム SksMinus の双方を現在建設している。本実験では (K^-, π^-) 反応を用いてハイパー核を生成する。(K^-, π^-) 反応はハイペロン生成断面積が大きいという利点があるが、$K^- \to \pi^-\pi^0$ および $K^- \to \mu^-\nu$ などのバックグラウンドも大きいため、これらのバックグラウンドをハイパー核生成事象と区別することが必須となる。本研究では $K^- \to \pi^-\pi^0$ からの π^0 崩壊からの γ 線を検出し、崩壊イベントをトリガー段階で除去するための検出器 SP0 の性能を陽電子ビームを用いて評価を行った。

π^0 同定カウンター SP0 は 7 層のプラスチックシンチレーターと鉛シートのサンドイッチ構造となった検出器である。γ 線が検出器に入射したさいに生じる電磁シャワーによる検出器の多重度を調べることによっ

*Present address: GSI, Germany

て、γ 線を同定する。標的下流に設置され、π^0 からの γ 線に対して大きなアクセプタンスを持つように、横幅 1200mm、高さ 1100mm および奥行き 116mm とした。シミュレーションによって鉛の厚さおよび層の数を最適化することによって、検出器にあたえられるスペースのなかで最大の検出効率を得るように検出器の設計を行った。シミュレーションによって $K^- \to \pi^-\pi^0$ 反応で生じる γ 線に対して、検出器の多重度 3 以上を選ぶことによって 78%の効率で検出することが可能であることが分かった。このシミュレーション結果の現実性を評価する必要がある。本実験では e^+ ビームを SP0 のプロトタイプに入射し、シミュレーションと実データの比較を行うことで、シミュレーターの評価を行った。

§2. 実験のセットアップ

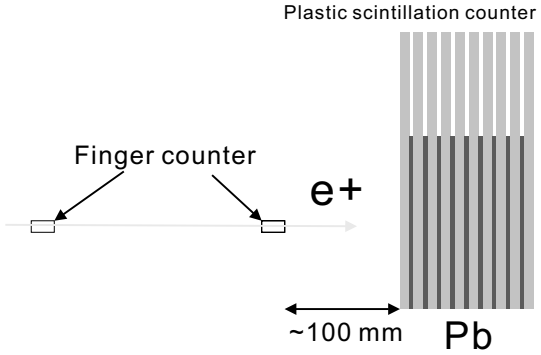

第 1 図　LNS 実験用セットアップ。プラスチックシンチレータは読み出し用光電子増倍管は R980 を使用した。鉛は厚さ 4mm と 6mm の二種類使用した。上流に設置したフィンガーカウンタでパスを選択し陽電子ビームを入射させた。

図 1 が実験セットアップである。フィンガーカウンタ ($10 \times 20 \times 10\text{mm}^3$) を設置し、同時測定を要求することでトリガーとした。設置したプロトタイプはプラスチックシンチレータ 10 枚、鉛 9 枚で構成されている。使用したカウンタは本実験で用いるプラスチックシンチレータ ($1100\times240\times8\text{mm}^3$) 及び光電子増倍管 (R980) を使用した。シミュレーションでは、単色エネルギーのビームをカウンタより 10 cm から表 1 の広がりをもって入射させた。コンバータとして使用した鉛はビーム軸方向の厚みが 4mm と 6mm の二種類、面積をモリエール半径を考慮して決定した。エネルギーの分かっている e^+ ビームをプロトタイプに入射しプロトタイプの振る舞いを、シミュレーションの結果と比較した。入射した e^+ ビームのプロファイルを表 1 に記す。

第 1 表　入射ビームのエネルギー分布及び位置分布

ビームエネルギー [MeV]	ビームの横幅 (horizontal) [mm]	ビームの縦幅 (virtical) [mm]
99±2	56±2	55±3
149±3	44±1	42.8±0.9
199±3	36.1±0.4	34.1±0.4

§3. 解　　析

STEP1：シミュレーションにおける、カウンタのエネルギー損失に対する閾値の決定。

SP0 の γ 線検出条件を見積もる上で、各カウンタの検出条件を考慮する必要がある。実際の実験における各カウンタの検出条件とは、カウンタからの信号をロジック信号へと変換するディスクリミネータの閾値である。実験的に可能なディスクリミネータの閾値を、シミュレーション内でのカウンタ毎の検出条件に反映させる。実験では、光電子増倍管のオペレーション電圧は 1 kV (最大定格)、ディスクリミネータの閾値は $\simeq$10 p.e. (40 mV) に設定した。

厚さ 4 mm の鉛を図 1 のように挿入し、エネルギー 150 MeV の陽電子ビームを入射させた場合のエネルギー分布を図 2 に示す。横軸は、各カウンタの最小電離損失の最頻値で規格化している。全イベントに対するスペクトルを黒線で、各カウンタにある 2 つの PMT を NIM レベル (リーディングエッジ型ディスクリミネータ) でロジック化した後同期が取れたイベントのものを青線で、規格化後に各カウンタにある 2 つのエネルギーが閾値以上であったイベントについて赤線で表している。ここで、閾値を陽電子による最小電離損失の最頻値の 3 割程度 (今解析では 32%) としている。青と赤を比べることで、陽電子による最小電離損失の 3 割程度とした閾値は実験的に可能な値 ($\simeq$10 p.e.) であることが分かる。

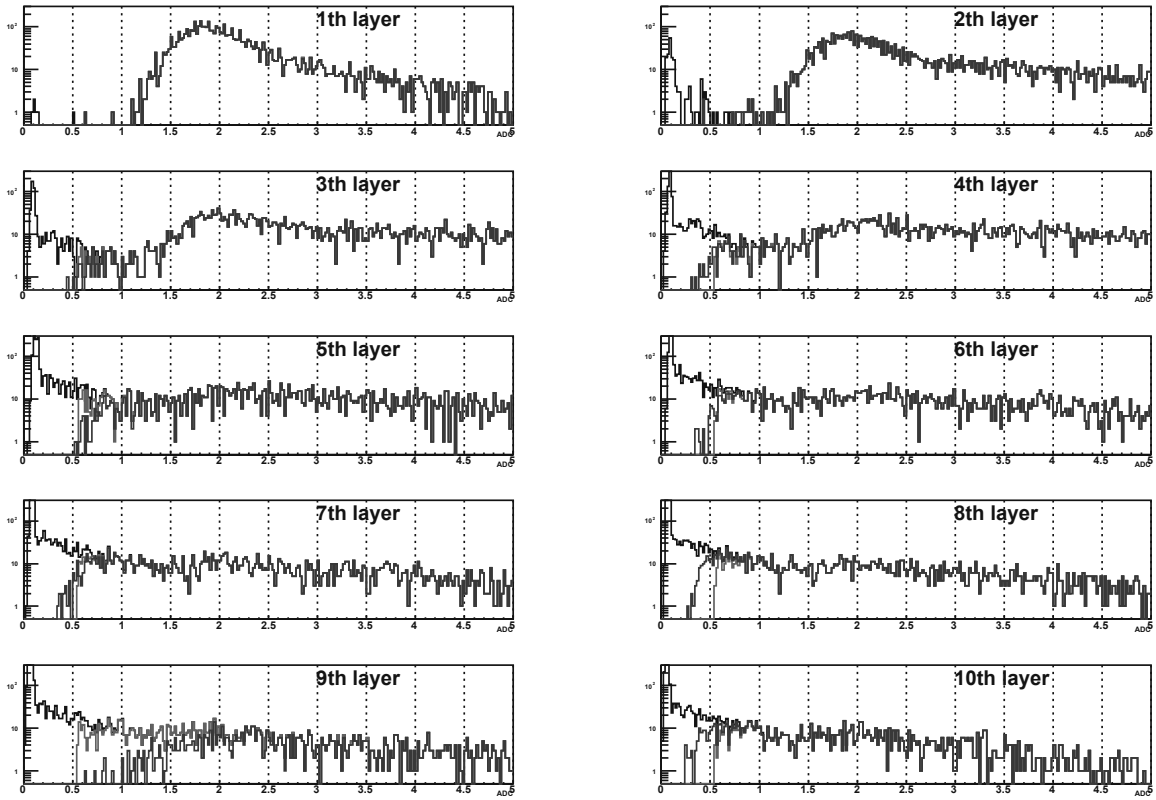

第 2 図　厚さ 4 mm の鉛プレートを挿入し、エネルギー 150 MeV の陽電子ビームを入射させた場合のエネルギー分布。横軸は、最小電離作用によるスペクトルの最頻値を与える位置で規格化している。各スペクトルの詳細は本文参照。

STEP2：シミュレーションと実験結果の比較によるシミュレータの評価。

シミュレーションと実験結果の比較はイベント毎の多重度の分布を用いる。STEP1 でカウンタの検出条件であるエネルギーに対する閾値を調整したため、シミュレーションで適切なカウンタの検出条件を与えることで実データを再現できることになる。実データとシミュレーションの多重度を比較し、最小二乗法を用い

ることで検出条件を決定した。

ここで実験での検出条件は、利得を調整した後、各カウンタにある 2 つの出力が閾値以上であることである。シミュレーションでの検出条件は、あるプラスチックシンチレータへのエネルギー損失がシミュレーション内で導入した各カウンターでのエネルギー損失に対しての閾値 Eth 以上となることである。χ^2 は、

$$\chi^2 = \sum_{i=1}^{n} (\frac{x_i - x_i^{'}(E_{th})}{\sigma})^2 \tag{1}$$

$$\sigma = \sqrt{x_i} \tag{2}$$

で定義される。ここで、n は比較するデータ数、x_i は実験データより得られた多重度 i のイベント数、$x_i^{'}(E_{th})$ はシミュレーションデータより得られた多重度 i のイベント数である。シミュレーションデータは実データの総数で規格化している。Eth を 0.55 MeV、鉛の厚さ 4 mm、入射 e^+ ビームのエネルギーを 150 MeV をとした場合の、実データとシミュレーションデータの比較例が図 3 である。左図は全イベント数で規格化した後の多重度の頻度分布となっており、青ヒストグラムが実データ、赤印がシミュレーションによる結果である。右図は左図の赤と青の差を多重度毎に表したもので、χ^2 はこの差の多重度 1 から 10 について総和を自由度 9 で割った値となる。最小 χ^2 を与える Eth を、各実験条件について決定する。ビームエネルギーと鉛の厚さを変えたそれぞれのデータについて、Eth をパラメータとしてフィッティングを行った結果が図 4 である。左側 (黒) が鉛の厚さ 4 mm の場合、右側 (青) が鉛の厚さ 6 mm の場合について表しており、それぞれ上から、ビームエネルギー 100、150、200 MeV を用いた場合である。最小 χ^2 を与えた Eth を中心値として、χ^2+1 の値を与えた Eth との差をエラーとした。エラーを見積もる際、χ^2 分布がパラボラ形であることを仮定している。結果として、鉛 4 mm の場合、各ビームエネルギーについて Eth は 0.70±0.02 MeV、0.58±0.01 MeV、0.57±0.01 MeV、鉛 6 mm の場合、それぞれ 0.61±0.03 MeV、0.56±0.01 MeV、0.52±0.02 MeV であった。

シミュレーション内で、鉛を挿入せずに、エネルギー 150 MeV の陽電子をカウンタの中心に入射させた場合のエネルギー損失の最頻値は 1.74 MeV である。実験データの全てのカウンタに対する閾値を最小電離損失の 32%に調整した (図 2 の赤スペクトル) ため、Eth は 1.74 MeV の 32%である 0.55 MeV になることが期待される。しかし結果として、最小 χ^2 を与えるパラメータ Eth は、各々エラー以上に異なっていた。さらに、最小 χ^2 の値はシミュレーションが実データを再現しきれていない可能性が高いことを示唆している。上記の結果は、Eth 以外のシミュレーション条件及びパラメータを固定して得られた結果であるため、他の条件を変えることで最小 χ^2 を与える Eth 及び誤差が変わる可能性がある。

STEP3：Eth による、SP0 の γ_K 線検出効率の系統誤差の見積もり。

STEP2 で、Eth のみでは、シミュレーションが実データを再現しきれないことが分かった。しかし、Eth の誤差が SP0 の γ 線検出条件に与える影響が小さい場合、γ 線検出効率を見積もる上で問題はないと考えられる。Eth を [0.55±0.15 (sys.)] MeV として、27%の誤差を与えた場合の SP0 の γ 線検出効率を見積もった結果が図 5 である。横軸は Eth、縦軸が SP0 の γ_K 線検出効率である。γ_K 線検出効率の中心値を Eth を 0.55 MeV とした場合の 78.7%とすると、シミュレーションと実データの相違による系統誤差は、1.5%である。以上のことから、Eth を [0.55±0.15 (sys.)] MeV として、SP0 の γ 線検出効率を見積もる上では問題ないと考えられる。

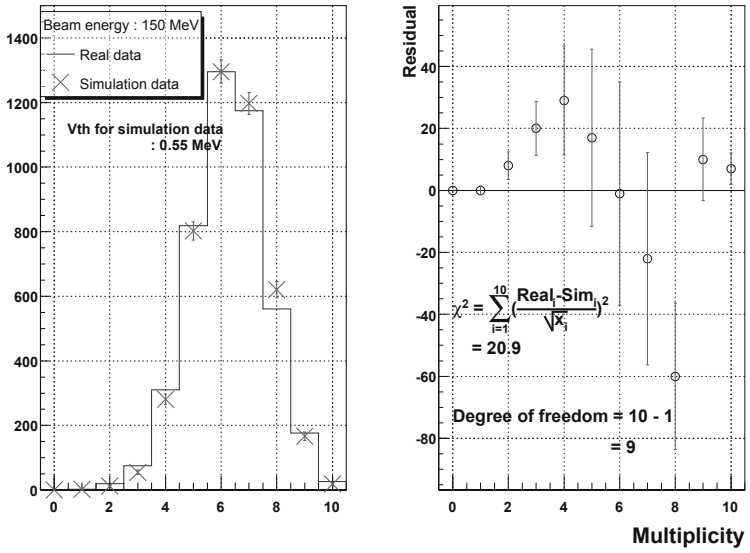

第 3 図　入射 e^+ ビームのエネルギーを 150 MeV、鉛の厚さ 4mm とした場合の、実験結果と、シミュレーション結果の比較例。
左図 : 実データによる多重度の頻度分布 (青ヒストグラム) と、シミュレーションによる多重度の頻度分布 (赤)。右図 : 多重度毎に見た左図の赤と青の差。

§4. ま と め

東北大学原子核理学研究施設で e^+ ビームを用いてテスト実験を行った。プラスチックシンチレータ 10 枚、鉛 9 枚で構成されたプロトタイプに対して、e^+ ビームのエネルギーを変えて入射させ、プロトタイプの応答を調べた。実データでの検出条件とシミュレーションでの検出条件を合わせるために、各カウンタのエネルギー損失に対する閾値と χ^2 の相関図よりシミュレータ内の検出条件を算出した。結果として、Eth を [0.55±0.15 (sys.)] MeV として SP0 の γ 線検出効率を見積もる必要があることが分かった。このシミュレータ内の検出条件の誤差による SP0 の γ 線検出効率の誤差は 1.5%程度であり、SP0 の γ 線検出効率はシミュレーションによる見積もりは高い信頼性があることが検証された。

謝　辞

実験中、非常に優れたビームを供給していただき、核理研の皆様に感謝いたします。特に石川助教には様々なユーザーの要求に対して対応していただきました。ありがとうございました。

参　考　文　献

[1] H. Tamura *et al.*: Nucl. Phys. **A804** (2008) 73.
[2] H. Tamura *et al.*: Nucl. Phys. **A805** (2008) 384.

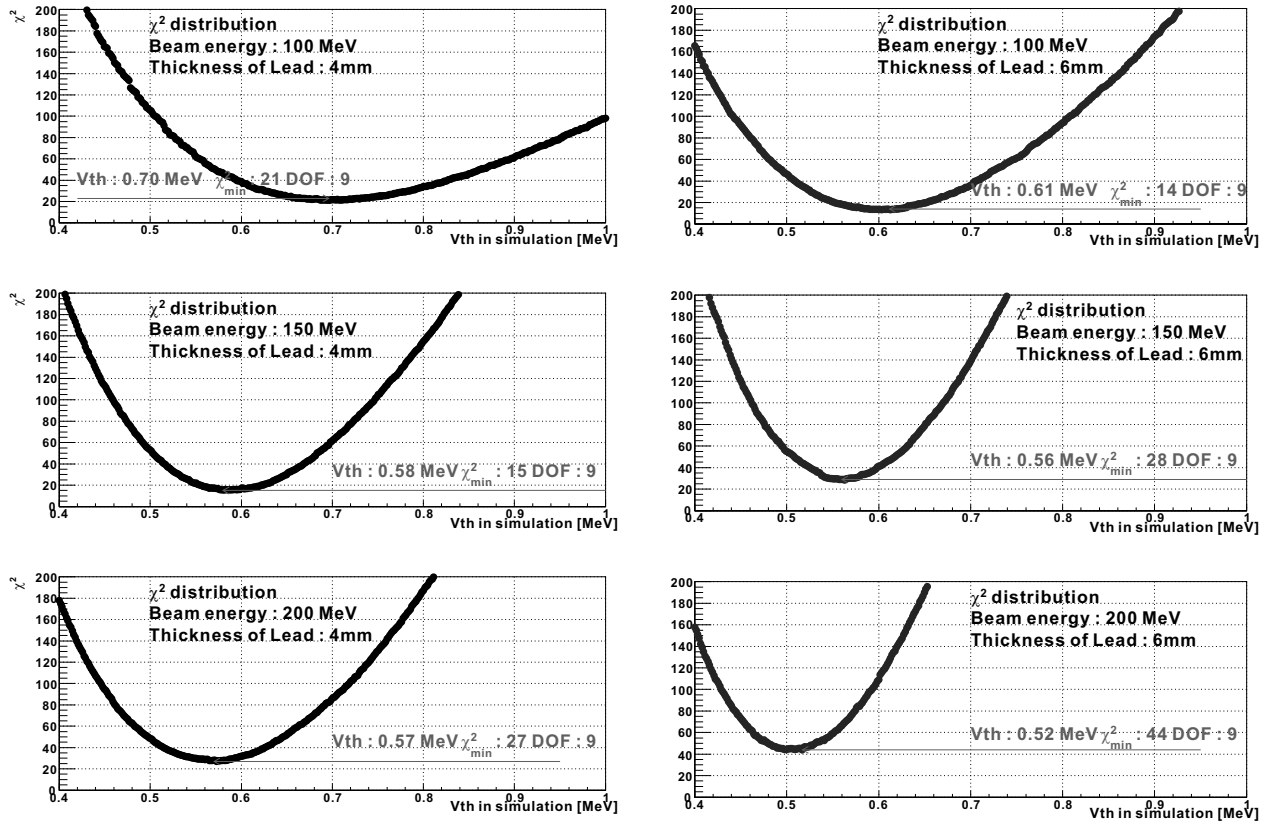

第 4 図　シミュレーション内の検出条件をパラメータとする χ^2 分布。左側 (青) が鉛の厚さ 4mm の場合、右側 (黒) が鉛の厚さ 6mm の場合、上からビームエネルギー 100、150、200 MeV に対応する。

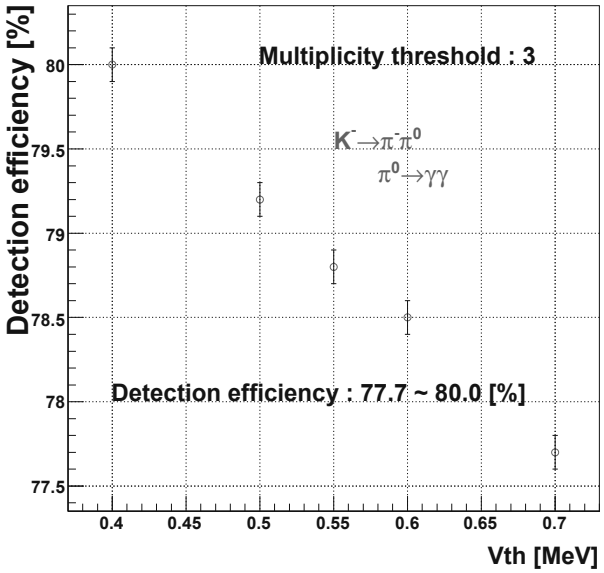

第 5 図　(Simulaiton) シミュレーションと実データの相違による SP0 の γ 線検出効率の系統誤差。横軸は Eth、縦軸は SP0 の γ 線検出効率である。

(LNS Experiment : #2634, #2653)

J-PARCハイパー核γ線分光実験のためのビームラインチェレンコフカウンターの性能評価実験

佐藤美沙子[1], 細見健二[1], 小池武志[1], 馬越[1*], 三輪浩司[1], 大谷友和[1], 白鳥昂太郎[1], 田村裕和[1], 山本剛史[1]

[1] 東北大学大学院理学研究科 (980-8578 仙台市青葉区荒巻字青葉)

Performance study of beamline cherenkov counters for hypernuclear γ-ray spectroscopy at J-PARC

M. Sato[1], K. Hosomi[1], T. Koike[1], Y. Ma[1*], K. Miwa[1], T. Otani[1], K. Shirotori[1], H. Tamura[1], and T.O. Yamamoto[1]

[1]*Department of Physics, Tohoku University, Sendai, 980-8578*

We are planning to perform hypernuclear γ-ray spectroscopy experiment with a germanium detector array Hyperball-J at J-PARC. Beam line cherenkov counters which are used to identify the (K^-, π^-) reaction are installed inside the Hyperball-J. Terefore,these counters are required to be a compact read-out system. As one possible solution, we are considering a read-out system using wave length shifting fibers. In this test experiment, positron beam ($p = 450$ MeV/c) was irradiated to the cherenkov counter which radiator was a Sillica aerogel($n = 1.05$). The cherenkov lights were detected by two types of read-out systems. One way was to use 3 inch PMT readout. The other way was usage of WLS fiber sheets. We mesured the photoelectron distribution of two types of read-out systems, and compared mean value of these distributions. The numbers of mean photo electron were $\sim$ 9 p.e. and 1.54 p.e. for 3 inch PMT and WLS fiber sheets, respectively. This result makes it clear that the fiber read-out system could not obtain sufficient light yield. It's absolutely essential for fiber read-out system that get more high light yield.

*Present address: GSI, Germany

§1. 開発の動機

我々は J-PARC において、ハイパー核 γ 線分光実験を計画している。様々な標的に対して、大立体角 γ 線検出器群 Hyperball-J を用いて、ハイパー核からの γ 線を検出する。ハイパー核を生成する反応として (K^-, π^-) 反応を用いるため、cherenkov 検出器を用いた粒子識別が必要となる。

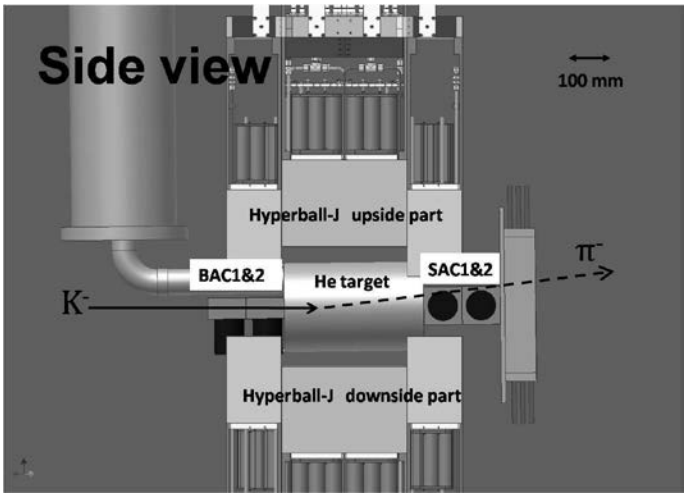

第 1 図　ターゲット周辺図

第 1 図は、He ターゲットの際のターゲット付近のセットアップである。ターゲットのまわりは、Ge 検出器群 Hyperball-J で密に取り囲まれているため、散乱側エアロジェルチェレンコフ検出器 (SAC) をターゲットの直後に設置すると、ターゲット後方の Ge 検出器と SAC の PMT とが干渉してしまう。またターゲットが LiO_2 などの小型のものの場合は、SAC は Hyperball-J の内部に入り込むため、SAC の PMT が影となって、ガンマ線の検出効率を低下させてしまう。これを避けるための一つの案として、波長変換ファイバーを用いたチェレンコフ光の読み出し方法の開発を行った。

§2. 波長変換ファイバーを用いた読み出し法の原理

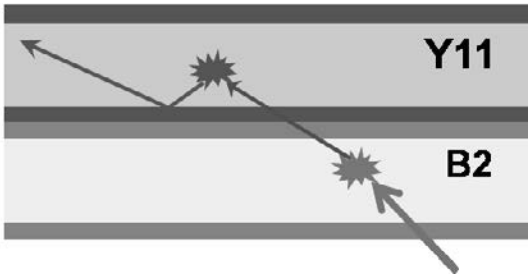

第 2 図
波長変換ファイバー読み出しの原理図

波長変換ファイバーを用いたチェレンコフ光読み出し法の原理について説明する。波長変換ファイバーを密にシート状に敷き詰め、ファイバーの端を光電子増倍管の光電面の大きさ以内に入るように束ねる。Y11 ファイバー、B2 ファイバー（クラレ社製）のそれぞれでファイバーシートをつくる。第 3 図は、実際に製作したファイバーシートの写真である。また、2 種類のファイバーの吸収・発光波長スペクトラムを第 4、5 図に示す [1]。このファイバーシートでエアロジェルチェレンコフ検出器の内壁の一部を覆い、ファイバーシートのファイバー側面から、光を入射させる。入射した光は、コア部の波長変換剤に吸収され、当方的に再発光される。再発光された光のうち、全反射条件を満たすものは、ファイバー中を伝播することができ、ファイバーの端面に到達することができる。端面に到達した光を光電子増倍管で読みだす。Y11、B2 の 2 種類のファイバーシートをチェレンコフ光入射面に近いほうから順に、B2、Y11 と並べて、チェレンコフ光の出口を覆うことで、散乱吸収されやすい紫外領域の光を B2 で先に吸収させ、B2 ファイバーシートを透過した、あるいはそこで再発光された Y11 の吸収波長領域の光を、後段に並べた Y11 ファイバーシートで吸収させる。この配置の狙いは第 2 図に模式的に示すように、B2 の発光波長領域と Y11 の吸収波長領域にオーバーラップがあることを利用して、前段に置いた B2 ファイバー内で、吸収、再発光された光のうち、全反射条件を満たさずに外部に出てしまう光を Y11 で再吸収させることにある。

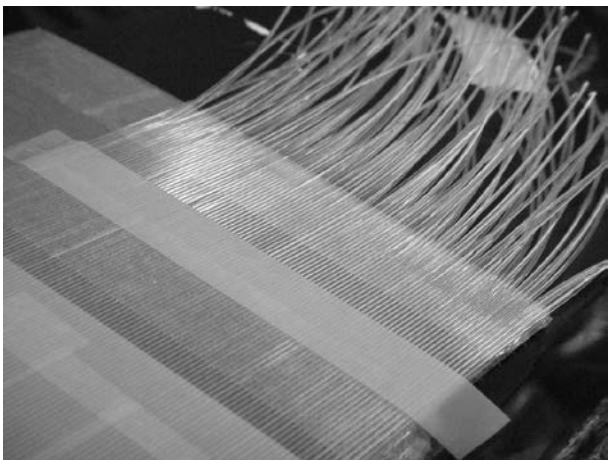

第 3 図　Y11 波長変換ファイバーシートの写真。

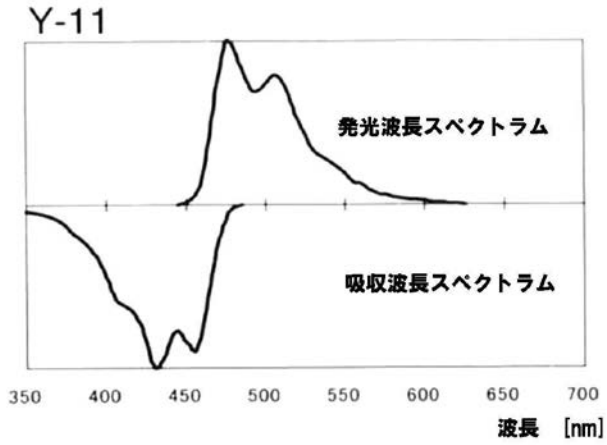

第 4 図　Y11 波長変換ファイバーの吸収、発光波長スペクトラム [1]

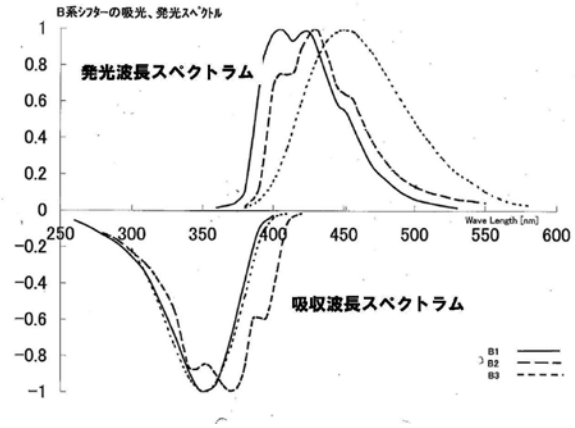

第 5 図　B2 波長変換ファイバーの吸収、発光波長スペクトラム [1]

§3. 波長変換ファイバーを用いた読み出し法の集光率測定

東北大学核理学研究施設の GeVγ 測定室で、屈折率 1.05 のシリカエアロゲルに $\beta = 1$ の陽電子を通過させて発生するチェレンコフ光をファイバーシートを重ね合わせて読みだした際にどれほどの光量が得られるかを調べるテスト実験を行った。

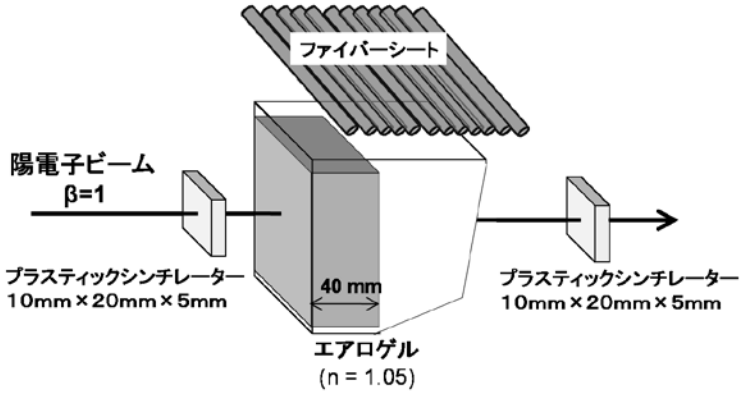

第 6 図　テスト実験のビームライン上セットアップ

第 6 図は、テスト実験のセットアップの模式図である。第 6 図に示すように、光量を調べたいエアロジェルチェレンコフ検出器の前後に、10 mm × 20mm の面積のプラスティックシンチレーションカウンター設置し、前後のカウンターのコインシデンスをデータ収集のトリガーとして、チェレンコフ検出器の ADC、TDC データを収集した。

テスト実験用に製作したカウンターは、ケント紙の箱の内側壁面に反射材としてフルオロトランスシートをしきつめたものに、断面積 110×110mm^2 ビーム方向の厚みが 40 mm^t のサイズのエアロジェルを入れ、タコ糸を用いて固定したものである。第 6 図のように、検出器内には、エアロジェルをビーム入射面直後におき、エアロジェルの後方に空気の層を作る。エアロジェルの厚み 40 mm に対して、空気層の厚みはおよそ 50 mm である。これに対して、ファイバーシートを用いた読みだしと、それとの比較のために、3 インチ径の光電子増倍管を用いて直接読み出しの 2 種類の読み出し方法でデータを収集する。

3 インチ径の光電子増倍管で読みだす際は、第 6 図中のファイバーシートで覆っている箱の壁面を 3 インチ径の光電子増倍管の窓の大きさにくりぬき、ここに直接光電子増倍管の窓を接続し、チェレンコフ光を読みだす。一方、ファイバーシートを用いた読み出しを行う際は、箱の一面を四角く切り開き、ファイバーシートで切り抜いた面を覆い、ファイバーの端を束ねて、$1\frac{1}{8}$ インチ径の光電子増倍管を合計 6 本使って読みだす。(第 7 図)

ファイバーシートは B2 を 2 枚、Y11 を 1 枚の合計 3 枚を用い、光が入射する側から B2-B2-Y11 の順に重ねた。各ファイバーシートのファイバーの両端に 1 本ずつの PMT を接着して両読みし、合計 6 チャンネルで得られる光量を足し合わせて全ファイバーシートで得らた光量とする。

第 8 図は全ファイバーシートで得られた光電子数と 3 インチ径 PMT で読みだして得られる光電子数のヒストグラムを示している。

白抜きは、3 インチ径径光電子増倍管を用いた読み出しで得られた光電子数分布で、平均光電子数は、~9 p.e. であり、斜線はファイバーシートを用いて読み出して得られた全光子数であり（6 本の光電子増倍管で得られた光量の和）、平均光電子数は 1.54 p.e. であった、これより、3 インチ径径光電子増倍管を用いた

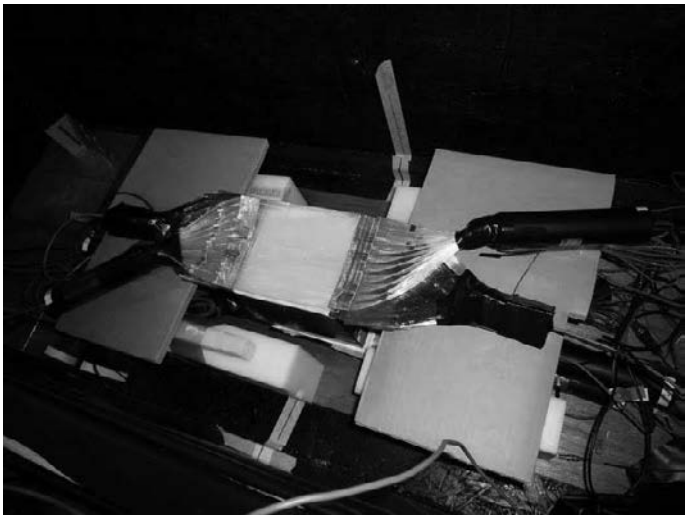

第 7 図　端面に光電子増倍管を接続したファイバーシートで検出器の壁面を覆っている。

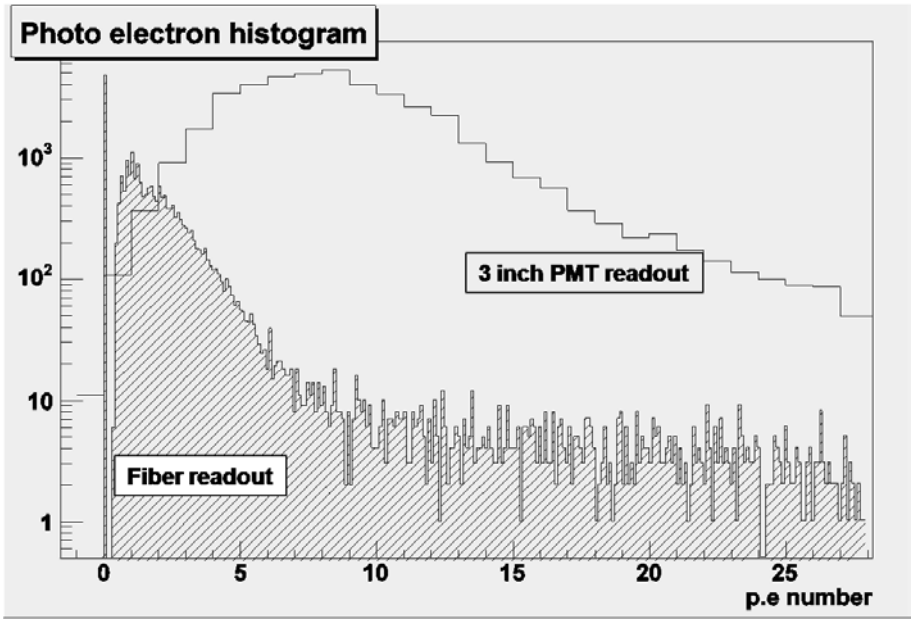

第 8 図　　全ファイバーシートで得られた光電子数 (白抜き)
と 3 インチ径 PMT で読みだして得られる光電子数のヒストグラム (斜線)。

読み出しと比較すると、ファイバーシートを用いた読み出し方法の集光効率は約 1/6 程度に下がることがわかった。表 1 に 3 インチ径径径光電子増倍管読み出しと、ファイバーシート読み出しで得られる光電子数の平均値と検出効率をまとめた。ここで、検出効率とは、全イベントに占める 0 p.e. ではないイベントの割合のことを指している。ファイバーシート読み出しの 0p.e. のイベント数を見積もるために、0p.e. と 1p.e. の間に閾値を決め、閾値以下をすべて 0 p.e. イベントとして数え、全イベント数で割ったものを P(0) とし、ファイバーシートで得られる検出効率は 1-P(0) と定義する。

表 2 は、3 枚の各ファイバーシートごとで得られた光量が全体に対して占める割合を表している。1 段目は一層目の B2 シート、2 段目は二層目の B2 シート、3 段目は三層目の Y11 シートである。この結果より、最前面においた B2 が集光の約半分を占めており、2 枚目の B2 シートでは、ほとんど集光は集光できてい

読み出し	平均光電子数	検出効率
3 インチ径 PMT	9.05 p.e	∼100 %
ファイバーシート	1.54 p.e	∼80%

第 1 表　平均光電子数と検出効率

	平均光電子数	全光量に占める割合
B2	0.90 p.e	∼54 %
B2	0.21 p.e	∼12 %
Y11	0.56 p.e	∼34 %

第 2 表　ファイバーシートごとが全体に対して占める割合。1 段目は一層目の B2 シート、2 段目は二層目の B2 シート、3 段目は三層目の Y11 シート

ない。これは B2 の吸収波長領域である、紫外領域の光が、2 枚目の B2 ファイバーに到達する確率は低く、ほとんど 1 枚目で吸収されているためと考えられる。また、Y11 の吸収領域である青色領域の光は、3 段目の Y11 ファイバーシートまで到達する確率が高く、Y11 での集光効率は、2 段目の B2 シートよりも高い値となっている。

この測定結果より、ファイバーシートを用いたチェレンコフ光の読み出しで、光電子増倍管で直接読みだす場合と比較して 1/6 程度に光電子数が落ち平均で、1.5 p.e. 程度である。E13 実験で、エアロジェルチェレンコフ検出器に要求される性能を満たすためには、最低でも平均 5 p.e. の光量が必要であるため、この読み出し方法は、現段階では実用は不可能である。
今後、ファイバーシートを用いたチェレンコフ光の読み出しのデメリットである、低集光効率という課題を解決する必要がある。

謝　辞

実験中、非常に優れたビームを供給していただき、核理研の皆様に感謝いたします。特に石川助教には実験のスケジューリングから様々なユーザーの要求に対して対応していただきました。ありがとうございました。

参　考　文　献

[1]　KURARAY CO.: SCINTILLATION MATERIALS.

(LNS Experiment : #2636)

PWO及びCsIを用いたγカウンターのプロトタイプテスト

鈴木史郎 [1], **下川哲司** [2], **山内秀元** [2], **山本智史** [2], **古川辰典** [2], **田島靖久** [3], **上林智亮** [4]

[1] 佐賀大学理工学部物理科学科　（840-8502 佐賀市本庄町 1 ）
[2] 佐賀大学大学院工学系研究科物理科学専攻　（840-8502 佐賀市本庄町 1 ）
[3] 山形大学基盤教育院　（990-8560 山形市小白川町 1-4-12）
[4] 山形大学大学院理工学研究科物理学専攻　（990-8560 山形市小白川町 1-4-12）

Prototype test of γ counters using PWO and CsI

Shiro Suzuki[1], Tetsushi Shimogawa[2], Hidemoto Yamauchi[2],
Satoshi Yamamoto[2], Tatsunori Furukawa[2], Yasuhisa Tajima[3],
and Kamibayashi[4]

[1]*Department of Physics, Faculty of Science and Engineering, Saga University, Saga, 840-8502*
[2]*Department of Physics, Grduate School of Science and Engineering, Saga University, Saga, 840-8502*
[3]*Institute of Arts and Sciences, Yamagata University, Yamagata 990-8560*
[4]*Department of Physics, Grduate School of Science and Engineering, Yamagata University, Yamagata 990-8560*

Prototype of the collar counter (gamma veto counter arond the beam area) for JParc-E14 experiment was tested with converted electron beam. Accumulation of the basic data on the energy resolution of the PWO counter, the uniformity of the counter, shower leakage to the neighboring counters and comparison with the GEANT-4 simulation, and evaluation of the light yield were made.

§1．実験の目的

鉛タングステン酸（PWO）結晶、および pure CsI を用いたプロトタイプカウンターのテストを陽電子ビームを用いて行い、JParc-E14 実験でのビーム軸を囲む「カラーカウンター」として用いる際の基本的データを収集すること、実機の素材の最終的決定を行うための情報を得る。特に、シャワーの広がりについての基本情報をシミュレーションと比較する。E14 用カウンターの実機サイズは $25 \times 25 \times 500\mathrm{mm}^3$ であり、実際には製作可能の $25 \times 25 \times 250\mathrm{mm}^3$ の結晶を２本接着して使用するので、接着面での光透過率を含む均一度、接合したカウンターの操作性などの実践的な問題点を明らかにする。

§2．セットアップ

テストすべきプロトタイプカウンターを、4 本の $50 \times 50 \times 500\mathrm{mm}^3$ の CsI ブロックで囲み、縦方向にビームを入射し、横方向へ漏れたシャワーを捕捉した。この CsI ブロックのエネルギー較正はこのセットアップの前にあらかじめ同ビームを用いて行った。入射ビームの位置は、直径 1mm のシンチレーション

第 1 図　プロトタイプカウンター

ファイバーを縦、横それぞれ８本づつ並べたホドスコープを用いて決定した。接着面での光透過効率を含むカウンター長さ方向の一様性測定、縦方向のシャワーの漏れの測定のためには、側面の CsI 1 ブロックを除去し、真横、あるいは斜め前からビームを入射した。

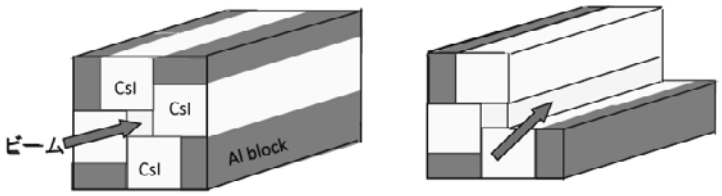

第 2 図　プロトタイプカウンター周りのセットアップ。(左) 正面入射の場合。(右) 側面入射の場合。

§3. 測定結果

3.1 PWO カウンターのエネルギー応答と横方向へのシャワーの漏れ

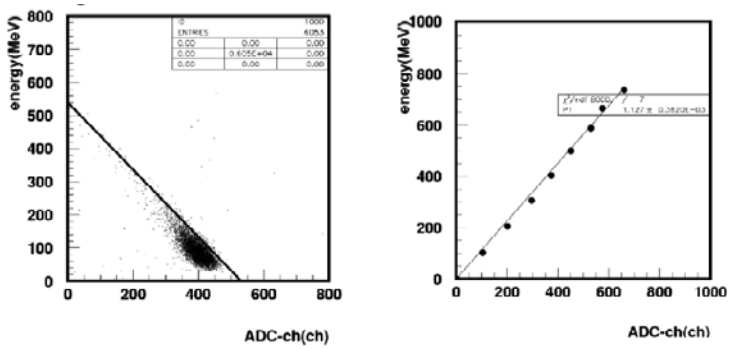

第 3 図　（左）PWO の応答 vs 漏れたエネルギー。直線は相関の傾きを示す（分布の中心ではない）。（右）入射ビームエネルギー vs 補正された PWO の応答

ビームを入射した際の PWO カウンターの出力の ADC 値と周囲の CsI カウンターへの漏れエネルギーを事象ごとに相関を取り、漏れゼロへの外挿をビームエネルギーに対応させることによって、PWO 自体へ

deposit されたエネルギーに対する応答の較正を行った。エネルギー分解能のエネルギー依存性を経験式

$$\frac{\sigma}{E} = \sqrt{\left(\frac{a}{\sqrt{E}}\right)^2 + b^2 + \left(\frac{c}{E}\right)^2} \qquad \%$$

（E in GeV）で評価すると、PWO のみの場合は $a = 3.45 \pm 0.10$, $b = 0.00 \pm 0.16$, $c = 2.23 \pm 0.08$ となり、さらに CsI へ漏れた分も加算すると $a = 2.55 \pm 0.05$, $b = 0.00 \pm 0.20$, $c = 1.47 \pm 0.04$ と改善され、1GeV では約 4% であった。

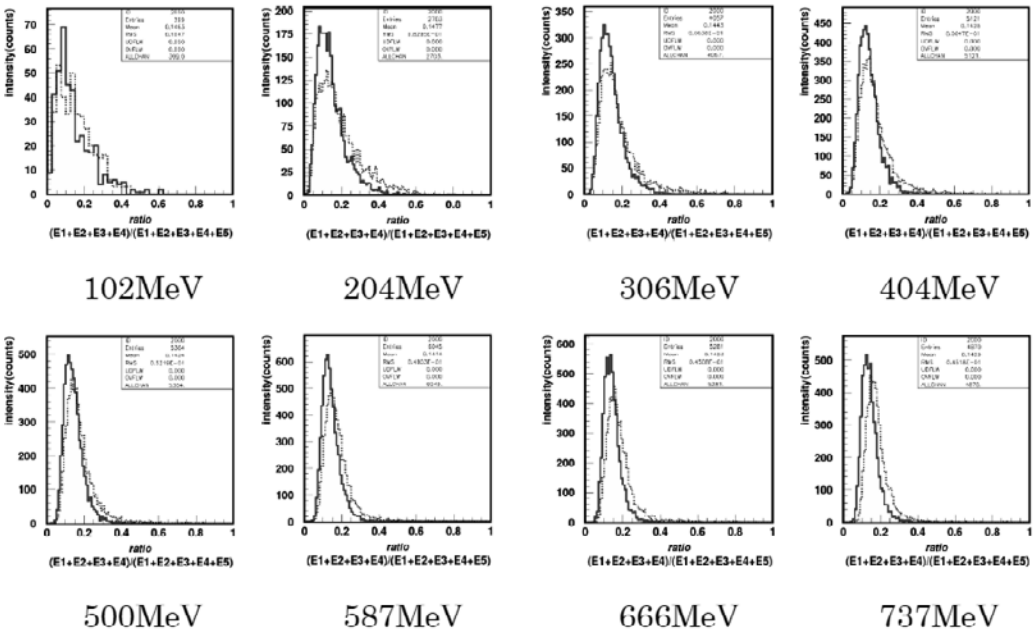

第 4 図　入射エネルギーごとの PWO からのシャワーの漏れの割合。実線がシミュレーション、波線がデータ。

横方向のシャワーの漏れの割合を入射エネルギーごとにみると、低エネルギーでは揺らぎが大きく、分布が広がっている。300MeV 以上では、PWO 中心入射の場合のシャワーの横方向への漏れの割合は約 18% である。これを GEANT-4 によるシミュレーションと比較した。高エネルギーでの分布に若干のずれはあるものの、分布の広がりのエネルギー依存性を含めよく再現している。

斜め入射で、ビームの縦方向へのシャワーの漏れに関しては解析中である。

3.2 カウンターの一様性

真横方向にビームを入射して、波高の場所依存性を測定することにより、カウンターの長さ方向の一様性をテストした。PWO に関しては接着面で約 88% の透過率が以前のテストで得られおり、今回もその結果が再現された。今回テストした CsI ベースのカウンターは、Type-A（プロトタイプとして自作したもの。$25 \times 25 \times 250\text{mm}^3$ 2 本を RTV で接着。）、Type-B（シャワー漏れ測定用に用いている KTeV 実験で使われたものと同タイプのもの。$50 \times 50 \times 250\text{mm}^3$ 2 本を EPOTEK-305 で接着）の 2 種類である。

2 つは対照的な結果を示し、EPOTEK-305 を用いた Type-B は接着面の透過率ほぼ 90%を示したのに対し、Type-A はわずかに 32% であった。Type-A ブロックは結晶の接着面処理が完全でなかったことを

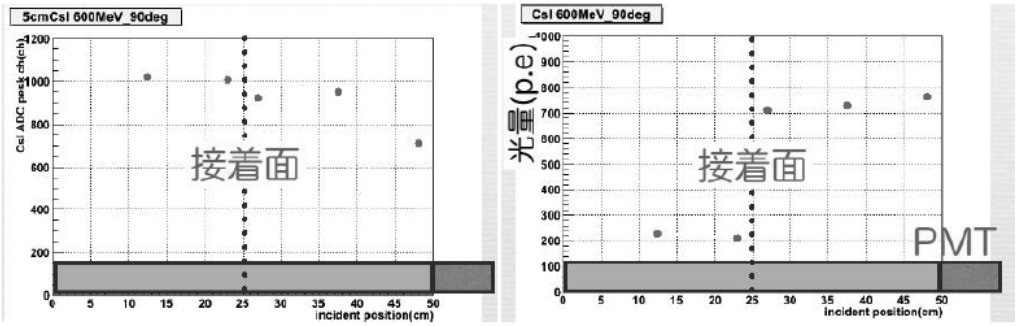

第 5 図　長さ方向の CsI カウンターの一様性。（左）$50 \times 50 \times 500\text{mm}^3$ カウンター Type-B（右）$25 \times 25 \times 500\text{mm}^3$ カウンター Type-A

考慮するとしても、紫外領域の寄与の大きい CsI 接着には EPOTEK-305 が優れているという明白な結論がでた。

3.3 発 光 量

光電面直径 15mm の光電子増倍管（HPK H6524）を用い、ビームを接着した $25 \times 25 \times 250\text{mm}^3$ 結晶の光電子増倍管に近い方のブロックの中心に入射して発光量を測定した。結晶にシャワーが与えた energy を Geant-4 で見積もり、測定光電子数 CsI 15.4p.e./MeV、PWO 2p.e./MeV を得た。発光量の観点からは PWO を使用した場合には敷居値の設定には制限が必要である。

§4. ま と め

カウンター内でのシャワーの漏れについてのデータを得、その振る舞いについて、Geant-4 が良い近似を与えることが確認された。また、実機のオプションを考えるにあたり考えるべき幾つかの点、PWO / CsI 双方の場合の結晶接着法、カウンターの一様性、発光量などについて、実機を設計するにあたっての基本情報を得ることができた。

安定したビームの供給と効率的な実験環境維持に奮闘してくださった LNS スタッフに感謝いたします。

(LNS Experiment : #2637)

中性K中間子ビームラインで使用するγ線/中性子測定用カロリメータのEMモジュールの性能測定

大津 亜樹[1], 田島 靖久[2], 吉田 浩司[2]

[1] 山形大学理学部 （990-8560 山形市小白川町 1-4-12）
[2] 山形大学大学院理工学研究科 （990-8560 山形市小白川町 1-4-12）

Performance of the EM module in gamma/neutron calorimeter for neutral kaon beam line

A. Otsu[1], Y. Tajima[2], and H. Y. Yoshida[2]

[1]*Department of Physics, Yamagata University, Yamagata, 990-8560*
[2]*Department of Physics, Yamagata University, Yamagata, 990-8560*

The J-PARC E14 KOTO experiment aims at the first observation of the $K_L^0 \to \pi^0\nu\bar{\nu}$ decay. In order to estimate the background in this experiment, it is important to measure the intensity and energy distribution of gamma and neutron in the K_L^0 beam line. "Cerberus" is a set of sandwich calorimeters to measure gamma and neutron in the beam line. The first module of Cerberus is aimed to measure the intensity and energy distribution of gamma, it called electro-magnetic (EM) module of Cerberus.

In this report, we have studied the linearity, energy resolution, position uniformity and the response in high rate environment for the EM module by using positron beam with the momentum between 300 and 800 MeV/c.

§1. Introduction

J-PARC E14 KOTO 実験は $K_L^0 \to \pi^0\nu\bar{\nu}$ 崩壊の分岐比の測定を目的とした実験 [1]である。2012 年の本実験開始を目指し準備中で、現在 K_L^0 ビームラインを J-PARC のハドロンホールに建設している。ビーム中に含まれる γ 線、中性子は $K_L^0 \to \pi^0\nu\bar{\nu}$ の測定の background に大きく影響するため、そのエネルギー分布、強度を測定して把握しておくことは大変重要である。ビーム中の γ 線、中性子を測定するために多段からなるカロリメータ Cerberus を使用する。今回の実験ではこの Cerberus の 1 段目である EM module の性能評価を行った。

§2. Cerberus

Cerberus は KOTO 実験の前身実験である KEK PS E391a 実験のときにビームライン測定用に制作された検出器 [2]である。今回 KOTO 実験のビームラインの測定でも使用する。その全体構成を第 1 図に示す。Cerberus は 6 台のサンドイッチカロリメータで構成されていて、それぞれのモジュールは上下に左右前後、8 本の光電子増倍管を配置して読み出している。最上流の 1 台は鉛–プラスチックシンチレータのサ

ンドイッチからなるモジュールで、鉛 4mm、プラスチックシンチレータ 3.4mm の 25 層からなり、全体の厚さは $18X_0$ となり、ほとんどの γ 線はこのモジュールでエネルギーを落として停止する。そのためこのモジュールは EM (electro-magnetic) module と呼ばれ、γ 線の強度、エネルギー分布の測定に使用する。2 から 6 台目が鉄–プラスチックシンチレータのサンドイッチからなり、EM module を veto 検出器とすることで、γ 線を reject して、突き抜けてきた中性子の測定が可能となる。そのため、この 2 から 6 段目を hadron module と呼ばれる。

§3. Experimental setup

今回の測定は GeVγ 照射室の陽電子ビームラインを利用し、Cerberus の EM module の入射エネルギーに対する線形性、エネルギー分解能、入射位置に対する一様性、入射ビーム強度に対する安定性の測定を行った。実験のセットアップを第 2 図に示す。測定のトリガーは 3 本のプラスチックシンチレータの coincidence で作成し、Cerberus 上で 10mm × 10mm の大きさでトリガーするように設定した。

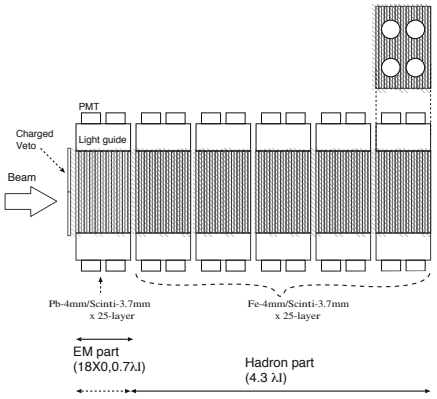

第 1 図　γ 線/中性子カロリメータ Cerberus

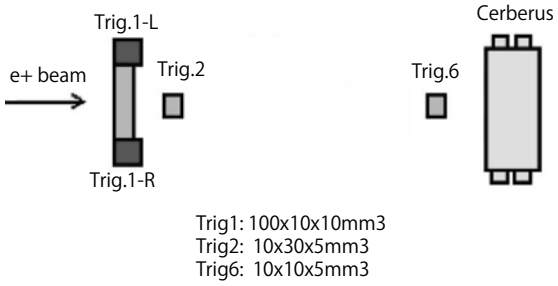

第 2 図　実験セットアップ

§4. Results

典型的な各光電子増倍管の ADC 出力を第 3 図に示す。光電子増倍管の出力は別途行った宇宙線測定の結果を用いて MIP (Minimum Ionizing Particle) が通過したときの deposit energy ($\simeq$ 18.5MeV/8PMT) で規格化した。以下の解析は規格化した 8 本の光電子増倍管の出力を足しあわせた値を用いて行った。

4.1 エネルギーに対する線形性、分解能

入射陽電子の運動量が 300 ~ 800MeV/c の範囲で測定を行い、その結果を第 4 図と第 5 図に示す。入射陽電子エネルギーに対する光電子増倍管の応答は線形性を示しており、

$$E_{dep}[\mathrm{MeV}] = (4.69 \pm 0.03) \times 10^{-2} \times \mathrm{E}[\mathrm{MeV}] + (-14.3 \pm 1.9) \qquad (1)$$

の関係が導かれた。ここで E_{dep} は Cerberus で検出されるエネルギー、E は入射エネルギーである。求めた直線が原点を通っていないのは、集光ロスが原因と推測される。

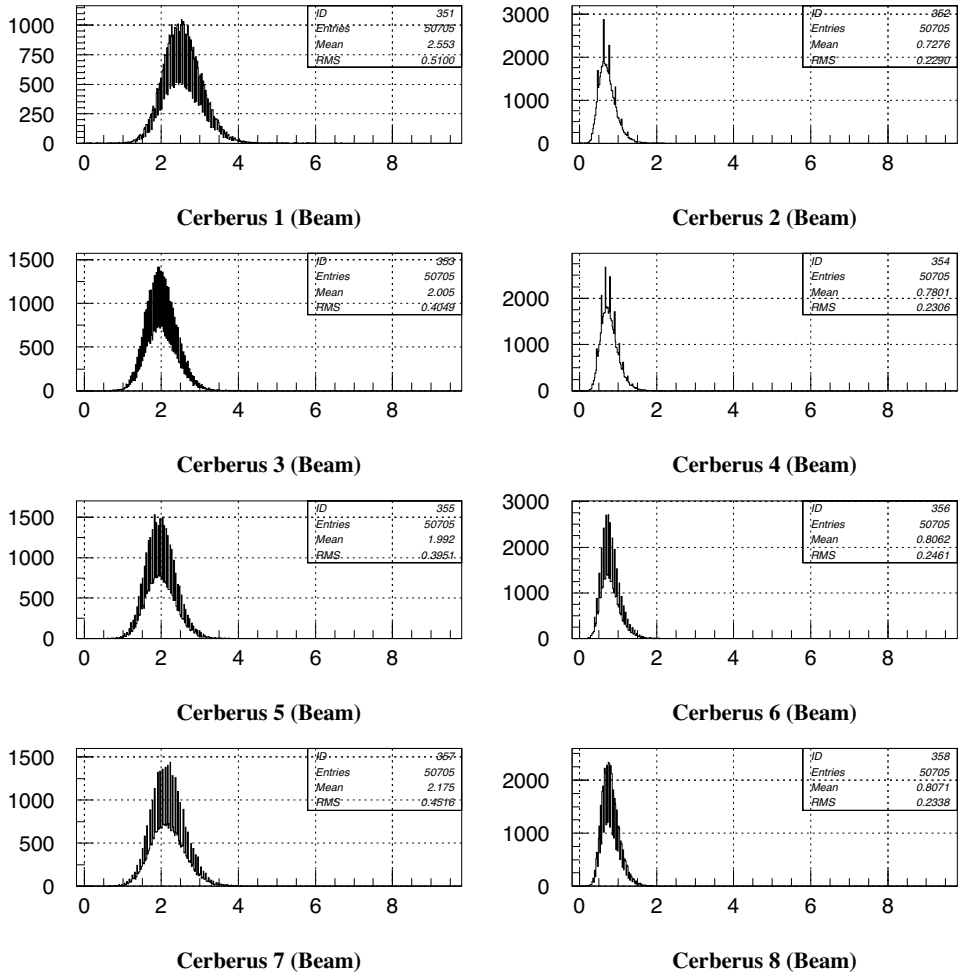

第 3 図　600MeV/c の陽電子を入射したときの Cerberus の各 PMT での ADC 分布。横軸は宇宙線測定で求めた MIP による deposit energy で規格化をしている。奇数番号の左列が上流側の PMT、偶数番号の右側が下流側の PMT になっている。

また、エネルギー分解能は

$$\frac{\sigma}{E} = \frac{0.1268 \pm 0.0015}{\sqrt{E}[\mathrm{GeV}]} \oplus (0.000 \pm 0.031) \tag{2}$$

となった。($\oplus$ は 2 乗和) ここではビームのエネルギー分解能は測定していないため、ビームのエネルギー分解能を含めた値となっている。

4.2　入射位置による一様性

KOTO 実験で使用する中性 K 中間子ビームラインでのビームの大きさは 10cm 角 (@z=27m) になる。[3] Cerberus はこの範囲内で入射エネルギーに対する光量、エネルギー分解能が一定であることが要求される。入射陽電子運動量を 600MeV/c に固定して、Cerberus の入射位置を水平方向 (PMT 方向) に 0mm と 150mm、垂直方向に 0mm と-100mm と移動させた 4 点で測定を行った。その結果が第 6 図である。獲得光量は ±5% 以内、分解能は ±2.5% 以内に入っており、前節で測定されたエネルギー分解能と比べて十分小さく、測定範囲 (±150mm,±100mm) で一様であることが確認できた。

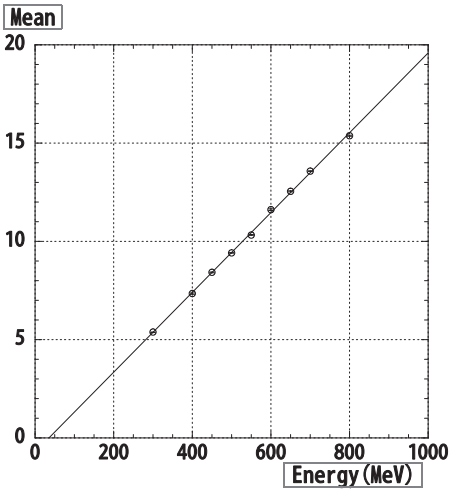

第 4 図　入射エネルギーに対する光電子増倍管出力の線形性

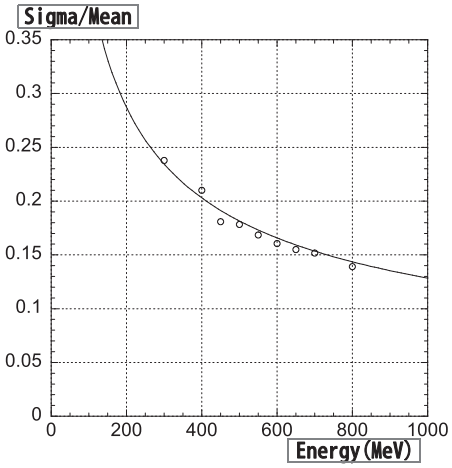

第 5 図　エネルギー分解能の入射エネルギー依存性

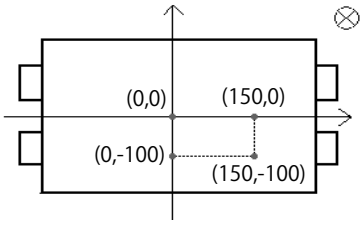

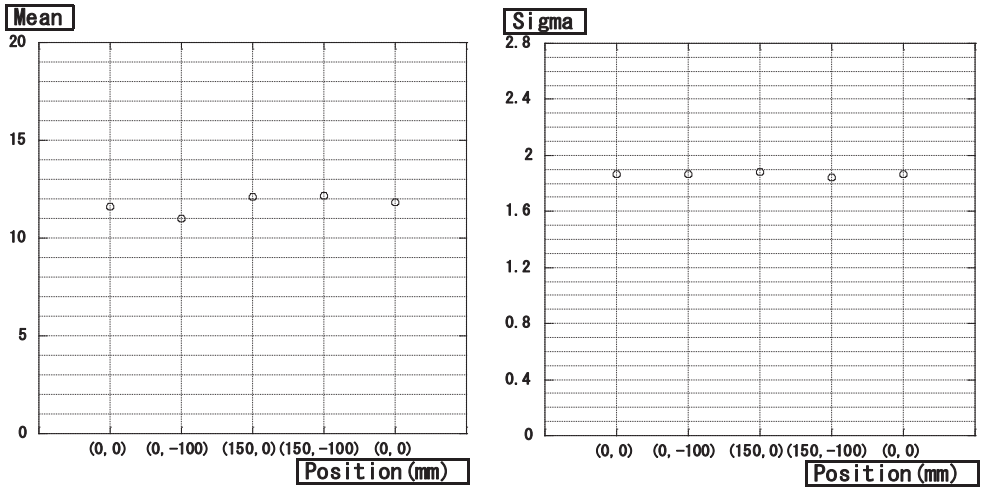

第 6 図　一様性測定結果。左図が光量、右図が分解能である。左図の縦軸は MIP で規格化した獲得光量の値である。

4.3　入射ビーム強度に対する安定性

J-PARC の K_L^0 ラインで Cerberus で測定する際のビーム強度は本実験のときの 1/100 以下の強度 (primary beam で 1KW) で行う予定であるが、それでも KEK PS の通常運転時のビーム強度に匹敵する。このビーム強度で Cerberus が運用可能であるか検証しておく必要がある。ここでは入射ビームを一番強度がでる $600MeV/c$ に設定し、取り出し時間を通常の 5sec. から 20msec. に短縮し、可能なかぎりビーム強度を高めた状態での測定を行った。Cerberus 全体に入射したビームの強度は Cerberus の TDC 分布から求

めることができ、通常強度の時が 8.5KHz、high rate 設定では 450KHz であった。それぞれのビーム強度で測定した ADC 分布が第 7 図である。high rate では 25MIP 付近に同時に 2 粒子が入射したときにみられるパイルアップのピークが見られるが、12MIP 付近の 1 粒子のピークは移動しておらず、450KHz 下でも Cerberus は問題なく動作していることが確認できた。

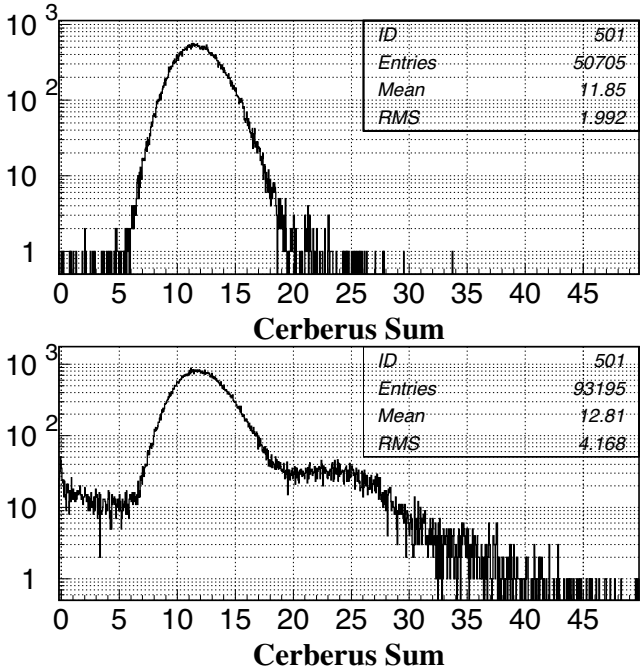

第 7 図　ビーム強度依存性測定結果。上図が通常ビーム時。(8.5KHz e^+ beam) 下図が high rate 時。(450KHz) 両図とも横軸は MIP で規格化した値である。12 MIP 付近の e^+ が 1 個入射したときのピークの位置は変わっていない。

§5. Summary

東北大学原子核理学研究施設の GeVγ 照射室の陽電子ビームラインを使って、γ 線/中性子測定用カロリメータ Cerberus の EM module の性能測定を行った。EM module のエネルギー応答の線形性が確認でき、入射エネルギーの 4.7%が検出できることがわかった。またエネルギー分解能は 1GeV で 12.7%が得られた。入射位置依存性も (± 150mm, ± 100mm) の範囲で ±5% 以内に収まっており、測定に影響がないこと、入射ビーム強度の影響も 450KHz までは光電子増倍管のゲインの劣化もなく測定出来ることがわかった。

参　考　文　献

[1] E14: Proposal for $K^0_L \to \pi^0\nu\bar{\nu}$ Experiment at J-Parc, approved July 2007.

[2] H.Watanabe *et al.*: Nucl. Instrum. Method **A545** (2005) 542.

[3] T.Shimogawa: Nucl. Instrum. Method **A623** (2010) 585.

(LNS Experiment : #2649, #2652, #2663, #2664)

K^{O}TO 実験の為の検出器試験

南條　創[1], 河崎　直樹[1], Jong-won Lee[2], 前田 陽祐[1], 増田　孝彦[1], 松村　徹[3], 内藤　大地[1], 野村　正[4], 笹尾　登[5], 佐々木 未来[6], 塩見　公志[1], 田島 靖久[6], 高橋　剛[1], 臼杵　亨[1], 吉田 浩司[6]

[1] 京都大学大学院理学研究科 (606-8502 京都市左京区北白川追分町)
[2] 大阪大学大学院理学研究科 (560-0043 豊中市待兼山町 1-1)
[3] 防衛大学応用物理学科　(238-8686 神奈川県横須賀市走水 1-10-20)
[4] 高エネルギー加速器研究機構素粒子原子核研究所 (305-0801 つくば市大穂 1-1)
[5] 岡山大学極限量子コア (700-8530 岡山市津島中 3-1-1)
[6] 山形大学理学部 (990-8560 山形市小白川町 1-4-12)

Detector tests for K^{O}TO experiment

H. Nanjo[1], N. Kawasaki[1], J. Lee[2], Y. Maeda[1], T. Masuda[1], T. Matsumura[3], D. Naito[1], T. Nomura[4], N. Sasao[5], M. Sasaki[6], K. Shiomi[1], Y. Tajima[6], G. Takahashi[1], T. Usuki[1], and H. Yoshida[6]

[1]*Department of Physics, Kyoto University, Kyoto, 606-8502*
[2]*Department of Physics, Osaka University, Osaka 560-0043*
[3]*Department of Applied Physics, Radiation Physics, National Defence Academy in Japan, 239-8686*
[4]*High Energy Accelerator Research Organization (KEK), Ibaraki 305-0801*
[5]*Research Core for Extreme Quantum World, Okayama University, Okayama 700-8530*
[6]*Department of Physics, Yamagata University, Yamagata 990-8560*

We developed detectors for K^{O}TO experiment, which aims to discover CP-violating mode, $K_L \to \pi^0\nu\nu$. This mode is a sensitive probe for the Standard Model and beyond. We developed a detector system to measure K_L yield and spectrum in the KL beamline at J-PARC. We also developed the K^{O}TO detector elements. Such prototypes were tested at LNS and performances were examined.

§1. K^{O}TO 実験

K^{O}TO 実験 [1]は J-PARC 加速器を用いて、$K_L \to \pi^0\nu\nu$ 崩壊 [2]を探索する実験である。$K_L \to \pi^0\nu\nu$ 崩壊は、CP を直接的に破るモードで、理論的な不定性が少なく、標準理論の検証及びそれを越える物理の探索が可能である。この崩壊の標準理論予測分岐比は 2.5×10^{-11} [3]であり、未だ発見されていない。K^{O}TO 実験はこの発見を目指している。$K_L \to \pi^0\nu\nu$ 事象の特徴は、π^0 からの 2γ 以外、他になにも存在しないということである。また、その π^0 が比較的大きな横運動量をもつことも特徴である。

第 1 図のように、K^OTO 実験では、崩壊領域下流に CsI カロリメータを配置し、π^0 からの 2γ を検出す

る。CsI カロリメータを含め、全体を検出器で覆い、π^0 からの 2γ 以外、他になにも存在しないということを保証する。ビームを細く絞っている為、π^0 の崩壊をビーム軸上として、π^0 を再構成することが出来る。

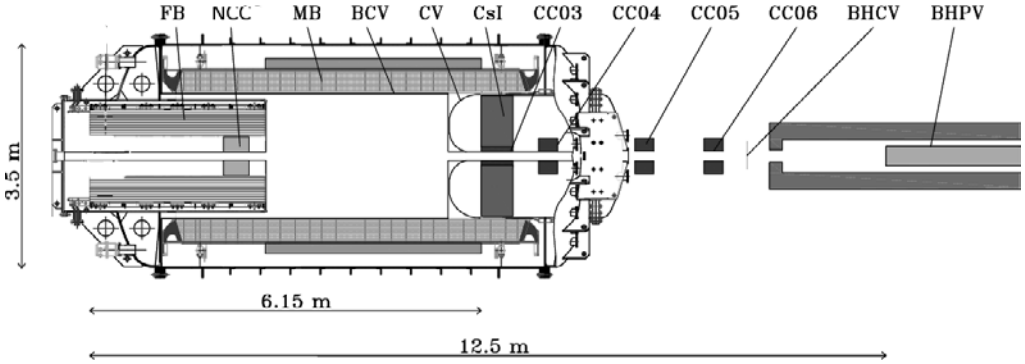

第 1 図　K^{O}OTO 検出器の断面図。

2009 年には、J-PARC に中性ビームラインが完成し、K_L フラックスやコアビームの性質の測定を行った。2010 年には、カロリメータ部分テストを終了し、フルカロリメータ建設中である。2011 年 4 月にフルカロリメータテストを行い、2012 年から、フル検出器での物理 Run を始める予定である。

§2．テスト項目

東北大学理学部附属原子核理学研究施設では、e^+ ビームを用いて、第 1 図の、NCC、CV、BHCV、BHPV のプロトタイプテストを行った。この他、2009 年度のビームサーベー実験に用いた、K_L フラックスを測定システムについても、テストを行っている。以下、それぞれについて詳述する。

2.1 ビームサーベー実験での K_L フラックス測定システム

2009 年度ビームサーベー実験において、KL フラックスを測定した。このシステムは、$K_L \to \pi^+\pi^- pi^0$ 崩壊を同定するもので、シンチレータホドスコーププレーン（プレーン当たり、水平、垂直両方向のホドスコープを備える）が 4 枚と、純 CsI 結晶バンク 2 個（7x7x30cm 結晶を 5x5 に積む。）からなる。ホドスコープにより、π^+ と π^- のトラックを要求し、崩壊点を求める。純 CsI 結晶バンク 2 個其々に、1 個ずつ γ 線があることを要求し、先に求めた崩壊点を利用し、2γ から π^0 が再構成できることを要求する。ビームが細く絞られているので、横方向運動量を 0 とすると、π^+ と π^- の運動量についても、完全に再構成出来、これを用い、K_L の質量を再構成することが出来る。

ホドスコープは、1cm 幅、5mm 厚、40cm 長 (垂直方向) もしくは、60cm 長 (水平方向) のストリップを並べることで構成する。表面に溝を堀り、1.5mmϕ の波長変換ファイバーを接着して、64ch マルチアノード PMT(浜松フォトニクス H8804) で信号を読み出す。まず、 東北大学理学部附属原子核理学研究施設ではホドスコープに用いるシンチレータ及び波長変換ファイバーの選定を行った (実験#2652)。以上より、コストにも優れる EJ230 と B2 の組合せを採用した。

次に 1 プレーン分のホドスコープを組み上げ、本番同様のエレクトロニクスを用いて、ホドスコープの性能評価を行った (実験#2664)。発光量については、MIP 貫通当たり、12∼22 p.e. を確保し、十分な性能を保証することが出来た (第 3 図)。検出効率については、全面に渡り 96%以上を確保し、必要な性能を保証した (第 4 図)。

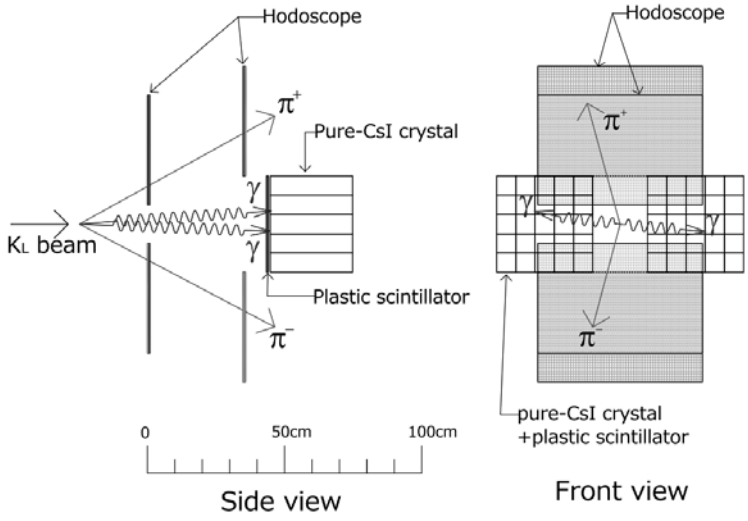

第 2 図　K_L フラックス測定システム。

第 1 表　5mm シンチレータを MIP が貫通した際の、波長変換ファイバーから読み出される光電子数。

Scintillator	WLS fiber	Light yield	
EJ212	Y11(200)	9 p.e.	青吸収、緑発光
EJ204	Y11(200)	13 p.e.	青吸収、緑発光
EJ230	B2(200)	13 p.e.	紫外吸収、青発光

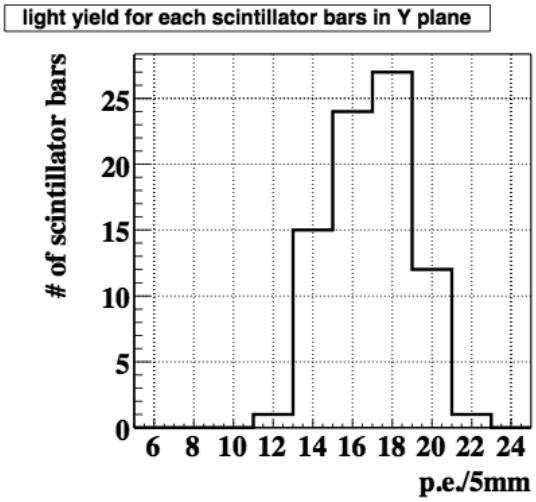

第 3 図　ホドスコープの MIP 貫通当たりの発光量の分布。

さらに、純 CsI 結晶、7cm x 7cm x 30cm の結晶を、3x3 に積み上げ、これに各種エネルギーのビームを照射し、エネルギー校正を行い、0.8 GeV に対し、0.2% のエネルギー分解能を達成した (第 5 図)。以上より、K_L 測定システム全般を事前にチェックすることができた。これを基に、全数製作し、J-PARC の KL ビームラインでの、最初の中性 K 中間子の同定に成功し、K_L のフラックス及びスペクトラムを実測する

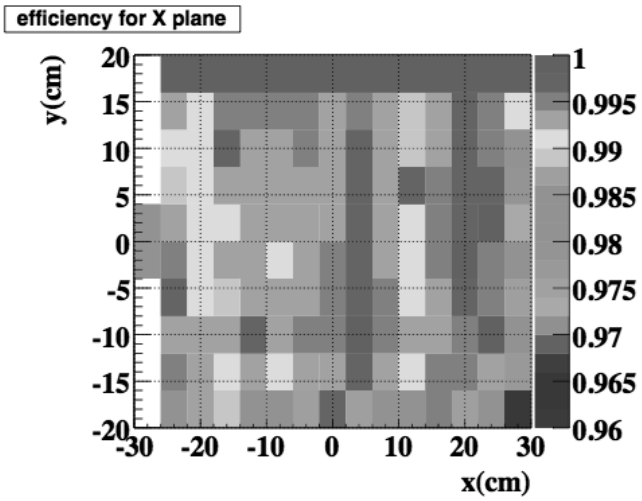

第 4 図　ホドスコープ全面での荷電粒子検出効率。

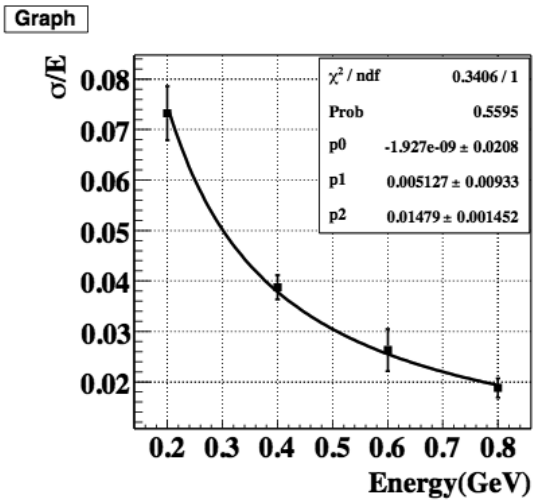

第 5 図　CsI 結晶の陽電子に対するエネルギー分解能。

ことが出来た。

2.1.1 NCC

NCC(Neutron Collar Counter) とは、第 1 図にあるように、上流部から崩壊領域への粒子の侵入を防ぎ、かつ崩壊領域から粒子が洩れるのを防ぐ役割を持つ、不可欠な検出器である。一方、ビームに最も近い検出器の一つであり、ビーム近傍に広がる、ハロー中性子により、NCC で π^0 が生成される。これからの 2γ が CsI カロリメータに入射することで生じる、ハロー中性子バックグラウンドの源にもなる。このバックグラウンドを抑制する為、以下の 3 つの純 CsI を用いるので、相互作用長さが長く、中性子と反応しにくい、かつ、輻射長が短く、π^0 からの γ を遮断しやすい。NCC 全体で、不感領域がないように作ることで、π^0 生成時の余剰粒子による抑制を効かしている。検出器の位置を上流に移動させ、崩壊領域中の信号検出区間から距離を離し、バックグラウンドを抑制している。

ビームに近いことより、積極的にハロー中性子を測定する役割を負わせている。結晶をビーム軸方向に分割することにより、中性子ガンマ線弁別能力を与え、ハロー中性子測定を行い、バックグラウンド評価の基礎とする。分割された結晶を読み出す為、溝を掘ったアクリル板に波長変換ファイバー (PMP) を敷き詰め、結晶に光学接触させることで、光を読み出すデザインとなっている。第 6 図のような、3 分割結晶に対して、ファイバーを敷設する。中央部の共通ファイバーは、本来のガンマ線検出が役割であり、外側の個別読み出しファイバーにより、中性子ガンマ識別を行いながら、ハロー中性子測定を行う。第 6 図のように、

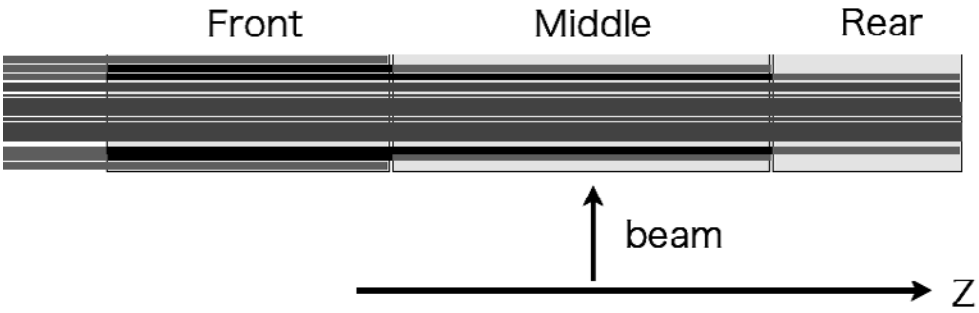

第 6 図　NCC の 3 分割とファイバー敷設。中央部ファイバーは 3 結晶に共通に光学コンタクト。外側のファイバーで、3 結晶から独立に光を読み出す。途中の黒色部は光学マスクされている。

Middle 結晶をビームでスキャンした際の、Middle 読み出しファイバーの光量の変化を、中心での光量で規格化して示したのが、第 7 図である。これから、概ね MC でのシャワー洩れの効果と同じ光量変化となり、3 分割ファイバー読み出しが有効であることを示している。同じ場合、第 8 図で、Front 結晶読み出し

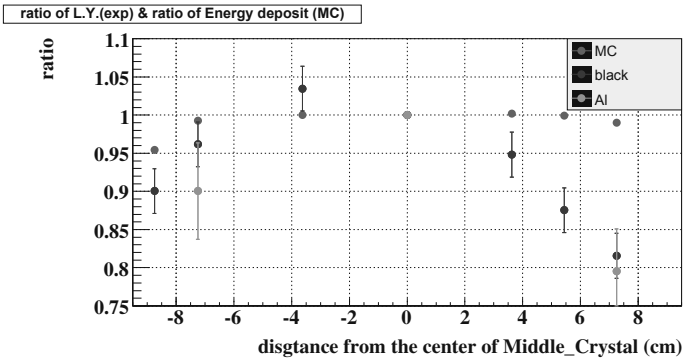

第 7 図　NCC の 3 分割結晶中、Middle 部をビームでスキャンした際の、Middle 読み出しの光量変化。端ではシャワー洩れにより、エネルギーが外に洩れる。図の balck、Al は測定データで、black は 3 分割アクリル板が黒塗料で遮光されているケース、Al はアルミ板で遮光されているケース。

ファイバーの光量変化を示す。Middle 読み出しで規格化しており、2%程度、光り漏れがあることを示している。この程度であれば、問題にはならない。以上より、3 分割モジュールでのファイバー読み出し方法について確立した (実験#2663)。

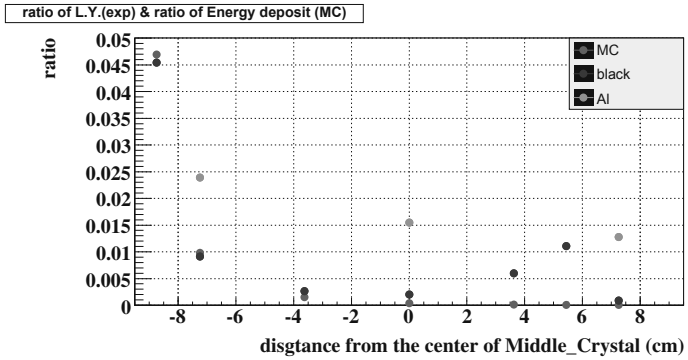

第 8 図　NCC の 3 分割結晶中、Middle 部をビームでスキャンした際の、Front 読み出しファイバーの光量変化。Middle 部の光量で規格化している。端では Middle 読み出しの 2%程度、光洩れにより光が入り込んでいる。

2.2 CV

CV(Neutron Collar Counter) とは、第 1 図の CsI カロリメータ全面を覆う荷電粒子を検出し、バックグラウンド事象を排除するための検出器である。3mm 厚のプラスチックシンチレータを 2 層、CsI カロリメータ直上流、及び 25cm 上流に配置する。1mmϕ の波長変換ファイバー Y11(300) が、1cm ピッチで敷設される。この両側より光を読み出し、7 本のファイバーを束ねて、3mm 角 MPPC で受ける。この MPPC は、直付けされたペルチェ冷却器により、5 ℃にまで冷却され、ダークカウントが抑制される。

まず CV について、東北大学理学部附属原子核理学研究施設で、シンチレータの選定を行った。20cmx10cmx3mm の小型プロトタイプを作成し、EJ212 と EJ204 を比較し、光量で 2 割上回る EJ204 に決定した (実験#2652)。

その後、実機サイズの 1m サイズのシンチレータを製作した。EJ204 は、厚み精度のある長尺ものに対応せず、同等の BC404 を用いることにした。波長変換ファイバーも Y11(300) に変更し、光量の増加を計った。さらにペルチェ冷却器付き 3mm 角 MPPC を導入し、7 本を束ねて読み出す。実際に東北大学理学部附属原子核理学研究施設で、e^+ ビームに対し、全面をスキャンした結果、100keV のエネルギー損失当たり、最低でも 3.7 p.e. をいう光量を得、K^{O}TO 実験の要求を満たすことが出来た。第 9 図に、光量の変化を示す。量読み出しの平均時間から求めた時間分解能についても 0.8ns と、良い結果を得た (実験#2664)。

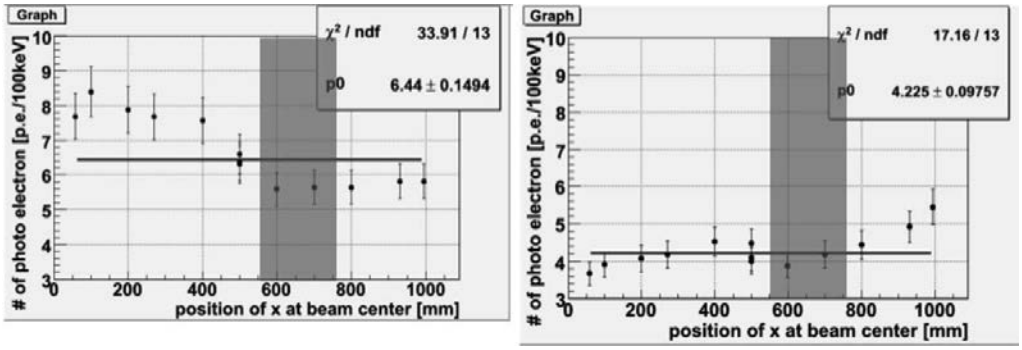

第 9 図　CV について、ビームをスキャンした際の、光量の変化。左がファイバーの短い方、右がファイバーが長い方の読み出し。

第 10 図に、量読みの時間差のビーム照射場所依存性を示す。光の伝搬によりビームスポットの場所との良

い相関が得れている。

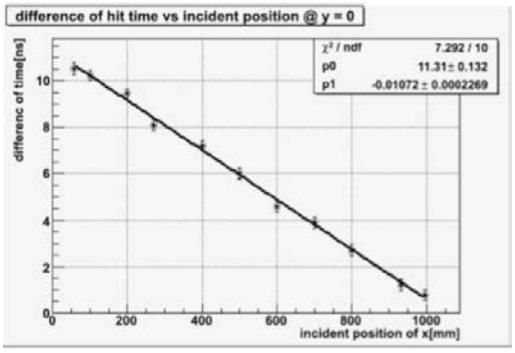

第 10 図　量読みの時間差のビーム照射場所依存性。

2.3 BHCV

BHCV は、ビームホールに存在する、荷電粒子検出器である。ビーム中の大量のガンマ線、中性子に不感である必要があるため、なるべく物質量の好くないデザインが良く、BHCV のプロトタイプとして、第 11 図のような、ガスシンチレーション比例計数管というオプションを検討した。動作ガスには、CF_4 を選

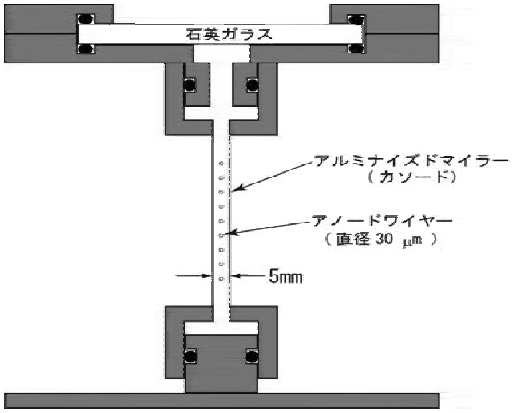

第 11 図　ガスシンチレーション比例計数管の構造。

定し、東北大学理学部附属原子核理学研究施設でテストを行った (実験#2652)。その結果、荷電粒子に対する不感率、0.1%以下を達成した。

2.4 BHPV

BHPV とは、ビームホール中におかれるガンマ線検出器である。ビーム中の中性子、及び比較的低エネルギーの γ 線に対して、不感である必要がある。この為、鉛コンバーターと、エアロゲルチェレンコフ放射体を組合せ、チェレンコフ光を PMT で読み出すデザインとなっている。PMT 当たりのカウントレートを削減するため、第 12 図のような、2 方向読み出しを考案し、プロトタイプを作成し、このテストを行った (実験#2664)。第 13 図に、ビームポジションをスキャンした際の、BHPV での光量の変化を示す。2 方

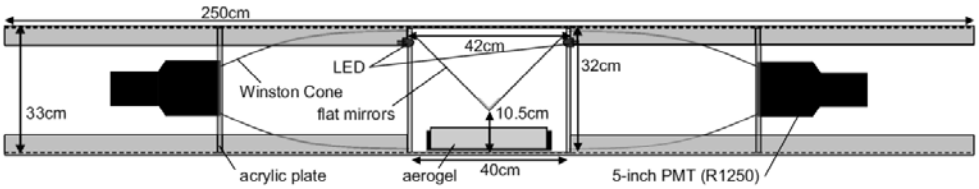

第 12 図　2 方向読み出しにした、BHPV モジュール。

向読み出しそれぞれと、その和をそれぞれ示している。和を取ることで、ほぼ一様な応答を示し、光量も 5 p.e. を上回ることが示せ、性能を保証した。

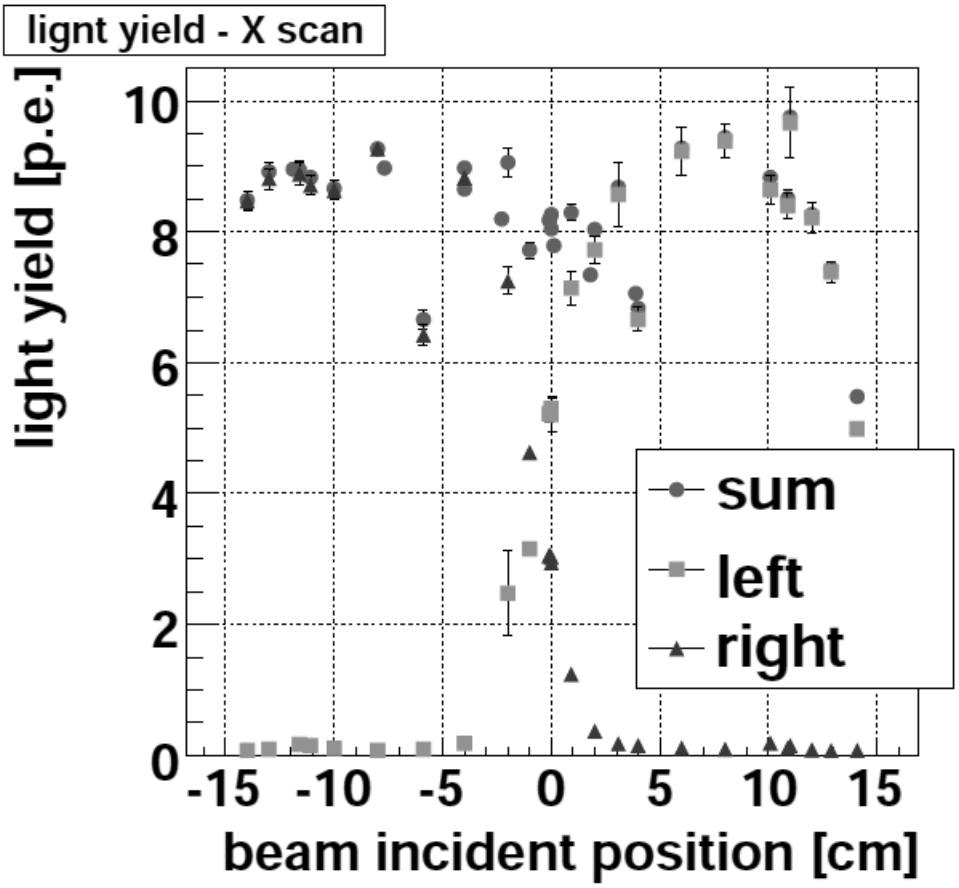

第 13 図　BHPV の光量のビーム位置依存性。

謝　　辞

K^{O}TO 実験の準備期に、貴重なビームテストのマシンタイムを頂き、多くのサポートを頂いた、東北大学理学部附属原子核理学研究施設の皆様に感謝申し上げます。良質なビームを提供頂いた加速器グループの皆様に感謝申し上げます。実験準備のサポートを頂いた石川貴嗣氏には、大変御世話になりました。特に感謝申し上げます。

参　考　文　献

[1] J. Comfort *et al.* (E14 collaboration): "Proposal for $K_L^0 \to \pi^0\nu\bar{\nu}$ Experiment at J-Parc" [http://j-parc.jp/NuclPart/Proposal_e.html].

[2] Andrzej J. Buras, Selma Uhlig, and Felix Schwab: Rev. Mod. Phys. **80**, 965 (2008), and references therein.

[3] F. Mescia and C. Smith: Phys. Rev. D **76**, 034017 (2007).

(LNS Experiment : #2657, #2697)

Test of GEM tracker for J-PARC E16 experiment

Y. S. Watanabe[1], K. Aoki[2], H. En'yo[2], T. Gunji[3], H. Hamagaki[3], Y. Hori[3], Y. Komatsu[1], S. Masumoto[1], K. Ozawa[1], M. Sekimoto[4], T. Tsuji[3], K. Utsunomiya[1], and S. Yokkaichi[2]

[1]*Department of Physics, University of Tokyo, Tokyo, 113-0024*
[2]*RIKEN Nishina Center, RIKEN, Wako, 351-0198*
[3]*CNS, University of Tokyo, Wako, 351-0198*
[4]*KEK, Tsukuba, 305-0801*

A tracker using Gas Electron Multiplier (GEM) has been developed for the J-PARC E16 experiment. The prototype tracker was successfull constructed adn its performance is evaluated at LNS at Tohoku University. As a result, the spatial resolution of 60, 100 and 140 μm was obtained for $0^\circ, 15^\circ$ and 30° beam, respectively. Arrival time information of electrons at readout strips turns out to be useful for tracking of inclined beam.

§1. Introduction

The main purpose of the J-PARC E16 experiment is to measure mass spectra of e^+e^- in nuclear medium with high precision and high statistics [1]. Such mass spectra will give us a clear evidence for possible restoration of chiral symmetry in nuclear matter. The counting rate of the most inner tracker is estimated to be $\sim$ 5kHz/mm^2. To cope with such high rate, GEMs are used in the experiment [2].

Momenta of electrons and positrons are mainly determined by three layers of Gas Electron Multiplier (GEM) trackers in a magnetic field. That is the minimum number of points to determine the momenta of a traversing particle. The required spatial resolution for the GEM tracker is 100μm, which gives the mass resolution of $\sim$ 5MeV. The incident angle of a particle is expected to be $0^\circ \sim 30^\circ$. Thus, we need to achieve the position resolution of100μm for tracks of incident angle of 0° to 30°. Even if particles go through radially, the incident angle is expected to be 15° when they hit the edge of the GEM tracker.

The purpose of the test experiment is to optimize a configuration of the GEM tracker to achieve required resolution.

§2. Prototype GEM tracker

A photograph and a schematic view of a prototype of the GEM tracker is shown in Fig 2. The prototype GEM tracker has an active area of 10cm $\times$ 10cm. From the top, a drift electrode, three GEM foils and a two-dimensional readout board are placed. In this manuscript, we call the setup with three GEM foils as a triple-GEM configuration. The gaps between GEM foils and a drift electrode are called

drift gap, transfer gap 1, transfer gap 2 and induction gap as shown in Fig 1.

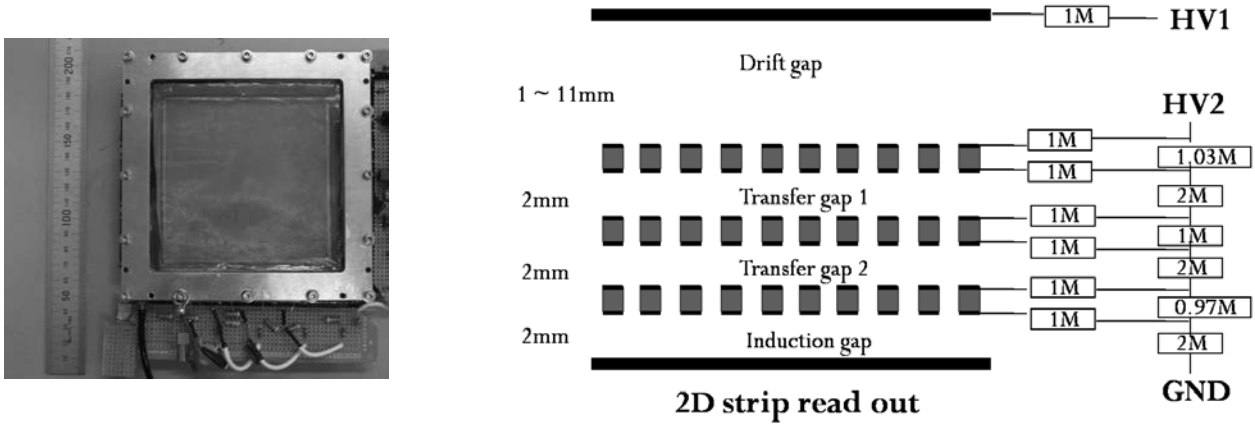

Fig.1. A photograph and a schematic view of the prototype GEM tracker

2.1 Mechanical structure

Conversion of photons into electron pairs in material is the huge background for E16 experiment. To suppress this background, the prototype tracker should be built with low material budget. Components in the active area of the tracker and their radiation lengths are summarized in Table 1. A mesh sheet is also used as a cathode. The setup with the mesh sheet has a radiation length of 2.98 per mil.

Component	Material	Thickness	Aperture ratio	Radiation length(per mil)
Lid	Mylar	25 μm		0.0871
Cathode	Aluminized Mylar	25 μm		0.0882
GEM1	Copper	8 μm	0.26	0.414
	Kapton	50 μm	0.17	0.146
	Total			0.56
GEM2				0.56
GEM3				0.56
Readout	Copper	$4\mu m$	0.8	0.0559
	Copper	$4\mu m$	0.171	0.232
	Kapton	$25\mu m$		0.0874
	Total			0.375
Total				2.53

Table 1. Radiation length of the sensitive area of the prototype chamber

2.2 GEM

Gas Electron Multiplier (GEM) is originally developed at CERN [3]. A GEM foil consists of an insulator and two thin copper layers on each sides, and they have many small holes. The specification of a GEM foil for the prototype chamber is summarized in Fig 2. The specification of a standard GEM foil at CERN is also shown.

	R_{PI}	R_{Cu}	P	D	d
Prototype	45	75	140	50	4
CERN	60	70	140	50	5

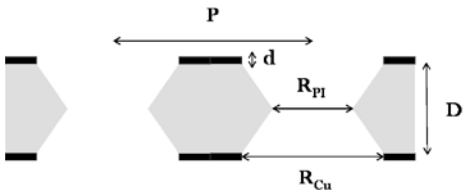

Fig.2. Specification of a GEM foil used in a prototype tracker

2.3 Readout

Two types of readout boards are tested. Both of them have two-dimensional Cartesian projective strips. The strip pitch and width are in common. The top strip width is 70μm, the bottom strip width is 290μm and the pitch is 350μm. One of the readout has effective pitch of 700μm by connecting two neighboring strips, while the other readout has separate readout electronics for each strip. The insulator is not etched away between the top and bottom side of strips. The bottom strips cannot be directly seen from the top side.

2.4 Gas

Two types of gases, a mixture of Ar 70%-CO_2 30% and a mixture of Ar 90%- CH_4 10% (Often denoted as P10) , are tested for the prototype tracker. In both cases, the gas flow rate was set at $\sim 100 ml/min$. Gas pressure was set at the atmospheric pressure.

A measurement of effective gain is performed for Ar 70%+CO_2 30% and P10. Isotope of ^{55}Fe is used as an X-ray radiation source for gain measurements. Since X-ray deposites the fixed energy on average, X-ray is suitable for gain measurement of gas chamber. An example of energy spectrum detected by a GEM chamber is shown in Fig 3. The signal around 6keV corresponds to full energy deposit peak, and the one around 3keV corresponds to an escape peak.

The result of gain measurement is shown in Fig 4. The setup with $ArCO_2$ requires high voltage but achieves higher gain than that with P10.

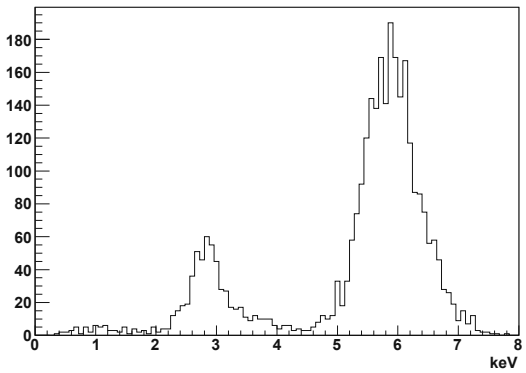

Fig.3. Energy spectrum of ^{55}Fe

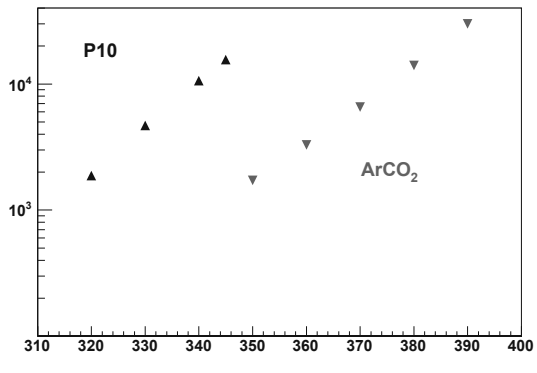

Fig.4. Comparing the gain of P10 and $ArCO_2$

Table 2. Setup of the test for the

No.	Gas	Pitch [μm]	d_D [mm]	E_D [V/cm]	Incident angle [deg]
1	$ArCO_2$	700	11	500	0, 15, 30
2	$ArCO_2$	350	1	2500	0, 15, 30
3	$ArCO_2$	350	3	2500	0, 15, 30
4	$ArCO_2$	350	6	600	0, 15, 30
5	P10	700	3	1500	0, 15, 30
6	P10	700	6	1500	0, 15, 30
7	P10	700	11	500	0, 15, 30

2.5 High voltage distribution

A high voltage is applied to GEM foils using a resistive chain through protection resistors as shown in Figure 1. The resistive chain applies high voltage asymmetrically to each GEM foil. The top GEM foil is operated with the highest voltage difference and the bottom GEM foil is operated with the lowest. Since the total charge of avalanche electrons becomes large at the bottom GEM foil, low voltage is preferable for the stable operation.

To vary the electric field of drift gap, HV is supplied separately for the drift cathode.

§3. Evaluation properties

Spatial resolution and efficiency of the GEM tracker were evaluated in the beam test: The measurement is performed only for the top side readout board. The goal of spatial resolution is 100μm for angle of 0° to 30°. Originally, the hit position is simply reconstructed from the charge information of strips. However, in that case, the degradation of spatial resolution is expected for tracks which is inclined from normal to the GEM tracker, because such tracks make additional spread in drift gap. Two methods to overcome this degradation is considered.

1. Use narrow drift gap

   Since narrow drift gap makes the spread of charge in drift gap smaller, small angular dependence of spatial resolution can be expected. The major concern is efficiency because narrower drift gap results a small charge.

2. Use wide drift gap and measure arrival time of electrons on strips

   The particle trajectory is reconstructed from timing information like Time Projection Chamber(TPC). Longitudinal diffusion and drift velocity as well as transverse diffusion can affect the accuracy of position determination. Those properties largely depend on an applied electric field. The optimum operational point needs to be determined.

The tested setups are summarized in Table 2.

§4. Tested setup

The test setup of the GEM tracker is shown in Fig 5. Five scintillators, 3 Silicon Strip Detector and the GEM tracker are aligned along the beam line at LNS. The beam energy is set at 660MeV.

A coincidence of five scintillators is used to have a beam trigger. Silicon Strip Detector (SSD) is used for tracking. Tracing accuracy of interpolation to GEM from SSD hit positions is estimated to be $\sim 60\mu$m. Table 3 summarizes sizes of scintillators and a silicon strip detector.

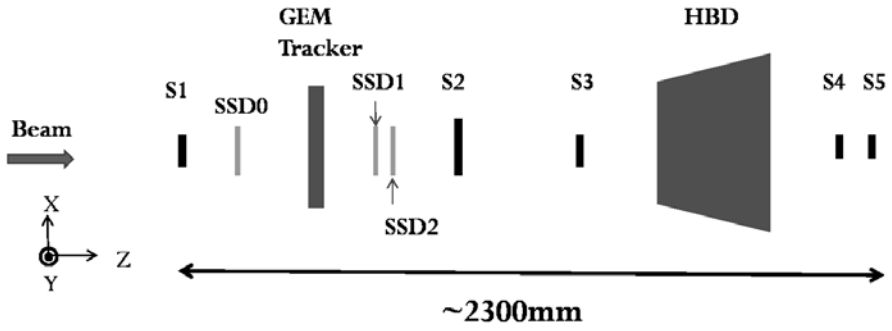

Fig.5. The tested setup

Table 3. Size of each detector[mm]

S1	S2	S3	S4	S5	SSD
30	50	30	10	10	30

4.1 Front End Electronics and DAQ

A preamplifier consists of 2 stages of amplification part. 1MΩ resistor and 1pF capacitance are used as feedback. As a result the time constant of the preamplifier is 1μsec. The second stage amplifies the signal by the factor of 3.2. The total gain of the preamplifier is 3.2V/pC. The preamplifier has differential output.

The preamplifier output is suitable for a flash ADC (RPV-160). RPV-160 has 8 channels and each channel has 8 bits resolution for the full range of $0 \sim -1$V. The sampling rate is 100MHz. A signal is recorded for 640 samples in one event. A 23m twisted cable is used between the preamplifier and RPV-160.

We build a DAQ system using VME system. Trigger circuit is shown in Fig 6. In this setup, the trigger rate is limited to $\sim$ 20Hz by the flash ADC module. An ADC module (CAEN V550) and a sequencer module (CAEN V551B) are used for SSD. Charge and timing information of scintillators are collected with ADC (CAEN V792) and TDC (CAEN V775).

4.2 GEM handling

The normal operation voltages of GEM foils for $ArCO_2$ and P10 are chosen as shown in Table 4. The value is selected to have the gain larger than 10000 and to be sufficiently lower than discharge voltage.

Our GEM foil has a double-conical-shaped hole and it is known that gain of a double-conical-shaped GEM foil increases with time because of charge-up at hole [4, 5]. In the beam test, the high voltage of the GEM tracker was supplied for a few hours before the test. Some test setups did not follow this procedure

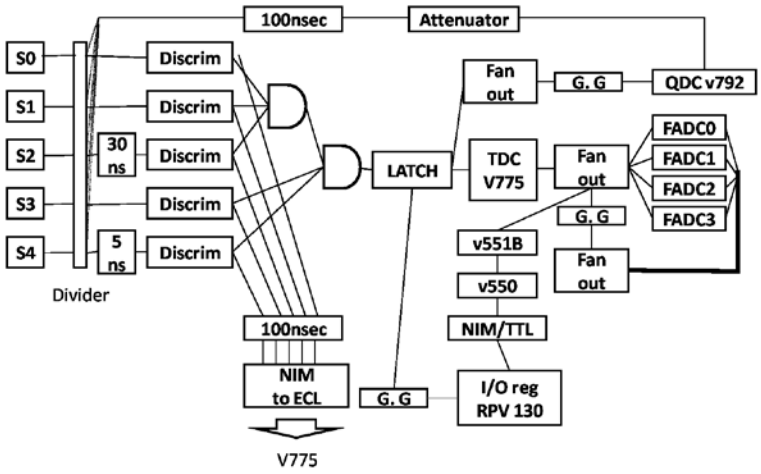

Fig.6. Trigger circuit

because of time constraint. However, note that a position sensing detector is not so sensitive to the total charge. Charge-sharing among strips plays an important role as described in the following section.

Gas	top GEM [V]	center GEM [V]	bottom GEM [V]	Transfer gap [V/cm]	Induction gap [V/cm]
P10	350	340	330	3400	3400
$ArCO_2$	391	380	369	3800	3800

Table 4. Operation voltage

§5. Analysis results

5.1 Data and analysis

A typical pulse shape is shown in Fig 7. The pulse height increases at first as electrons moving towards readout strips in induction gap, and then decreases with the decay time constant of its readout circuit. The maximum pulse height (V_p) and its arrival time (T_a) of each channel are used for further analysis. The ADC pedestals (V_{ped}) are subtracted from V_p. T_a is defined as the time when pulse height exceeds the half of V_p.

After the pedestal subtraction, a program scans through all the strips and find the strip with the maximum V_p, and then recognizes as a cluster including the strips with $V_p > 3\sigma_N$. Here, $\sigma_N = \sigma_{ped}$. In addition, a cluster is validated if its total charge exceeds $5\sigma_N$. Hit position of the GEM tracker is calculated using this cluster. Details of hit position calculation are shown below.

Using this computed hit position and a track position provided by SSDs, efficiency and spatial resolution are evaluated. Figure 8 shows a typical residual distribution between the hit position of the GEM tracker and SSD interpolated position. A Gaussian fit to the distribution provides a standard deviation σ_{fit}. Spatial resolution is defined as $\sqrt{\sigma_{fit}^2 - \sigma_{\mathrm{SSD}}^2}$, where σ_{SSD} is 60 μm. Efficiency calculation is done for events, which are found in 5 σ_{fit}.

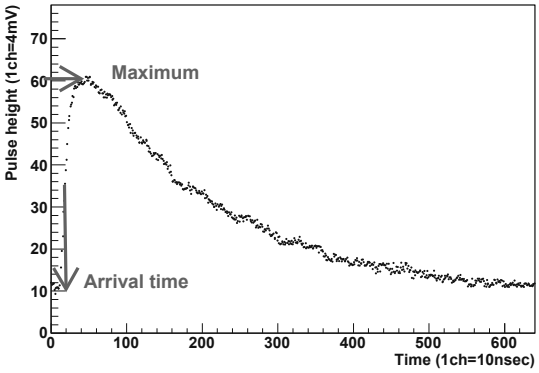

Fig.7. A typical pulse shape

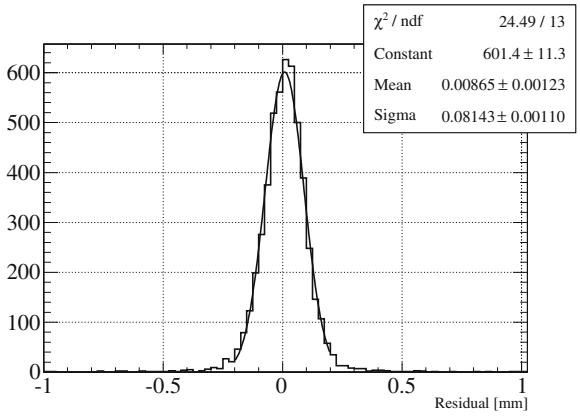

Fig.8. A typical residual distribution

5.1.1 Analysis without timing information

Two methods to compute the hit position in a cluster are applied, Center Of Gravity (COG)- method and digital method.

COG-method

In the Center Of Gravity(COG)-method, hit position, X_{COG}, is given by the following expression [6].

$$X_{COG} = \frac{\sum_{i \in cluster} X_i (Q_i - B)}{\sum_{i \in cluster} (Q_i - B)} \tag{1}$$

$$B = b \sum_{i \in cluster} Q_i \tag{2}$$

where Q_i Charge on the i-th strip
X_i Position of the i-th strip
b Constant

The parameter B is a fraction of total charge and is subtracted from Q_i in calculation of center of gravity to eliminate systematic fluctuation caused by total charge fluctuation. b is selected to give a best value of σ_{fit}.

Digital method

In the digital-method, the hit position, X_{dig}, is given by the following expression.

$$X_{dig} = \frac{X_l + X_r}{2} \tag{3}$$

where X_l The position of a strip with the smallest strip number
X_r The position of a strip with the largest strip number

The threshold value is selected to give the best value of σ_{fit} with efficiency above 0.97.

5.1.2 Analysis with timing information

Inclined tracks causes arrival time difference in a cluster, as shown in Fig 9.

Hit positions are reconstructed in the following way. First, a program searches the number of strips above a preset threshold in a cluster. This threshold is set higher than that for the analysis without

timing threshold. If the number is below 1, the hit position is calculated with digital-method. Second, tracks are reconstructed with arrival time information of each strip in the cluster. Track position in z-direction at each strip is calculated by multiplying the arrival time with drift velocity of electrons. We obtain tracks in GEM tracker by fitting those points with a linear function. Slope of the linear function is fixed to the value known beforehand. Finally, hit position is defined as the point with a fixed z. This z is determined so that the center of residual distribution coincides with that of digital-method. Drift velocity is determined to give the smallest σ_{fit}. An example of residual distribution with the setup $ArCO_2$, 350μm, d_D=6mm, E_D=600V/cm is shown in Fig 10. In this example, drift velocity is determined to be 1.5μm/sec, which is consistent with the drift velocity calculated with Magboltz [7].

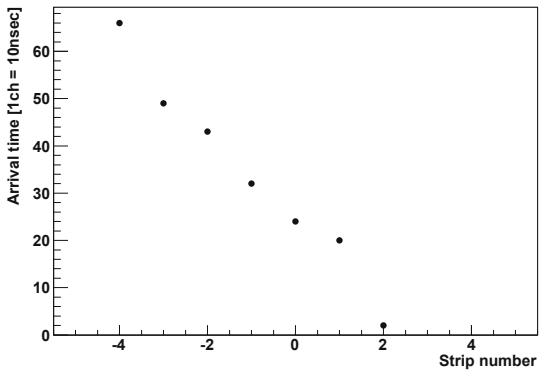

Fig.9. Arrival time distribution in a event with the setup $ArCO_2$, 350μm, d_D=6mm, E_D=600V/cm

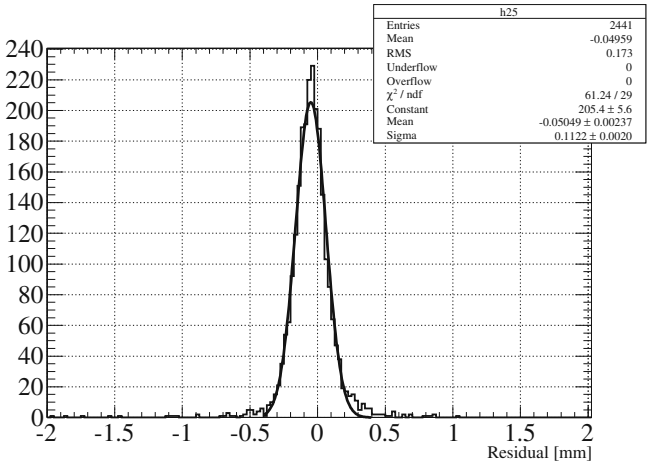

Fig.10. Typical residual distribution when hit position of GEM tracker is computed with timing information

5.2 Results for top-side readout

Several setups are tested and only good setups are discussed below. Setup number 1, 2, 3 and 4 in table 2 achieves spatial resolution less than 200μm for 15° inclined track. The spatial resolution is plotted against the track's angle for those setups in Fig 11-14. When only charge information is used, the degradation of spatial resolution with incident angle is smaller for narrower drift gap. However, the spatial resolution for a 30° tracks is 270μm even with d_D = 1mm. That is far beyond our goal. We can see that timing-methods improves σ_{fit} for the setup 3 and 4. Timing methods become effective with the setup having large number of hit strips and large arrival time difference in a cluster. From this point of view, setup 1 and 2 are not suitable for timing methods because they have narrow drift gaps and large drift velocity. In the end, the best spatial resolution for 30° inclined beam is 140μm with the setup 3 using timing method.

§6. Conclusions

prototype GEM tracker was constructed for J-PARC E16 experiment. The required spatial resolution is 100 μm for tracks of incident angle of 0° to 30°.

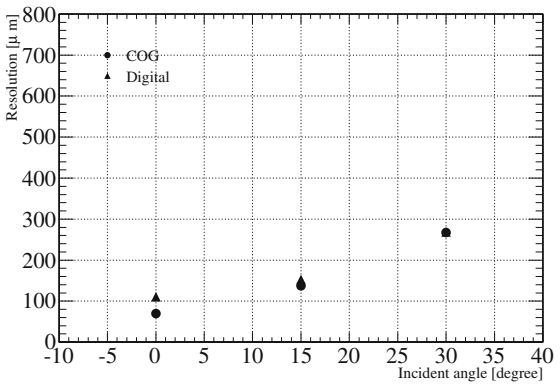

Fig.11. $ArCO_2$, 350μm pitch, d_D = 1mm, E_D = 2500V/cm

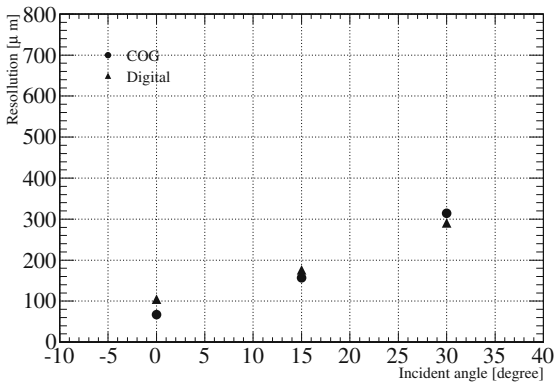

Fig.12. $ArCO_2$, 350μm pitch, d_D = 3mm, E_D = 2500V/cm

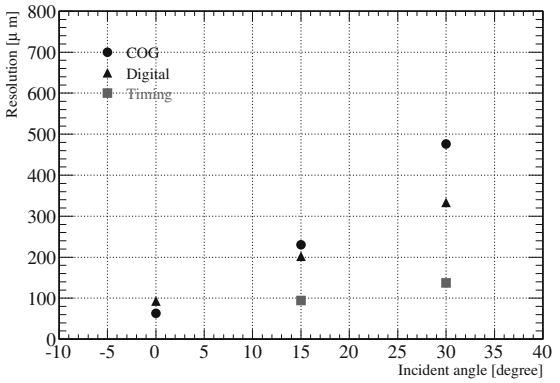

Fig.13. $ArCO_2$, 350μm pitch, d_D = 6mm, E_D = 600V/cm

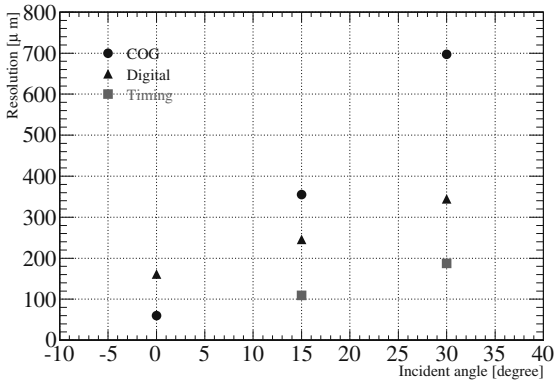

Fig.14. $ArCO_2$, 700μm pitch, d_D = 11mm, E_D = 500V/cm

Two methods to overcome the problem of a resolution degradation for non-perpendicular tracks are considered. One way is to use narrow drift gap and the other way is to use wide drift gap and measure arrival time of electrons on strips. As a result, the best spatial resolution for 15° and 30° inclined beam are 100μm and 140μm with the following setup. The goal of 100μm is achieved for 15°, while it is not for 30°. The effect on mass resolution is being investigated. Please note that the effect is expected to be small since the probability to have such large incident angle is small.

Gas	Pitch	d_D	E_D	Method
$ArCO_2$	350μm	6mm	600V/cm	Timing method

Acknowledgment

The authors are grateful to Prof. H. Shimizu, Dr. T. Ishikawa, Dr. H. Yamazaki and other LNS staffs for their various help and stable operation of the accelerator during the beam test.

This study was partly supported by the Japan Society for the Promotion of Science (JSPS), RIKEN Special Postdoctoral Researchers Program, and Grant-in-Aid for Scientific Research (No. 19340075 and 21105004) from the Japan Ministry of Education, Culture, Sports, Science and Technology (MEXT).

References

[1] http://j-parc.jp/NuclPart/pac_0606/pdf/p16-Yokkaichi_2.pdf

[2] B. Ketzer *et al.*: IEEE Trans. Nucl. Sci., vol. 47 No. 5 (2002) 2002.

[3] F. Sauli, Nucl. Instr. and Meth. **A386** (1997) 531

[4] C. Altunbas et al., Nucl. Instr. and Meth. **A490** (2002) 177

[5] O. Bouianov, Nucl. Instr. and Meth. **A450** (2000) 277

[6] G. Charpak et al., Nucl. Instr. and Meth. **148** (1978) 471

[7] S.F. Biagi, Nucl. Instr. and Meth. **A421**(1999) 234

(LNS Experiment : #2662)

Development of a Beam Profile Monitor for GeV-γ Beamline

H. Fujimura[1], S. Ogushi[1], R. Hashimoto[1], T. Ishikawa[1], K. Nanbu[1], H. Shimizu[1], H. Sugai[1], K. Suzuki[1], and H. Yamazaki[1]

[1]*Laboratory of Nuclear Science, Tohoku University, Sendai, 982-0826*

We have developed a γ beam profile monitor (γ-BPM) for the GeV-γ beamline. It consists of two 1 mm thick plastic scintillators and two plastic scintillating fiber hodoscopes. To determine the incident position of the photon, a reconfigurable logic module which mounts a field programmable gate array (FPGA) is used. The data acquisition efficiency of 98 % is achieved with 800 kHz trigger rate.

§1. γ Beam Profile Monitor

For a 4π EM calorimeter complex FOREST [1] at the GeV-γ beamline, the center position of an incident γ beam is used to obtain physical quantities such as particle momentum. The γ beam profile is determined from the position distribution of the electron-positron pairs which are created from the γ beam.

The γ beam profile monitor (γ-BPM) was originally designed for the SCISSORS II experiments [2]. A data acquisition (DAQ) system was developed by using a PCI board PCI-2772C (Interface Corporation). The typical data taking rate is about 40 kHz. For the FOREST experiment, we removed a converter and changed the DAQ system. The front-end modules of a REPIC TDC RPT-140 and a HOSHIN ADC T004 in a TRISTAN/KEK Online (TKO) system are used with the FOREST DAQ [3].

The previous γ-BPM system for the FOREST experiments consists of three plastic scintillators and two plastic scintillating fiber (SciFi) hodoscopes. The upstream plastic scintillator is a veto counter to reject charged particles created at the upstream materials on the GeV-γ beamline. It is also used as a converter to create an e^+e^- pair. The two downstream scintillators are trigger counters to select an e^+e^- event. The trigger condition is

$$\overline{[\text{Veto Counter}]} \otimes [\text{Trigger Counter 1}] \otimes [\text{Trigger Counter 2}],$$

where $\otimes$ means coincidence of signals. The two SciFi hodoscopes are placed at downstream as a 2-dimensional position counter. Each hodoscope has 16 fibers with 3 mm square. The active area is 48×48 mm^2. Since we require one hit in each hodoscope, an e^+e^- pair which goes in the same direction is selected. Fig. 1 (Left) shows the previous detector setup. γ-BPM is placed at 2.2 m downstream of FOREST.

The singles rates of the veto, trigger, and central SciFis are 4 MHz, 2.5 MHz, and 1.3 MHz, respectively, at 1×10^7 tagged photons/sec under the normal operation of the STB ring. Since the thickness of the plastic scintillators are 5 mm, the e^+e^- creation rate in these counters is not negligible to take

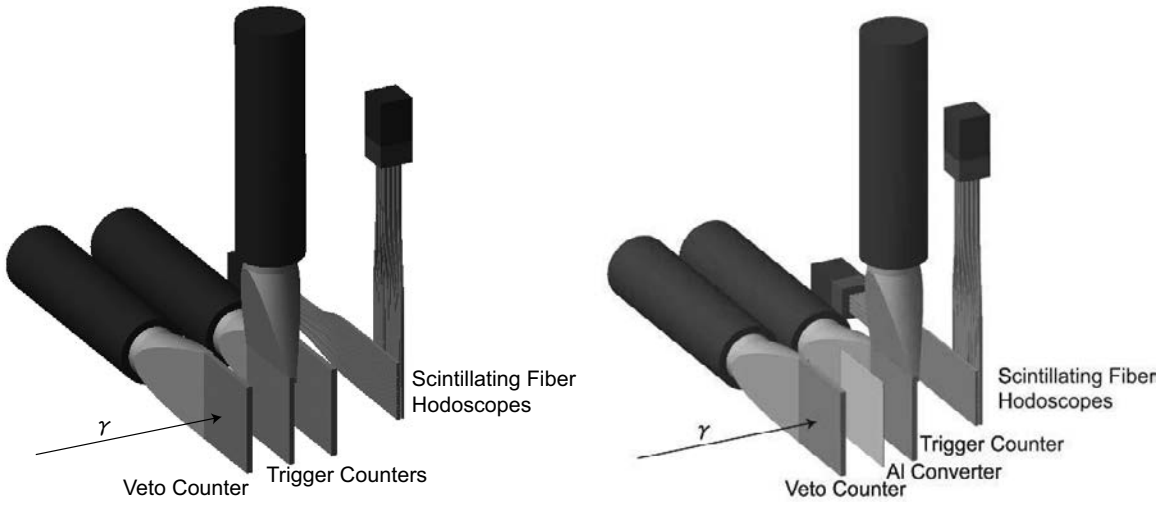

Fig.1. Schematic view of γ-BPM. Left: Previous γ-BPM setup consists of a plastic veto counter and two plastic trigger counters. The thickness of each counter is 5 mm. Right: New γ-BPM setup consists of a plastic veto counter and a plastic trigger counter with the thickness of 1 mm. A thin Al plate of 0.5 mm thickness is used as a converter. In both setup, the plastic scintillating fiber (SciFi) hodoscopes are placed downstream as a 2-dimensional position counter. Each hodoscope has 16 SciFis with 3 mm square. The active area is 48×48 mm^2.

data efficiently. We measure the γ beam profile once a day during long term FOREST experiments. The typical trigger rate is 1.8 kHz with the DAQ efficiency of 72% using faint beam.

A new γ-BPM system has been developed to measure the γ beam profile with the FOREST data taking simultaneously. To decrease the singles rate, it is essential to reduce materials of the veto and the trigger counters. New γ-BPM consists of a plastic veto counter and a plastic trigger counter with thickness of 1 mm. The trigger counter has two Hamamatsu H6410 photo multiplier tubes (PMT). Between the veto and trigger counters, a thin Al plate of 0.5 mm thickness is placed as a converter. The trigger condition is

$$\overline{[\text{Veto Counter}]} \otimes [\text{Trigger Counter PMT-1}] \otimes [\text{Trigger Counter PMT-2}].$$

The two SciFi hodoscopes used for the previous γ-BPM setup are placed at downstream. Fig. 1 (Right) shows the new detector setup of γ-BPM.

To reject charged particles from the upstream beamline, the threshold of the veto counter should be set lower than the level corresponding to the energy deposit of minimum ionizing particle (MIP), where MIP means a particle whose mean energy loss rate through matter is close to the minimum. Since the trigger counter selects e^+e^- events, its threshold should be set to the level between 1 MIP and 2 MIP energy deposits. To check a 1.0 mm thick plastic scintillation counter was enough to observe MIP events, we used the positron beam at the energy of 460 MeV. Fig. 2 (Left) shows the pulse height distribution of the veto counter. Signals originating from the MIP particles (solid line) are clearly separated from the pedestal distribution (dotted line). Fig. 2 (Right) shows the waveforms of the trigger counter measured with a oscilloscope with the γ beam. The circulating electron current in the STB was 18 mA with the

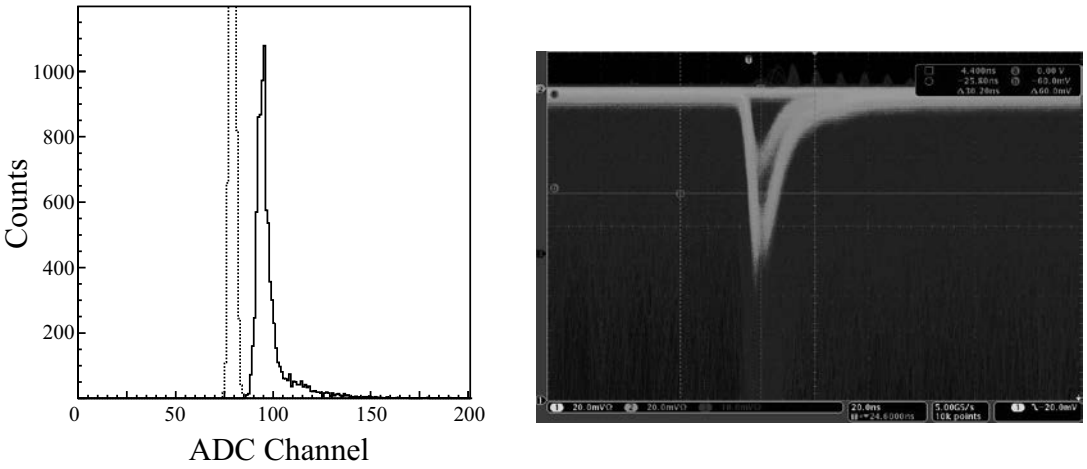

Fig.2. Left: Pulse height distribution of the veto counter. Incident electron beam energy is 460 MeV. Signals originating from the MIP particles (solid line) are clearly separated from the pedestal distribution (dotted line). Right: Waveforms of the trigger counter measured with an oscilloscope with the γ beam. Waveforms corresponding to 1 MIP and 2 MIP are clearly observed.

energy of 1200 MeV and the flattop of 8 sec. Waveforms corresponding to 1 MIP and 2 MIP are clearly observed. The singles rates of the veto, trigger, and central SciFis are 2.0 MHz, 1.5 MHz, and 0.8 MHz, respectively. The average trigger rate is 800 kHz.

§2. High-Speed Data Acquisition System

For the data acquisition (DAQ) system, we use a reconfigurable logic module which mounts a field programmable gate array (FPGA). This FPGA based module is a modified version of multi-purpose logic module (MPLM) [4]; the number of input/output channels are changed. It is housed in a double span NIM standard module, having 36 NIM-standard logic inputs and 4 NIM-standard logic outputs. Fig 3 shows a photo of the FPGA based module and Table 1 summarizes the specifications.

Table 1. Specifications of the FPGA based module

FPGA Family	Xilinx SPARTAN-3
Device	XC3S200
Package	4TQ144
System Gate	200k
Logic Cells	4,320
Distributed RAM (bits)	30k
Block RAM (bits)	216k
Multipliers	12
DCMs	4
Output	NIM 4 channels
Input	NIM 36 channels
Clock	33.33 MHz

Fig.3. Photo of the FPGA based module.

The γ-BPM DAQ program for the FPGA based module is written in VHDL (VHSIC hardware description language) using Xilinx ISE 10.1. A clock frequency for the signal synchronization is 66.66 MHz (15 nsec) which is obtained by multiplying the module internal clock frequency of 33.33 MHz by 2 using Digital Clock Managers (DCMs).

The DAQ program is designed as a stand alone DAQ system and is composed of a command com-

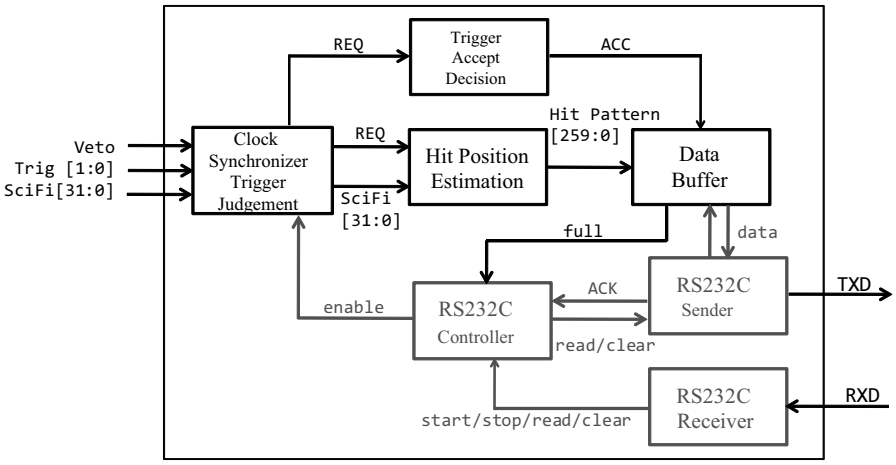

Fig.4. Block diagram for the γ-BPM DAQ system. There are two main functions. One handles data taking (black) and the other handles command communications thorough a RS232C serial interface (gray).

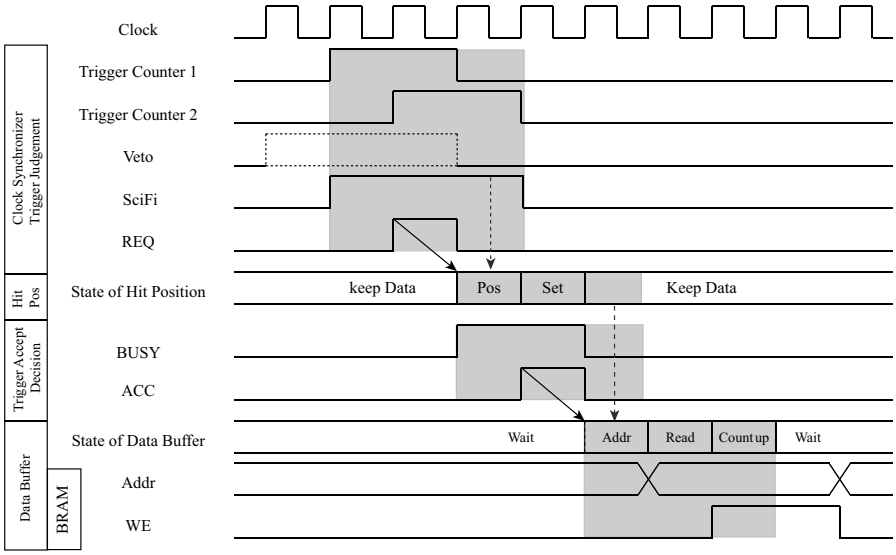

Fig.5. Timing chart of the data taking part for the FPGA based module. All signals in this chart are clock-synchronized. Shaded areas show the dead time of each block and correspond to 3 clocks (45 nsec). Left boxes show the block names which handle the signals shown right. “Hit Pos” in the box means the“Hit Position Estimation” block. This block is a state machine with “Keep Data”, “Hit Position Estimation (Pos)” and “Set Data (Set)” states. The “Data Buffer” block is also a state machine to communicate with the BRAM memory. The state of “Addr” is “set address of BRAM”, “Read” is “read the number of counts”, “Count up” is “increment the number of counts by one”, and next “Wait” state is “set the data to BRAM”. The synchronized pulse widths of the trigger counter are set to 2 clocks, and those of the veto and SciFis are set to 3 clocks.

munication part and a data taking part. To control the DAQ system, command communications between the FPGA based module and a personal computer (PC) are done via a RS232C serial interface. For serial data transmission lines of TxD and RxD, one NIM-standard logic input and one NIM-standard logic output are used. Analog signals from the veto, trigger, and SciFi counters are discriminated to make the input logic signals. The FPGA based module receives three logic signals from the veto and trigger counters, and 32 logic signals from the SciFis. The trigger condition is tested in the data taking part of the DAQ program. Since the number of hit positions of the SciFi hodoscopes is $16 \times 16 = 256$, a frequency distribution of 256 bins is stored in a block RAM (BRAM) memory.

Fig. 4 shows a block diagram of the γ-BPM DAQ system. Fig. 5 shows the timing chart of the data taking part. To reduce the DAQ dead time, the program of the data taking part is separated into 4 blocks. Each block spends 3 clocks for one event and works separately. The dead-time is 45 nsec (3 clocks) and the total processing time is 105 nsec (7 clocks).

All logic input signals are synchronized with doubled frequency at the “Clock Synchronizer and Trigger Judgement” block. This block sends a signal REQ when the synchronized trigger counter signals match the trigger condition. The “Trigger Accept Decision” block receives the REQ signal and makes a signal ACC when the block is not busy and ready to accept an event. The “Hit Position Estimation” block always receives the synchronized SciFi signals. When this block receives the REQ signal, a hit position is estimated. If the number of hits in each hodoscope is one, a signal corresponding to the hit position is sent to the “Data Buffer” block. When the “Data Buffer” block receives the ACC signal, it reads the number of counts corresponding to the hit position from BRAM and increments it by one, then saves it to BRAM.

The “RS232C Controller” block starts/stops the data taking, when the “RS232C Receiver” block receives a “start” or ”stop” command. The frequency distribution in BRAM is read and sent by the “RS232C sender” when a “read” command is received. A “clear” command clears the data in BRAM. Both “read” and “clear” commands are valid when the data taking is stopped. For each command, the FPGA based module sends a reply to tell the PC whether the command is accepted or not.

§3. Data-Handshaking with the FOREST DAQ

Since the FOREST DAQ has 5 collectors [3], one of the collectors is used to communicate with the PC which is connected to the FPGA based module through the RS232C serial interface. The FPGA based module accumulates the frequency distribution measured by γ-BPM during the flattop. Every spill off, the collector asks the PC to send the γ-BPM data via the Transmission Control Protocol/Internet Protocol (TCP/IP). Then the PC sends “stop”, “read”, “clear”, and “start” commands to the FPGA based module through RS232C. After receiving the γ-BPM data, the PC sends it to the collector. The collector converts the γ-BPM data from the FPGA based module to the FOREST data format, and combines it with the FOREST data into a single output stream, then sends it to the event builder process. Fig. 6 shows the data-flow of the γ-BPM and the FOREST DAQ system.

A performance study using γ beam was carried out. The circulating electron current in the STB

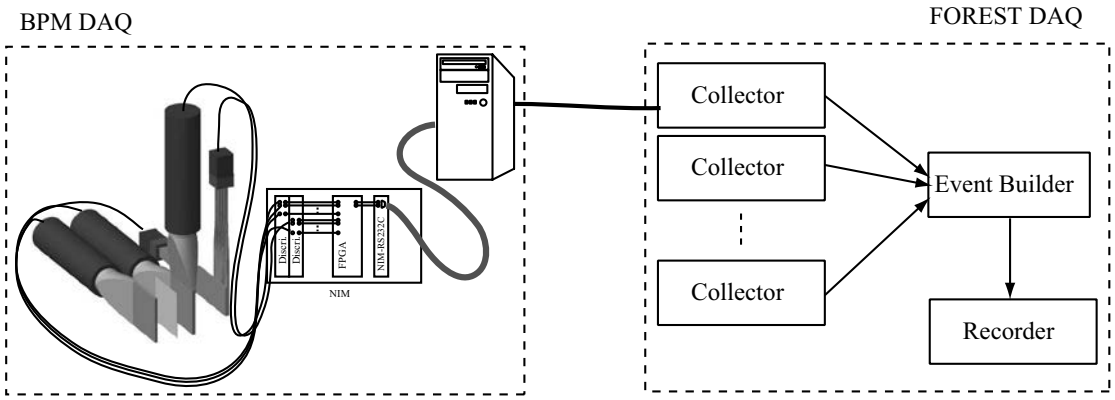

Fig.6. Data-flow architecture. One of the collectors of the FOREST DAQ system asks the PC to send the frequency distribution of γ-BPM via TCP/IP every spill off. Then the PC sends "stop", "read", "clear", and "start" commands to the FPGA based module through RS232C. After receiving the γ-BPM data, the PC sends it to the collector. The collector converts the γ-BPM data from the FPGA based module to the FOREST data format, combines it with the FOREST data into a single output stream, and sends it to the event builder process.

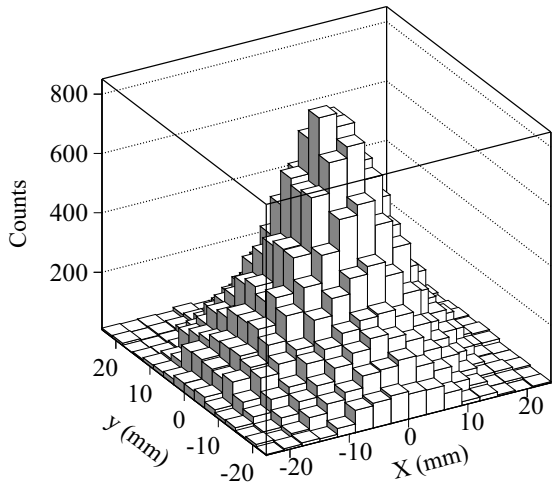

Fig.7. Typical γ beam profile taken by a new high-speed DAQ system with the FOREST DAQ.

was 18 mA with the energy of 1200 MeV. The flattop time was 8 sec. Fig. 7 shows a typical example of the beam profile obtained with the γ-BPM and FOREST DAQ system. The DAQ efficiency of 98% is achieved with 800 kHz trigger rate.

References

[1] T. Ishikawa *et al.*: Research Report of LNS. Tohoku Univ. **41** (2008) 7.

[2] M. Nanao *et al.*: Research Report of LNS. Tohoku Univ. **36** (2003) 56.

[3] H. Fujimura *et al.*: Research Report of LNS. Tohoku Univ. **41** (2008) 26.

[4] K. Nanbu *et al.*: Research Report of LNS. Tohoku Univ. **40** (2007) 27.

(LNS Experiment : #2695)

Development of a plastic and BGO phoswich detector

S. Kaida[1], T. Ishikawa[1], H. Fujimura[1], R. Hashimoto[1], H. Shimizu[1], K. Suzuki[1], Y. Tajima[2], S. Takahashi[1], H. Yamazaki[1], and H.Y. Yoshida[2]

[1]*Laboratory of Nuclear Science (LNS), Tohoku University, Sendai 982-0826, Japan*
[2]*Department of Physics, Yamagata University, Yamagata 990-8560, Japan*

Construction of a 4π electro-magnetic (EM) calorimeter with BGO crystals is planned to study a nucleon resonance $N^*(1670)$ which is a candidate of anti-decuplet penta-quark baryons. Since an EM calorimeter module itself cannot distinguish whether the incident particle is neutral or charged, thin plastic scintillator hodoscopes are usually placed in front of it. A plastic and BGO phoswich detector as an EM calorimeter module for charge identification has been tested at the electron beamline for testing detectors in Laboratory of Nuclear Science, Tohoku University.

§1. Introduction

Study of exotic hadrons has been a subject of great interest in nuclear physics since Θ^+ was observed at SPring-8/LEPS for the first time [1]. The Θ^+ is thought to be a member of anti-decuplet penta-quark baryons with the lowest mass [2]. After the LEPS experiment, both the positive and negative results have been reported by many other facilities. Searching for other members is important to establish the penta-quark picture. Recently, a narrow bump was observed at GRAAL [3], LNS [4], and CB-ELSA [5] in η photo-production on the deuteron. This bump would be attributed to a member of anti-decuplet baryons with hidden strangeness since no signature corresponding to this bump has been observed so far in η photo-production on the proton [6].

Fig. 1 shows the baryon octet and anti-decuplet penta-quark baryons. Adjacent two baryons to the Θ^+ are members with hidden strangeness. We call the left one N_5^0 and the right one N_5^+. The N_5^0 can be photo-produced from the neutron because both the charge and U-spin are conserved in the reaction. On the other hand, photo-production of N_5^+ having a U-spin of $3/2$ from the proton is forbidden since the U-spins of the photon and the proton are zero and a half, respectively.

To investigate the relevant nucleon resonance precisely, construction of a new electromagnetic (EM) calorimeter with BGO crystals is planned at Laboratory of Nuclear Science (LNS), Tohoku University.

§2. 4π EM calorimeter with BGO crystals

The planned EM calorimeter consists of 1,260 BGO crystals, and it covers the polar angle from 24 to 138 degrees. Fig. 2 shows the schematic view of the planned EM calorimeter. The details of the design are described elsewhere [8].

Since an EM calorimeter module itself cannot distinguish whether the incident particle is neutral

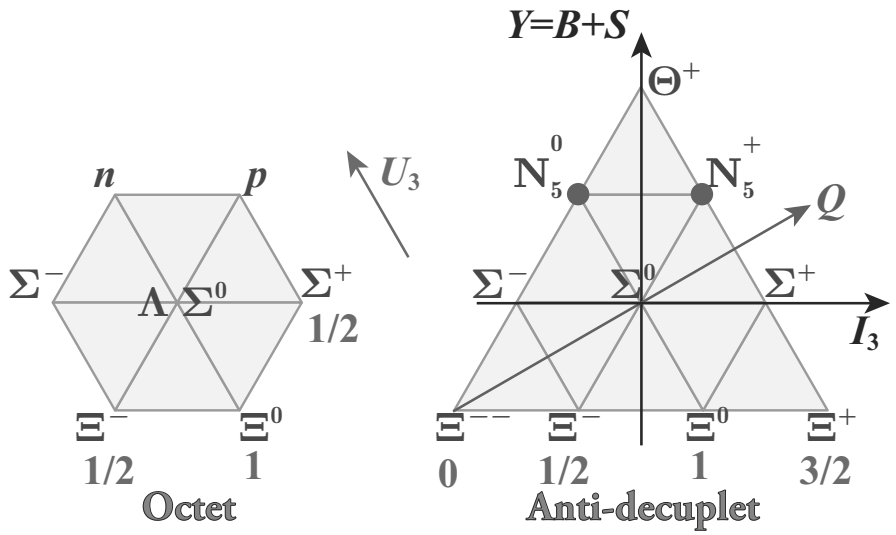

Fig.1. Octet baryons and anti-decuplet penta-quark baryons.

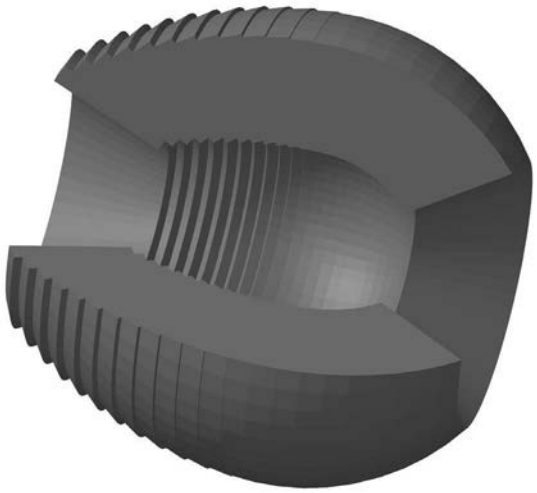

Fig.2. Planned EM calorimeter with 1,260 BGO crystals. It takes a shape like an egg, and covers the polar angle from 24 to 138 degrees.

or charged, thin plastic scintillator hodoscopes are usually placed in front of it. We discuss a plastic and BGO phosphor-sandwich (phoswich) detector as an EM calorimeter module. In this phoswich detector, a 10 mm thick plastic scintillator is connected on the front face of a BGO crystal and emitted scintillation photons are converted to the analog signal with a single photomultiplier tube. Fig. 3 shows the side view of the phoswich detector.

Scintillation photons are generated in the plastic scintillator only when the incident particle is charged. Because the decay time of a BGO crystal is much longer ($\sim$300 ns) than that of a plastic scintillator (several ns), the pulse shape of the output signal help us to know the charge of the incident particle. Fig. 4 shows the expected pulse shape of the phoswich detector. By adopting a phoswich detector, we can

1. decrease the readout channels, and

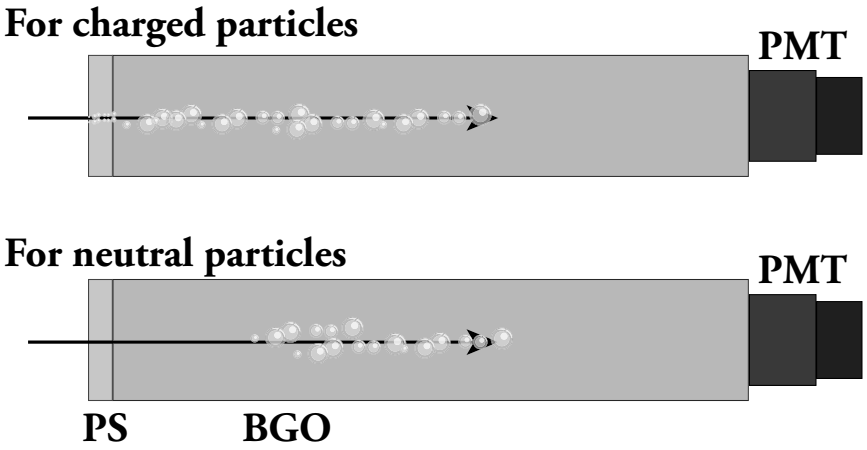

Fig.3. Plastic (PS) and BGO phoswich detector. Emitted scintillation photons are converted to the analog signal with a single photo-multiplier tube (PMT). The scintillation photons are generated in PS only when charged particles are incident on the detector.

2. suppress the dead area coming from light guide materials or readout devices.

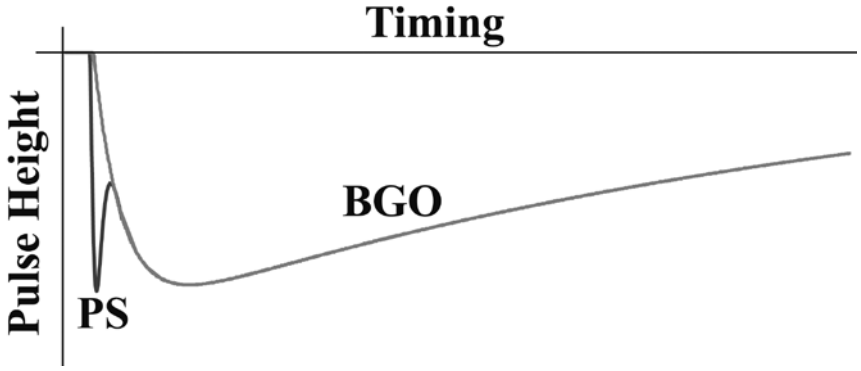

Fig.4. Expected pulse shape of a phoswich detector. The signal from the plastic scintillator (PS) is expected to be observed only when the incident particle is charged.

§3. Light attenuation loss in a BGO crystal

The scintillation photons generated at the plastic scintillator should reach the photo-multiplier tube so that the phoswich detector can identify the charge of the incident particle. We have estimated the light attenuation length from the measured transmittance of a BGO crystal with a finite length according to Ref. [9].

The reflectance of the perpendicularly incident light at a surface is described as

$$R = \left(\frac{n-1}{n+1} \right)^2 \tag{1}$$

where n denotes the refractive index of BGO, and the transmittance at the surface is given by

$$T = 1 - R. \tag{2}$$

The light intensity after traveling a length l becomes

$$\alpha = \exp\left(-l/L_{\mathrm{att}}\right) \tag{3}$$

in a crystal with a light attenuation length of L_{att}. Therefore, the transmittance of a crystal with a length of l is calculated as

$$T_l = T\alpha\left\{\sum_{n=0}^{\infty}(R\alpha)^{2n}\right\}T = \frac{\alpha(1-R)^2}{1-R^2\alpha^2} \tag{4}$$

by taking into account multiple bounces between two ends and the light attenuation loss in BGO.

The transmittance of BGO crystals with thicknesses of 16.8 ($1.5X_0$) and 40.0 mm was measured with a spectrophotometer Shimadzu UV-230. Fig. 5a) shows the measured transmittance as a function of the wavelength of the incident light. The transmittance of the 40.0 mm thick BGO crystal is almost the same as that of the 16.8 mm one, suggesting the light attenuation length is long.

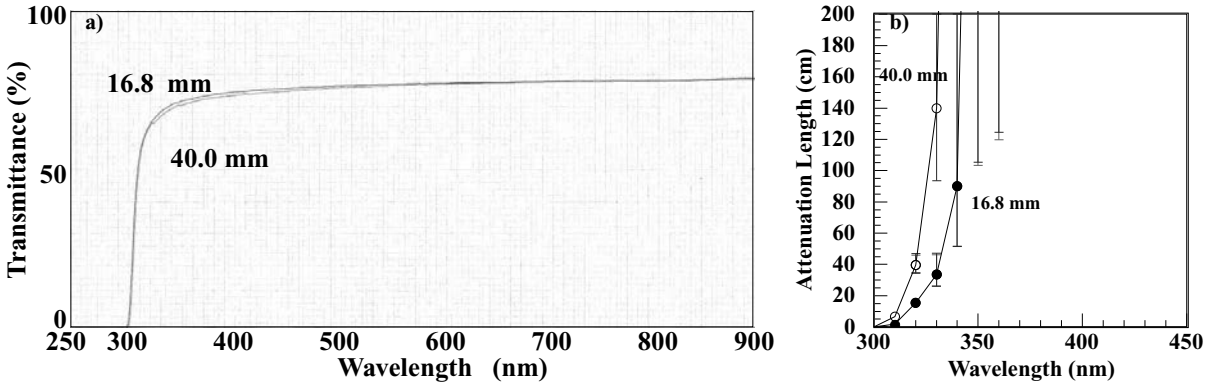

Fig.5. a) Transmittance of BGO crystals with thicknesses of 16.8 and 40.0 mm as a function of the wavelength of the incident light. b) Light attenuation length of BGO crystals determined from the crystals with thicknesses of 16.8 and 40.0 mm. The attenuation length is longer than 2 m for the wavelength from 350 to 900 nm.

The light attenuation length has been estimated from Eq. (4) by using the refractive index as a function of the wavelength given in Ref. [10]. Fig. 5b) shows the light attenuation length of the BGO crystals. It is shorter than 20 cm at the wavelength less than 320 nm, and is enough longer at the longer wavelengths. The details of the analysis are described elsewhere [11].

§4. Experimental Setup

The pulse shapes of the phoswich detector in response to the electron beams with several momenta from 200 to 800 MeV/c have been acquired at Laboratory of Nuclear Science, Tohoku University. To determine the incident timing and the trigger for the data acquisition, a 10 mm square plastic scintillator (PS) with a thickness of 3 mm was placed in front of the detector. Both sides of the PS are connected to photo-multiplier tubes (PMT) Hamamatsu R4125GMOD. A metal-packaged PMT Hamamatsu R8900U with a breeder E5996MOD was used for the detector. All the output signals are directly input to a digital phosphor oscilloscope Tektronix DPO-4104, which is remotely controlled using the Ethernet [12]. Fig. 6 shows the experimental setup for the beam test of the phoswich detector.

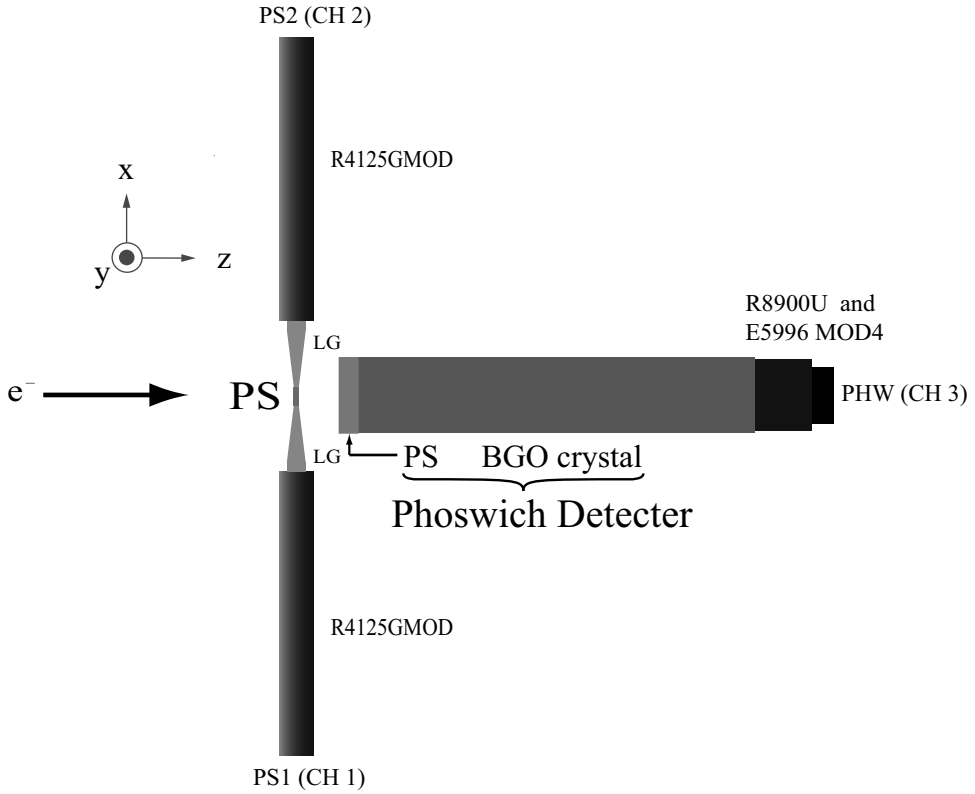

Fig.6. Experimental setup for the beam test of the phoswich detector. A 10 mm square plastic scintillator with a thickness of 3 mm, both sides of which are connected to a PMT's Hamamatsu R4125GMOD, is placed in front of the phoswich detector. All the signals are directly input to a digital phosphor oscilloscope Tektronix DPO-4104.

Since the scintillation photons are emitted only in the BGO crystal of the phoswich detector when neutral particles are incident on it. The pulse shapes of the phoswich detector without PS (BGO crystal only) in response to the electron beams were also acquired in order to know the pulse shapes for neutral particles. Fig. 7 shows the typical pulse shapes of the BGO crystal and phoswich detector in response to the electron beam with a momentum of 457 MeV/c. The pulse shapes in the leading edge region are different between the BGO crystal and phoswich detector, and the PS component is clearly observed in the pulse shape of the phoswich detector.

§5. Charge Identification Efficiency

In order to estimate the charge identification efficiency of the phoswich detector, a PS component in the pulse shape was obtained by subtracting the average BGO pulse shape from the phoswich detector one event by event. The average BGO pulse shape was given for each incident electron momentum, and it was normalized event by event so that the charge integration in the tail region ($[+20, +300)$ ns) became the same. The charge excess was integrated in the leading edge region ($[-20, +10)$ ns). Fig. 8 shows the charge excess distribution with several $\mathcal{R}$TAGX currents which specifies the momentum of the electron beam.

By setting the appropriate threshold for the charge excess, the charge identification efficiency of

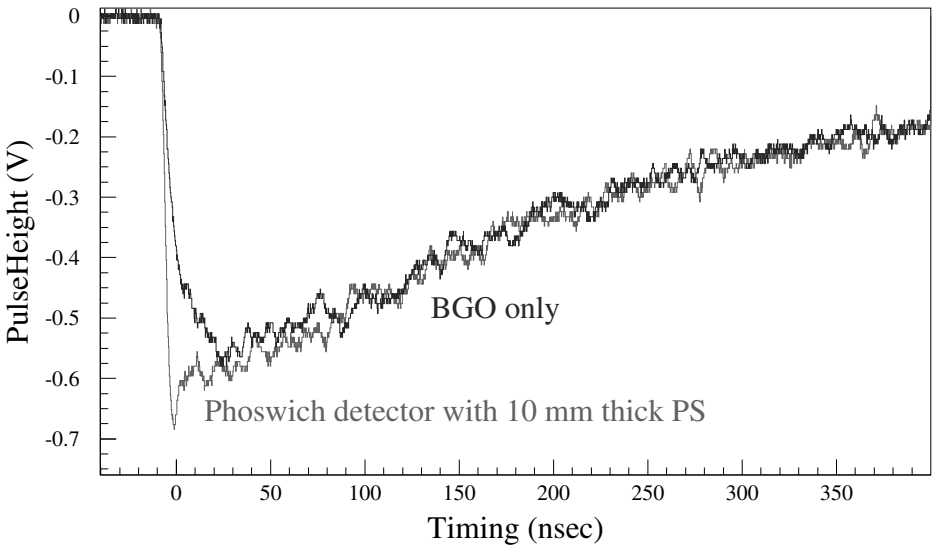

Fig.7. Typical pulse shapes of the BGO crystal and the phoswich detector in response to the electron beam. The pulse shapes have been taken at $E_e = 457$ MeV/c.

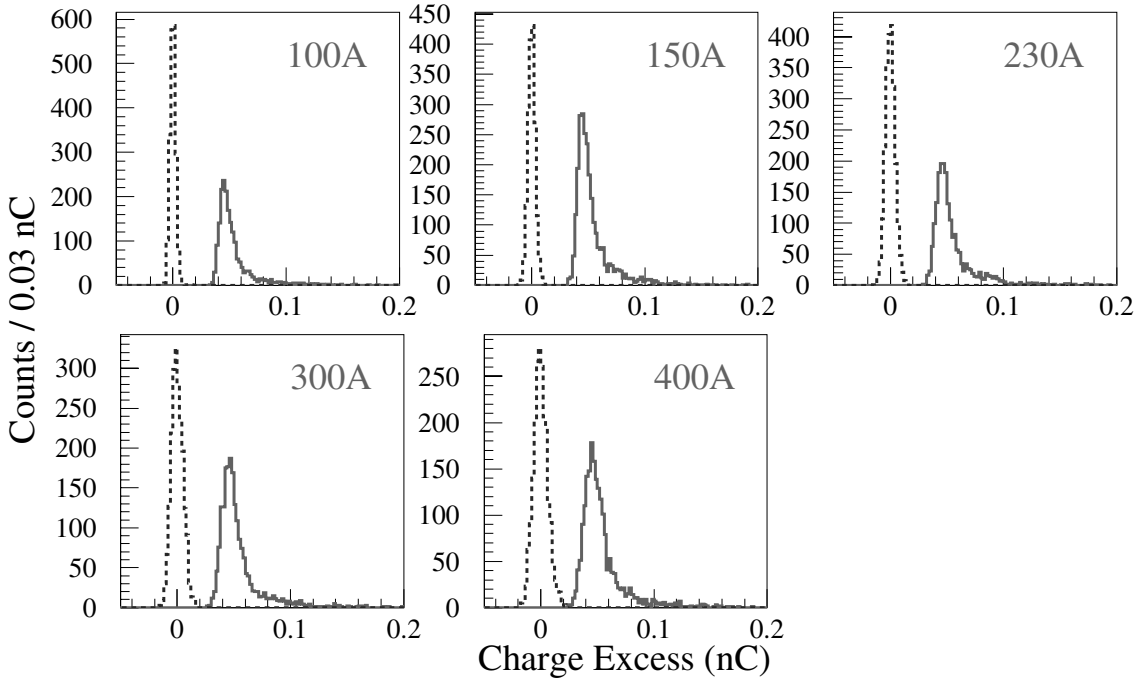

Fig.8. Charge excess distribution with several $\mathcal{R}$TAGX currents. The $\mathcal{R}$TAGX current is described in each panel. The dotted and solid lines show the charge excess distributions for the BGO crystal and phoswich detector, respectively. The $\mathcal{R}$TAGX currents of 100. 150. 230, 300, and 400 A correspond to the electron momenta of 200, 300, 357, 589, and 744 MeV/c, respectively.

100% was obtained for all the $\mathcal{R}$TAGX currents. The details of the analysis are described elsewhere [13]. In Ref. [13], the various methods of the charge identification, the stability of it by varying the timing regions for the charge excess integration and the pulse shape normalization, and a phoswich detector with a 5 mm thick PS are also discussed.

§6. Summary

A plastic and BGO phoswich detector as an EM calorimeter module for charge identification was tested at the electron beamline for testing detectors in Laboratory of Nuclear Science, Tohoku University. The charge excess for the PS component was obtained by subtracting the average BGO pulse shape from the phoswich detector one. Assuming the pulse shapes of the phoswich detector without PS (BGO crystal only) in response to the electron beams are the same as those for neutral particles, 100% of the charge identification was achieved for all the electron momenta from the charge excess information.

Acknowledgement

This work was supported in part by Grant-in-Aid for Specially promoted Research (19002003).

References

[1] T. Nakano *et al.*: Phys. Rev. Lett. **91**, 012002 (2003).
[2] D. Diakonov, V. Petrov, M. Polyakov: Z. Phys. A **359**, 305 (1997).
[3] V. Kuznetsov *et al.*: Phys. Lett. B **647**, 23 (2007).
[4] F. Miyahara *et al.*: Prog. Theor. Phys. Suppl. **168**, 90-96 (2007); H. Shimizu: talk at NSTAR2007.
[5] I. Jaegle *et al.*: Phys. Rev. Lett. **100**, 252002 (2008).
[6] T. Nakabayashi *et al.*: Phys. Rev. C **74**, 035202 (2006).
[7] T. Ishikawa *et al.*: Research Report of LNS **40**, Tohoku University, 6 (2008).
[8] T. Ishikawa, H. Fujimura, and H. Shimizu: Internal GeV-γ Analysis Note No. **132** (2009).
[9] D.A. Ma and R.Y. Zhu: Nucl. Instr. and Meth. **333**, 422 (1993).
[10] M.V. Lalic and S.O. Souza: Opt. Mater. **30**, 1189 (2008).
[11] S. Kaida: Internal GeV-γ Analysis Note No. **156**$\mathcal{D}$ (2009).
[12] T. Ishikawa: Internal GeV-γ Analysis Note No. **150**$\mathcal{A}$ (2009).
[13] S. Kaida: Internal GeV-γ Analysis Note No. **176**$\mathcal{D}$ (2010).

(LNS Experiment : #2661)

J-PARC ハイパー核γ線実験のためのビームラインチェレンコフカウンターおよびビームベトカウンターの性能評価

佐藤美沙子[1], 本多良太郎[1], 細見健二[1], 小池武志[1], 三輪浩司[1], 白鳥昂太郎[1], 田村裕和[1], 八木一也[1], 山本剛史[1], 米本慶央[1]

[1] 東北大学大学院理学研究科 （980-8578 仙台市青葉区荒巻字青葉）

Study of beamline aerogel cherenkov counters to identify the (K^-, π^-) reaction for the hypernuclear γ-ray spectroscopy at J-PARC

M. Sato[1], R. Honda[1], K. Hosomi[1], T. Koike[1], K. Miwa[1], K. Shirotori[1], H. Tamura[1], K. Yagi[1], T.O. Yamamoto[1], and Y. Yonemoto[1]

[1]*Department of Physics, Tohoku University, Sendai, 980-8578*

We have studied beamline aerogel cherenkov counters (BAC, SAC1, SAC2) which are used to identify the (K^-, π^-) reaction for the hypernuclear γ-ray spectroscopy experiment E13 at J-PARC. The efficiencies for these counters for 1.4 GeV/c π^- are required to be more than 99% in order to identify the real (K^-, π^-) reaction and to reject background due to the misidentification of π^- or K^- beam particles. The photo-electron numbers of these counters for 450 MeV/c positron beam were measured to optimize the structure of the counters to obtain a large photo-electron number with a reasonable thickness of the counter. The obtained photo-electron numbers were ∼28, 27 and 22 for BAC, SAC1 and SAC2, respectively. The efficiency for 1.4 GeV/c π^- is estimated to be more than 99.9% by setting the threshold at 6∼8 photo-electron level. The photon-electron contribution from the materials other than the aerogel was also measured to be 1.9 p.e. as a mean value. By setting the same threshold level (6∼8 p.e.), the misidentification due to this effect is suppressed to be less than 0.1%.

§1. ハイパー核γ線分光実験における (K^-, π^-) 反応同定システム

我々は J-PARC K1.8 ビームラインにおいて、大立体角ゲルマニウム検出器群 Hyperball-J を用いて、ハイパー核からのγ線分光実験 (E13) を計画している [1]。(K^-, π^-) 反応を用いて Λ ハイパー核を生成し、磁気スペクトロメーターによって Λ ハイパー核生成事象を選択し、γ線を Hyperball-J によって検出する。トリガーレベルで (K^-, π^-) 反応を同定し、さらにビーム起因のダミートリガーを抑制することが実験を遂行する上で必須となる。我々は 1.5 GeV/c の K^- ビームを用いるため、図 1 に示すように、標的前後に屈折率 1.03 のエアロジェルチェレンコフカウンターを設置し (K^-, π^-) イベントを同定する。標的上流の検出器 BAC1 および BAC2 では、ヒットがないことから K^- ビームを選択し、下流側の SAC1 およ

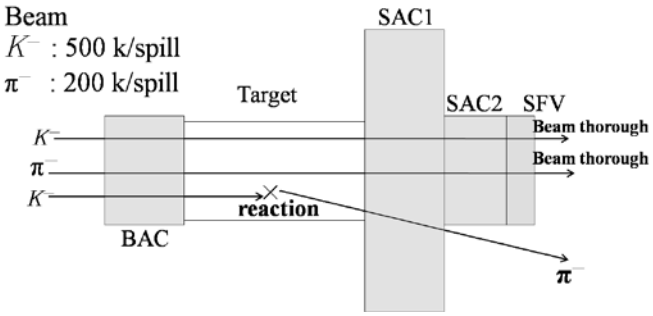

第 1 図　E13 実験での標的前後に設置される (K^-, π^-) 反応同定システムの模式図。

び SAC2 ではヒットを要求することによって散乱 π^- を選択する。K^- ビームの強度は 500 k/spill であり、これに混入する π^- が 200 k/spill 程度であると予想される。π^- ビームによるバックグラウンドを抑制するために、BAC1,2 にそれぞれ 99%以上の efficiency が必要となる。2 段の BAC1,2 を用いることによって 20 count/spill まで抑制する。一方、SAC の efficiency はそのまま (K^-, π^-) トリガーの efficiency になるため、最低でも 99%以上の効率が求められる。また SAC1 において、K^- ビームに対して δ 線などによる粒子識別の誤認が 2%程度生じると予想される。このダミートリガーを抑えるために、ビームが通り抜ける領域を覆うように SAC2 と SFV(プラスチックシンチレーター) を設置して、SFV にヒットがあったときに、SAC2 にヒットがないイベントを K^- ビームとみなし除去を行なう。

(K^-, π^-) 反応によるハイペロン生成イベントの頻度が 700 count/spill に対して、ビーム起因のバックグラウンドを 70 count/spill まで抑制することが、BAC、SAC および SFV によるオンライン粒子識別システムに求められる。我々はこれを達成するためにエアロジェルチェレンコフカウンターの製作を行なった。カウンターの設計をシミュレーションをもとに行ない、大きな光量が期待できるいくつかのデザインの中から最適な形状を選ぶために、検出器の形状による光量の比較および集光効率の位置依存性を調べることを目的として、陽電子を用いたテスト実験を行なった。

§2．エアロジェルチェレンコフカウンターの基本的なデザイン

我々は運動量が 1.4 GeV/c 程度の K^- と π^- を識別するために屈折率が 1.03 のエアロジェルを用いた。用いたエアロジェルはパナソニック電工で販売している標準品 SP-30 であり、密度は 0.11 g/cm^3 である。用いた光電子増倍管は HAMAMATSU の H6614-70UV である。これはファインメッシュタイプの光電子増倍管であり、UV 窓かつスーパーバイアルカリ (SBA) の光電面を持つため、紫外領域の光に対しても感度を有し、全波長領域で量子効率が 1.3 倍程度良くなることが期待できる。反射剤としてはテフロンを用いた。テフロンは 250 nm から 650 nm の広い波長領域の光に対して、高い反射率を持つ。このテフロンを 3 枚重ねて反射剤として用いた。図 2 に各検出器の典型的な形状を示す。

§3．陽電子ビームを用いた性能評価実験

3.1 実験のセットアップ

チェレンコフ検出器の集光効率は、エアロジェルの厚み、後方の空気層の厚み、光電子増倍管の配置に依存する。Geant4 シミュレーションでの集光率の見積もりから、集光率の高い、いくつかの形状に検討を選

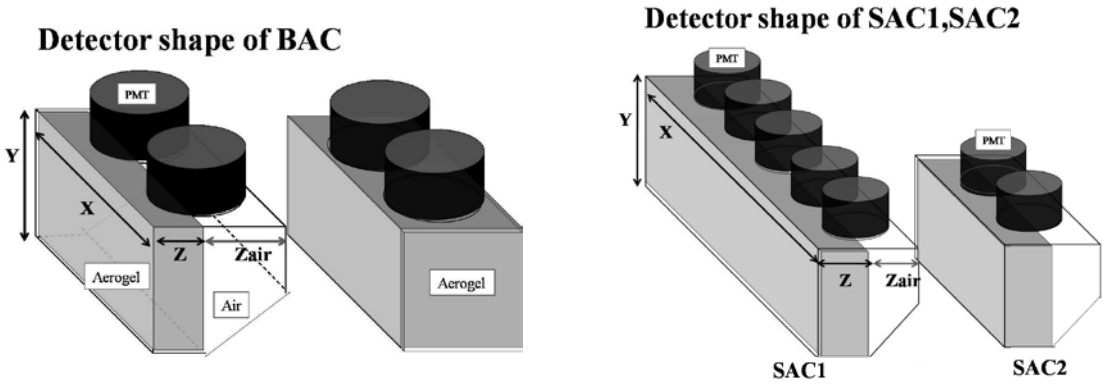

第 2 図　BAC の典型的な形状 (左図) および SAC の典型的な形状 (右図)。本テスト実験ではエアロジェルの厚さおよび空気層の厚さの異なる形状の検出器に対し、光量の比較を行なう。また SAC1 では PMT の数 (5 本および 6 本) を変えて、光量を測定した。

び、そのなかから、最適なものを選択するために、東北大学核理学研究施設 GeV-γ 測定室の陽電子ビームラインでテスト実験を行った。均一な運動量の荷電粒子を、均一の path length で検出器内を通過させてデータを収集し、検出器の形状による光量の比較と、集光効率の位置依存性を比較することが、ビームを用いたテスト実験の目的である。使用する陽電子ビームの運動量は 450 MeV/c で $\beta = 1$ である。また、ビームの広がりはエアロジェルチェレンコフ検出器を設置する位置で、直径およそ 3 cm 程度である。

図 3 に実験のセットアップを示す。2 台のチェレンコフカウンターの前後にビームを識別するためのプラスチックシンチレーター (T1 および T2) を設置する。またエアロジェルの内部で陽電子ビームがシャワーを生成したようなイベントを除去するために、チェレンコフカウンターよりも十分大きなプラスチックシンチレーター (2EV) をチェレンコフカウンター下流に設置し、その ADC の分布から検出器を 1 粒子のみが通過したイベントを選択する。測定項目を以下に挙げる。

- それぞれの検出器の形状に対しての光量の依存性を調べ、最適な形状を決定する。
- ビーム通過位置依存性があるかどうかを調べる。
- 反射剤による蛍光による影響を調べる。

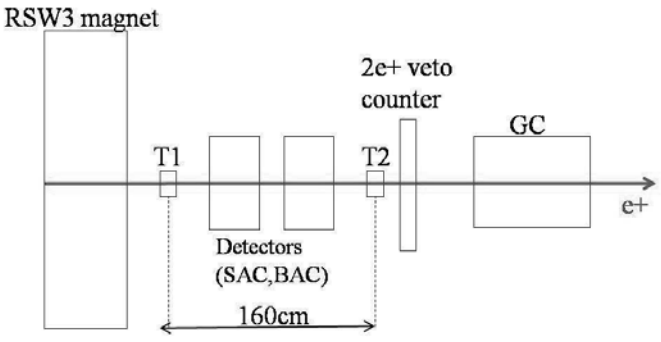

第 3 図　ビームライン上のセットアップの模式図

3.2 検出器の形状依存性

本テスト実験ではエアロジェルの厚さおよび空気層の厚さ (図 2 中の Z および Z_{Air}) の異なる形状の検出器に対し、光量の比較を行なった。また、SAC1 に関しては光電子増倍管の数を 5 本および 6 本の場合に対し光量を比較した。以下にビームをエアロジェルの中央に照射したデータに対して、各検出器の形状を変化させたときの平均光電子数の結果をまとめる。図 4 に BAC および SAC1 での典型的な光電子数分布として、それぞれエアロジェルの厚み 60 mm、空気層の厚み 0 mm およびエアロジェルの厚み 40 mm、空気層の厚み 50 mm の形状での光電子数分布を示す。

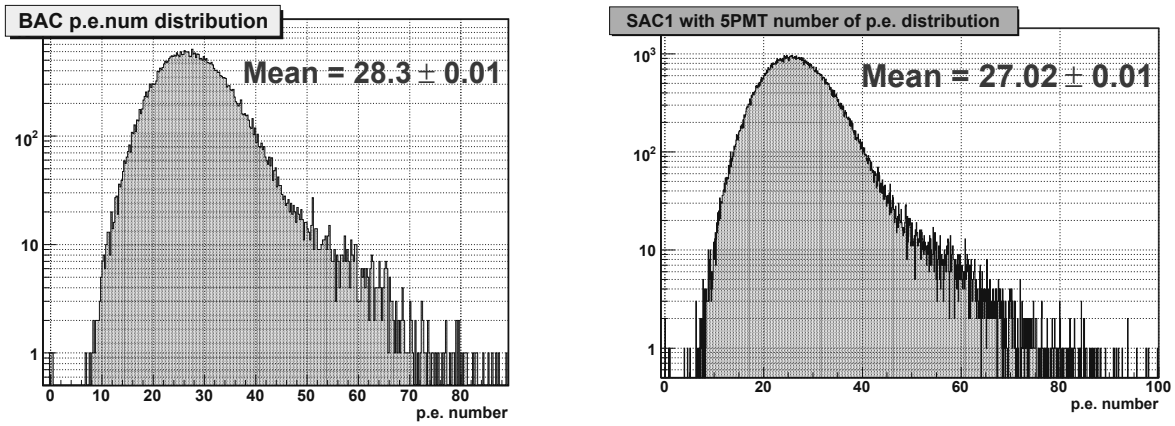

第 4 図　BAC(左図) および SAC1(右図) の光電子数分布。BAC の形状はエアロジェルの厚み 60 mm、空気層の厚み 0 mm である。平均光電子数は、28.3±0.01 である。SAC1 の形状はエアロジェルの厚み 40mm、空気層の厚み 50 mm であり、光電子増倍管の数は 5 本である。平均光電子数は、27.02±0.01 である。ともに十分な検出効率が得られる光量が得られた。

3.2.1 BAC

表 1 は BAC の検出器の構造を (a)∼(e) まで変化させたときの光電子数分布の平均光電子数の結果をまとめたものである。最も多くの光量がえられたのは、(c) の 30.0 p.e. であるが、検出器内部の空気層部（不感領域）を最小限におさえるべきであること、検出器内部の物質量を小さくしたいことを考慮すると、(e) のエアロジェルの厚み 60 mm、空気層の厚み 0 mm を BAC のデザインとして採用する。

	Aerogerl (Z)	Air (Z_{Air})	反射材	平均光電子数
(a)	40 mm^t	40 mm^t	テフロン	21.6±0.01
(b)	40 mm^t	50 mm^t	テフロン	23.6±0.01
(c)	80 mm^t	0 mm^t	テフロン	30.0±0.01
(d)	30 mm^t	30 mm^t	テフロン	20.4 ±0.01
(e)	60 mm^t	0 mm^t	テフロン	28.3±0.01

第 1 表　BAC の検出器の形状ごとの平均光電子数

3.2.2 SAC1, SAC2

表 2 は SAC1 の検出器の構造の違う (a)、(b) および (c) の 3 種類についての光電子数分布の平均光電子数の結果をまとめたものである。最も多くの光量をえられたのは、(b) の 28.1 p.e. である。同じエアロジェ

ルの厚みかつ空気層の厚みで、読み出しに使用している光電子増倍管が 5 本の場合でも、平均光電子数が 27.0 p.e. であり、十分な光量が得られている。SAC1 は Hyperball-J の内側に入り込むため、光電子増倍管は Ge 検出器に入射する γ 線にとって影になる。よって、SAC1 に使用する光電子増倍管の数は少ないほうがよい。よって、(a) のエアロジェルの厚み 40 mm、空気層の厚み 50 mm、光電子増倍管の数 5 本のデザインを採用する。

SAC2 は 1 つのデザインでのみ光量を測定した。表 3 に結果を示す。

	Aerogerl (Z)	Air (Z_{Air})	光電子増倍管本数	平均光電子数
(a)	40 mm^t	50 mm^t	5	27.0±0.01
(b)	40 mm^t	50 mm^t	6	28.1±0.03
(c)	20 mm^t	70 mm^t	5	20.4±0.04

第 2 表　SAC1 の検出器の形状ごとの平均光電子数

	Aerogerl (Z)	Air (Z_{Air})	反射材	平均光電子数
(a)	40 mm^t	50 mm^t	テフロン	21.6±0.01

第 3 表　SAC2 の検出器の平均光電子数

3.3 ビーム通過位置依存性

光量の測定結果から決定した BAC、SAC1 の形状に対して、ビームの通過位置を変化させ光量を測定し、光量のビームの位置依存性を調べる。

3.3.1 BAC

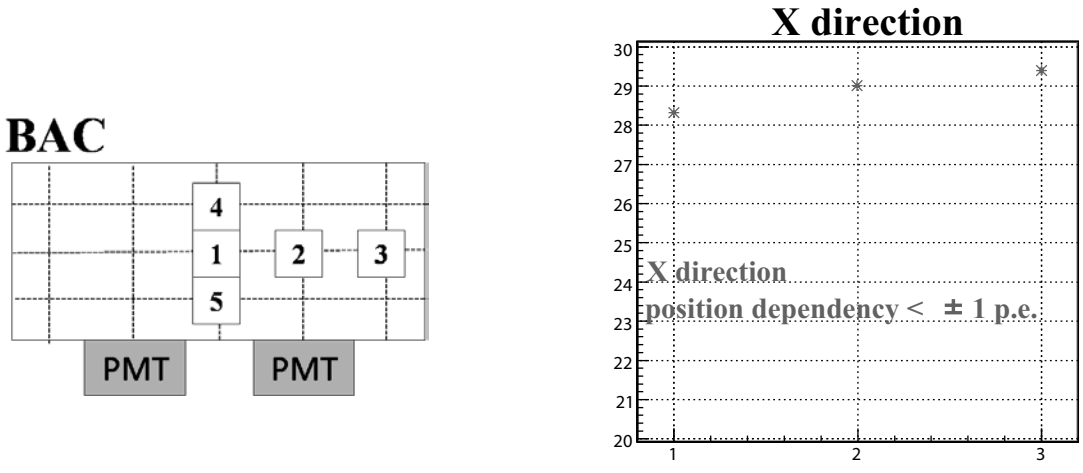

第 5 図　BAC に対する光量の位置依存を調べた位置 (左図)。合計 5 箇所で光量を測定した。1、2、3 方向を X 方向、4、2、5 の方向を Y 方向と定義する。右図に光電子数の x 方向依存性を示す。

ビームの通過位置依存性を測定した際の BAC の検出器形状は、エアロジェルの厚みは 60 mm、空気層の厚みは 0 mm である。この BAC に対して、図 5 に模式図を示したように、合計 5 箇所の位置依存性を調べた。1、2、3 の方向を X 方向、4、2、5 の方向を Y 方向と定義する。光量の位置依存性の結果を図 5

の右図に示す。これは X 方向に位置依存性（1、2、3）の結果であり、光量の位置依存性は、± 1 p.e. 以下であることがわかった。Y 方向での光量の位置依存性についても、± 3 p.e. 以下であった。

3.3.2 SAC1

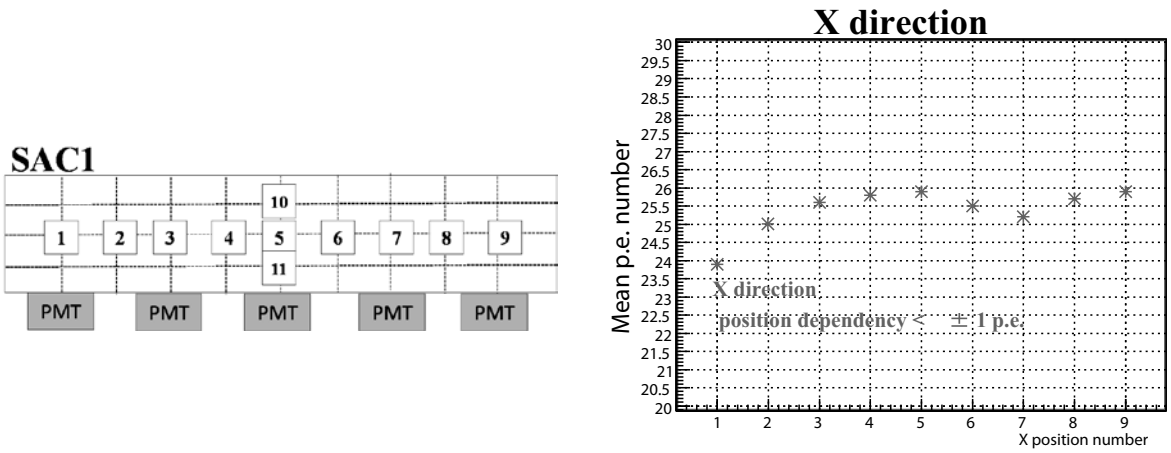

第 6 図　SAC1 のビーム照射位置の模式図。合計 11 箇所の位置依存性を調べた。1 ～ 9 の方向を X 方向、10、5、11 の方向を Y 方向と定義する。

SAC1 に対しても図 6 に模式図を示したように、合計 11 箇所の位置依存性を調べた。1 ～ 9 の方向を X 方向、10、5、11 の方向を Y 方向と定義する。1 ～ 9 での光量を比較することで、X 方向の光量変化を、10、5、11 を比較することで、Y 方向の光量を比較するために、このような位置での光量を測定した。SAC1 の光量の X 方向の位置依存性の結果を 図 6 の右図に示す。X 方向での光量の位置依存性は、± 1 p.e. 以下であることがわかった。また Y 方向での光量の位置依存性についても、± 3 p.e. 以下であった。

以上 BAC、SAC1 の光量の位置依存性結果より、BAC、SAC1 ともに、光量の位置依存性は、Y 方向のほうが変化が大きく、光電子増倍管からの距離に依存しており、ビーム通過位置が、光電面から離れるほど、集光効率が低下するといえる。また、X 方向も光電子増倍管の直上の位置をビームが通過している場合が光量が高い傾向である。BAC、SAC ともに、光量の位置依存性は ± 3 p.e. 以内であり、この程度の変動では、平均光電子数が十分多いため、位置に依存せずに十分な検出効率が得られると期待できる。

3.4 1.4 GeV/c π^- に対する検出効率および反射剤による蛍光の影響

450 MeV の陽電子に対しての光電子数をテスト実験から求めることが出来た。E13 実験では 1.4 GeV/c の π^- に対して、99%以上の efficiency が要求される。このテスト実験のデータをもとに 1.4 GeV/c の π^- に対しての検出器の応答を求め、予想される検出効率を見積もる。

1.4 GeV/c の π^- に対して発生するチェレンコフ光は、陽電子との β の違いから、約 8 割程度になると考えられる。この効果を検出効率に反映するための第 1 次近似として、450 MeV/c の陽電子で得られた光電子数分布を 0.8 倍したものを π^- の光電子分布とする。efficiency を見積もるためにトリガーの閾値を決定しなければならない。低い閾値を設定すれば高い検出効率が期待できるが、一方で検出器内部に使用した反射剤であるテフロンや容器などの物質が荷電粒子の通過によって若干の蛍光を発するため、この蛍光をトリガーしてしまうとダミートリガーを生成することになってしまう。このエアロジェル以外からの光量を調

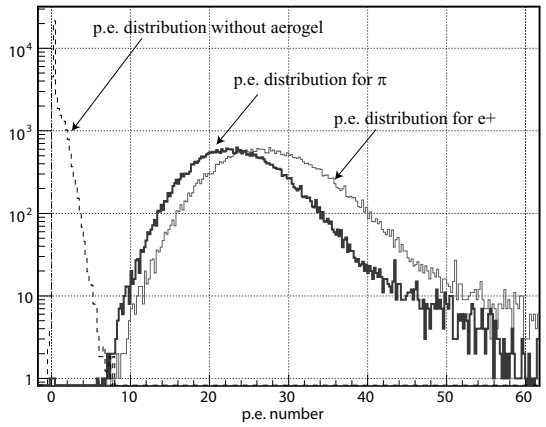

第 7 図　点線の分布：エアロジェルチェレンコフ検出器のエアロジェルだけをぬいた空箱の状態でビームを照射し得られた光電子数分布。赤い細線：e^+ をエアロジェル入りの検出器に照射した際に得られる光電子数分布。青い太線：近似的につくった π^- 分布。

べるために、検出器のエアロジェルだけをぬいた空箱の状態でビームを照射し、光量を測定した。図 7 に BAC に対して陽電子を照射したときの光電子数分布およびこれをもとに 1.4 GeV/c の π^- に対して予想される分布を示す。また、空箱の状態で反射剤などの蛍光から得られた光電子数分布もともに示す。反射剤などの蛍光による平均光電子数は 1.9 p.e であった。このプロットからトリガーの閾値を 1∼10 p.e. まで変化させていき、π^- に対しての検出効率および反射剤などの蛍光によるフェイクヒットの割合を調べた。閾値を 6∼8 p.e. に設定することで π^- に対して 99.9%以上の検出効率が得られることが分かった。一方でフェイクヒットの割合に対しても同じく閾値を 6∼8 p.e. に設定することで 0.1%以下に抑えることが出来ることが確認できた。

§4. ま と め

運動量 450 MeV/$c(\beta = 1)$ の陽電子を照射し、エアロジェルチェレンコフ検出器で得られる光量を調べ、いくつかの試作した検出器のなかから 最適なものを選択した。最適な形状の検出器で得られる光量は BAC の場合 28 p.e. 程度、SAC1 の場合 27 p.e. であった。また、閾値を 6 p.e ∼ 8 p.e. に設定しても π^- に対して 99.9 %以上と十分な検出効率が得られる。粒子が検出器内を通過していく際、反射材として仕様しているテフロンシートおよび検出器を構成している厚紙が蛍光を放出していることがわかった。光電子増倍管で検出できた蛍光の光量は、平均 1.9 個であった。閾値を 6 p.e ∼ 8 p.e. に設定することによって、蛍光によって発生する Fake hit の割合は 0.1 %以下に抑えることが出来る。

謝　辞

実験中、非常に優れたビームを供給していただき、核理研の皆様に感謝いたします。特に石川助教には様々なユーザーの要求に対して対応していただきました。ありがとうございました。

参　考　文　献

[1]　H. Tamura *et al.*: J-PARC proposal E13 “Gamma-ray spectroscopy of light hypernuclei” (2006).

(LNS Experiment : #2677)

Performance study of gas Cherenkov counter and glass Cherenkov counter with positron beam

Hiroyuki Fujioka[1], Satoshi Adachi[1], Yuta Sada[1], Hitoshi Sugimura[1], and Kohtaroh Yoshida[2]

[1]*Department of Physics, Kyoto University, Kyoto, 606-8502*
[2]*Department of Physics, Osaka University, Osaka, 560-0043*

We performed a test experiment to investigate the performances of a gas Cherenkov counter (for the J-PARC K1.8 beamline), and a total-internal-reflection glass Cherenkov counter (for the P28 experiment at J-PARC K1.8BR beamline). As for the gas Cherenkov counter, we found the number of photoelectrons can be large enough by adjusting the isobutane gas pressure to 1.7 atm, through the measurements between 1.0 and 1.4 atm. We also demonstrated total internal reflection at the surface of a borosilicate glass with optical polishing for Cherenkov light, while the loss due to multiple reflections is not negligible.

§1. Introduction

A test experiment was carried out in June 2009 by irradiating the positron beam on two kinds of detectors, a gas Cherenkov counter and a glass Cherenkov counter. The gas Cherenkov counter, whose purpose is to distinguish electrons (positrons) from others, is now installed at the K1.8 beamline. The glass Cherenkov counter is prepared for K^-/p separation in the P28 experiment [1] at the K1.8BR beamline. The detail of each counter will be described below.

§2. Gas Cherenkov Counter

A new gas Cherenkov counter had to be developed, because the previous one used at the KEK-PS K6 beamline is too thick to install between the mass slit and the BH1 hodoscope in the K1.8 beamline (Fig. 1). The clearance at the K1.8 beamline is only about 30 cm. It is used for e/π separation in the beam ($> 1\,\mathrm{GeV}/c$), which is difficult by use of the time-of-flight analysis. It is crucially important to achieve a high detection efficiency of $e^{\pm}$, which was more than 99.9% at the KEK-PS K6 beamline, even with a thinner Cherenkov counter, so as to reduce the contamination of $e^{\pm}$ in π-beam trigger events.

The refractive index of the Cherenkov radiator should be around 1.002, since the maximum beam momentum available is around $2.0\,\mathrm{GeV}/c$. (Pressured) isobutane had been considered as a candidate, instead of freon-12 used at the KEK-PS K6 beamline.

Figure 2 shows the design of the new gas Cherenkov counter. The mirror reflector, whose shape is a paraboloid of revolution, is a borosilicate glass with aluminum evaporation coated with MgF_2, which is transparent to ultraviolet light. The reflected Cherenkov light is detected by a 5-inch PMT (R1250-03)

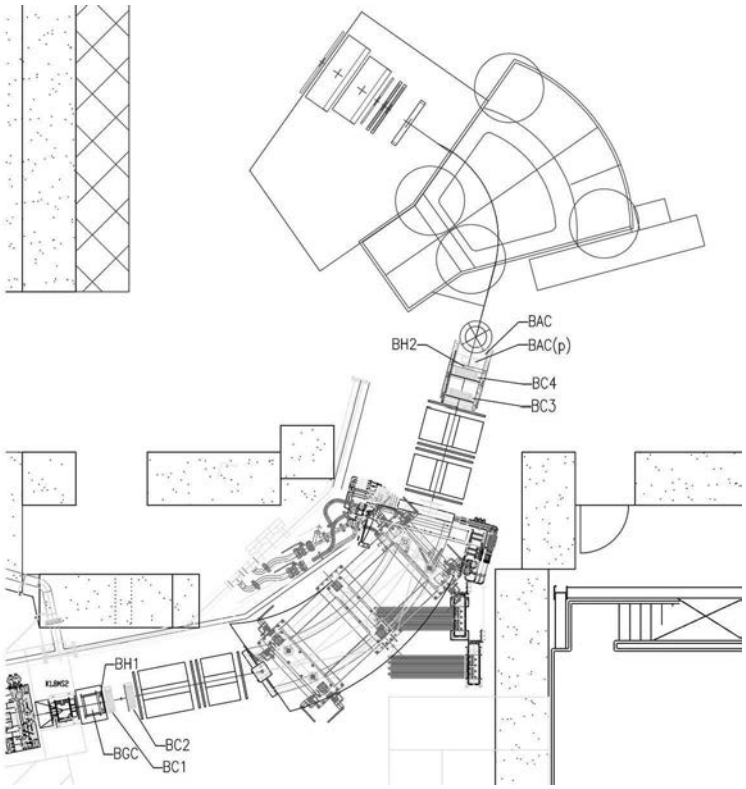

Fig.1. Layout of the K1.8 beamline and the SKS spectrometer. The gas Cherenkov counter (BGC) is located between the second mass slit (K1.8MS2) and the BH1 hodoscope.

with a UV-transparent window.

Before installing the counter in the K1.8 beamline, the detection efficiency of $e^{\pm}$ was evaluated by irradiating 450 MeV positron beam at LNS. Figure 3 shows an experimental setup, when the beam was injected in the center of the entrance of the Cherenkov counter. The position and incidence angle dependence was also investigated, as well as the dependence on the gas pressure.

An example of the ADC distribution is shown in Fig. 4. It was fitted with a Poisson distribution, taking into account the finite resolution of the ADC for a single photoelectron, and the average number of photoelectrons was estimated to be 3.7. It was found that around 0.4 photoelectron was not from the Cherenkov radiation in isobutane gas, by comparison with the ADC distribution of the Cherenkov counter filled with argon, whose Cherenkov light should be much less than the isobutane-filled one. The origin of this photoelectron is considered to be Cherenkov radiation in the borosilicate glass of the mirror. After the test experiment at LNS, we painted the inner surface as well as the opposite side of the mirror with matte-black paint. As expected, a single-photoelectron peak has been disappeared when a pion was injected at J-PARC.

The result on the position and incidence angle dependence is shown in Fig. 5. Since the light focussing is optimized for the central injection, a smooth dependence was observed. The reason why the dependence on the horizontal position is not symmetric, while the counter itself should be symmetric, is now found to be a small misalignment of the mirror.

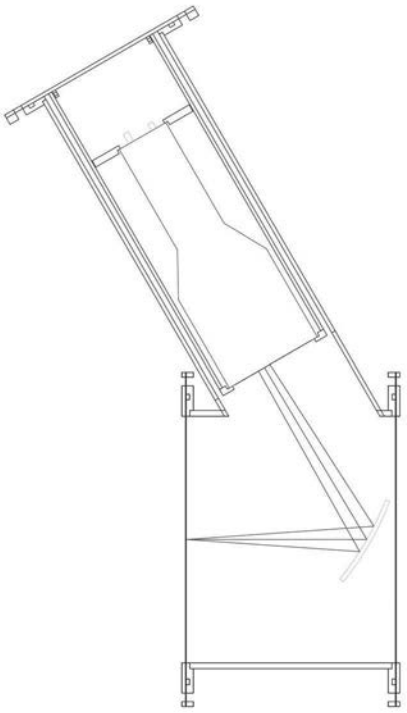

Fig.2. Side view of the gas Cherenkov counter. The beam will be injected from the left.

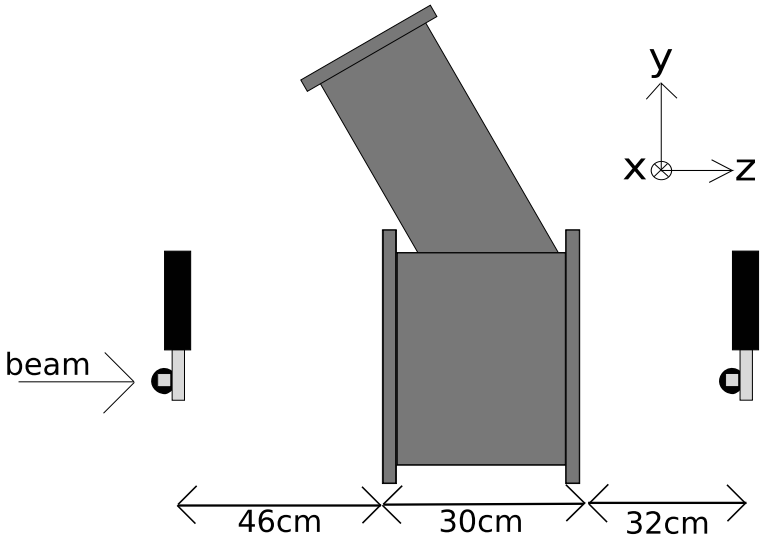

Fig.3. Experimental setup at LNS. The gas Cherenkov counter was located between two sets of beam defining counters.

The pressure dependence was also studied by changing the pressure from 1.0 atm to 1.4 atm, and it is confirmed that the number of photoelectron is almost proportional to the pressure, which is naturally explained by the approximation that $n-1$ (n: refractive index) is proportional to the pressure.

Based on these results, it has been concluded that the number of photoelectrons will be large enough (>5), and the detection efficiency will be at least 99.4%, for the normal incidence of $e^{\pm}$'s within 100 mm

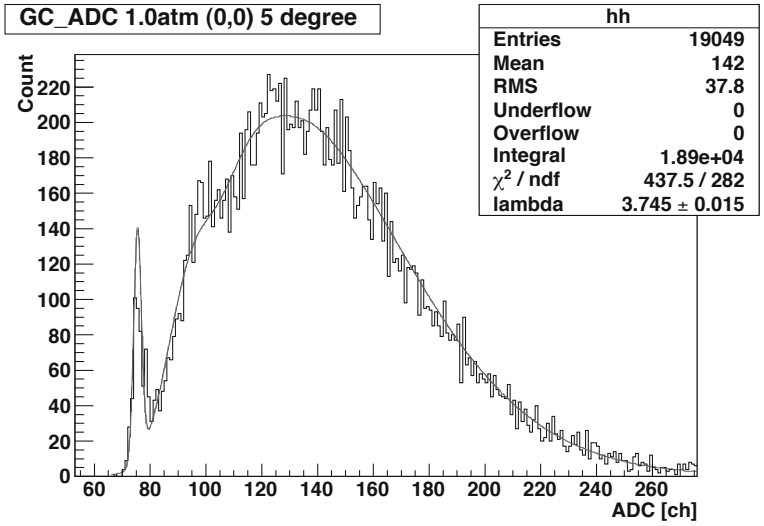

Fig.4. ADC distribution for the Cherenkov counter filled with 1 atm isobutane. The positron beam was injected in the center of the entrance, with the incidence angle 5°.

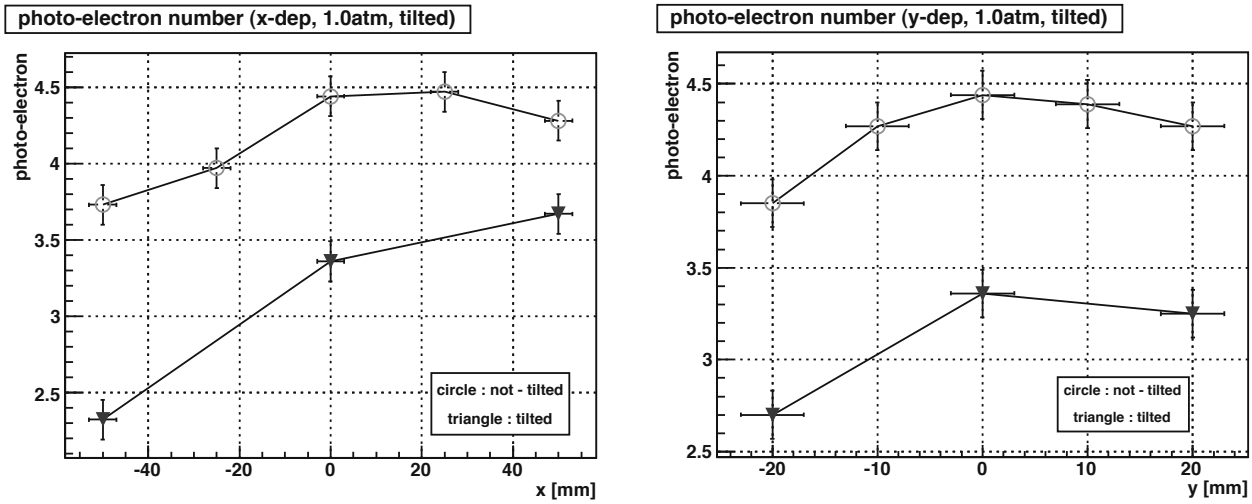

Fig.5. Position dependence of the number of photoelectrons along the horizontal (left) and vertical (right) direction. The circle and triangle marks correspond to normal incidence and 5°-tilted incidence, respectively.

(horizontal) and 20 mm (vertical) from the center, if the gas pressure is increased to 1.7 atm.

§3. Glass Cherenkov Counter

The E15 experiment [2] at the J-PARC K1.8BR area aims to investigate the possible existence of deeply-bound kaonic nuclear state, $K^- pp$, by the (K^-, n) reaction on ^{3}He. The 1.0 GeV/c K^- beam guided by the K1.8BR beamline will irradiate the helium-3 target, located at the center of the Cylindrical Detector System (CDS) for the detection of decay particles. In order to separate ejected neutrons from non-interacting K^-'s, a sweeping magnet will be installed downstream of the CDS (Fig. 6).

By the way, it is known that $\overline{K}N$ interaction has a strong isospin dependence. Hence, the com-

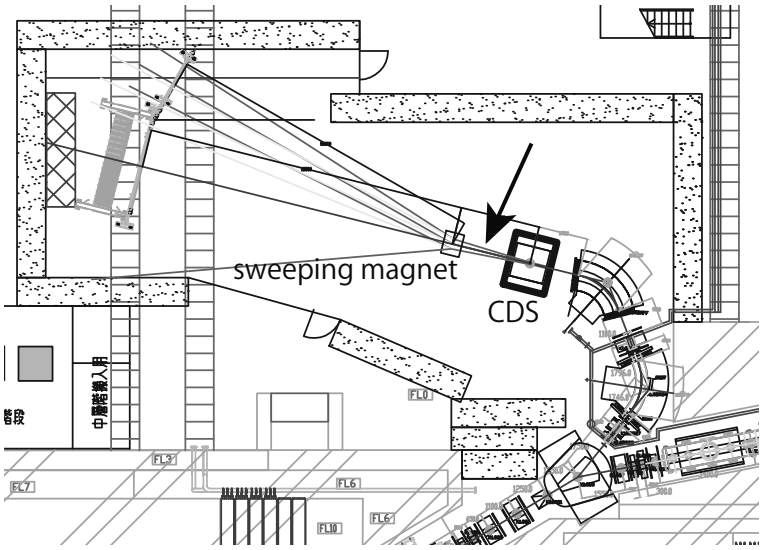

Fig.6. Experimental setup of the E15 experiment at the K1.8BR beamline. A glass Cherenkov counter will be installed between the Cylindrical Detector System and the sweeping magnet, as indicated by the arrow.

parison between two kinds of reaction spectroscopy with the (K^-, n) and (K^-, p) reactions, which is proposed as the P28 experiment [1], may be meaningful so as to extract information on isospin dependence of antikaon-nucleus interaction.

Scattered protons by the (K^-, p) reaction on the target will be bent by the sweeping magnet opposite to beam kaons, and they will be detected by additional plastic scintillation counters, located close to neuron counters. We plan to install a beam veto counter in between the CDS and the sweeping magnet. The momentum of the kaon beam will be 1.0 GeV/c, optimized for the E15 experiment. Assuming a momentum bite of 3%, its velocity (in terms of the light velocity) β spreads between 0.891 and 0.902. On the other hand, the proton between 1.0 and 1.4 GeV/c (corresponding to the missing mass between 2200 and 2550 MeV/c^2) has its velocity betwen 0.729 and 0.831. Therefore, the threshold must be set between 0.831 and 0.891.

Instead of an aerogel Cherenkov counter with its refractive index around 1.20, a glass Cherenkov counter under total internal reflection condition is under investigation. The threshold for a normally incident particle is $1/\sqrt{n^2-1}$. The threshold with a borosilicate glass of BK7, whose refractive index is about 1.53 at 400 nm is roughly estimated to be 0.864, which may satisfy the requirement. The threshold dependence on the incidence angle can been evaluated by a Monte Carlo simulation, taking into account the beam spreading and the acceptance of the proton counter.

The main purpose of this test experiment was to verify the transmission of Cherenkov light with multiple reflections at the surface of a commercially available glass with optical polishing, which has some degree of non-flatness and roughness. A prototype counter of a $200 \times 200 \times 0.5\text{mm}^3$ BK7 glass (the same size to be installed) viewed by two PMT's (H6522) at one side, was developed. They were covered by a black box for light shielding, but no reflective material was used. The counter together with the beam defining counters, like those shown in Fig. 3, was installed downstream of the gas Cherenkov counter

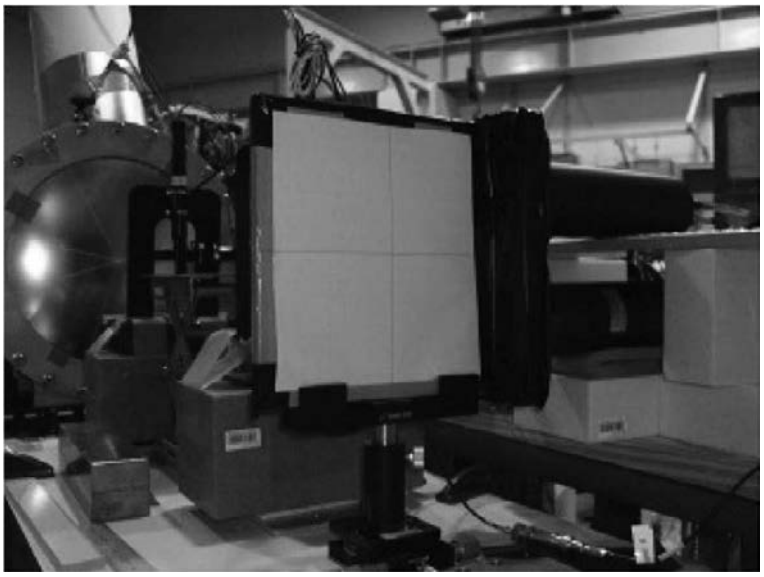

Fig.7. Prototype glass Cherenkov counter at the positron beamline.

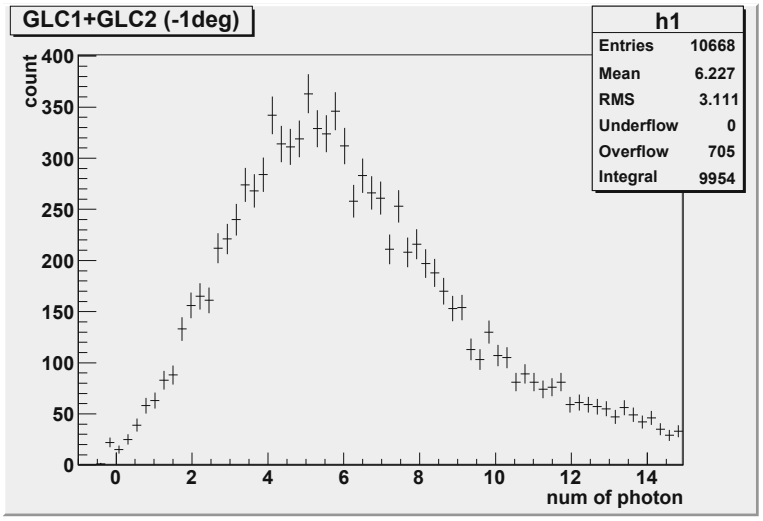

Fig.8. Number of photoelectrons of the glass Cherenkov counter, 1°-tilted against the beam axis. The signals of the two PMTs are added.

(Fig. 7), and the position and incidence angle dependence was measured.

Figure 8 shows the distribution of the number of photoelctrons. The average number was found to be around 6, which was about 1/3 of the expected value assuming no transmission loss, which is partly attributed to the imperfection of the surface. Except for the absolute value, the dependence on the incident position and angle was almost consistent with the expectation.

Based on these results, we reached the conclusion that we had to increasing the number of photoelectrons by changing the radiator. While a BK7 glass is opaque to UV light, a *NSG Super Clear* glass(Nippon Sheet Glass Co., Ltd.) has a high transmittance for $> 220\,\mathrm{nm}$, and a refractive index similar to a BK7 glass in the visible light region [3].

§4. Summary

The performances of two kinds of Cherenkov counters for experiments at the the K1.8 beamline, and the P28 experiment at the K1.8BR beamline, J-PARC, were examined at the LNS positron beamline. It is confirmed that the gas Cherenkov counter has a detection efficiency good enough for electrons (positrons). The surface of an optical-polished glass is found to have a fairly good flatness and small roughness for total internal reflection of Cherenkov light, although further R&D is necessary for increasing the number of photoelectrons.

Acknowledgment

The authors are grateful to Prof. H. Shimizu, Dr. T. Ishikawa, Dr. H. Yamazaki, Dr. H. Fujimura, Mr. K. Suzuki, and Mr. R. Hashimoto for supporting us to carry out the test experiment. This work was supported by Grant-in-Aid for Research Activity Start-up (No. 20840047) from JSPS.

References

[1] H. Fujioka *et al.*: J-PARC P28 proposal (2009). (http://j-parc.jp/NuclPart/pac_0907/pdf/Fujioka.pdf)

[2] M. Iwasaki and T. Nagae *et al.*: J-PARC E15 proposal (2006). (http://j-parc.jp/NuclPart/pac_0606/pdf/p15-Iwasaki.pdf)

[3] Nippon Sheet Glass Co., Ltd., private communication (2009).

(LNS Experiment : #2698)

Development of an Electromagnetic Calorimeter for the COMET Experiment

A. Sato[1], T. Tachimoto[1], S. Takahashi[1], E. Matsushita[1], and Y. Kuno[1]

[1]*Department of Physics, Osaka University, Toyonaka, 560-0043*

A prototype electromagnetic calorimeter for the $\mu - e$ conversion experiment, COMET, has bee tested with 100 MeV electron beams. Four MPPCs were directly connected to the LYSO crystal. This is the first beam test for this crystal calorimeter directory connected to the MPPCs. Photon yields to the MPPCs were measured with this system.

§1. Introduction

Charged Lepton Flavor Violation (cLFV) processes are highly suppressed to the unobservable level in the Standard Model (SM). Therefore, the discovery of the process implies existence of the physics beyond the SM. Muon to electron conversion in a muonic atom ($\mu - e$ conversion) is one of the cLFV processes. In many theoretical models, such as the SUSY-GUT, predict its branching ratio at experimentally-reachable levels. The COMET experiment (J-PARC E21) [1] was proposed to search the $\mu - e$ conversion with a single event sensitivity of BR($\mu^- Al \rightarrow e^- Al$) $< 10^{-16}$. The experiment was approved as the stage-1 by the J-PARC PAC in July 2009, and many R&Ds are underway to start the experiment as soon as possible.

In the COMET experiment, momenta of converted electrons are measured by a straw tube tracker then total energies of the electrons are measured by an electromagnetic (EM) calorimeter. In order to distinguish converted electrons from background electrons and to get hit timings, a high energy resolution σ_E of < 5 % at 105 MeV and fast time response are required for the EM calorimeter. The detector need to be operated in the Vacuum and strong magnetic field (1 Tesla). In order to fulfill these requirements, an EM calorimeter based on LYSO ($Lu_{1.8}Y_{0.2}SiO_5$) crystals with MPPC (Multi-Pixel Photon Counter) read-out has been proposed. LYSO has large light-yield outputs of 75% compared to NaI and small Moriele radius of 2.3cm. MPPC is a silicon photo multiplier detector, comprised of multi APD pixels operated at Geiger mode by applying low voltages under 100V, which can be operated at room temperature under strong magnetic field in the super-conductive solenoid. MPPCs are recently used or considered to be used in some particle physics experiments, such as in T2K and ILC. These MPPCs are connected to scintillators using a optical fiber. However, In the COMET experiment, a MPPC are connected directly to a crystal to make a crystal calorimeter. This is the first calorimeter which adopt the direct-connection of the MPPC.

We made a simple prototype calorimeter to test this new system, and carried out a beam test with

electron beams at GeV-γ experimental area of the Research Center for Electron Photon Science, Tohoku University, from 14th to 19th December 2009. This report describes results of the beam test.

§2. Beam test for the calorimeter prototype

The beam test aimed to measure light yields of the prototype with electrons of 100 MeV, same energy of the conversion electron. This is important to estimate the number of photons and the energy resolution of the EM calorimeter in a Geant4 based simulation.

The prototype consists of a single LYSO crystal of dimension of 6cm diameter and 20cm long with four MPPCs attached on an end of the crystal. Figure 1 is a picture of the LYSO crystal. Model number of the MPPC is S20362-33-025C of HAMAMATSU Photonics K.K. Its active area is 3mm$\times$3mm, and the number of pixels per MPPC is of 14,400 pixels, as shown in Fig.2. A teflon tape was wound around the crystal except for regions where MPPCs were attached to increase photon collection efficiencies.

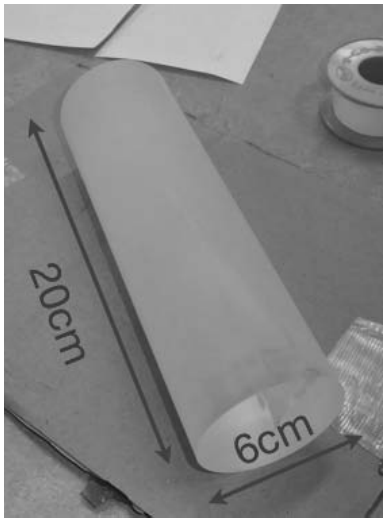

Fig.1. A Picture of the LYSO crystal.

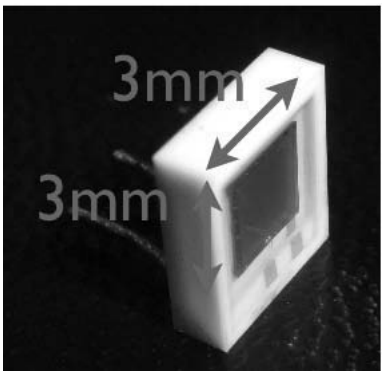

Fig.2. A Picture of the MPPC, S20362-33-025C of HAMAMATSU Photonics K.K., used in the beam test.

The prototype was installed in a light-tight box of dimension of 50cm$\times$50cm$\times$60cm (Figure 3). A trigger counter (10mm$\times$10mm$\times$3mm) was located at the upstream of the crystal. Beam data were taken when both PMTs of the trigger counter had hits in the spill gate and LED data were taken with 10 Hz at the end of spills.

We took data for electron beams energy of 48 MeV, 73 MeV and 100 MeV, as shown in Fig.4. The lower two energies were used to check the linearity of the light yields.

The number of photons was estimated from the measured ADC distribution using a deposit energy distribution calculated by a Geant4 simulation. The number of photons $N_{p.e.}$ is given by

$$N_{p.e.} = E_{ed} \times I \times p_0 \times e^{L/\lambda_I} \times \alpha_{PDE} \quad (1)$$

, where E_{ed} [MeV] is a deposit energy, I (= 33,000 [photon/MeV]) is the number of photons produced by 1 MeV deposit energy, p_0 is a photon collection efficiency (acceptance) of a MPPC, L (= 20 cm) is an average path length of photons to a MPPC, λ_I (= 20.9 cm) is an attenuation length of LYSO and α_{PDE}

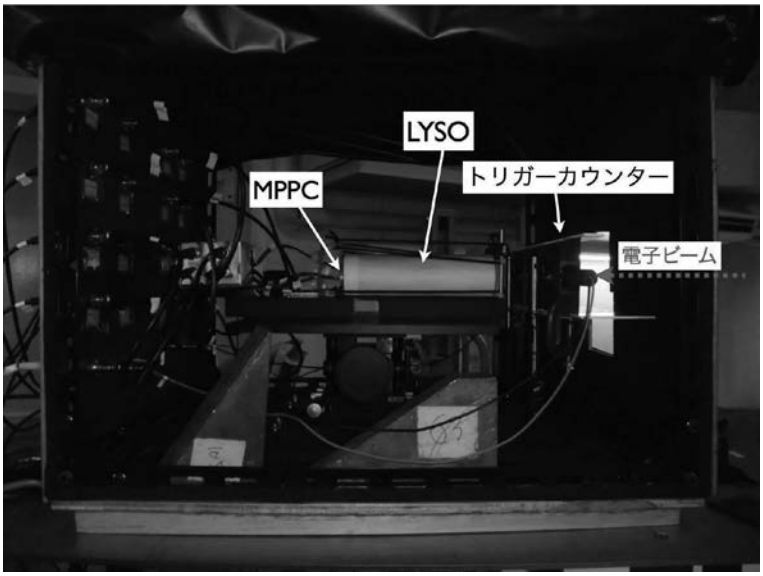

Fig.3. Setup of the beam test. Prototype calorimeter, trigger counters and a LED were installed in the light-tight box.

(= 0.25) is the photo detectiion efficiency of MPPC. And, expected ADC values are calculated by

$$\boldsymbol{ADC_{sim}} = \boldsymbol{f}(\boldsymbol{N_{p.e.}},\sqrt{\boldsymbol{N_{p.e.}}}) \times \boldsymbol{G_{MPPC}} \times \boldsymbol{e} \times \boldsymbol{p_1} \times \boldsymbol{G_{ADC}} \tag{2}$$

, where $\boldsymbol{f}(\boldsymbol{\mu},\boldsymbol{\sigma})$ is the Gaussian distribution, $\boldsymbol{G_{MPPC}}$ (= 2.5×10^5) is a MPPC gain, $\boldsymbol{e}$ (= 1.6×10^{19} [C]) is the elementary electric charge, $\boldsymbol{p_1}$ is an amplifier's gain and $\boldsymbol{G_{ADC}}$ [pC/count] (= 0.25) is a conversion factor of the ADC. The free parameters $\boldsymbol{p_0}$ and $\boldsymbol{p_1}$ were determined by fitting with data and MC so as the $\boldsymbol{\chi^2}$ to be minimum. The $\boldsymbol{\chi^2}$ is defined as

$$\boldsymbol{\chi^2} = \frac{\Sigma(\boldsymbol{ADC_{sim}} - \boldsymbol{ADC_{exp}})^2}{\boldsymbol{\delta^2_{sim}} + \boldsymbol{\delta^2_{exp}}} \tag{3}$$

, where $\boldsymbol{\delta_{sim}}$ and $\boldsymbol{\delta_{exp}}$ are statistic errors at each bin of ADC distribution for the simulation and data, respectively. A measured ADC distribution at 100-MeV electron beams and the calculated number of photons are shown in Figure 5. The number of photons per MPPC $\boldsymbol{N_{p.e.}}$ was determined to be 311 ± 72 for 100 MeV electrons.

§3. Conclusion

We have been developing the EM calorimeter to measure energy of converted electrons for the COMET experiment, the next generation $\mu - e$ conversion search experiment. A calorimeter prototype composed of a single LYSO crystal with MPPC readout was tested with 100-MeV electron beams at Tohoku University. The number of photons per MPPC $\boldsymbol{N_{p.e.}}$ was 311 ± 72 for 100 MeV electrons. From this number, we can estimate performance of the calorimeter and optimize its design with Monte Carlo simulations. A preliminary result of the simulation study, which used the beam test result, showed that an energy resolution of 5% can be achieved by using two $25\mu m \times 25\mu m$-MPPCs at each LYSO crystal segment with a size of ϕ 6 cm $\times$ 20 cm.

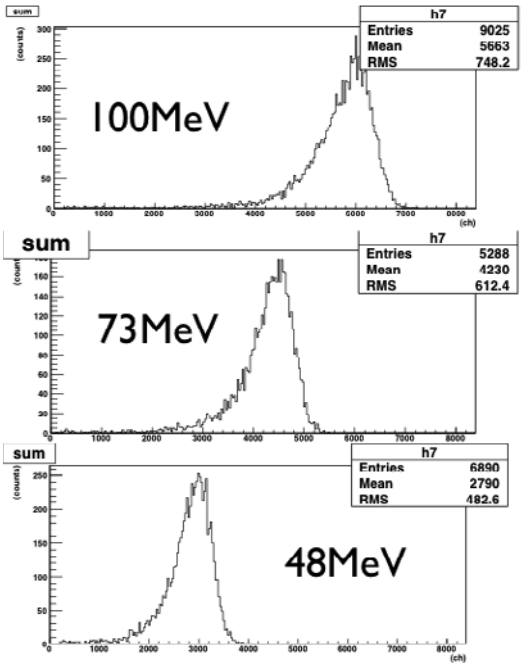

Fig.4. ADC distributions for the electron energy of 100 MeV, 73 MeV, and 48 MeV, respectively. The shape and mean of the ADC distribution showed good agreement with expectations from Monte Carlo simulations.

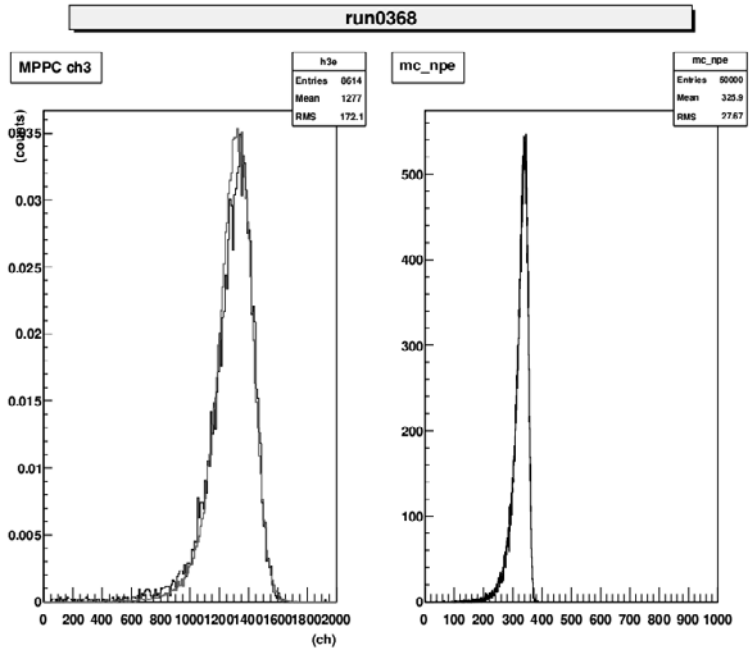

Fig.5. (Left) Measured ADC distribution A_{exp} and fitted ADC distribution A_{sim}. (Right) Number of photons calculated from the ADC distribution

Acknowledgment

We greatly appreciate every support for the experiment from the staffs of the Research Center for Electron Photon Science, in particularly, Prof. T. Ishikawa and Prof. H. Yamazaki.

References

[1] "An Experimental Search for Lepton Flavor Violating $\mu - e$ Conversion at Sensitivity of 10^{-16} with a Slow-Extracted Bunched Proton Beam."

Scintillation characteristics of a $Bi_4Si_3O_{12}$ (BSO) crystal

T. Ishikawa[1], H. Fujimura[1], S. Kaida[1], H. Shimizu[1], Y. Tajima[2], and H.Y. Yoshida[2]

[1]*Laboratory of Nuclear Science (LNS), Tohoku University, Sendai 982-0826, Japan*
[2]*Department of Physics, Yamagata University, Yamagata 990-8560, Japan*

Techniques of growing $Bi_4Si_3O_{12}$ (BSO) crystals have been improved, so that clear and large ones have become available. We have investigated the scintillation characteristics of a newly produced BSO crystal. The excitation-emission spectrum, and the light attenuation length of a BSO crystal are reported.

§1. Introduction

Bismuth silicate $Bi_4Si_3O_{12}$ has been developed as an alternative to BGO, and it is produced by replacing Ge in BGO with Si. Although BSO resembles BGO in physical and optical properties, the decay time of BSO ($\sim$ 100 ns) is much shorter than that of BGO ($\sim$ 300 ns), and it is welcome for constructing electro-magnetic (EM) calorimeters. Techniques of growing BSO crystals have been refined, and clear and large ones have become available. We have investigated the properties of a newly produced BSO crystal from various aspects [1–3].

§2. Excitation-emission spectra

The excitation and emission spectra of BSO were measured with a fluorescence spectrophotometer Hitachi F-4500. The excitation light from a 150 W xenon lamp was selected with a 2.5 nm width slit after analyzing it with diffraction grids. The emission light from the BSO surface was also analyzed with the same condition and was measured with a photo-multiplier tube (PMT).

All the emission spectra were obtained by subtracting background spectra measured without the lamp. The intensity of the lamp and the sensitivity of the PMT as a function of the wavelength were corrected. The second and third harmonics of the excitation light appears when it reflects on the BSO surface and comes into the diffraction grids for the emission light. To reject these harmonics, we used a cut filter Shimadzu UV-39. Fig. 1 shows the emission spectra of a BSO crystal for all the excitation wavelengths.

The measured spectra with UV-39 were corrected by using its transmittance. The emission spectra were obtained by combining the measured spectra with and without UV-39. Fig. 2 shows the intensity correlation of BSO between emission and excitation wavelengths, and Fig. 3 shows the excitation and emission spectra of BSO. The peak excitation wavelength is 285 nm at an emission wavelength of 480 nm, and the peak emission wavelength is $\sim$ 480 nm at an excitation wavelength of 280–290 nm.

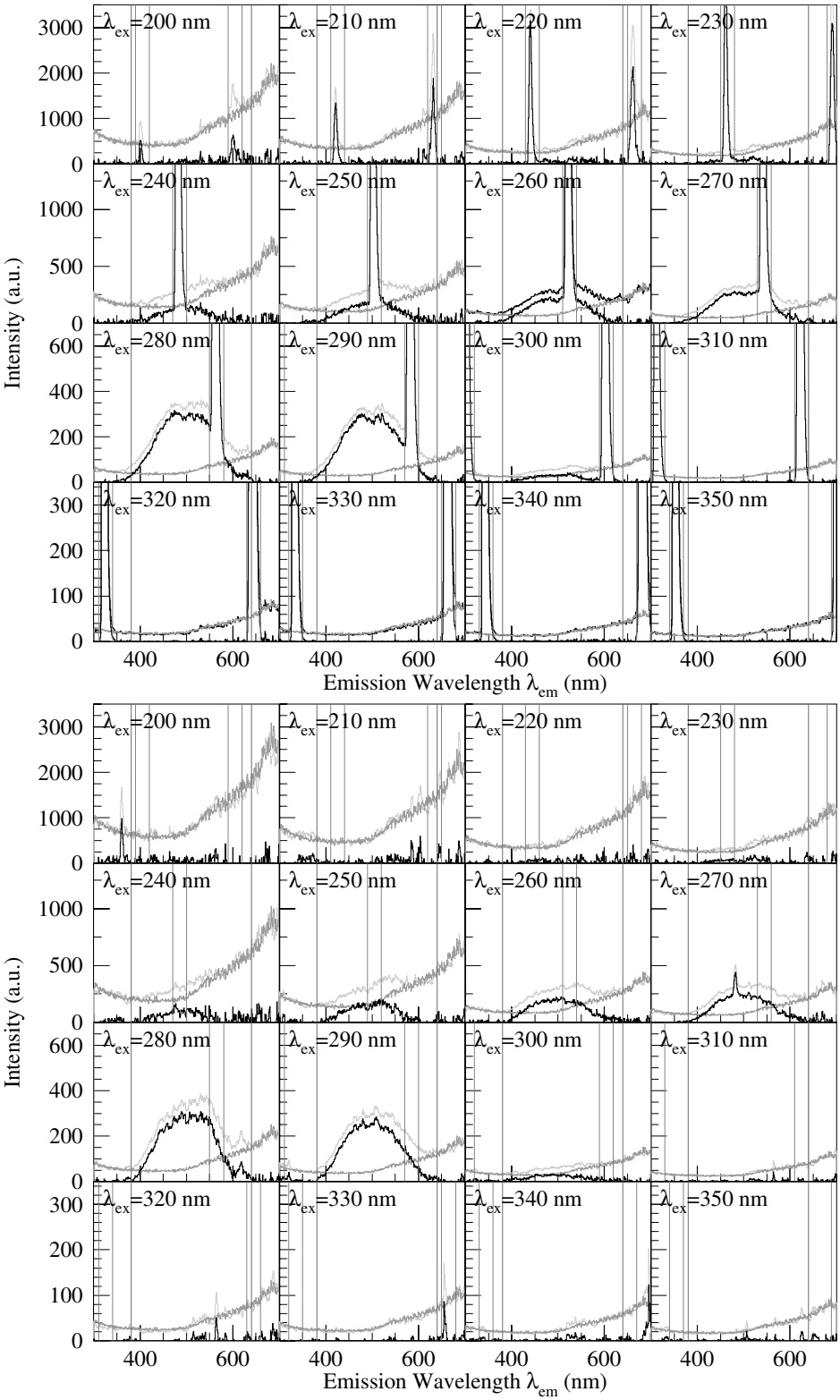

Fig.1. Emission spectra of a BSO crystal for all the excitation wavelengths. The upper panel shows the emission spectra without using the cut filter UV-39, and the lower shows those with UV-39. The excitation wavelength is described in each spectrum. The second and third harmonics of the excitation light disappear by using UV-39. The gray curves show the measured and background spectra, and the black show the background subtracted emission spectra.

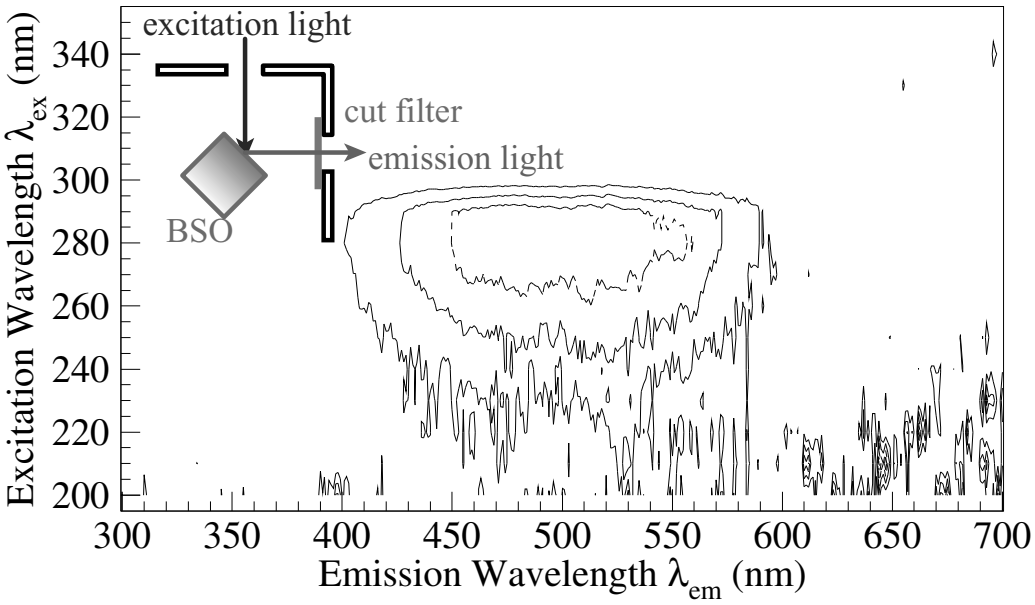

Fig.2. Intensity correlation of BSO between emission and excitation wavelengths. The setup is illustrated in the inset.

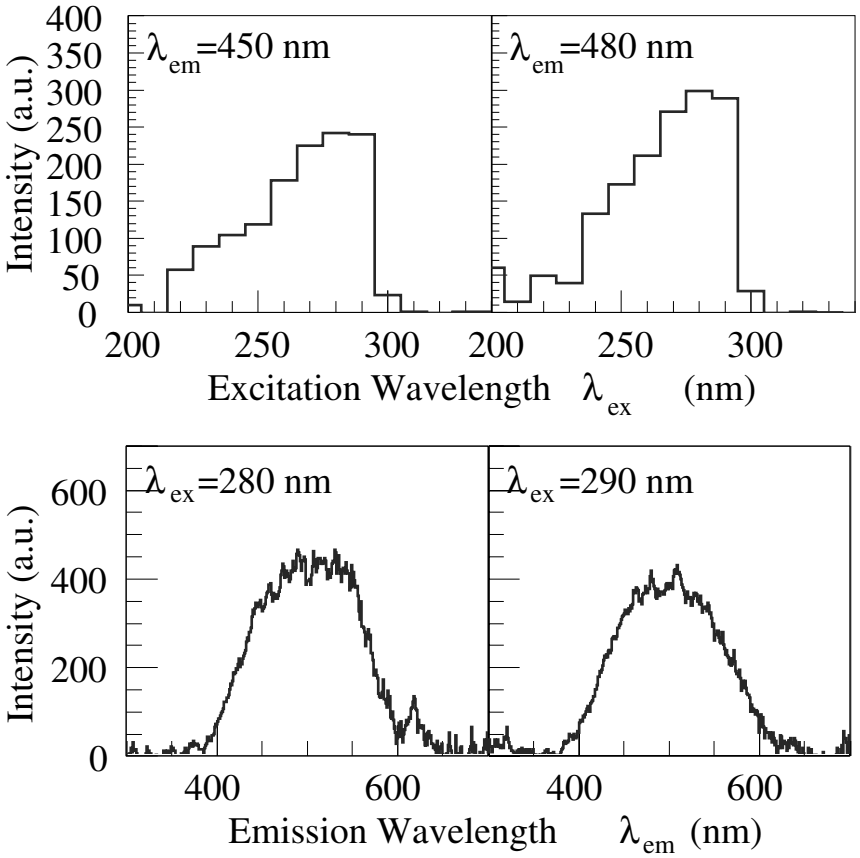

Fig.3. Excitation and emission spectra of BSO. The upper panel shows the excitation spectra at the emission wavelengths of 450 and 480 nm. The lower one shows the emission spectra at the excitation wavelengths of 280 and 290 nm.

The emission spectra of BSO were measured by Kobayashi *et al*. twice. The first measurement was made with a spectro-fluoro-photometer Shimadzu RF-510 [4] and the second one was made with a fluorescence spectrophotometer Hitachi F-4500 [5]. These spectra differ and the present results are similar to the spectra obtained in the first measurement although it has a fake peak at 570 nm due to the instrumental problem. It seems that the background spectra which can be obtained without the lamp have not been subtracted in the second measurement. The details of the analysis are described elsewhere [7].

§3. Light attenuation length

The light attenuation length is an important parameter for an EM calorimeter module. We have estimated it from the measured transmittance of a BSO crystal with a finite length according to Ref. [8].

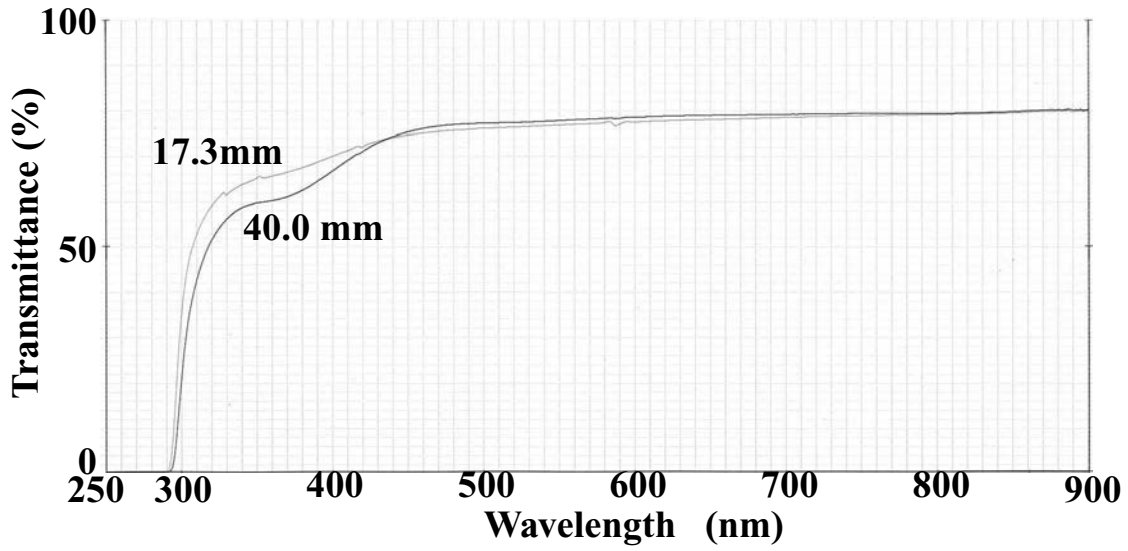

Fig.4. Transmittance of BSO crystals with thicknesses of 17.3 and 40.0 mm as a function of the wavelength of the incident light.

The reflectance of the perpendicularly incident light at a surface is described as

$$R = \left(\frac{n-1}{n+1} \right)^2 \tag{1}$$

where n denotes the refractive index of BSO, and the transmittance at the surface is given as

$$T = 1 - R. \tag{2}$$

The light intensity after traveling a length l becomes

$$\alpha = \exp\left(-l/L_{\mathrm{att}}\right) \tag{3}$$

for a crystal with a light attenuation length of L_{att}. Therefore, the transmittance of a crystal with a length of l is calculated as

$$T_l = T\alpha \left\{ \sum_{n=0}^{\infty} (R\alpha)^{2n} \right\} T = \frac{\alpha(1-R)^2}{1-R^2\alpha^2} \tag{4}$$

by taking into account multiple bounces between two ends and the light attenuation loss in BSO.

The transmittance of BSO crystals with thicknesses of 17.3 and 40.0 mm was measured with a spectrophotometer Shimadzu UV-230. Fig. 4 shows the measured transmittance as a function of the wavelength of the incident light. The transmittance of the 40.0 mm thick BSO crystal is 10% lower than that of the 17.3 mm one at the wavelength from 300 to 400 nm, suggesting the light attenuation length is shorter at these wavelengths.

The light attenuation length has been estimated from Eq. (4) by using the refractive index as a function of the wavelength given in Ref. [9]. Fig. 5 shows the light attenuation length of the BSO crystals. It is shorter than 30 cm at the wavelength from 300 to 400 nm, and is enough longer at the longer wavelengths. The details of the analysis are described elsewhere [10].

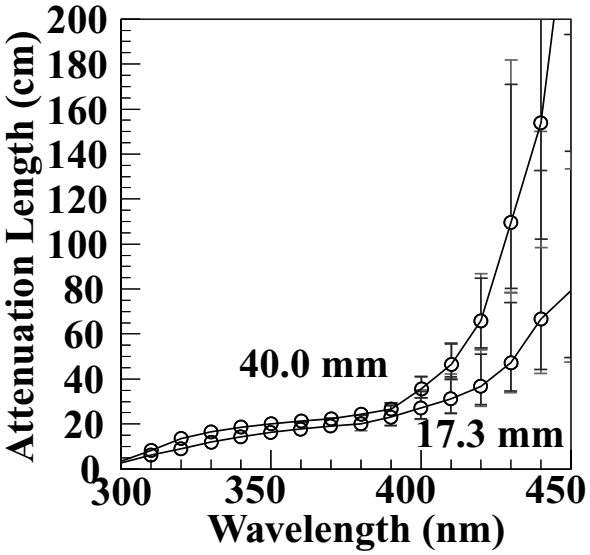

Fig.5. Light attenuation length of BSO crystals determined from the crystals with thicknesses of 17.3 and 40.0 mm.

§4. Summary

The scintillation characteristics of a BSO crystal have been investigated. The peak excitation and emission wavelengths are 285 and 480 nm, respectively. The light attenuation length is shorter than 30 cm at the wavelength from 300 to 400 nm, and is enough longer at the longer wavelengths.

Acknowledgement

This work was supported in part by Grant-in-Aid for Scientific Research (B) (17340063) and for Specially promoted Research (19002003).

References

[1] S. Kuwasaki, T. Ishikawa *et al.*: Research Report of LNS **41**, Tohoku University, 11 (2009).

[2] H. Shimizu, et al., Nucl. Instr. and Meth. in Phys. Res. 550 (2005) 258.

[3] M. Sato, T. Ishikawa *et al.*: in this Research Report of LNS, Tohoku University.

[4] M. Kobayashi, et al., Nucl. Instr. and Meth. 205 (1983) 133.

[5] M. Kobayashi, et al., Nucl. Instr. and Meth. in Phys. Res. A 372 (1996) 45.

[6] M. Kobayashi, et al., Nucl. Instr. and Meth. in Phys. Res. A 400 (1997) 392.

[7] T. Ishikawa: Internal GeV-γ Analysis Note No. **131***D* (2009).

[8] D.A. Ma and R.Y. Zhu, Nucl. Instr. and Meth. in Phys. Res. 333 (1993) 422.

[9] M.V. Lalic and S.O. Souza, Opt. Mater. 30 (2008) 1189.

[10] S. Kaida: Internal GeV-γ Analysis Note No. **156***D* (2009).

(LNS Experiment : #2577)

Erratum: Energy Resolution of a Prototype EM Calorimeter with BSO Crystals [Research Report of LNS **41**, 11 (2008)]

T. Ishikawa[1], R. Hashimoto[1], J. Kasagi[1], S. Kuwasaki[1], Y. Okada[1], M. Sato[1], H. Shimizu[1], K. Suzuki[1], and H. Yamazaki[1]

[1]*Laboratory of Nuclear Science (LNS), Tohoku University, Sendai 982-0826, Japan*

We found a bug in the fitting procedure of the ADC distribution with a logarithmic Gaussian. The energy resolution of the BSO calorimter reported is higher than it is.

§1. Logarithmic Gaussian

The logarithmic Gaussian which incorporates the asymmetry [1] is described as

$$G_L(x) = N \exp\left[-\frac{1}{2\sigma_L^2}\left\{\log\left(1-\frac{x-\mu}{\sigma_E}\eta\right)\right\}^2 - \frac{\sigma_L^2}{2}\right], \tag{1}$$

where N is the normalization factor, μ is the mean, σ_E is the experimental resolution, and η is the asymmetry. The σ_L is expressed by the asymmetry as

$$\sigma_L = \frac{2}{\xi}\sinh^{-1}\frac{\eta\xi}{2}, \tag{2}$$

where ξ is a constant $2\sqrt{\log 4}$. The limit of the logarithmic Gaussian at $\eta = 0$ is a nominal Gaussian.

The fitting procedure with a logarithmic Gaussian in Ref. [2] omitted $2/\xi$ in Eq. (2), and

$$\sigma_L = \sinh^{-1}\frac{\eta\xi}{2} \tag{3}$$

was mistakenly adopted. Thus, the ratio of the width to the mean reported in Ref. [2] is about $\xi/2 = 1.177$ times as large as it is.

§2. Energy Resolution

The measured energy distirbutions were fitted with a logarithmic Gaussian correctly, and the mean and width were obtained. Fig. 1 shows the re-analyzed width-mean ratio σ/μ and energy resolution σ_E/E.

The energy resolution σ_E/E as a function of the incident energy E_i was fitted with

$$\frac{\sigma_E}{E}(E_i) = \left\{\left(\frac{0.000\pm0.118}{E_i}\right)^2 + \left(\frac{1.786\pm0.016}{\sqrt{E_i}}\right)^2 + (1.306\pm0.044)^2\right\}^{1/2}, \tag{4}$$

where the units of the resolution and E_i are % and GeV, respectively. The energy resolution for 1 GeV positrons corresponds to 2.04%. The details of re-analysis are described elsewhere [3]. In Ref. [3], the energy resolutions estimated for the various incident positions to discuss the crystal boundary effects.

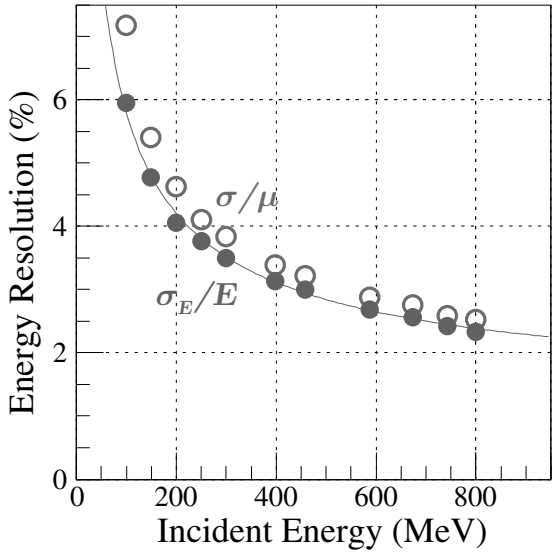

Fig.1. Energy resolution as a function of the incident positron energy. The open circles show σ/μ and the filled ones show σ_E/E. The data points for σ_E/E are compared with the fitted function (4).

References

[1] H. Ikeda, et al: Nucl. Instr. and Meth. A **441**, 401 (2000).

[2] S. Kuwasaki, T. Ishikawa *et al.*: Research Report of LNS **41**, Tohoku University, 11 (2009).

[3] T. Ishikawa: Internal GeV-γ Analysis Note No. **129$\mathcal{D}$** (2009).

Ⅱ. Radiochemistry

(LNS Experiment : #2627, #2643, #2665, #2683)

光量子放射化分析法による大気浮遊粒子中の炭素の定量 (II)

大浦泰嗣, 鈴木智誠, 海老原充

首都大学東京大学院理工学研究科 (192-0397 東京都八王子市南大沢 1-1)

Photon Activation Analysis of Carbon in Atmospheric Suspended Particulate Matters (II)

Yasuji Oura, Tomonori Suzuki, and Mitsuru Ebihara

Graduate School of Science and Engineering, Tokyo Metropolitan University,1-1 Minami-Ohsawa, Hachiouji, Tokyo 192-0397

Total carbon contents in atmospheric suspended particulate matters, PM_{10} and $PM_{2.5}$, collected at Hachioji, Tokyo from 2003 to 2009 were determined nondestructively by instrumental photon activation analysis. Particulate concentrations and carbon concentrations for 7 years were observed to be roughly constant. And all $PM_{2.5}$ particulate concentration values were larger than environmental quality standard value. The concentration values in this work were compared with those obtained by Tokyo metropolitan government.

§1. はじめに

大気中には様々な起源を持つ粒径の異なる粒子が多数漂っているが，空気動力学径 10μm 以下の粒子 (PM_{10})，中でも特に 2.5μm 以下の粒子 ($PM_{2.5}$) は，呼吸により肺の奥深くまで吸い込まれ，健康に重大な害を及ぼす可能性があるため，その特性や動態に高い関心が持たれている．大気中に浮遊する粒子の環境基準は，これまで PM_{10} 粒子に対してのみ規定されていたが，2009 年に $PM_{2.5}$ 粒子に対する環境基準も設定された．我々は 2002 年より PM_{10} 粒子を，2005 年より PM_{10} に加えて $PM_{2.5}$ 粒子を捕集し，その元素組成を中性子放射化分析法 (NAA) にて調べてきた．しかしながら，浮遊粒子の主要元素の一つで，自動車からの排出粒子がその主な起源の一つであると考えられる炭素は，NAA では定量できないため，光量子放射化分析法により浮遊粒子中の炭素濃度定量してきた [1, 2]．本稿では 2009 年まで採取した試料についての炭素濃度を報告する．

§2. 実　　験

PM_{10} ならびに $PM_{2.5}$ 粒子の採取は，首都大学東京南大沢キャンパス 8 号館屋上にて毎月行った．流量 16.7 L/min にて大気を石英製フィルタ (QMA，Whatman) を通して約 2〜5 日間ポンプで吸引して粒子を捕集した [2]．PM_{10} は隔週で，PM_{10} と $PM_{2.5}$ の同時採取は月に 1 度行った．

採集された粒子の質量を秤量後，直径 10mm の円盤状に 2 枚切り出し，粒子捕集面を向き合わせて Al

箔で包み，照射用試料とした．炭素定量用の比較標準試料として Al 箔で包んだ直径 10mm の炭素板 (約 2mg) を用いた．これらをスタック状にしてフラックス補正用金箔とともに石英管に封入し，最大エネルギー 25MeV の制動放射線で 20 分間照射した．照射後，ただちに γ 線の測定を行い，その後約半日の間に測定を繰り返し行った [1, 2].

§3．結果と考察

2003 年から 2009 年 10 月までに採取した PM_{10} 粒子の粒子濃度と炭素濃度の採取年ごとの箱ヒゲ図を第 1 図に示す．7 年の間，粒子濃度に大きな変化はなく，粒子濃度の 1 年中央値は 26〜32$\mu g/m^3$ でほぼ一定であり，環境基準を満たしている．2003 年以降で黄砂が観測された日数が最も多かったのは，2006 年であった．2006 年に観測された高濃度の試料 (図中の○) の採取日 (4 月 18-19 日, 5 月 1 日) には，全国で黄砂が観測されており，この高濃度は黄砂の影響と考えられる．PM_{10} 粒子の炭素濃度は，1 年中央値として 4.9〜7.9$\mu g/m^3$ であり，重量ベースでは PM_{10} 粒子の約 20%を炭素が占めた．粒子濃度と同様に 7 年間大きな変化は見られなかったが，2008 年 (中央値: 4.9 $\mu g/m^3$) と 2009 年 (中央値: 5.6 $\mu g/m^3$) は 2007 年までと比較して，少し炭素濃度が減少した．粒子濃度の場合とは異なり，2006 年に見られる高濃度試料は黄砂の影響ではない．黄砂の影響が見られた試料での PM_{10} 粒子中の炭素の重量濃度は約 8%と小さく，黄砂による微小粒子は炭素成分の主要な起源でないことがわかる．

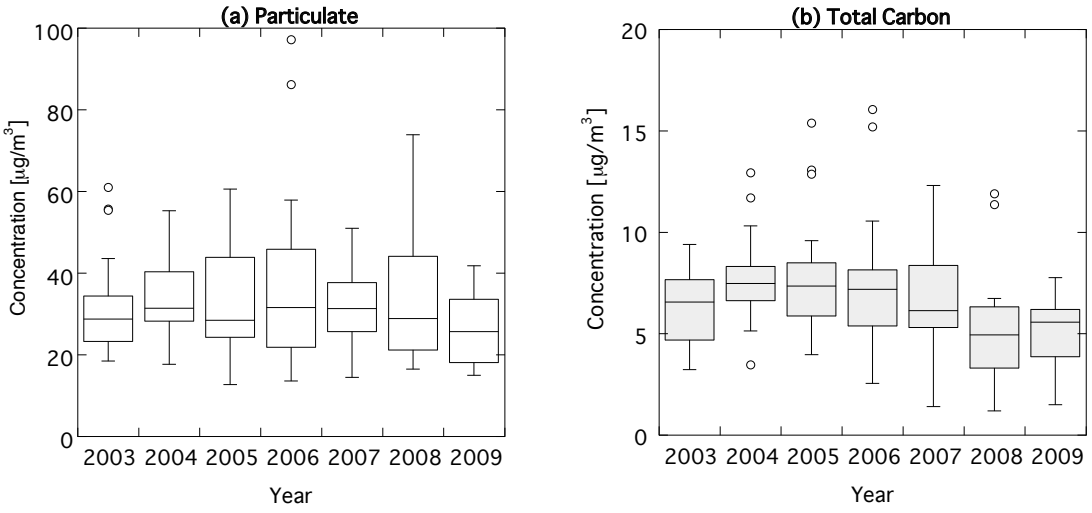

第 1 図　2003 年から 2009 年に八王子市で採取した PM_{10} 粒子の (a) 粒子濃度と (b) 全炭素濃度の箱ヒゲ図．2009 年は 11 月と 12 月の採取は無し．

第 2 図に 2007 年から 2009 年 10 月までに採集した $PM_{2.5}$ 粒子の濃度を PM_{10} 粒子と同様に示す．粒子濃度は 3 年間でほぼ一定 (1 年中央値: 15〜18$\mu g/m^3$) であり，炭素濃度も同様 (1 年中央値: 3.4〜4,5$\mu g/m^3$) であったが，2007 年から減少傾向にあるようにも見える．新しく設定された $PM_{2.5}$ 粒子の環境基準は,「1 年平均値が 15$\mu g/m^3$ 以下であり、かつ、1 日平均値が 35$\mu g/m^3$ 以下」である．1 日平均値は測定していないが，本研究での採集期間 (2〜5 日間) での粒子濃度から考えると，おそらく 1 日平均値は基準を達成していると思われる．しかしながら，1 年平均値はすべての年において基準値を上回った.

粒子濃度と炭素濃度における $PM_{2.5}$ と PM_{10} 粒子間の相関を第 3 図に示した．PM_{10} と $PM_{2.5}$ の粒子濃

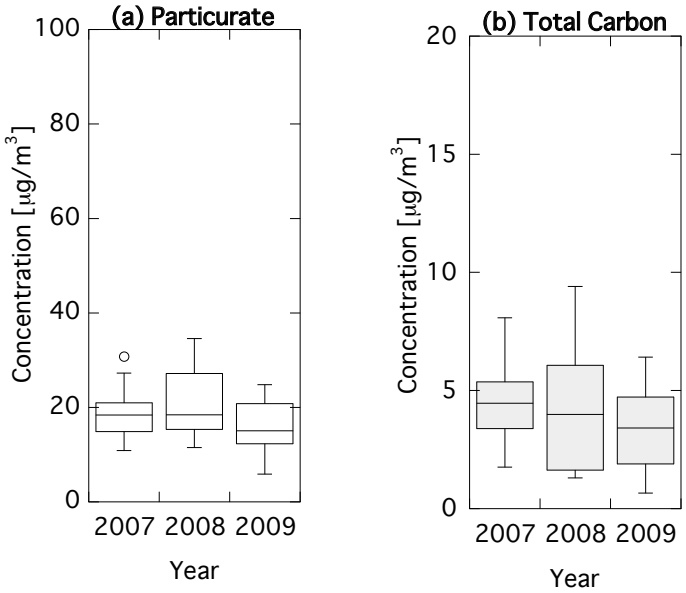

第 2 図　2007 年から 2009 年に八王子市で採取した $PM_{2.5}$ 粒子の (a) 粒子濃度と (b) 全炭素濃度の箱ヒゲ図．2009 年は 11 月と 12 月の採取は無し．

度には良い相関が観測された．PM_{10} 粒子質量のおよそ 65%が $PM_{2.5}$ 粒子の寄与であり，1 年を通してほぼ同じ割合であった．一方，炭素濃度においても，粒子濃度よりもばらつきは大きいが，PM_{10} と $PM_{2.5}$ の間に相関が見られ，PM_{10} 粒子の炭素の約 80%が $PM_{2.5}$ の寄与であった．残り 20%は，PM_{10} 粒子の中で $PM_{2.5}$ よりも粒径の大きな粒子の寄与となる．人為起源に由来する元素は，粒径の小さい粒子に濃集することが多いので，炭素は主に人為起源であると推測される．

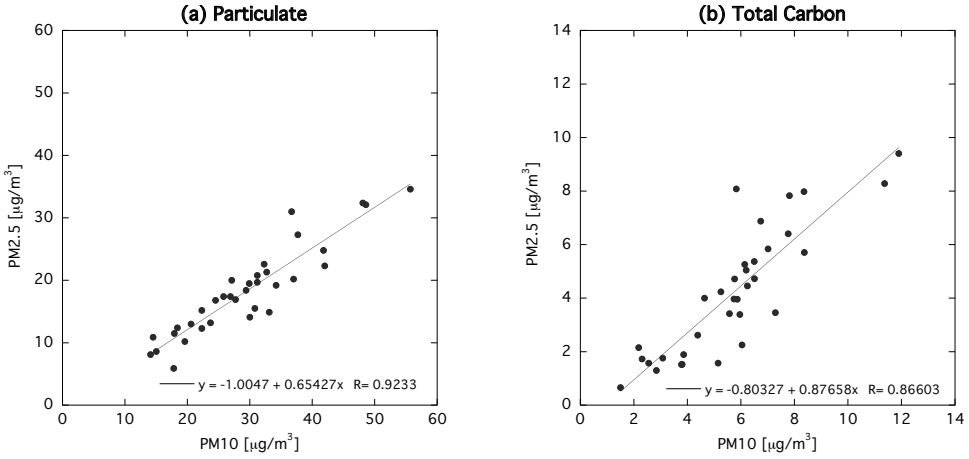

第 3 図　PM_{10} 濃度と $PM_{2.5}$ 濃度の比較．(a) 粒子濃度の相関．(b) 全炭素濃度の相関．

東京都は 2008 年度に微小粒子状物質検討会を設置し，都心部や郊外の複数の地点において季節ごとに $PM_{2.5}$ 粒子を採取し，その実態を調査した．採取方法や採取期間が異なるので直接比較は難しいが，比較可能な採取期間での本研究の結果と東京都の調査結果を第 1 表にまとめた．東京都調査結果は，本研究での採取地点に最も近い多摩市にて採取された $PM_{2.5}$ によるものである．東京都調査は 24 時間ごとの計測

のため，粒子濃度として採取期間の平均値を採用した．また，有機炭素 (OC) と元素状炭素 (EC) の分別定量のため，採取期間における OC 濃度と EC 濃度の和として炭素濃度を示した．第 1 表より明らかな通り，本研究と東京都の調査の結果はよく一致しているといえる．本研究における 2007 年に採取した PM_{10} と $PM_{2.5}$ 粒子中の EC と OC の分別定量結果を以前本誌で報告した [2]．$PM_{2.5}$ 粒子での OC/EC 比は，0.85〜2.2 であった．東京都による報告では 2〜4 であり，本研究で得られた OC/EC 比は小さかった．本研究では，350 ℃で加熱した試料の分析から得た EC 濃度と，加熱処理無しの試料から得た全炭素濃度との差から OC を求めた．OC が 350 ℃ですべて揮発しておらず，EC が系統的に高めに定量されていた可能性がある．また，東京都は，2008 年度における都心部を含む複数の一般大気観測局での SPM(粒径 10μm 以下の粒子．PM_{10} と若干粒径分布が異なる) と $PM_{2.5}$ 粒子の相関から，$PM_{2.5}$ 粒子の質量は SPM 質量の約 70%と報告した [3]．第 3 図に示した通り，本研究での観測結果は 65%であり，これと矛盾しなかった．これらより，東京都心と郊外である多摩ニュータウン地域で大気中の $PM_{2.5}$ 環境に大きな差はないことがわかる．$PM_{2.5}/PM_{10}$ 比より，$PM_{2.5}$ の環境基準を満たす場合の PM_{10} 濃度は，21$\mu g/m^3$ 以下と見積もることができる．2003 年から実施されたディーゼル車規制により都心部では，毎年 SPM 濃度が減少し，現在ではほとんどの観測局で SPM の環境基準が達成されている．しかし，八王子では，2003 年以降も PM_{10} 粒子濃度の減少は観測されず，約 30$\mu g/m^3$ でほぼ横ばい状態である．$PM_{2.5}$ の環境基準をクリアするには，$PM_{2.5}$ 粒子の発生起源を明らかにして，それぞれ対策を講じないと困難ではないだろうか．

第 1 表　東京都による PM2.5 粒子調査結果との比較．本研究は八王子市，東京都は多摩市において採取．

採取期間	粒子濃度, $\mu g/m^3$		炭素成分, %	
	本研究	東京都調査[a]	本研究[b]	東京都調査[c]
2008/5/20 - 23	32	26	29	28 (4)
2008/8/5 - 8	20	19	24	25 (2)
2008/11/5 -7	35	30	20	32 (2)

[a]24 時間ごとの粒子濃度の平均値.
[b]全炭素濃度.
[c]有機炭素 (OC) 濃度と元素状炭素 (EC) 濃度の和．24 時間ごとの濃度の平均値．( ) 内は，OC/EC 比.

謝　辞

本研究を行うにあたり良質な電子ビームを供給していただいた東北大学原子核理学研究施設マシングループの方々と試料照射ならびに放射線測定でお世話になった大槻勤准教授と廣瀬健太郎博士に深く感謝する．また，ガンマ線測定を手伝っていただいた首都大学東京宇宙化学研究室の渡部良氏と浜中芳文氏に感謝する．

参　考　文　献

[1]　大浦他：核理研報告 37 (2004) 67.
[2]　大浦他：核理研報告 41 (2008) 71.
[3]　東京都環境局：平成 20 年度微小粒子状物質 ($PM_{2.5}$) 等大気環境調査結果報告書 (2008).

(LNS Experiment : #2628, #2646, #2667, #2687)

Half-life Measurement of ^{7}Be in Host Metals

T. Ohtsuki and K. Hirose

Research Center for Electron Photon Science, Tohoku University, Sendai, 982-0826

In order to see how the decay rate is changed by artificially, we have measured the half-life of ^{7}Be in beryllium(Be) metal at room temperature (T=293 K) and at close to the temperature of liquid helium (T=5 K). We found that the half-life of ^{7}Be in Be metal at T=293 K is 53.25$\pm$0.04 days, which is slightly longer than those in the hosts of graphite, lithium fluoride and other minerals, surveyed so far. Furthermore, that at T=5 K is 53.39 $\pm$0.04 days, which is 0.26% longer than that at T =293 K.

§1. Introduction

In one of the β-decay modes, the electron-capture (EC) decay rate depends on the density of atomic electrons within the nucleus as first suggested by Segr'e *et al.* [1]. Therefore, some studies have reported on how external factors, such as chemical form [2], host metal [3], pressure [4], and even temperature [5] alter the decay rate(half-life).

Recently, we have produced several radioactive fullerenes [6–8], such as the ^{7}Be endohedral C_{60} (^{7}Be@C_{60}) and ^{7}Be in Be metal (Be metal(^{7}Be)). We have measured the half-life of ^{7}Be in the sample of ^{7}Be@C_{60} and Be metal(^{7}Be) by using a reference method and standard clock time. It was revealed that the half-life of ^{7}Be inside C_{60} at T=5K was almost 1.5% shorter than that in Be metal at room temperature [5, 9]. This implied that the ^{7}Be atoms are located in a unique environment inside C_{60}. This large change in the half-life is firmly caused by the electron density at the nucleus position and the magnitude of the change has also been explained theoretically [10].

Because of the uniform lattice structure (*hcp*) included ^{7}Be in Be metal(^{7}Be), the EC decay rate of the ^{7}Be nucleus in the structure is also essentially intriguing and should be surveyed in order to compare any other situations in chemical forms, pressure, and even temperature. In the present study, we have measured the half-life of ^{7}Be in Be metal(^{7}Be) at both room temperature (T=293 K) and close to the temperature of liquid helium (T=5 K) by using a reference method. We compare the half-life of ^{7}Be in Be metal(^{7}Be) at T=293 K and 5 K, as well as in other materials.

§2. Experimental Procedure

Be metal (*hcp* lattice structure) 10 mm in diameter and 0.3 mm in thickness was utilized to produce ^{7}Be uniformly in the Be metal. After being washed with weak HCl solution, the Be metal was sealed in a quartz tube (vacuum packed) that was 12 mm in diameter as a target. Irradiation with a bremsstrahlung (generated by 50 MeV electrons) was carried out at the Electron Linear Accelerator,

Laboratory of Nuclear Science, Tohoku University. The experimental setup for the irradiation is shown in Fig. 2. The sample in a quartz tube was set in the middle of a sweep magnet placed on the axis of the electron beam. A platinum plate converter 2 mm in thickness was set in front of the sweep magnet in order to generate a bremsstrahlung. Then, the sample was irradiated only by the bremsstrahlung,

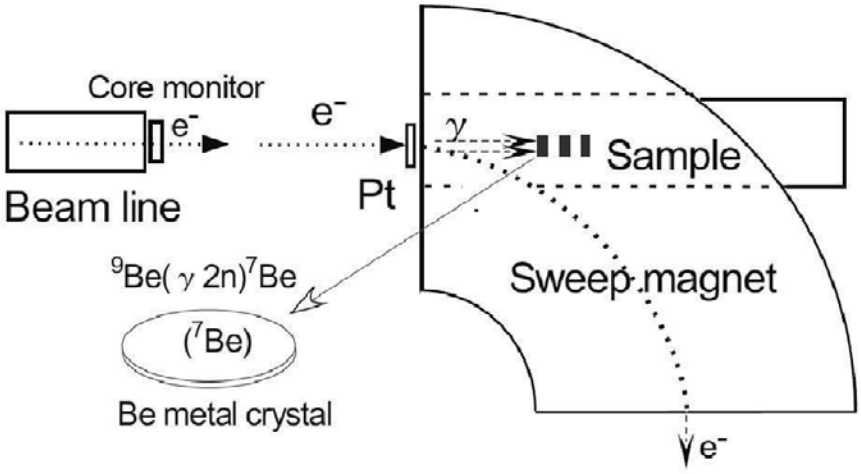

Fig.1. Setup for irradiation of Be metal using the Electron Linear Accelerator at Tohoku University.

and all the electrons were ruled out by the magnetic field (see Fig. 2). Therefore, the damage to the lattice of Be metal was confined to the minimum. ^{7}Be can be produced in Be metal uniformly by the photonuclear reaction ^{9}Be$(\gamma, 2n)^{7}$Be. After irradiation, the sample was baked in an electric oven with vacuum packing at 1150 degrees C for a few hours to recover the lattice defect even if the defect occurs by nuclear reactions. Finally, the sample was washed again with weak HCl solution to clean the surface.

Two samples of Be metal(^{7}Be) were prepared in the present experiment. To measure the half-life at T=293 K and 5 K, one sample of Be metal(^{7}Be) was placed at the top of a helium (He) closed-cycle cryostat, and the other was placed at the top of a sample holder, in an automated sample changer, respectively. The samples could then be moved precisely in front of a γ-ray detector. This allowed the decay rates of the two samples to be measured in a comparable way. The activities of the 478 keV γ-rays emanating from ^{7}Be were measured with a high-purity germanium (HPGe) detector coupled to a 4096-channel pulse-height analyzer. Due to the excellent energy resolution of the HPGe-detector, a good signal-to-noise ratio was obtained. The background was reduced by a lead shield. Therefore, the background peaks did not impair the determination of the half-life of ^{7}Be in the present experiment. The radioactivities of ^{7}Be were uniquely detected by means of its characteristic γ-rays, and any other sources were ruled out. Here, we set the measurement duration to T_d=21600 seconds (21480 seconds for the live measurement time and 120 seconds for the dead time of the measurement system plus the sample exchange time) for one data point. The total measuring time was 166 days, which is more than three half-lives of ^{7}Be. The start time was taken from a time standard signal distributed via a long-wave radio center in Japan. Therefore, the uncertainty in the time measurements can be neglected.

Furthermore, the low-temperature and room-temperature samples were alternatively measured each for approximately 6 hours by turns. Therefore the systematic uncertainties are properly reduced in the measurements.

§3. Results and Discussion

A typical γ-ray spectrum obtained in the sample of Be metal(^{7}Be) at T=293 K is shown in Fig. 3. The decay scheme of ^{7}Be is also shown in the figure. The expected γ line at E_γ=478 keV and the natural

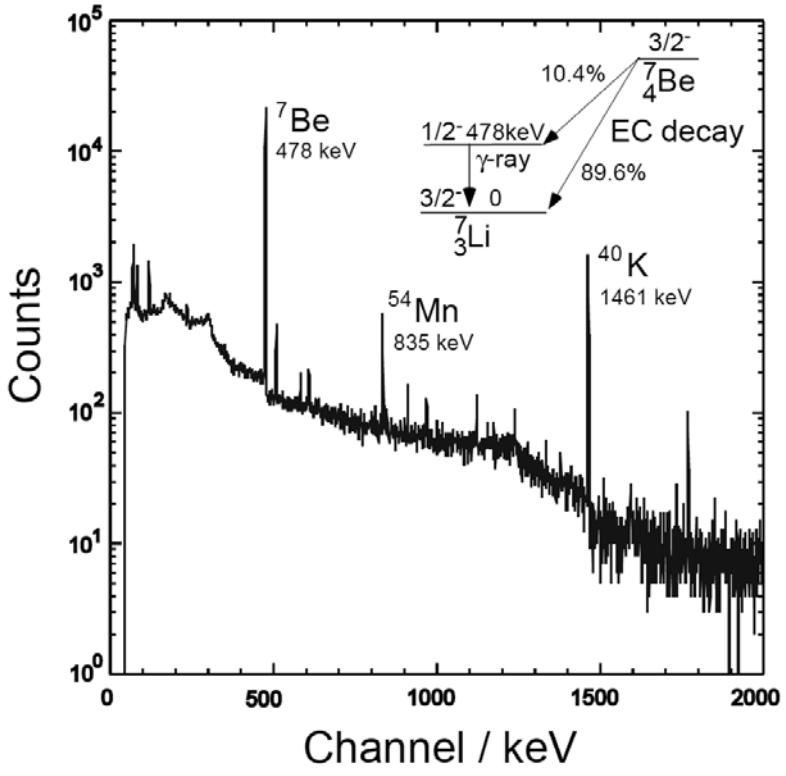

Fig.2. Typical γ-ray spectrum for the^{7}Be in the sample of Be metal(^{7}Be) and decay scheme of ^{7}Be nucleus.

background of ^{40}K γ line at E_γ=1461 keV can be seen as two giant peaks. No peaks were seen at around E_γ=478 keV when the ^{7}Be source was absent. The exponential decay curve of the ^{7}Be activities for the sample of Be metal(^{7}Be) at T=293 K is also shown as a function of time (days) in Fig. 3. The decay curve obtained in the present measurement was fitted including statistical errors by a Minuit program distributed from the CERN Program Library. The statistical error dominates the uncertainty in each data point in Fig. 3. The uncertainty of our measurement is given by the uncertainty of the exponential line fitted to the counts (*i.e.* counts per second) of the decay spectrum. The change in the dead time in the data acquisition system is evaluated to be about 815 sec for all running case. Therefore, the uncertainty due to the dead time is estimated to be less than 0.04% and this value is smaller than the fitting errors of the half-life of ^{7}Be. For the sample of Be metal(^{7}Be) at T=293 K, the half-life was also obtained not only for this run but also as a reference run for that of ^{7}Be in the sample of ^{7}Be@C_{60}. Therefore, the averaged half-life of $T_{1/2}$=53.25$\pm$0.04 days was precisely determined for the sample of Be metal(^{7}Be) at T=293 K.

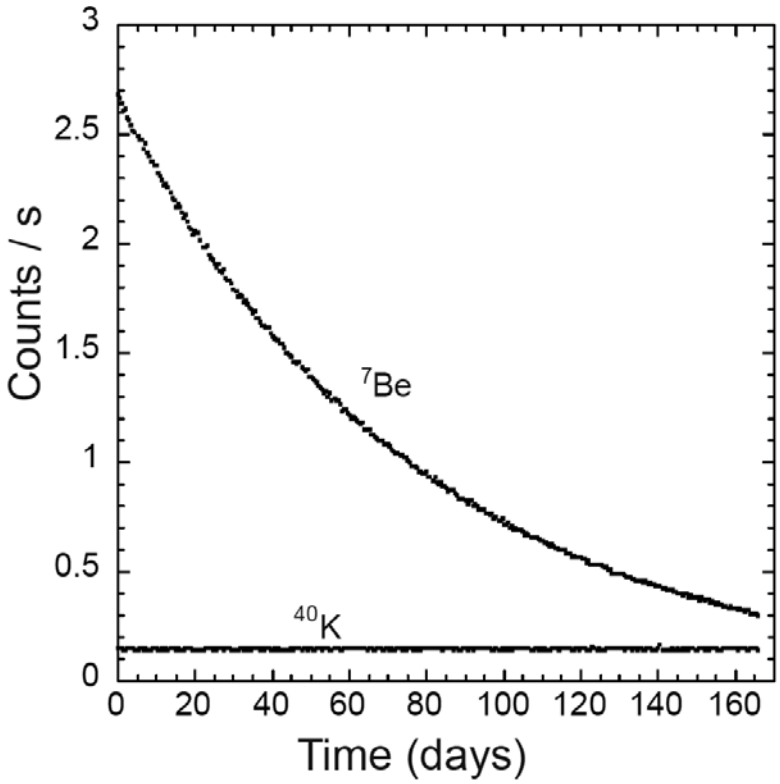

Fig.3. Exponential decay line of ^{7}Be in a sample of Be metal(^{7}Be). Background count rate of radioactivities for ^{40}K are also shown.

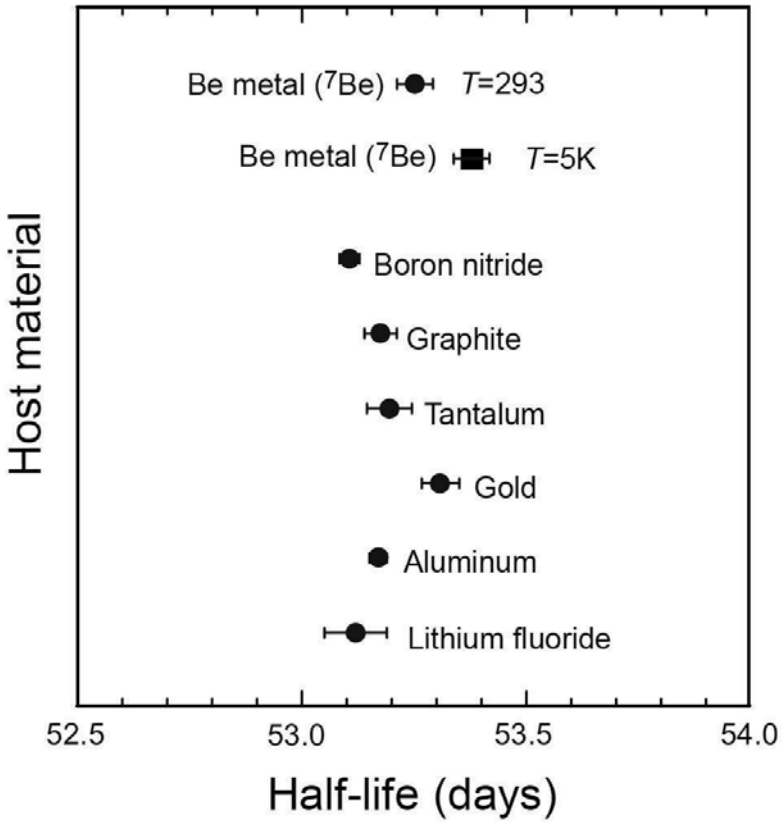

Fig.4. Half-life values of ^{7}Be in Be metal(^{7}Be) as determined with a least-squared fit (solid circle for T=293 K and solid square is for T=5 K). Half-lives previously measured are also shown for comparison [3].

In the sample of Be metal(^{7}Be) at T=5 K, a half-life of $T_{1/2}$= 53.39±0.04 days was obtained in the present experiment. The counting rates of the natural background emanating from ^{40}K (the 1461 keV γ-rays) are also shown in Fig. 3. The obtained value in counts/s for ^{40}K was also fitted using the same procedures. It was found that the fitted line infinitely corresponds to a horizontal line. This also secures the reliability of our measurements.

In the present study, the half-lives of ^{7}Be in the samples of Be metal(^{7}Be) at both T=293 K and 5 K were determined as $T_{1/2}$=53.25±0.04 days and $T_{1/2}$= 53.39±0.04 days, respectively, as seen in Fig. 3. The observed change is 0.14±0.06 days. This difference is almost a one sigma. The half-life values obtained for ^{7}Be in several other host materials such as graphite and boron nitride have been reported so far [3]. In Fig. 3, the half-lives previously measured are also plotted as a comparison. The values stay in the range of about 53.1-53.3 days. We find that the half-life value of ^{7}Be in Be metal(^{7}Be) by the measurement at T=293 K may be almost in agreement with the available data, but can be slightly longer than the value for graphite, boron nitride etc. Furthermore, the figure clearly shows that the half-life of ^{7}Be in the Be metal(^{7}Be) at T=5 K is 0.26% longer than that in the Be metal(^{7}Be) at T=293 K, and is also longer than any ^{7}Be half-life in metals reported in any environment up to now. We suppose that this can be due to the temperature dependence of a lattice constant in the structure (*hcp*) of Be metal. We are investigating this by theoretical calculations.

Acknowledgements

We thank the operators of the Linear Accelerator of Laboratory of Nuclear Science , Tohoku University. This work was supported by Grants-in-Aid for Co-operative Research Nos. 10640535, 12640532 and 17350024 from the Ministry of Education, Culture, Sports, Science, and Technology of Japan, by the REIMEI Research Resources of JAERI, and especially by the MITSUBISHI fund in 2006.

References

[1] E. Segr'e,: Phys. Rev. **71** (1947) 274.

[2] H.W. Johlige, D.C. Aumann, H.J. Born: Phys. Rev. **C2** (1970) 1616.

[3] E.B. Norman, G.A. Rech, E. Browne *et al.*: Phys. Lett. **B519** (2001) 15.

[4] W.K. Hensley, W.A. Bassett, J.R. Huizenga: Science **181** (1973)1164.

[5] T. Ohtsuki, K. Ohno, T. Morisato *et al.*: Phys. Rev. Lett. **98** (2007) 252501.

[6] T. Ohtsuki, K. Masumoto, K. Ohno *et al.*: Phys. Rev. Lett. **77** (1996) 3522.

[7] T. Ohtsuki, K. Ohno, K. Shiga *et al.*: Phys. Rev. Lett. **81** (1998) 967.

[8] T. Ohtsuki, K. Masumoto, K. Sueki *et al.*: J. Am. Chem. Soc. **117** (1995) 12869.

[9] T. Ohtsuki, H. Yuki, M. Muto *et al.*: Phys. Rev. Lett. **93** (2004) 112501.

[10] T. Morisato, K. Ohno, T. Ohtsuki *et al.*: Phys. Rev. **B 78** (2008) 125416.

(LNS Experiment : #2648, #2672, #2688)

Development of a Nuclear Fuel Process for Reprocessing and Fabrication by using Carbonate Solution and Hydrothermal Process

K. Shirasaki, T. Yamamura, S. Ohta, I. Satoh, and T. Shikama

Institute for Materials Research, Tohoku University, Sendai 980-8577

We have recently focused on application of hydrothermal synthesis to fabrication and reprocessing of MOX fuel in order to improve the nuclear fuel cycle much simpler and safer. This process enables us to reduce amounts of radioactive wastes and possible risks of fire and/or explosion, and also to control various specifications of the MOX fuel.

§1. Introduction

Uranium dioxides or the solid solution with plutonium dioxides, i.e. so-called The "mixed oxides" (MOX), with high melting point (>2800°C) used exclusively in the commercial nuclear power plants, accompanies troublesome processes with fabrication and reprocessing. The fuel fabrication consists of complicated solid-chemical processes including a precipitation from solution, its calcination followed by H_2 reduction, and crush and granulation to control the stoichiometry and the particle size. Once the fuel is used, its reprocessing to extract burnable uranium and plutonium includes troublesome solution processes using flammable organic solvents. In spite of recent developments, Improved Purex method [1], Ion-Exchange method [2], Supercritical Fluid Direct Extraction Method [3], Fluoride Volatilization Method [4] with a potential to produce pure plutonium may arise a potential problem in proliferation resistance.

We have been involved in the removal of fission product (FP) from dissolved solution of spent nuclear fuel by using carbonate solutions (Fig. 1, Step-1) [5]. Strong carbonate complexation is one of the characteristic exclusive to actinides; the concentration in actinide(VI) carbonate solution is as high as 0.2 mol dm^{-3} (hereafter abbreviated as "M"). In contrast, most of FP such as rare earths forms hydroxide precipitate under such conditions. On the basis of this character of actinides, neutron poisons, a part of FPs, can be removed from actinides by simple engineering processes. Recently, this process have attracted interests also in United States [7].

Our recent development also include the hydrothermal process of actinides. The lower dielectric constant of the high-temperature water leads to equilibrium shifts from solvated actinide ions to solid actinide oxides. The supercritical hydrothermal synthesis was widely reported for metallic oxides with fluorite structure such as CeO_2, ZrO_2, HfO_2 and ThO_2. In spite of the lack of experimental report for AnO_2 (An = U, Np, Pu), the fluorite-type AnO_2 is expected to be produced under the hydrothermal

condition.

Figure 1 shows a schematic flow-sheet of the proposed hydrothermal process. The first step (Step-1) is the reprocessing, i.e. a removal of fission products from actinides owing to the nature of actinide ions which exclusively form stable coordination compounds with carbonate anion (CO_3^{2-}). The second step (Step-2) is the combination of the reprocessing and the fabrication of MOX fuel, i.e. the hydrothermal process at 450°C for 30 minutes with a reductant.

Since the whole process is composed of two steps, we have investigated in the following way. Firstly, we have focused on the Step-2 and determined decontamination factors (DF) for Np and alkaline metals (Cs and Na contaminated). This is because the previous report [5] gave detailed information on composition of starting solution for the step (Exp-1). Secondly, the whole process was investigated in terms of DF (Exp-2). The amount of neptunium was set to the expected summation of neptunium, plutonium, and americium in the used fuel. In this report, we would like to present interim report including results on the evaluation of DF by using RIs prepared by the linear accelerator of LNS.

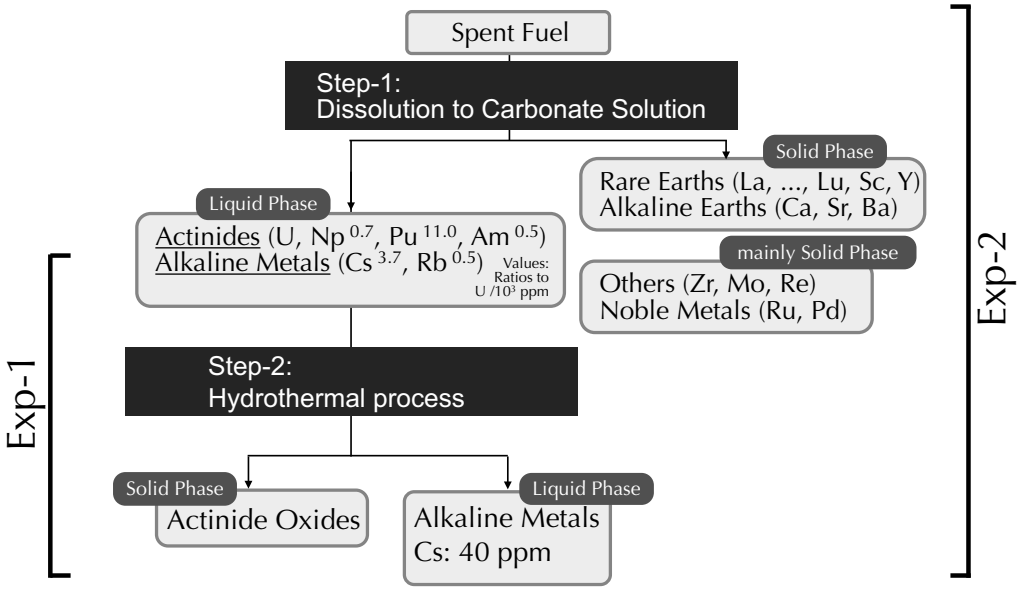

Fig.1. Hydrothermal process for MOX fuel fabrication and reprocessing and two experiments (Exp.s-1 and -2) presented in this report

§2. Experimental

2.1 Reagents, RI and quantitative analysis

All reagents were purchased as commercial reagents and used without further purification. Uranyl nitrate, $UO_2(NO_3)_2$, was obtained by dissolving triuranium octoxide to concentrated nitric acid and the nitric acid concentration was adjusted to 1.0 M.

^{137}Cs and ^{22}Na were purchased from Perkin Elmer Life and Analytical Sciences, Boston, MA, USA and The Radiochemical Centre, England, U. K., respectively. ^{85}Sr, ^{87}Y, ^{139}Ce, ^{141}Ce, ^{147}Nd, ^{97}Ru, ^{103}Ru, ^{183}Re, ^{184}Re, ^{184m}Re, and ^{186}Re were prepared by irradiation of bremsstrahlung γ-ray at linear accelera-

tor in LNS, Tohoku University, at operation of 30 MeV at 0.12 mA for 10 hours.

γ-ray spectrometry for solid and liquid phases were carried out by using a germanium semiconductor detector (EG&G ORTEC, GEM-10175). Division of the ratio of amount of uranium to impurity found in product by the ratio found in starting solution yielded decontamination factors (DF). In the cases for quantitative analysis of RI, γ-ray intensities were monitored for ^{22}Na (0.511, 1.27 MeV), ^{137}Cs (0.661 MeV), ^{88}Y (0.898, 1.836 MeV), ^{139}Ce (0.166 MeV), ^{141}Ce (0.145 MeV), ^{147}Nd (0.398, 0.440, 0.531, 0.686 MeV), ^{85}Sr (0.514 MeV), ^{97}Ru (0.216, 0.324 MeV), ^{103}Ru (0.497, 0.557, 0.610 MeV), ^{95m}Tc (0.204, 0.582, 0.786, 0.820, 0.835, 1.039 MeV), ^{186}Re (0.137 MeV), ^{183}Re (0.162, 0.208, 0.292 MeV), $^{184/184m}$Re (0.253, 0.539, 0.642, 0.792, 0.895, 0.903, 1.023 MeV), and ^{184}Re (1.121, 1.275 MeV).

Table 1. Compositions of used fuel [d)] and concentration of elements in simulated solution

Group	Elements	g/t	Added conc. for Step-2 (Exp-1) /ppm		Added conc. for Step-1&2 (Exp-2) /ppm	
			Calcd.	Found	Calcd.	Found[c)]
Actinide	U	9.42×10^5	5.40×10^4	5.40×10^{4}[c)]	4.76×10^5	4.76×10^5
	Np	6.78×10^2	3.89×10^1	4.60×10^{2}[d)]		
	Pu	1.04×10^4	5.96×10^2			
	Am	4.54×10^2	2.60×10^1			
Alkaline Metals	Cs	3.50×10^3	2.01×10^2	9.89×10^{1}[c)]	1.77×10^3	1.98×10^3
	Rb	4.84×10^2				
Alkaline Earths	Sr[b)]	1.16×10^3			5.88×10^2	5.94×10^2
	Ba	2.19×10^3				
Rare earth	Y[b)]	6.38×10^2			3.22×10^2	3.28×10^2
	La	1.66×10^3				
	Ce[b)]	3.24×10^3			1.64×10^3	1.67×10^3
	Pr	1.52×10^3				
	Nd[b)]	5.51×10^3			2.79×10^3	2.82×10^3
	Sm	9.98×10^3				
Noble metal	Ru[b)]	2.98×10^3			1.50×10^3	1.58×10^3
	Rh	5.67×10^2				
	Pd	1.82×10^3				
Others	Zr	4.92×10^3				
	Mo	4.56×10^3				
	Re[b)]	1.02×10^3			5.13×10^2	3.03×10^2
	Tc	6.40×10^2				

a) calculated by ORIGEN software for PWR spent nuclear fuel under conditions of ^{235}U 4.5%, burnup 45,000 MWd/tonne U, specific power 38 MWd, cooling for 4 years

b) Irradiation by linac, c) determined by weight, d) determined by radioactivity,

2.2 DF determination in Step-2

Simulated solution were prepared by adjusting concentrations of elements (Table 1, Exp-1), and hydrothermal process was applied under the defined conditions (Table 2). The solution (1 mL) was pipetted to inside of the autoclave reactor described previously [9, 10]. The mixed solution of sodium carbonate and sodium hydrogen carbonate (0.9 M for each; hereafter abbreviated as "SC"; pH is 10 by equilibrium between $[CO_3]^{2-}$ and $[HCO_3]^{-}$) or the solution (1.8 M) of ammonium carbonate (abbreviated

as "AC"; pH8.5) was added to this solution. Finally, ethanol was added to contain 10-20v% of ethanol, and the solution was adjusted to 3.0 cm^3. The reactor was heated to 450-500°C and after 30 min the reactor was immediately cooled. The solid and the liquid phases were recovered by separation by using a centrifuge. The solid phase was dried under reduced pressure and X-ray diffractions (XRD) were measured with a RIGAKU X-ray diffractometer RINT 2500V. Rietveld refinement was carried out on the basis of WPPD (Whole-powder-pattern decomposition) method by using WPPF software [11].

Table 2. Definitions of conditions for hydrothermal process in Step-2 (Cn)

Temp./°C	system	SC			AC	
	pH	7	9		8.5	
	EtOH conc.	10v%	10v%	20v%	10v%	20v%
390			C6		C8	
450		C2	C3	C5	C1	C9
500			C4		C7	

2.3 Exp-2: DF determination through Steps-1 and -2

In conversion of simulated solution (Table 1, Exp-2) in 1 M HNO_3 to carbonate basic solution, titration with SC or AC as titrant was carried out by using automated titration system (COMTITE-900, Hiranuma Sangyo Co., Ltd., Japan). Thermostated jacketed cell was kept at 25 ± 0.1°C. Addition of titrant is suspended while potential change is larger than 1 mV/sec. In an attempt to improve DF of Cs, Cs separation, either 0.1 M STPB solution (same volume with converted solution) or 50 mg mL^{-1} of SiO_2 was added.

§3. Results and discussions

3.1 Exp-1: Distribution of Np and alkaline metals in Step-2

XRD measurements of products of hydrothermal synthesis shows all products have fluorite-type crystal structure, as illustrated in Fig. 2. γ-ray spectra of ^{237}Np and its daughter ^{233}Pa (103 keV) were found only in solid phase but not at all in liquid phase (Fig. 3). This observation revealed that neptunium is completely transferred to oxides in this step.

The large contamination of oxides with Na (10^4-10^5 ppm; i.e. $< 10\%$), as shown in Fig. 3, indicates formation of $(U,Na)O_2$ especially at low temperature. Alkaline metal ions such as Cs, Rb, K, Na, and Li do not form solid solutions with UO_2 [7]. For example, sodium forms no compound at the uranium oxidation state of +4 but forms compounds such as Na_2UO_4, $Na_2U_2O_7$, Na_4UO_5, $NaUO_3$, and Na_3UO_4 at the oxidation states of +6 or +5 [7, 8].

The composition of Cs in SC and AC systems were similar (< 100 ppm). In AC system, the concentration increases with increasing the temperature (Fig. 4) up to 100 ppm below 450°C. The observation suggests nonexistence of Na promote the alternative inclusion of Cs in UO_2.

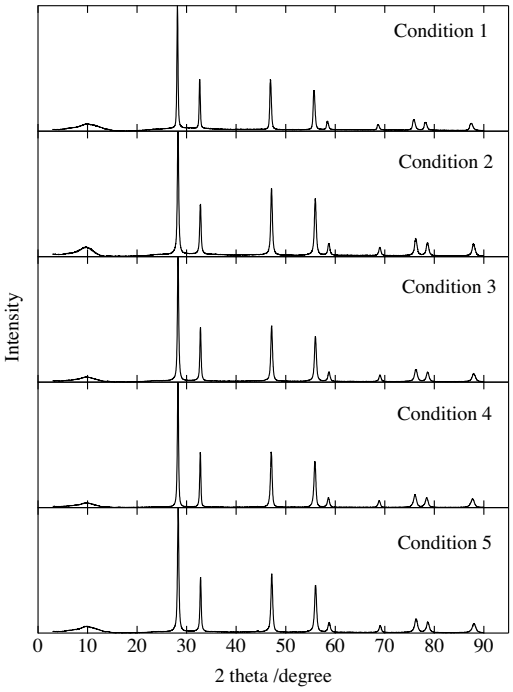

Fig.2. XRD of solid phase obtained under conditions defined in Table 2

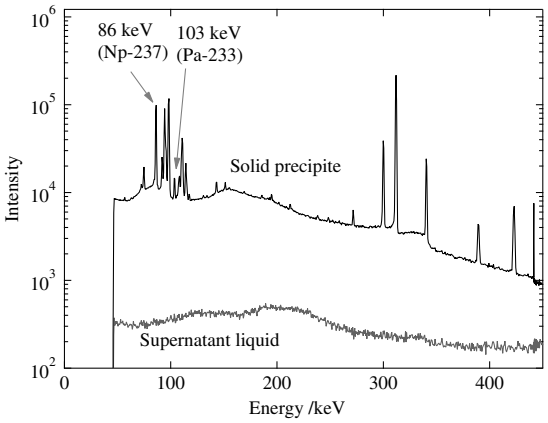

Fig.3. γ-ray spectra of solid and liquid phases obtained in AC system, measured for 20,000 and 2,000 sec (Live time), respectively

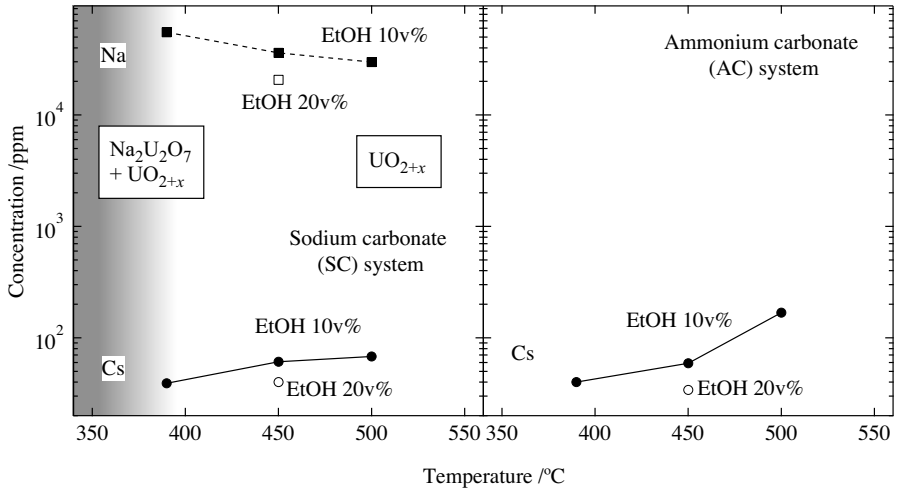

Fig.4. Concentrations of Cs and Na in SC and AC systems after hydrothermal process with ethanol at 10v% and 20v%

3.2 Exp-1: DF for FP

Since uranium is dominant species in dissolved solution, i.e.>99% in concentration, the titration curves in both systems of SC and AC are expected to be almost identical to that of uranium. The curve shows plateau at pH 3 where the former corresponds to formation of hydroxide precipitate of uranium. The generated precipitation gradually dissolved and it completed at around pH 8, where both of SC and AC have another plateau.

The difference was observed at higher pH (> pH8). In the AC system, after the hydroxide dissolved

at pH8.35, another precipitation was generated. In the SC system, just after the complete dissolution of hydroxide at pH10.5, pH turned to decrease. In the both systems, brownish precipitation and yellow supernatant were produced. Though the precipitation formation of FP elements cannot be detected in these titration curves, the curves dose not contradict to the reported precipitation region from pH6 to pH8 [5]. The reason why pH increased up to pH10.5 and then decrease in the SC system may be ascribed to the consumption of $[HCO_3]^-$ when uranium hydroxide dissolved.

In the SC system DF was >10 for lanthanides (Ce and Nd) and Ru, whereas others were <10 (Table 3). The precipitation ratio of 72.5% for Y、95.5% for Ce, 93.2% for Nd, and 90.3% for Ru. However, the ratio for alkaline earths is as low as 17.8% for Sr. The values for AC is even smaller than those of SC. Compared with DF >100 reported by Asano et al. [5], the present result should be carefully checked again. One possible explanation is that the coexistence of uranium at high concentration in this study may affect the precipitation equilibrium of FP. The previous report carried out experiments without uranium because it interferes measurements of FP concentration by ICP-AES or flame spectrophotometer. We are engaged in the further careful analysis.

The obtained liquid phase were hydrothermally treated under the condition of ethanol 10v%, 450°C, 30 min (Table 2, C3). Logarithm of DF for Sr, Y, Ru, and Re are zero (Table 4), indicating complete oxigenation.

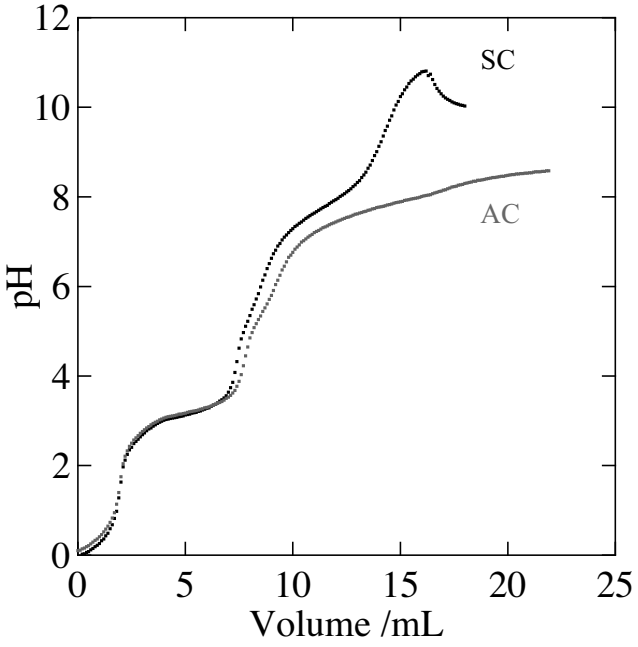

Fig.5. Titration of simulated solution containing 6 mmol U by SC or AC at 25 ± 0.1°C

3.3 Preliminary removal of Cs by addition of STPB or SiO_2

Since even total DF values, i.e. SC for Step-1 and SCH for Step-2, are low (Table 3), additional removal process is necessary to attain high DF values. For removal of Cs, two process were proposed previously; One is the complete removal of Cs by STPB (DF $>$ 234) [5], and the other is removal of Cs by

Table 3. Log of DF of the simulated FPs in the conversion process to carbonate solutions

	Step-1						Step-2	Total DF[a)]	
	SC			AC					
	None	STBP	SiO_2	None	STBP	SiO_2		w/o STBP	w STBP
Cs	0.0	2.6	0.3	0.0	1.1	0.2	2.6	2.6	5.1
Sr	0.1	0.1	0.2	0.0	0.1	0.2	0.0	0.1	0.1
Y	0.6	0.6	1.2	0.3	0.4	0.9	0.0	0.6	0.6
Ce	1.3	1.4	1.9	0.7	0.8	1.7	n.d.	1.3[b)]	1.4[b)]
Nd	1.2	1.3	1.7	0.5	0.7	0.8	n.d.	1.2[b)]	1.3[b)]
Ru	1.0	1.1	1.2	0.3	0.3	1.4	0.0	1.0	1.1
Tc	0.0	0.0	0.0	0.0	0.0	0.0	n.d.	0.0	0.0
Re	0.0	0.1	0.1	0.0	0.1	0.1	0.2	0.2	0.3

n.d. : not determined

a) DF for whole process (SC with STBP, SCH)

b) without Step-2

SiO_2 ($DF > 2 \times 10^4$) [12]. In addition to removal of Cs, lanthanide and Ru were also removed by STBP in SC, SiO_2 have similar effectiveness for lanthanides and Ru. Total DF (Table 4) shows effective removal of Cs ($DF > 10^5$).

Table 4. Cs concentration in UO_2 matrix

Items	Temperature /°C	In Metal /wt%	In Oxides /at%	Ref.
Maximum conc.	1000	0.5 ± 0.3	1.2	2
Maximum conc.	1900	0.16 ± 0.04	0.3	2
Conc. in SC system	390	—	39×10^{-4}	Present study
Conc. in AC system	390	—	40×10^{-4}	Present study

§4. Conclusions

A new method for recycle of MOX fuel was developed by combining FP separation using carbonate solution (the Step-1) and hydrothermal synthesis (the Step-2). In the Step-1, large values of >10 were obtained for lanthanides and Ru in SC system. Furthermore, DF for Cs was 380 in SC system. In AC system, similar results were obtained. Uranium at large concentration may affect precipitation of FP. In the Step-2, DF for Cs was as large as 356. This process removed cesium ion from actinide oxides (MOX fuel) down to 40 ppm. The concentration is enough low for fabrication of MOX fuel because of smaller value than solid-solution limit of actinide oxide (Table 4). Since DF for other elements were less than 2, these are found to converted to oxides.

Acknowledgements

The authors would like to thank Prof. T. Ohtsuki, and stuffs of Beam Physics group of Laboratory of Nuclear Science, Tohoku University. We also wish to acknowledge helpful cooperations by Mr. Mitsuyuki Takahashi of Laboratory for α-ray Emitters, Institute for Materials Research (IMR), Tohoku University.

The present study was supported by a grant for Innovative Nuclear Research and Development Program from the Japan Science and Technology Agency (JST).

References

[1] M. Nakahara, Y. Sano, Y. Koma, M. Kamiya, A. Shibata, T. Koizumi, T. Koyama,

[2] H. Mimura, I. Yamagishi, J. Ion Exchange, **20** (2009) 86.

[3] T. Shimada, S. Ogumo, N. Ishihara, K. Sawada, Y. Enokida, I. Yamamoto: Transactions of the Atomic Energy Society of Japan **6** (2007) 214-224.

[4] F. Kawamura: Energy and resources **23** (2002) 417-421.

[5] Y. Asano, N. Asanuma, T. Ito, M. Kataoka, S. Fujino, T. Yamamura, W. Sugiyama, H. Tomiyasu, K. Mizumachi, Y. Ikeda, Y. Wada, M. Aso: Nucl. Chem. **120** (1997) 198-210.

[6] G.D. Jarvinen, Plutonium Futures The Science 2010, Tutorial Session, Keystone, Colorado, USA (2010).

[7] Y. Hinatsu, J. Atom. Ener. Soc. Jpn., **36** (1994) 714-726.

[8] T. B. Lindemer, T. M. Besmann, C. E. Johnson, J. Nucl. Mater., **100** (1981) 178-226.

[9] T. Yamamura, N. Okumura, Y. Shiokawa, M. Oku, H. Tomiyasu, W. Sugiyama, J. Electrochem. Soc., **152** (2005) B540-B546.

[10] T. Yamamura, K. Yubuta, I. Satoh, Y. Yoshida, Y. Shiokawa, T. Sekine, W. Sugiyama, K.-C. Park, H. Tomiyasu, J. Supercrit. Fluids, **43** (2007) 317-323.

[11] H. Toraya, J. Appl. Cryst., **19** (1986) 440-447.

[12] T. Nishi, T. Baba, T. Fukazawa, S. Matzuda, K. Senno, T. Ikeda, JP Pat. Tokukai 1993-34497 (1993). J. Nucl. Sci. Technol., **44** (2007) 373.

(LNS Experiment : #2651, #2666)

Determination of Trace Amount of Nickel in Magnetic Spherules by Photon Activation Analysis

S. Sekimoto[1], K. Hirose[2], T. Ohtsuki[2], and S. Shibata[1]

[1]*Research Reactor Institute, Kyoto University, Asashiro-nishi 2-1010, Kumatori, Sennan, Osaka 590-0494*

[2]*Laboratory of Nuclear Science, Tohoku University, Mikamine, Taihaku-ku, Sendai, Miyagi 982-0826*

Trace amount of nickel in high-purity metal samples was determined by PAA. It was confirmed that PAA was able to determine 0.015 μg of nickel in the high-purity iron sample within uncertainty of 20%. Then, applying PAA to the determination of trace amount of nickel in cosmic spherules, nickel was able to be determined by PAA more accurately than by INAA which has so far been applied to analysis of spherule samples.

§1. Introduction

Magnetic spherules, which have magnetism and various diameters ranging from several tens to hundreds of μm, exist in deep sea sediments and Antarctic ice and so on. The fact that magnetic spherules were present in deep sea sediments was disclosed by the report of the Challenger Expedition and some of them were reported to be extraterrestrial in origin [1]. The contents of iron, cobalt, nickel, iridium, scandium, chromium, and manganese in over 200 magnetic spherules separated from deep sea sediment were determined by instrumental neutron activation analysis (INAA) [2]. Based on the contents of iron and cobalt, nickel, and iridium which are classified into siderophile elements in magnetic spherules, the spherules which were judged to be extraterrestrial in origin were selected as cosmic spherules [3].

Most of those cosmic spherules were suggested to be formed as follows; when chondrites as the precursor matter enter into the atmosphere, an outer part of chondrite is heated and melted, and transformed into a lot of droplets, and then those droplets are cooled down and solidified as spherules. Most of those cosmic spherules also have CI normalized elemental abundances shown by solid line in Fig. 1 [4].

On the other hand, we discovered some spherules whose CI-normalized abundances for Ir, Co, Ni, Fe, Mn, Cr and Sc have approximately identical values, shown by dashed line in Fig. 1. It was suggested that the formation mechanism of spherules shown by dashed line in Fig. 1 was different from that of the most of cosmic spherules explained above [4].

Spherule samples have been the most frequently analyzed by INAA because of following two reasons. One reason is that INAA is non-destructive method. Non-destructive analysis of samples can be the most significant characteristics in determining chemical compositions of small-sized and precious

samples like cosmic spherules. Another is that INAA has high sensitivity and accuracy for iridium, which can be the best marker to discriminate cosmic spherules from other terrestrial materials. Since nickel is classified into siderophile elements like iridium, nickel contents in extraterrestrial materials

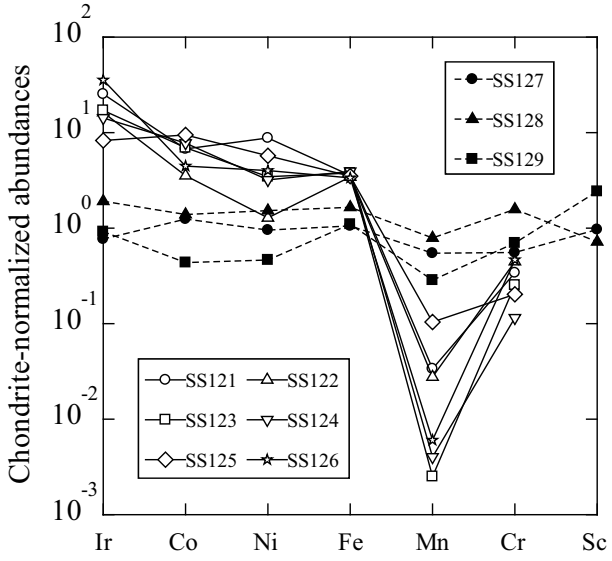

Fig.1. CI normalized abundances of Ir, Co, Ni, Fe, Mn, Cr, and Sc in extraterrestrial spherules (SS121-129:Sample ID)

are also important. However, sensitivity and accuracy for nickel in INAA using the research reactor which is dominated by thermal neutron are less higher than those for iridium because nickel is determined by INAA using fast neutron induced reaction $^{58}Ni(n,p)^{58}Co$. Therefore, nickel contents were lower than detection limits in half of about 200 spherule samples which had been analyzed by INAA [2]. Nickel contents were scarcely determined in the cosmic spherules which were judged to be similar to the three spherules shown by dashed lines in Fig. 1 on the basis of six elemental abundances except for Ni. To study the formation mechanism of those spherules in detail, it is essential to determine nickel with higher sensitivity and accuracy than the conventional INAA.

In this work, the photon activation analysis (PAA) was adopted for the determination of trace amount of nickel. As a preliminary experiment, trace amount of nickel as an impurity in high-purity metal samples was determined by PAA to confirm whether PAA could be applied to the determination of trace amount of nickel in cosmic spherules or not. And then, the spherule whose nickel content was determined by INAA was analyzed by PAA to compare nickel content in the spherule obtained by PAA with that by INAA.

§2. Experimental

The high-purity iron sample (JSS003-5), iron oxide (JSS009-2), cobalt foil, and the magnetic spherule (sample ID: SS833 [2]) were analyzed by PAA. As the reference standard samples, JCh-1, JG-1, JMn-1, and JMS-2 whose nickel contents were 8.76±1.14 mg・kg^{-1} [5], 7.47±2.56 mg・kg^{-1} [6, 7], 12632±828 mg・kg^{-1} [8], and 311±3 mg・kg^{-1} [9], respectively, were used. 30-100 mg of JSS003-5, JSS009-2, and

the reference standards were sealed into high-purity aluminum foil and shaped into pellet of 10 mm diameter. The high-purity cobalt foil which was cut into square with about 3×3 mm^2 and the spherule were sealed into high-purity aluminum foil.

Those samples, reference standards and gold foils (10 mm$\phi\times$0.02 mm) as the fluence rate monitor of bremsstrahlung photons were enclosed in a quartz tube for irradiation with bremsstrahlung photons. The irradiation was carried out using the Electron Linear Accelerator at the Laboratory of Nuclear Science in Tohoku University. The accelerator was operated at electron energy of 25 or 30 MeV with a mean current of around 0.11 mA for 8-10 hours. The quartz tube including irradiation samples was placed in the back of a platinum converter and cooled with running tap water. After the irradiation, γ rays of ^{57}Ni (1377 keV) produced by the photon induced reaction of ^{58}Ni$(\gamma, n)^{57}$Ni in each sample were measured by a low background Ge detector.

§3. Results and Discussion

3.1 Determination of trace amount of nickel in high purity metal samples

The contents of nickel in the high-purity metal samples measured by PAA are listed in Table 1. The certified values of nickel contents in these samples are also included. The correction of bremsstrahlung photon fluence rate using gold foil monitors in the irradiated quartz tube was referred to Oura et al.(1999)[10].

Table 1. Result of Ni content (in mg·kg^{-1})

Sample	Run #1	Ref. Std. #1	Run #2	Ref. Std #2.	Certified value
JSS003-5	0.376±0.076	JCh-1, JMn-1	0.473±0.035	JG-1	0.4±0.1[a]
JSS009-2	0.305±0.047	JCh-1, JMn-1	0.308±0.038	JCh-1	<2[b]
Co-foil	528±26	JMn-1	527±23	JMn-1	95[c]
	358±17	JMS-2			

[a]Reference [11]. [b]Reference [12]. [c]Reference [13].

For JSS009-2, the PAA results were reproducible on two runs and consistent with the certified values. Since about 50 mg of JSS009-2 was subjected to PAA in the Run #1, it is possible to determine about 0.015 μg of Ni within uncertainties of 20% using PAA in this work. It was confirmed that PAA used in this work made it possible to determine 1% of Ni at least in a few μg of magnetic spherules.

For JSS003-5, the PAA results of two runs agreed with the certified value within experimental uncertainties. However, the result obtained by using JCh-1 and JMn-1 as the reference standard is a little different from that by JG-1.

For Co-foil, the PAA results obtained by using JMn-1 as the reference standard were reproducible on two runs, whereas the result by JMS-2 was lower than that by JMn-1. The reason that the PAA results for cobalt-foil were three to five times higher than the certified values could not be explained at the present stage.

Table 2. Result of Ni contentin spherule sample

Sample	Weight (μg)	**PAA (%)**	NAA (%)
SS833	5.5	**1.58±0.07**	1.19±0.42[d]

[d]Reference [2]

For JSS003-5 and Co-foil, to elucidate whether the difference between the results of two runs is affected by the difference in reference standard samples, further studies along this line are in progress.

3.2 PAA of spherule sample

Photon activation analysis was applied to the determination of trace amount of nickel in the spherule sample (Sample ID: SS833 [2]) whose nickel content was determined by INAA. The contents of nickel in the spherule measured by PAA is shown in Table 2. As the reference standard, JMS-2 was used in the PAA. The INAA result of the spherule is also included. In INAA, neutron irradiation was carried out for 50 min using Pn-2 at Kyoto University Reactor.

For the spherule sample, the PAA result agreed with the result obtained by INAA within experimental uncertainties. While the uncertainty in case of INAA was about 35%, that in PAA was within 5% for determination of trace amount of nickel. It was confirmed that nickel was able to be determined by PAA in this work more accurately than by INAA which has so far been applied to analysis of spherule samples.

§4. Conclusion

Trace amount of nickel in high-purity metal samples was determined by PAA. It was confirmed that PAA was able to determine about 0.015 μg of nickel in the high-purity iron oxide sample within uncertainty of 20 % and that PAA used in this work made it possible to determine 1% of Ni at least in a few μg of magnetic spherules. Then, applying PAA to the determination of trace amount of nickel in cosmic spherules, nickel was able to be determined by PAA more accurately than by INAA which has so far been applied to analysis of spherule samples.

References

[1] Murray and Renard: Report, Scientific Result Voyage H. M. S. Challenger,Vol. 3, Neill and Co. (1891).

[2] Sekimoto: Ph. D. Thesis, Faculty of Engineering, Kyoto University (2008)

[3] Sekimoto *et al.*: Journal of Radioanalytical and Nuclear Chemistry, **272** (2007) 447-450.

[4] Sekimoto *et al.*: Journal of Radioanalytical and Nuclear Chemistry, **278** (2008) 319-322.

[5] Imai *et al.*: Geostandards Newsletter **20** (1996) 165-216.

[6] Imai *et al.*: Geostandards Newsletter **19** (1995) 135-213.

[7] Imai *et al.*: Geochemical Journal **29** (1995) 91-95.

[8] Imai *et al.*: Geostandards Newsletter **23** (1999) 223-250.

[9] Terashima *et al.*: Geostandards Newsletter **26** (2002) 85-94.

[10] Oura *et al.*: Research Report of LNS, Tohoku University **32** (1999) .

[11] Japanese Iron and Steel Certified Reference Materials, Certificate of Analyses, JSS003-5 (2004).

[12] Japanese Iron and Steel Certified Reference Materials, Certificate of Analyses, JSS009-2 (1994).

[13] Certified by A.D. MACKAY, Inc. for the Co-foil in the Nilaco corp.(#103321) (2008).

(LNS Experiment : #2628, #2646, #2667, #2687)

How precisely can we measure half-lives with Ge detectors?

K. Hirose[1], H. Kikunaga[2], and T. Ohtsuki[1]

[1]*Laboratory of Nuclear Science, Tohoku University, Sendai, 982-0826*
[2]*Graduate School of Science, Osaka University, Toyonaka, Osaka, 560-0043, Japan*

By measuring the half-lives of ^{196}Au and ^{202}Tl with high statistics using germanium detectors and many sources, systematic uncertainties were estimated by the deviation from the weighted average. In the measurement, the dead-time correction was performed by the simultaneous detection of the 662-keV γ ray from a ^{137}Cs reference source. The half-lives of $6.1474 \pm 0.0001(\text{sta.}) \pm 0.0124(\text{sys.})$ d for ^{196}Au and $12.467 \pm 0.001(\text{sta.}) \pm 0.020(\text{sys.})$ d for ^{202}Tl were obtained.

§1. Introduction

Long-standing efforts have been made since it was firstly suggested by Segré [1] and Daudel [2] that the nuclear decay rate may change due to external factors such as temperature, pressure and chemical forms. An orbital-electron capture (EC) and isometric transition with a large internal-conversion coefficient are affected by electron density around a nucleus. It was reported that the decay rate of a ^{7}Be in a fullerene of C_{60} at 5 K is almost 1.5% shorter than that in beryllium metal at room temperature [3]. Another example is the change in the decay rate of ^{99m}Tc, it was widely investigated and reported that the change is very small (10^{-2}–10^{-1}%, for example [4–10]).

In the studies mentioned above, a germanium detector as well as an ionization chamber was used for γ-ray detection. Half-lives for many radioactive isotopes have been obtained with relatively small statistic uncertainties using these detectors [11, 12]. The advantage of using germanium detectors is that backgrounds from impurities contained in samples can be discriminated by detecting specific γ rays from nuclides of interest. However, as the statistic error becomes smaller, the systematic one becomes more important, especially in the investigation of the half-life change where the changes are expected to be very small.

In this study, the half-lives of ^{196}Au and ^{202}Tl were precisely measured for many samples using germanium detectors in order to reduce the statistic uncertainty. The systematic error is estimated from the deviation from the averaged value obtained by many samples and detectors.

§2. Experiment

The sample production was performed at the Laboratory of Nuclear Science, Tohoku University. The ^{196}Au and ^{202}Tl samples were produced by the (γ, n) reaction. A gold foil (typically 20 mg) and Tl_2O_3 powder (150 mg) were irradiated by the bremsstrahlung photons with the end-point energy of 30 MeV. These samples were irradiated for about 10 hours at the electron beam current of about 130 μA.

The γ rays from the samples were detected using high-purity germanium (HPGe) detectors. The 662-keV γ ray from a ^{137}Cs reference source was also measured for the dead-time correction described later. The HPGe detector is coupled with an automated sample changer. Two samples mounted on the arms of the sample changer were moved and alternately located in front of the HPGe detector according to a time period. In order to estimate systematic errors, four sets of the HPGe detector and automated sample changer were used. The energy spectra for each sample were accumulated with a 4096-channel pulse-height analyzer for 3,550 (or 7,150) seconds every two (or four) hours. The time clock of the data-acquisition system was periodically calibrated using the Japan standard time distributed via a long-wave radio signal. The decays of 40 sources of ^{196}Au and 16 sources of ^{202}Tl were followed for several half-lives.

§3. Results and discussion

Typical spectrum around 356 keV of ^{196}Au is shown in Fig.1. The dashed curve is a fitting result by a combination of a gaussian and error function.

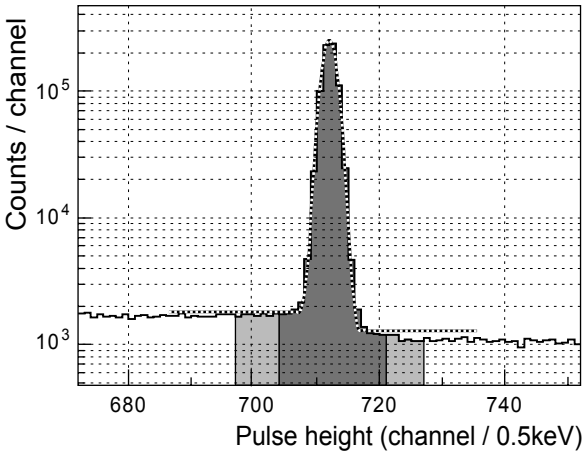

Fig.1. The pulse height spectrum around 356 keV of ^{196}Au. The dashed curve is a fitting result by a gaussian and error function. The peak area is counted in $\pm 3\sigma$ around the peak center (hatched with dark gray). The backgrounds are estimated from the 2σ-width regions on both sides of the peak (hatched with light gray).

The peak region of counting was determined as $\pm 3\sigma$ around the center of the peak. The background was estimated by the counts in the 2σ-width regions on both sides of the peak. Then, the peak area $P(t)$ at time t is counted as,

$$P(t) = \sum_{\text{Peak}} C(t) - \frac{3}{2} \sum_{\text{BG}} C(t) \tag{1}$$

The peak areas of 333 (^{196}Au), 440 (^{202}Tl) and 662 keV (^{137}Cs) were counted in the same manner.

In the present work, the reference method using a ^{137}Cs source was employed for the dead-time and pile-up correction. In this method, the half-life is obtained from the ratio of the activity of interest ($Ae^{-\lambda t}$) to that of the reference source ($A'e^{-\lambda' t}$). However, the ratio of the counts integrated over the finite time period, not the activity, can be obtained in practice. Therefore, the ratio is given as,

$$\frac{P(t)}{P'(t)} \equiv R(t) = \frac{\int_t^{t+\Delta t} Ae^{-\lambda x}\eta(x)dx}{\int_t^{t+\Delta t} A'e^{-\lambda' x}\eta(x)dx} \tag{2}$$

where Δt is a measurement period for one data point (3,550 or 7,150 s in this work). The $\eta(t)$ is the ratio of a live time to a real time. If the activity of the reference source is assumed to be constant for Δt, $\eta(t)$ is expressed as $a(1-be^{-\lambda t})$. This is valid considering that the dead-time is proportional to the rate of input signals. The initial value of η is $a(1-b)$ and a is smaller than unity due to the activity of the reference source. Then, one can calculate $R(t)$ as,

$$R(t) = \frac{A}{A'}e^{-\lambda t} \cdot \frac{1 - e^{-\lambda\Delta t} - \frac{b}{2}(1-e^{-2\lambda\Delta t})e^{-2\lambda t}}{\lambda\Delta t - b(1-e^{-\lambda\Delta t})e^{-\lambda t}} \tag{3}$$

The last factor of this is a monotone increasing function but its time dependence is extremely small. The difference of this factor is only $0.8 \times 10^{-3}\%$ between $t = 0$ and $t = \infty$, assuming $\lambda = 4.8135 \times 10^{-3}$ h^{-1}(6 days), $\Delta t = 2$ h and $b = 0.5$. The decrease of the ^{137}Cs activity has to be corrected when $R(t)$ at different t are compared, although it was neglected in the equation (3). The reason is that the decay of ^{137}Cs for Δt (2 hours) is small ($0.5 \times 10^{-3}\%$) but that for 30 days becomes 0.2%. After the correction, one can derive the half-life from $R(t) \sim Ae^{-\lambda t}/A'e^{-\lambda' t}$.

The decay curve obtained from 356-keV γ ray of ^{196}Au is shown in the upper panel of Fig. 2. The thin line is the result of the least square fitting by an exponential function. The lower panel shows the deviations from the fitted function, divided by the statistic errors.

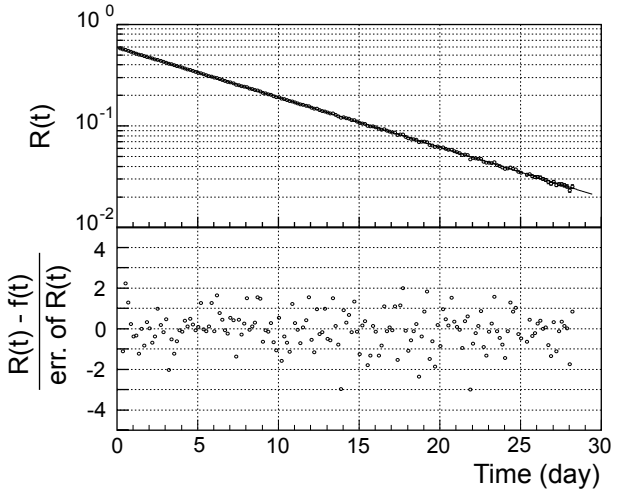

Fig.2. The upper panel shows the decay curve for ^{196}Au. The thin line is the fitting result by an exponential function. The lower panel shows the normalized residuals.

The center panels of Fig. 3 show the all results obtained from 333, 356-keV γ rays (^{196}Au) and 440-keV γ ray (^{202}Tl), respectively. The value of the half-lives is determined as a weighted average. Owing to many times of measurements, the statistic uncertainties are very small, $2 \times 10^{-3}\%$ for ^{196}Au and $8 \times 10^{-3}\%$ for ^{202}Tl. However, the deviations from the weighted averages, shown in the right panels of Fig. 3, are much larger than the statistic uncertainties. The systematic uncertainties were estimated as the root-mean-squares and determined to be 0.20% for ^{196}Au and 0.16% for ^{202}Tl.

In the left panels of Fig. 3, the results of the present work (closed circles) are compared to the other experimental data, open triangle [13], open square [14], open circle [15], closed-inverted triangle [16], open-inverted triangle [17], closed triangle [18], and closed square [12] for ^{196}Au, open star [19], closed

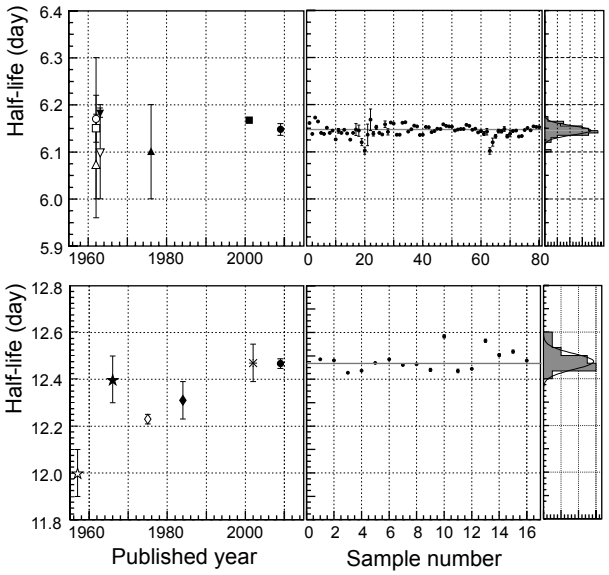

Fig.3. The center panels show the all results of the present work. The half-lives are determined as the weighted averages. The deviations from the weighted average, shown in the right panels, are much larger than the statistic uncertainties. The systematic uncertainties are estimated from these deviations. Our results (closed circles) are compared with the other data referred from [11–22].

star [20], open diamond [21], closed diamond [22], and asterisk [11] for ^{202}Tl. Although the statistic uncertainty of the results of Ref. [12] (closed square) is 0.01%, the systematic uncertainty is estimated to be 0.1%. Hence, our results are in good agreement the latest measurement.

§4. Conclusion

The results of the present work are summarized in Table 1. In the present work, the statistic uncertainties were reduced by using many sources and detectors. Most parts of the uncertainties are due to the systematic ones. The half-life of ^{196}Au was determined to be $6.1474 \pm 0.0001(\text{sta.}) \pm 0.0124(\text{sys.})$ d, which agrees well with the latest value [12]. The half-life of ^{202}Tl was determined to be $12.467 \pm 0.001(\text{sta.}) \pm 0.020(\text{sys.})$ d with 75% smaller uncertainty than that of the latest value [11].

Table 1. The half-lives obtained in the present study.

	Number of sources	Number of half-lives followed	half-life (day)	statistic error	Other error
^{196}Au	40	1.8 – 8.5	6.1474±0.0124	0.0001	0.0124
^{202}Tl	16	1.8 – 4.0	12.467±0.020	0.001	0.020

Although our measurement system gives the systematic uncertainty of about 10^{-1}%, it is available for investigations on half-life changes of the order of 10^{-1}% with several-time measurements. Further research is also needed to find the sources of the systematic uncertainties and to reduce them, if it is possible.

Acknowledgement

We would like to thank the accelerator and technical staff at the Laboratory of Nuclear Science for operation of the accelerator and for other experimental supports.

References

[1] E. Segré: Phys. Rev. **71** (1947) 274
[2] R. Daudel: Rev. **85** (1947) 162
[3] T. Ohtsuki *et al.* : Phys. Rev. Lett. **98** (2007) 252501
[4] K. T. Bainbridge, M. Goldhaber, E. Willson: Phys. Rev. **84** (1951) 1260
[5] K. T. Bainbridge, M. Goldhaber, E. Willson: Phys. Rev. **90** (1953) 430
[6] D. H. Byers, R. Stump: Phys. Rev. **112** (1958) 77
[7] R. A. Porter, W. G. McMillan: Phys. Rev. **117** (1960) 795
[8] H. Mazaki, T. Nagatomo, S. Shimizu: Phys. Rev. C**5** (1972) 1718
[9] M. Nishi, S. Shimizu: Phys. Rev. B**5** (1972) 3218
[10] H. Mazaki, S. Kakiuchi, S. Shimizu: Z. Phys. B**29** (1978) 285
[11] M. P. Unterweger: Appl. Radiat. Isot. **56** (2002) 125
[12] K. Lindenberg *et al.* : Phys. Rev. C**63** (2001) 047307
[13] E. W. A. Lingeman *et al.* : Nucl. Phys. **31** (1962) 584
[14] A. H. Wapstra *et al.* : Nulc. Phys. **31** (1962) 575
[15] N. A. Bonner *et al.* : Phys. Rev. **127** (1962) 217
[16] H. Ikegami *et al.* : Nucl. Phys. A**41** (1963) 130
[17] R. S. Tilbury, L. Yaffe: Can. J. Chem. **41** (1963) 2634
[18] R. G. Helmer: ERDA/NDC-3/U (1976) 2
[19] H. C. Hamers, A. Marseille, Th. J. de Boer: Physica **23** (1957) 1056
[20] H. Leutz, G. Schulz, H. Wenninger: Nucl. Phys. **75** (1966) 81
[21] I. M. Cohen, R. O. Koro, G. B. Baro: Int. J. Appl. Radiat. Isot. **26** (1975) 403
[22] H. W. Taylor: Int. J. Appl. Radiat. Isot. **35** (1984) 421

(LNS Experiment : #2675, #2679)

Measurement of the half-life of $^{99}Tc^m$ in Tc Metal and $KTcO_4$ materials

H. Kikunaga[1], K. Takamiya[2], K. Hirose[3], and T. Ohtsuki[3]

[1]*Nishina Center for Accelerator-Based Science, RIKEN, Wako, Saitama, 351-0198*
[2]*Research Reactor Institute, Kyoto University, Kumatori, Osaka, 590-0494*
[3]*Laboratory of Nuclear Science, Tohoku University, Sendai, Miyagi, 982-0826*

The half-life of $^{99}Tc^m$ in metal and $KTcO_4$ chemical conditions has been measured precisely. Relative differences in the decay constant of $^{99}Tc^m$, $\{\lambda(TcO_4^-) - \lambda(\text{metal})\}/\ \lambda(\text{metal})$ obtained from this work is determined to be $(53.6\pm9.8)\times10^{-4}$ which is larger than the previous value $(37.4\pm0.8)\times10^{-4}$.

§1. Introduction

The half-life of the metastable state of ^{99}Tc ($^{99}Tc^m$) is affected by environmental factors such as chemical state [1, 2]. Almost all $^{99}Tc^m$ nuclei decays via a 2.2-keV transition from the 142.7-keV level to the 140.5-keV level in ^{99}Tc [3]. Because of the high internal conversion coefficient and low transition energy, the probability of the transition is expected to vary with changes in the chemical structure affecting the electron density at the nucleus.

The nuclide $^{99}Tc^m$ is useful for medical applications. Information of the chemical structures of $^{99}Tc^m$ is important for radiopharmaceutical development. The variation measurement of half-life of $^{99}Tc^m$ have a potential for a probe of its chemical conditions. The goal of our research is to clarify the effects of chemical structure on the decay constants of $^{99}Tc^m$. We have measured the half-life of $^{99}Tc^m$ within the good precision of the magnitude of 0.1% [4]. In this work, the half-life of $^{99}Tc^m$ which is in the chemical form of metal and $KTcO_4$ has been determined.

§2. Experimental Procedure

The procedures for production and purification of $^{99}Tc^m$ were similar to those described in Ref. [4]. The isotope $^{99}Tc^m$ was produced in the nuclear reaction $^{100}Mo(\gamma, n)^{99}Mo$, followed by disintegration to $^{99}Tc^m$. A sample of about 18 mg of enriched ^{100}Mo was enclosed in a quartz tube for bremsstrahlung irradiation. The irradiation was carried out for 10 h with the Electron Linear Accelerator at Tohoku University. The accelerator was operated at an electron energy of 30 MeV with mean current of around 0.1 mA.

After the irradiation, the ^{100}Mo target was dissolved in 1 mL of 7 M (mol/dm^3) HNO_3 and then heated to dryness. The residue was dissolved in a few drops of 7 M NH_3aq. and then added 0.1 M HCl to adjusted to neutral pH. The solution was passed through an anion exchange resin column (Dowex 1×8, 200-400 mesh, 5.5 mm$\phi\times$ 40 mm) to eliminate Tc from the Mo solution.

To allow the decay of ^{99}Mo ($T_{1/2}$ = 66.0 h) and the growth of ^{99}Tc^m, the purified Mo solution was left to stand for about 24 h after the end of the purification of the Mo solution. The solution containing ^{99}Tc^m was passed through an anion exchange resin column (Dowex 1×8, 200-400 mesh, 5.5 mmϕ×40 mm) to adsorb the Tc isotopes. The resin was washed with 8 mL of 1 M HCl to remove Mo isotopes from Tc fraction. The Tc isotopes were eluted from the column with 12 mL of 7 M HNO_3 and adjusted to 0.12 M KCl solution. The solution was passed through an alumina column (Wako Pure Chemical Industries, Ltd., 300 mesh, 5.5 mmϕ×40 mm) to reduce the content of ^{99}Mo. The alumina column procedure was repeated twice using a fresh column each time. Additionally, the Tc isotopes was purified by the anion exchange column procedure, the alumina column procedure (three times), and the anion exchange column procedure in this order. The purified Tc solution was finally adjusted to 7 M HNO_3 solution and divided into several fractions. A carrier of ^{99}Tc^g (500 μg per a counting source) was added to the purified solution. The Tc fractions were heated to dryness and prepared to counting sources as below.

The metal technetium sample was prepared by reduction of Tc electro-deposited on a stainless-steel plate. The Tc residue was dissolved in 1 mL of 1.8 M H_2SO_4 and then added 7 M NH_3 water to adjust a pH level of the solution to be about 2. The solution was transferred into the electrodeposition cell. Electrolysis was carried out at 0.5 A for 3 h. 1 mL of 7 M NH_3 water was then added into the cell about 1 min before turning off the current. The stainless-steel plate was rinsed with distilled water and dried with a Bunsen burner. The Tc deposit was reduced to metal by heating in a stream of hydrogen gas at 1000 $^\circ$C and then coated with paraffin. To prepare pertechnetate sample, the Tc fraction was dissolved in 0.7 M KCl solution. The solution was evaporated to dryness on a glass plate and then coated with paraffin.

The two samples of metal and $KTcO_4$ were set in an automated sample changer [5] and placed alternately in front of a high-purity (HP) Ge detector at interval of 1800 s. The 140 keV γ-rays from ^{99}Tc^m were measured for a real time of 1750 s at one data point. The procedures were repeated over at least 42 h (T / $T_{1/2}$ > 7). A ^{137}Cs source was attached to near the HP-Ge detector as a radiation reference source. The half-life of ^{99}Tc^m was determined based on a reference source method [6]. The internal clock time of the computer for data acquisition was constantly calibrated by a time-standard signal distributed via a long-wave radio transmission station in Japan.

§3. Results and discussion

A typical γ-ray spectrum for a $KTcO_4$ sample measured for 1750 s is shown in the Fig. 1. No peaks were seen at around E_γ = 181, 739.5, and 777.9 keV which are the expected energy regions for ^{99}Mo, followed by disintegration to ^{99}Tc^m. If the activity ratio A(Mo)/A(Tc) is smaller than about 10^{-6} at the beginning of the measurement, the activity of ^{99}Mo has no influence on determining the half-life of ^{99}Tc^m. Unfortunately, the amount of ^{99}Mo in the counting sample was not determined exactly because it was too small to detect. However, ^{99}Tc^m was isolated from ^{99}Mo by using three anion exchange column processes. The decontamination factor of one anion exchange process is expected to be 400-800 described above. A(Mo)/A(Tc) at after the 24 h growth time of ^{99}Tc^m is approximately 1. Therefore, A(Mo)/A(Tc)

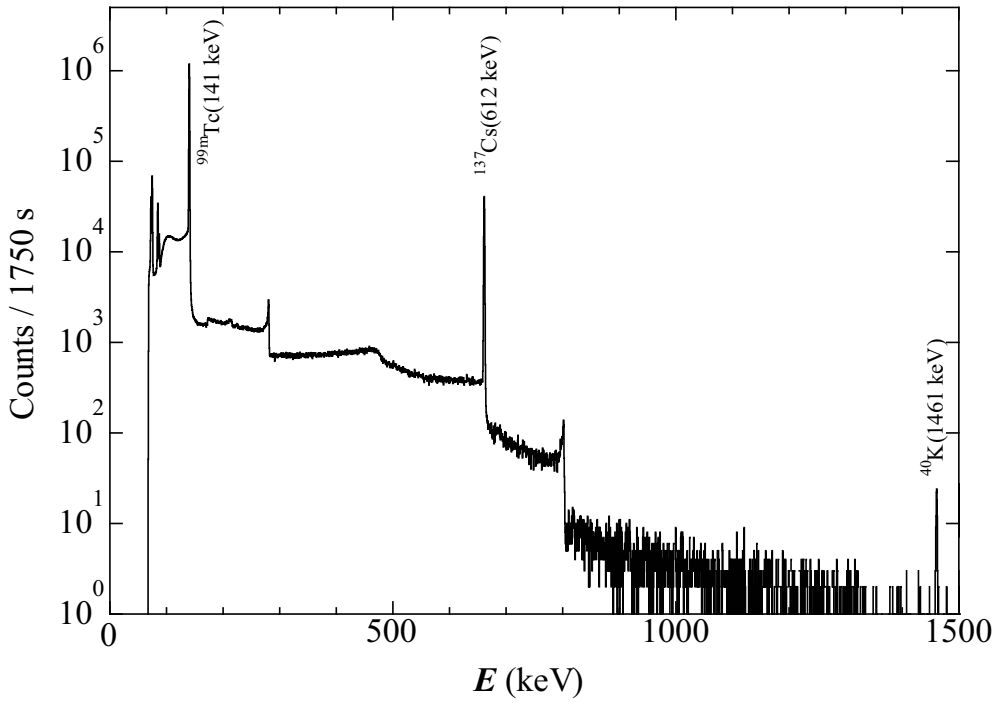

Fig.1. A typical γ-ray spectrum for a $KTcO_4$ sample measured for 1750 s.

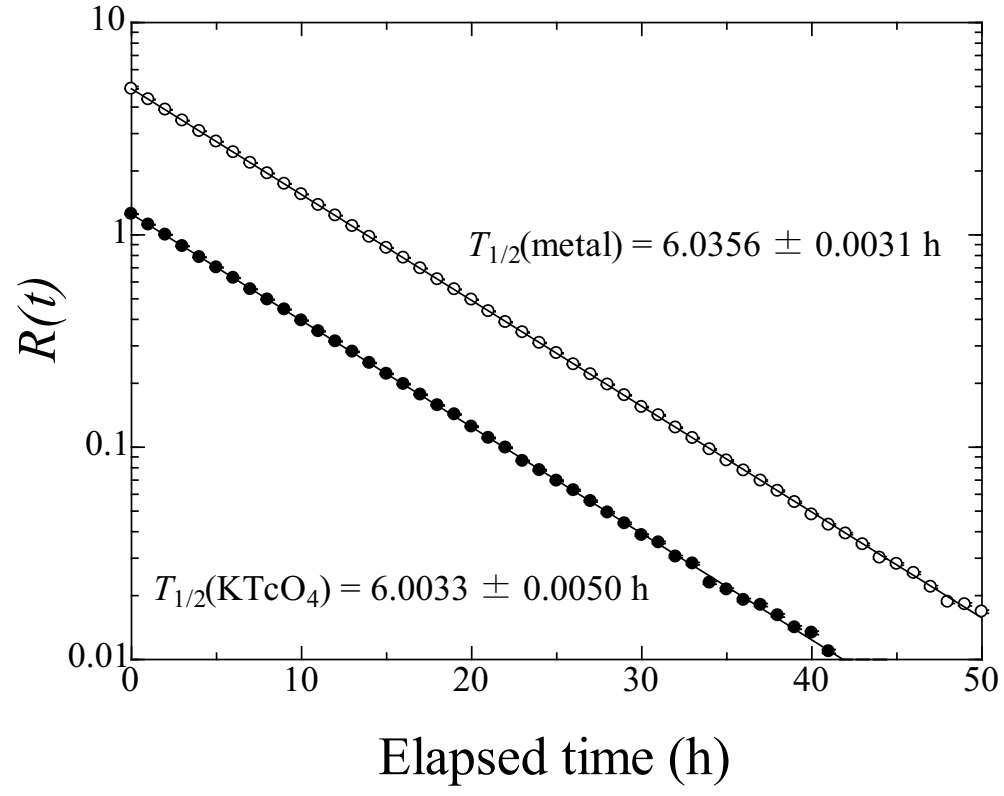

Fig.2. Exponential curves for the $R(t)$ obtained using a least-squares fitting procedure.

is expected to be smaller than 10^{-6} by the three anion exchange column processes. Additionally, we carried out five alumina column processes to eliminate ^{99}Mo from ^{99}Tc^{m} completely.

A typical exponential curve for $R_{(t)}$ obtained using a least-squares fitting procedure are plotted as a function of time in Fig. 2. The ratio $R_{(t)}$ is given by following equations:

$$R_{(t)} = \frac{C_{sample(t)}}{C_{ref(t)}}, \tag{1}$$

where $C_{sample(t)}$ and $C_{ref(t)}$ are count rates of a sample and a reference source at the beginning of each data acquisition, respectively. The half-life of ^{99}Tc^{m} with the chemical form of metal and $KTcO_4$ are determined to be (6.0356±0.0031) h and (6.0033±0.0050) h, respectively. The uncertainty is given by the uncertainty of the slope of the straight line fitted to the logarithm of $R_{(t)}$ and the uncertainty of the half-life of ^{137}Cs (0.09% [7]) used as a reference source. From the results, relative differences in the decay constant of ^{99m}Tc, $\{\lambda(TcO_4^-) - \lambda(\text{metal})\}/\ \lambda(\text{metal})$ obtained from this work is determined to be (53.6±9.8)×10^{-4} which is larger than the previous value (37.4±0.8) ×10^{-4} [2].

Acknowledgement

The authors would like to thank the technical staff of Laboratory of Nuclear Science, Tohoku University for their excellent accelerator operation.

References

[1] K. T. Bainbridge *et al.*: Phys. Rev. **90** (1953) 430.

[2] H. Mazaki *et al.*: Phys. Rev. C **21** (1980) 344.

[3] R. B. Firestone and V. S. Shirley Eds.: Table of Isotopes, 8th ed.(Wiley & Sons, New York, 1996).

[4] H. Kikunaga *et al.*: Radiochim. Acta (in press).

[5] T. Ohtsuki *et al.*: Phys. Rev. Lett., **93** (2004) 112501.

[6] M. A. L. da Silva *et al.*: J. Radioanal. Nucl. Chem. **264** (2005) 571.

[7] M. P. Unterweger: Appl. Radiat. Isot. **56** (2002) 125.

(LNS Experiment : #2678, #2689)

Production of paramagnetic centers in polyethylene with an electron beam for polarized polymer targets.

T.Iwata[1], N.Doshita[1], K.Hirose[2*], N.Kubota[1], L.Wang[3], H.Matsuda[1], T.Ohtsuki[2*], M.Sasaki[1], and Y.Tajima[4]

[1]*Department of Physics, Faculty of Science, Yamagata University, Yamagata, 990-8560,Japan*
[2]*Laboratory of Nuclear Science, Tohoku University, Sendai,982-0826,Japan*
[3]*Physics Department, School of Science, Donghua University, 200051 Shanghai, China*
[4]*Institute of Arts and Sciences, Yamagata University, Yamagata, 990-8560,Japan*

Polarized polymer targets operated in Dynamic Nuclear Polarization technique have characteristic advantages that they can be easily processed into various forms. The DNP requires require introduction of paramagnetic centers in the target material. Polyethylene samples were irradiated by 11 MeV electrons beam at room temperature. Existence of the paramagnetic centers is confirmed by ESR measurements.

§1. Polarized polymer targets with DNP techniques

Polarized solid targets have been widely employed in nuclear physics experiments. They rely on the Dynamic Nuclear Polarization(DNP) technique [1] which transfers the electron polarization to the nuclear spins by means of a microwave. This process requires a material containing some amount of paramagnetic centers. In order introduce paramagnetic centers following two methods have been developed: chemical method and irradiation method. The former one was firstly applied to lanthanum magnesium nitrate $La_2Mg_3(NO_3)_{12}{\cdot}24H_2O$ (LMN) [2]. Since then the same method has been also applied to alcohol- and diol materials.

Parallel to the improvements in the chemical method, research was focused on the improvement of the target materials with a high dilution factor which is defined as the number of the polarizable nucleons divided by that of all the uncleons in the target material.

At the end of the 1960s ammonia was considered as a possible candidate due to its high-dilution factor f=0.176 compared, e.g. to that of butanol with f=0.135. However, the devlopements of the material in the chemical method were not successful [3].

Instead of the chemical method, the irradiation method was firstly applied to the ammonia material resulting in high polarizations beyond 90 % [4] . Since then, improvements of materials in the irradiation method has been accelerated. It was also applied to ND_3 and ^{6}LiD [3].

Comparing the target materials mentioned above, polymer type materials such as polyethylene(PE)

*Present address: Research Center for Electron Photon Science, Tohoku University, Sendai, 982-0826,Japan

have characteristic advantages. They can be processed into various forms, e.g. even into very thin foil. Thus they allow polarized targets in thin foil form which can be employed in low energy nuclear physics experiments. In their development, the chemical method has been usually applied. A polystyrene based plastic scintillator doped with free radical TEMPO has been developed as an polarized active proton target [5] However, the obtained polarizations were not very high although they were sufficient for the experiment. On the other hand, the irradiation method has not been well studied for the polymer materials. We performed irradiation to the PE material which is one of the common polymer materials with the molecular structure as shown in Figure 1.

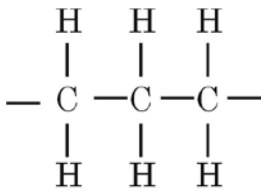

Fig.1. Molecular structure of Polyethylene.

§2. Irradiation

Two kinds of PE samples were prepared; a thin foil with thickness of 50 μm and a fiber with thickness of 12 mum. The former sample is a typical low density PE foil consisting of crystal and amorphous parts. [†]. On the contrary, the latter is a special product [‡] made up with linear molecules with very high molecular weight aligned in the same direction along the fiber. They have been irradiated by a 11 MeV electron beam with a time-averaged beam current of 100 μA delivered by the LNS Linac , Tohoku University. The irradiation was done not cooling the samples contrary to a usual way. Although permission is required in order perform irradiation of the sample in liquid nitrogen, we could not obtain it. However, the samples were stored in liquid nitrogen immediately after the irradiation. The accumulated dose range was from 3×10^{17} e/cm^2 to 9.9×10^{18} e/cm^2. Table 1 shows the summary of the irradiation.

Table 1. Summary of the irradiation.

irradiation No.	1	2	3	4	5	6
sample form	foil	foil	foil	foil	fiber	fiber
duration(s)	600	2,940	9,560	18,000	60	600
dose (e/cm^2)	$3.3\times^{17}$	1.6×10^{18}	5.3×10^{18}	9.9×10^{18}	3.3×10^{16}	3.3×10^{17}

§3. ESR spectra

In order to study paramagnetic centers, we have performed ESR measurements at liquid nitrogen temperature. Figure 2 shows the ESR spectra for the foil samples.

[†] Ohkura Kogyo Co.Ltd, Linear-low-density-PE(L-LDPE).

[‡] Toyobo Co.Ltd. Dynima

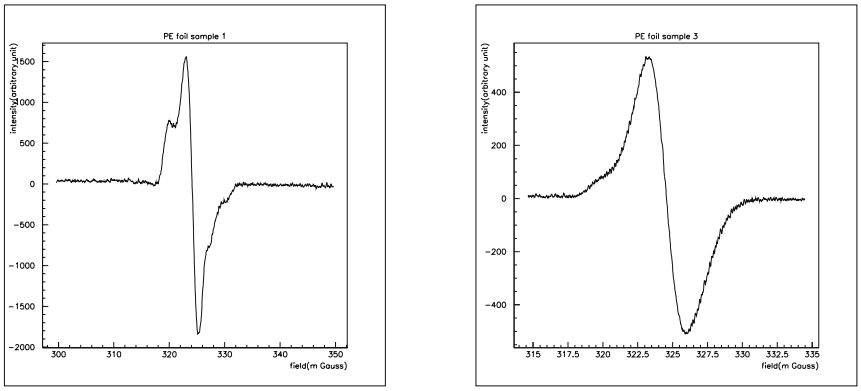

Fig.2. The ESR spectra(1st differential) for the foil samples. Left:irradiation number 1. Right:irradiation number 3.

They show a basic structure as manifested by the large peak-dip structure in the 1st differential spectrum. It is considered to be due to the paramagnetic center left after the proton knocked out as shown in Figure [**?**]. The spectrum for the sample with the lower doze shows a fine structure as well as

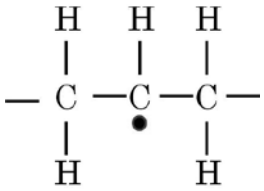

Fig.3. Paramagnetic centers produced by irradiation.

the basic structure. As the does increases, the structures becomes broader. While, the spectrum for the fiber sample as shown in Figure 4 gives interesting structures due to hyper fine interaction caused by the protons surrounding the paramagnetic centers. The number of the corresponding protons is five so that one can observe the same number of hyper fine structure. While, four structures are clearly seen in the spectrum and the last one is a little bit indistinct.

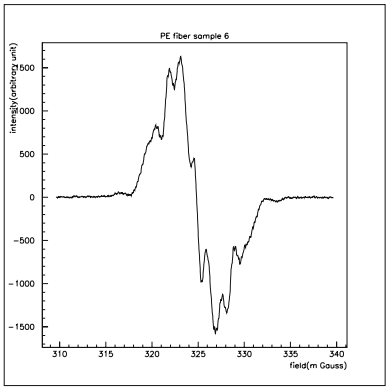

Fig.4. One of the ESR spectra for the fiber samples. Irradiation number 6.

The reason why the fine structures are prominently seen only for the fiber sample is that it has much higher crystallinity than the foil samples.

As well as the ESR spectrum, the density of the paramagnetic centers is important and interesting. However, the density measurement requires careful calibration of the ESR signal with a standard sample with a known number of paramagnetic centers. We plan to perform the measurement as soon as possible.

§4. Conclusion

The polymer type materials allow polarized targets in any form. We have performed irradiation for the polyethylene samples at room temperature with 11 MeV electron beam at LNS. The ESR spectra show existence of paramagnetic centers. It is confirmed that paramagnetic centers are produced in irradiation even at room temperature and can be kept at liquid nitrogen temperature.

References

[1] A. Abragam, The Principles of Nuclear Magnetism, The Clarendon Press, Oxford, 1961.

[2] T.J. Schmugge, C.D. Jeffries, Phys. Rev. **122** (1962) 1781; T.J. Schmugge, C.D. Jeffries, Phys. Rev. **A 138** (1965) 1785.

[3] See the review: W. Meyer, Nucl. Instr. and Meth. **A 526** (2004) 12-21.

[4] T.O. Niinikoski, J.-M. Rieubland, Phys. Lett. 72A (1979) 141.

[5] B.van den Brandt et al.Czech.J.Phys.52:C689-C694,2002.

(LNS Experiment : #2684, #2724)

電子線照射による ^{85}Sr の製造と溶媒抽出実習プログラムへの応用
―核燃料サイクル分野におけるグローバル人材育成―

佐藤修彰 [1], 大槻 勤 [2], 桐島 陽 [1]

[1] 東北大学多元物質科学研究所 (980-8577 仙台市青葉区片平 2-1-1)
[2] 東北大学電子光理学研究センター (982-0826 仙台市太白区三神峯 1-2-1)

Production of ^{85}Sr Isotope by Electron Irradiation and Its Application to the Solvent Extraction Training
― Development of Student Training Program for Fuel Cycle Chemistry ―

N. Sato[1], T. Ohtsuki[2], and A. Kirishima[1]

[1]*Institute of Multidisciplinary Research for Advanced Materials, Tohoku University, 2-1-1 Katahira, Aoba-ku, Sendai, Miyagi, 980-8577*
[2]*Research Center for Electron Photon Science, Tohoku University, 1-2-1 Mikamine, Taihaku-ku, Sendai, Miyagi, 982-0826*

For the increasing demand on nuclear energy, human resources development in nuclear engineering is needed. Especially, human resources program in nuclear fuel cycle field is urgently required. In our institute, the experimental program on uranium chemistry in both front- and back-end fields has been developed for the graduate student. Then, the global training program for undergraduate students for fuel cycle chemistry was developed by Kyunghee University and Tohoku University. The program was performed for the nuclear engineering student of Korean Universities. The main program consists of two experiments in the solid-state chemistry field and solution chemistry as well as the radio isotope production (^{85}Sr) by using accelerator. In the solution chemistry experiments, U(VI) was mixed with FP radio isotope ^{85}Sr and separated from FP in a nitric acid solution by the solvent extraction technique using TBP and dodecane mixed solvent. Then, separation factors were obtained by α- and γ-ray measurements for uranium and ^{85}Sr, respectively. After the experimental training for three days, presentations for each experiment were given by students and evaluated by professors based on the subjects such as understanding, construction, discussion etc.

§1. 緒　　言

原子力への需要増加とともに、原子力工学における研究者、技術者といった人材の育成が急務である。特に、核燃料サイクル分野における人材育成が重要であり、国内においては種々のプロジェクトが進められている。東北大多元研においても 2008 年度文部科学省人材プログラム「フロントおよびバックエンドにおけるウラン化学の実験的理解」を実施した。しがしながら、アジア地域における原子力発電の普及とともに、

日	班	A	B	C	D
2	午前	放射線取扱従事者登録			
	午後	電子光理学研究センター（加速器施設）見学			
3		固体化学実験		溶液化学実験	
4		溶液化学実験		固体化学実験	
5		実験レポート作成			
8	午前	実験レポート作成			
	午後	発表			

第 1 図　Training schedule at Tohoku University.

国際的な協力が不可欠となってきている。特に持続性のある原子力発電の利用にあたっては、核燃料サイクル分野における人材育成が重要となってくるが、放射性物質の取扱や核不拡散防止など、実施にあたっては課題も多い。そこでわれわれの研究グループでは、外国人を対象とした核燃料サイクルにおけるウランの固体および溶液化学を中心とする実習プログラム「原子燃料サイクルにおけるウランの溶液および固体化学の実験的理解」を開発し、2009 年度韓国研究財団原子力分野における人材育成事業に採択された。実際に韓国 7 大学の原子力工学科選抜学生を対象に、同プログラムを実施した。同プログラムは 2010 年度も採用され、プログラム実施による持続的な人材育成を目指している。ここでは、プログラムの全体概要と、東北大学における実習内容について報告する。本プログラムは、1) 韓国における事前講習、2) 東北大電子光学研究センターにおける放射性核種製造と加速器見学、3) 多元物質科学研究所におけるウランの固体および溶液化学実験、4) 日本原子力研究開発機構における高速炉「常陽」および HTGR 見学からなる。全体のプログラム韓国の原子力関係学科を有する 7 大学（ソウル大、漢陽大、慶熙大、KAIST、東国大、朝鮮大、済州大）の院生および学部生からそれぞれ数名を選抜した。来日前に韓国慶熙大にて、放射線作業従事者資格取得のための事前講習ならびに多元研放射線作業従事者教育訓練を実施した。また、JAEA 施設見学のための事前申請を行った。来日後は、仙台におけるウランに関する実習と、加速器施設見学を行った。Fig. 1 には東北大学における実習内容を示した。まず、多元研において、放射線従事者登録を行った。次に電子光理学研究センターを訪問した。ここでは、核物理および放射化学に関する講義を受講した後、２班に分かれて、線形加速器やストレッチャーブースターリングを見学した。特に、線形加速器の試料照射装置を確認し、高強度電子の Bremsstrahlung による (γ, n) 反応を利用した RI 製造法について理解した。また、多元研においては、A から D までの 4 班に分けて固体および溶液化学実験を行った。

§2．加速器照射による RI 製造

SrO ターゲットの作製と照射後試料の溶解手順を Fig. 2 に示した。

和光純薬製の特級炭酸ストロンチウム ($SrCO_3$) を 1M 硝酸に溶解し、蒸発・乾固後、硝酸塩を NO_x が出なくなるまで加熱分解し、SrO を得た。これを石英アンプル (10 mmϕ) に真空封入し、照射 SrO ターゲット（約 100 mg）を作製した。この封入石英管を制動放射照射用の L 字型石英管に封入（L 字管部分は開放）して、東北大学原子核理学研究施設（LNS）の電子ライナック第 1 ビームコース照射設備の白金コンバータの後方に取り付け、水冷しつつ、電子エネルギー 50 MeV(最大電流約 120 μA) で、約 10 時間照射した。

照射済 SrO 試料を多元研へ移動し、真空封入した石英管をガラスビーカー内で破壊し、1M 硝酸により

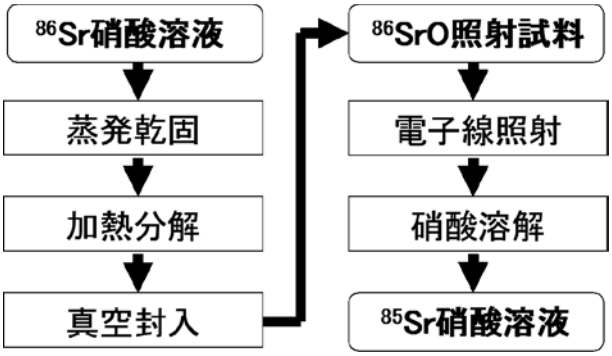

第 2 図　Preparation of SrO and ^{85}Sr solution.

常温にて溶解して ^{85}Sr 硝酸溶液とした。ガラス破片および不純物除去のため、この溶液をろ過して実験に供した。調製した ^{85}Sr(II) 溶液について Ge 半導体検出器により γ 線測定を行い、約 176 kBq の放射能強度を持つ 0.17M Sr(II) 溶液を得た。

§3. 溶液化学実験

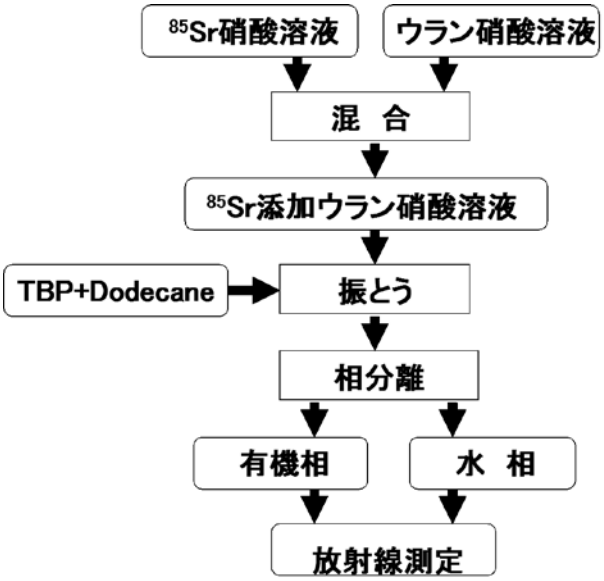

第 3 図　Flowchart of solution chemistry experiment.

Fig. 3 には、本実習で行ったウランの溶液化学実験の手順を示した。§ **2**§ 2 の加速器による RI 製造実習にて調製した ^{85}Sr 硝酸溶液をウラン硝酸溶液と混合し、^{85}Sr 添加ウラン硝酸溶液を調製した。また、予め 1M 硝酸と予備平衡にある 30 vol% TBP ドデカン溶媒 3 ml と Sr 溶液 3 ml とをガラス管に量り取り、振とうにより混合した。再び有機相および水相に分離後、それぞれから 0.1 および 2 ml ずつ量り取り、α 線測定および γ 測定に供した。

γ 線測定は、Canbella 製 Ge 半導体検出器を用いて行った。Fig. 3 には、800 秒間測定したときの γ 線スペクトルを示す。500 keV 付近に ^{85}Sr の 514 keV に相当するピークが見られる。これより高エネルギー側に見られる小さいピークは、天然ストロンチウムに含まれる ^{84}Sr の $(n, 2n)$ 反応により生成した ^{83}Sr の娘核種 ^{83}Rb からの γ 線と思われる。

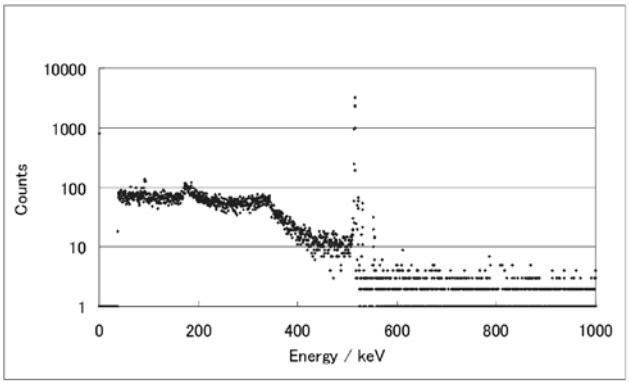

第 4 図　γ ray spectrum of ^{85}Sr doped uranium solution.

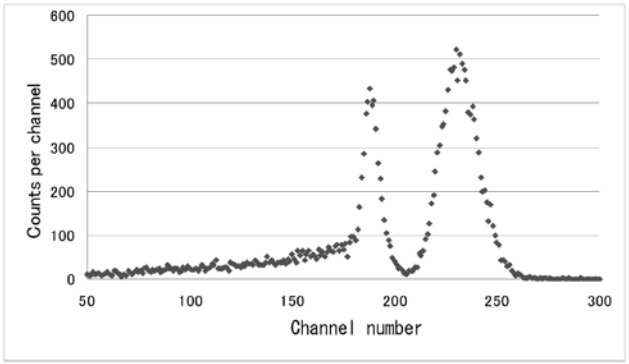

第 5 図　Alpha-spectrum of U_3O_8 doped by ^{85}Sr.

次に、有機相および水相から 0.1 ml 分取した溶液に液体シンチレーション発光剤 1 ml を添加し、よく混合した後、Si 半導体検出器を用いて α 線測定を行った。Fig. 3 には 1000 秒間測定したときの α スペクトルを示す。横軸のチャンネル数は蛍光の消滅時間に、縦軸はそれぞれの時間に検出した数に対応している。この図を見ると、2 つのピークが観測された。低チャンネル側のピークは ^{235}U, ^{238}U および ^{85}Sr からの β, γ 線に、高チャンネル側のピークは ^{235}U および ^{238}U からの α 線に対応している。2 つのピークは重なっておらず、α 線のピークからウランの計測値が得られる。

有機相および水相において得られた計数値をそれぞれ $(\mathrm{cps})_{\mathrm{org.}}$、$(\mathrm{cps})_{\mathrm{aq.}}$ とすると、次式のようにして、分配係数を求めることができた。

$$D_{\mathrm{M}} = \frac{[\mathrm{M}]_{\mathrm{org.}}}{[\mathrm{M}]_{\mathrm{aq.}}} = \frac{(\mathrm{cps})_{\mathrm{org.}}}{(\mathrm{cps})_{\mathrm{aq.}}}, (\mathrm{M} = \mathrm{U(VI)}, \mathrm{Sr(II)}) \tag{1}$$

このように、Sr 添加ウラン試料を用いることにより、α 線および γ 線スペクトロメトリーを利用してウランおよび Sr の定量分析が可能であり、反応前後における物質収支から分配係数を求め、抽出・分離挙動を調べることができた。

§4. 固体化学実験

ここでは、ウラン酸化物 U_3O_8 の酸溶解と ADU の加熱による U_3O_8 回収実験と、U_3O_8 の高温水素還元による UO_2 生成実験とを行った。Fig. 4 には実習の手順を示した。まず、U_3O_8 を 1M 硝酸に溶解する。この際、異なる酸濃度を用いたり、加熱したりして、溶解挙動を調べた。次に、12 %アンモニア水を添加

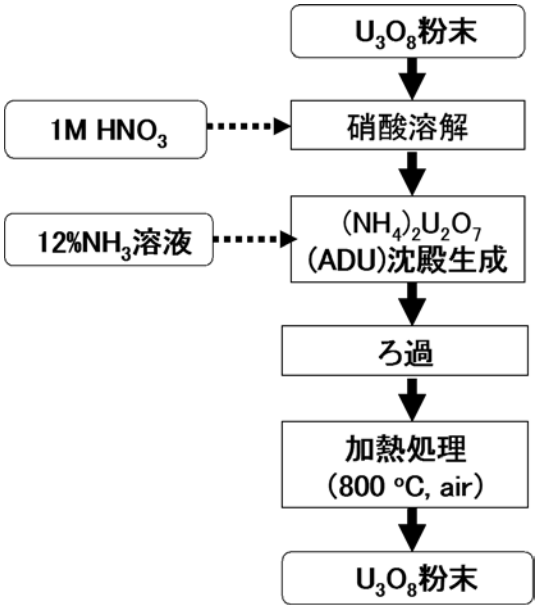

第 6 図　Flowchart for U_3O_8 dissolution.

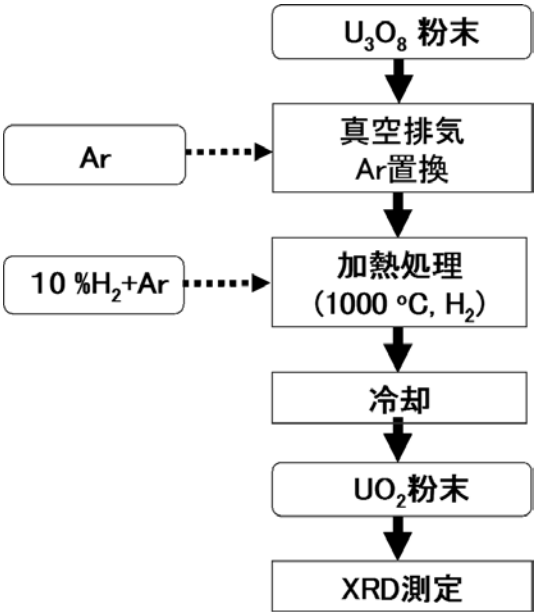

第 7 図　Flowchart for H_2 reduction.

し、重ウラン酸アンモニウム（ADU）沈殿を生成した。ADU を減圧ろ過により分離後、ADU のろ紙をアルミナ坩堝にいれ、空気中 800° にて加熱処理することにより、U_3O_8 として回収した。回収した U_3O_8 試料について XRD 測定により相の同定を行った。さらに、重量変化より回収率を求めたところ、90〜95 %の回収率が得られた。

次に、水素還元実験の手順を Fig. 4 に示す。U3O8 粉末を石英ボートに載せて秤量後、石英反応管にセットした。この反応管内を真空排気し、Ar 置換した。この操作を 2 回繰り返した後、Ar+10%ガスに置換した。室温から 1000° まで 10°/分で加熱後、1 時間反応させ、炉冷した。黒色の U_3O_8 試料が暗茶色の UO_2 に変化したことを確認し、UO_2 試料の XRD 測定を行い、UO_2 相を同定した。XRD 測定により得られた U_3O_8 試料および還元反応後の試料の回折パターンを Fig. 4(a), (b) に示す。還元反応後の回折パターン (b) は既存の UO_2 のパターン (●) とピークが一致しており、U_3O_8(a) を水素還元することにより UO_2 を生成することが分る。UO_2 が面心立方構造であることから、得られたピークの面指数を利用して格子定数を求め、XRD 測定による結晶構造の解析について理解した。

§5．プレゼンテーション

溶液化学および固体化学実習終了後、得られた結果についてま、A〜D 班がそれぞれ 1) 硝酸溶解実験、2) 水素還元実験、3) 溶媒抽出実験、4) 放射線測定実験についてまとめ、プレゼンテーションを行った。20 分の発表と 10 分の質疑応答を行い、理解度、構成力、実験結果、質疑応答および英語表現の観点から評価した。

§6．結　　言

以上、東北大学および慶熙大学にて開発した人材育成プログラム「原子燃料サイクルにおけるウランの溶液および固体化学の実験的理解」について、東北大電子光学研究センターにおける放射性核種製造と加速器見学および多元物質科学研究所におけるウランの固体および溶液化学実験を中心に、実習内容、結果を含め

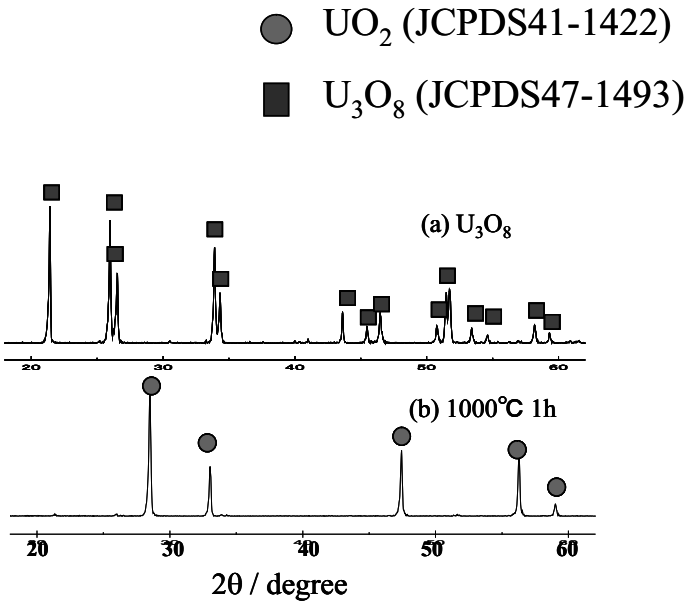

第 8 図　XRD patterns for U_3O_8(a) and reduction product(b)

て紹介した。韓国原子力工学科においては核燃料サイクル関する講義はあるものの、同分野における化学実験はほとんどない。本プログラムによる効果は以下のようにまとめられる。

1) 原子力工学科の学部生が、放射線に関する事前教育を受け、放射線作業従事者としての資格を取得したこと。

2) 加速器を用いた RI 製造を通して核化学の理解を深めたこと。

3) RI 使用施設において RI 実験を行うことにより、RI 実験技術を習得したこと。

4) ウラン酸化物の酸化・還元実験を通して、放射性固体の取扱技術を習得し、固体化学への理解を深めたこと。

5) ウランおよび 85Sr を含む溶液化学実験を通して、放射性液体の取扱技術を習得し、溶液化学への理解を深めたこと。

6) α 線および γ 線測定実験と通じて、放射線の種類に対応した測定技術を習得したこと。

7) 実習およびプレゼンテーションにより英語でのコミュニケーション能力が向上したこと。

このように本プログラムにより学生の核燃料サイクル分野における知識、実験技術を飛躍的に向上させ、理解力、実践力を有する学生を育成することができ、大きな人材育成効果をもたらしたものといえる。

Ⅲ. List of Publication

List of Publication (論文リスト) (2008.1∼2009.12)

Papers Published in Refereed Journals

Electron-capture decay rate of ^{7}Be@C_{60} by first-principles calculations based on density functional theory.

T. Morisato, K. Ohno, T. Ohtsuki, K. Hirose, M. Slater, Y. Kawazoe

Phys. Rev. **B 78** (2008) 125416(1–7).

Proton elastic scattering from tin isotopes at 295-MeV and systematic change of neutron density distributions.

S. Terashima, H. Sakaguchi, H. Takeda, T. Ishikawa, M. Itoh, T. Kawabata, T. Murakami, M. Uchida, Y. Yasuda, M. Yosoi, J. Zenihiro, H. P. Yoshida, T. Noro, T. Ishida, S. Asaji, and T. Yonemura

Phys. Rev. **C 77** (2008) 024317(1–10).

Wolfenstein parameters for $s_{1/2}$ proton knockout $(p, 2p)$ reactions.

T. Noro, M. Kawabata, G. C. Hillhouse, S. Akimune, H. Akiyoshi, I. Daito, K. Hatanaka, M. Itoh, Y. Maeda, N. Matsuoka, S. Morinobu, M. Nakamura, A. Okihana, H. Sagara, H. Sakaguchi, K. Takahisa, H. Takeda, A. Tamii, K. Tamura, H. Toyokawa, H. Yamazaki, H. P. Yoshida, and M. Yosoi

Phys. Rev. **C 77** (2008) 044604.

Effects of nuclear orientation on the mass distribution of fission fragments in the reaction of ^{36}S+^{238}U.

K. Nishio, H. Ikezoe,S. Mitsuoka, I. Nishinaka, Y. Nagame, Y. Watanabe, T. Ohtsuki, K. Hirose, S. Hofmann

Phys. Rev. **C 77** (2008) 064607(1–5).

Photoproduction of $\Lambda(1405)$ and $\Sigma^0(1385)$ on the proton at E_γ=1.5-2.4 GeV.

M. Niiyama, H. Fujimura, D. S. Ahn, J. K. Ahn, S. Ajimura, H. C. Bhang, T. H. Chang, W. C. Chang, J. Y. Chen, S. Date, S. Fukui, H. Funahashi, K. Hicks, K. Horie, T. Hotta, K. Imai, T. Ishikawa, Y. Kato, K. Kino, H. Kohri, S. Makino, T. Matsumura, T. Mibe, K. Miwa, M. Miyabe, N. Muramatsu, M. Nakamura, T. Nakano, Y. Nakatsugawa, Y. Ohashi, D. S. Oshuev, J. D. Parker, N. Saito, T. Sawada, Y. Sugaya, M. Sumihama, J. L. Tang, M. Uchida, C. W. Wang, T. Yorita, and M. Yosoi

Phys. Rev. **C 78** (2008) 035202(1–10).

Photoproduction of neutral kaons on the liquid deuterium target in the threshold region.

K. Tsukada, T. Takahashi, T. Watanabe, Y. Fujii, K. Futatsukawa, O. Hashimoto, K. Hirose, K. Ito, S. Kameoka, Hiroki Kanda, K. Maeda, A. Matsumura, Y. Miura, H. Miyase, S. N. Nakamura, H. Nomura, K. Nonaka, T. Osaka, Y. Okayasu, H. Tamura, H. Tsubota, M. Ukai, H. Yamauchi, M. Wakamatsu, T. Ishikawa, T. Kinoshita, F. Miyahara, T. Nakabayashi, H. Shimizu,

T. Tamae, H. Yamazaki, A. Sasaki, O. Konno, P. Bydžovský, and M. Sotona

Phys. Rev. **C 78** (2008) 014001(1–10).

Status and overview of production targetnfor BigRIPS separator at RIKEN.

A. Yoshida, T. Suda, T. Ohtsuki, H. Yuki, T. Kubo

Nucl. Instr. Meth. Phys. Res. **A 590** (2008) 204–212.

Development of new μ-e decay counter in new multi-channel μSR spectrometer for intense pulsed muon beam

D. Tomono, Y. Hirayama, M. Iio, K. Ishida, M. Iwasaki, H. Outa, H. Ohnishi, T. Matsuzaki, Y. Matsuda, H. Yamazaki, J. Kasagi, R. Klein, and S.N. Nakamura

Nucl. Instr. Meth. Phys. Res. **A 600** (2008) 44–46.

Taper angle dependence of the focusing effect of high energy heavy ion beams by glass capillaries

T. Nebiki, D. Sekiba, H. Yonemura, M. Wilde, S. Ogura, H. Yamashita, M.Matsumoto, K. Fukutani, T. Okano, J. Kasagi, Y. Iwamura, T. Itoh, S. Kuribayashi, H. Matsuzaki and T. Narusawa

Nucl. Instr. Meth. Phys. Res. **B 266** (2008) 1324–1327.

Development of micro-beam NRA for 3D-mapping of hydrogen distribution in solids: Application of tapered glass capillary to 6 MeV 15N ion

D. Sekiba, H. Yonemura, T. Nebiki, M. Wilde, S. Ogura, H. Yamashita, M. Matsumoto, J. Kasagi, Y. Iwamura, T. Itoh, H. Matsuzaki, T. Narusawa and K. Fukutani

Nucl. Instr. Meth. Phys. Res. **B 266** (2008) 4027–4036

Study of activation cross-sections of proton induced reactions on erbium for practical applications.

F. Tarkanyi, S. Takacs, A. Hermanne, F. Ditroi, B. Kiraly, M. Baba, T. Ohtsuki, S.F. Kovalev, A.V. Ignatyuk

Nucl. Instr. Meth. Phys. Res.**B 266** (2008) 4872–4876.

Ultra-sensitive detection of p-process nuclide ^{146}Sm produced by (γ,n), (,p, pn), (n, $2n$) reactions

N. Kinoshita, T. Hashimoto, T. Nakanishi, A. Yokoyama, H. Amakawa, T. Mitsugashira, T. Ohtsuki, N. Takahashi, I. Ahmad, J.P. Greene, D.J. Henderson, C.L. Jiang, M. Notani, R.C. Pardo, N. Partel, E.K. Rehm, R. Scott, R. Vondrasek, L. Jisonna, P. Collon, D. Robertson, C. Schmitt, X.D. Tang, Y. Kashiv, H. Nassar and M. Paul

J. Phys. G **35** (2008) 014033(1–7).

Comment on ‘ The screening effect of D-D fusion in Sm in sub-low energy region (¡= 20 keV) ’

T.S. Wang, Z. Yang, H. Yonemura, A. Nakagawa, H.Y. Lv, J.Y. Chen, S.J. Liu and J. Kasagi

J. Phys. G **35** (2008) 068001.

Tracer diffusion of Cu in CVD β-SiC.

A. Suino, Y. Yamazaki, H. Nitta, K. Miura, H. Seto, R. Kanno, Y. Iijima, H. Sato, S. Takeda, E. Toya, T. Ohtsuki

J. Phys. Chem. Solids **69** (2008) 311–314.

Linear electron accelerator for radioanalytical studies at Tohoku University.

Y. Oura, T. Ohtsuki, K. Hirose, M. Ebihara

J. Radioanal. Nucl. Chem. **278** (2008) 723–726.

Study of double pion photoproduction on the deuteron.

K. Hirose, M. Ejima, T. Fujibayashi, Y. Fujii, K. Futatsukawa, O. Hashimoto, T. Ishikawa, S. Kameoka, H. Kanda, F. Kato, S. Kinoshita, T. Kinoshita, T. Kon, O. Konno, K. Maeda, A. Matsumura, Y. Miura, F. Miyahara, H. Miyase, T. Nakabayashi, S. N. Nakamura, H. Nomura, K. Nonaka, A. Ohtani, Y. Okayasu, M. Oyamada, A. Sasaki, H. Shimizu, T. Takahashi, 3, T. Tamae, H. Tamura, T. Terasawa, H. Tsubota, K. Tsukada, D. Uchida, M. Ukai, M. Wakamatsu, T. Watanabe, H. Yamauchi, H. Yamazaki, and K. Yawata

Phys. Lett. **B 674** (2009) 17.

Near-threshold photoproduction of $\Lambda(1520)$ from protons and deuterons.

N. Muramatsu, J. Y. Chen, W. C. Chang, D. S. Ahn, J. K. Ahn, H. Akimune, Y. Asano, S. Dat´e, H. Ejiri, H. Fujimura, M. Fujiwara, S. Fukui, S. Hasegawa, K. Hicks, K. Horie, T. Hotta, K. Imai, T. Ishikawa, T. Iwata, Y. Kato, H. Kawai, K. Kino, H. Kohri, N. Kuma-gai, S. Makino, T. Matsuda, T. Matsumura, N. Matsuoka, T. Mibe, M. Miyabe, M. Miy-achi, T. Nakano, M. Niiyama, M. Nomachi, Y. Ohashi, H. Ohkuma, T. Ooba, D. S. Oshuev, C. Rangacharyulu, A. Sakaguchi, P. M. Shagin, Y. Shiino, H. Shimizu, Y. Sugaya, M. Sum-ihama, Y. Toi, H. Toyokawa, A. Wakai, C. W. Wang, S. C. Wang, K. Yonehara, T. Yorita, M. Yoshimura, M. Yosoi, and R. G. T. Zegers

Phys. Rev. Lett. **103** (2009) 012001.

Evidence for the Θ^+ in the $\gamma d \to K^+K^-pn$ reaction by detecting K^+K^- pairs.

T. Nakano, N. Muramatsu, D. S. Ahn, J. K. Ahn, H. Akimune, Y. Asano, W. C. Chang, S. Date, H. Ejiri, H. Fujimura, M. Fujiwara, S. Fukui, H. Hasegawa, K. Hicks, K. Horie, T. Hotta, K. Imai, T. Ishikawa, T. Iwata, Y. Kato, H. Kawai, Z. Y. Kim, K. Kino, H. Kohri, N. Kumagai, S. Makino, T. Matsuda, N. Matsuoka, T. Matsumura, T. Mibe, M. Miyabe, Y. Miyachi, M. Niiyama, M. Nomachi, Y. Ohashi, H. Ohkuma, T. Ooba, D. S. Oshuev, C. Rangacharyulu, A. Sakaguchi, P. M. Shagin, Y. Shiino, A. Shimizu, H. Shimizu, Y. Sugaya, M. Sumihama, Y. Toi, H. oyokawa, A. Wakai, C. W. Wang, S. C. Wang, K. Yonehara, T. Yorita, M. Yoshimura, M. Yosoi, and R. G. T. Zegers

Phys. Rev. **C 79** (2009) 025210(1–15).

Half-life estimation of the first excited state of ^{229}Th by using α-particle spectrometry

H. Kikunaga, Y. Kasamatsu, H. Haba, T. Mitsugashira, M. Hara, K.Takamiya, T. Ohtsuki, A. Yokoyama, T. Nakanishi, and A. Shinohara

Phys. Rev. **C 80** (2009) 034315(1–4).

Comparison of the ^{12}C$(e, e'p)$ cross section at low momentum transfer with a relativistic calculation

T. Tamae, Y. Sato, T. Yokokawa, Y. Asano, M. Kawabata, O. Konno, I. Nakagawa, I. Nishikawa, K. Hirota, H. Yamazaki, R. Kimura, H. Miyase, and H. Tsubota, C. Giusti and A. Meucci

Phys. Rev. **C 80** (2009) 064601.

Temperature dependence of YAlO3(Ce) scintillation response for alpha-ray excitation

Y. Toriyabe, E. Yoshida and J. Kasagi

Nucl. Instr. Meth. Phys. Res. **A 611** (2009) 69–75.

Excitation functions for production of medically relevant radioisotopes in deuteron irradiations of Pr and Tm targets.

A. Hermanne, F. Tarkanyi, S. Takacs, F. Ditroi, M. Baba, T. Ohtsuki, I. Spahn, A.V. Ignatyuk

Nucl. Instr. Meth. Phys. Res. **B 267** (2009) 727–736.

Investigation of production of the therapeutic radioisotope 165Er by proton induced reactions on erbium in comparison with other production routes.

F. Tarkanyi, S. Takacs, A. Hermanne, F. Ditroi, B. Kiraly, M. Baba, T. Ohtsuki, S.F. Kovalev, A.V. Ignatyuk

Appl. Radiat. Isot. **67** (2009) 243–247.

Development of a rapid source preparation method for high-resolution α-particle spectrometry.

H. Kikunaga, Y. Kasamatsu, K. Takamiya,T. Ohtsuki, H. Yuki, A. Yokoyama, T. Nakanishi, T. Mitsugashira

Appl. Radiat. Isot. **67** (2009) 539–543.

Papers Published in International Conference Proceedings

Double pion photoproduction experiment at LNS-Tohoku.

H. Kanda, N. Chiga, Y. Fujii, K. Futatsukawa, Y. C. Han, O. Hashimoto, K. Hirose, K. Hosomi, A. Iguchi, T. Ishikawa, M. Kaneta, M. Kawai, D. Kawama, T. Kawasaki, S. Kiyokawa, T. Koike, O. Konno, Y. Ma, K. Maeda, A. Matsumura, M. Mimori, K. Miwa, F. Miyahara, S. N. Nakamura, Y. Okayasu, T. Otani, A. Sasaki, H. Shimizu, K. Shirotori, K. Suzuki, T. Takahashi, T. Tamae, H. Tamura, N. Terada, K. Tsukada, M. Ukai, T. Wang, T. Watanabe, and H. Yamazaki (NKS and NKS2 Collaborations). Mod. Phys. Lett. **A 23** (2008) 2313

Development of THz Light Source Using Pre-bunched FEL.

M. Yasuda, H. Hama, F. Hinode, K. Kasamsook, M. Kawai, A. Kurihara, K. Nanbu, Y.Shibasaki, and S.Takahashi

Proc. of the 30th International Free Electron Laser Conference, FEL2008, Geyongju, Korea (2008)

Space Charge Effect for Short Electron Bunches in an Alpha Magnet.

H. Hama, F. Hinode, K. Kasamsook, M. Kawai, K. Nanbu, M. Yasuda

Proc. of the 30th International Free Electron Laser Conference, FEL2008, Geyongju, Korea (2008)

Orientation effects of deformed ^{238}U target nuclei on the fusion probability for heavy element synthesis

K. Nishio, S. Hofmann, F.P. Hessberger, H. Ikeoze, D. Ackermann, S. Antalic, V.F. Comas, Z. Gan, S. Heinz, J.A.Heredia, J. Khuyagbaatar, B. Kindler, I. Kojouharov, P. Kuusiniemi, B. Lommel, R. Mann, M. Mazzocco, S. Mitsuoka, Y. Nagame, T. Ohtsuki, A.G. Popeko, S.Saro, H.J. Schoett, B. Sulignano, A. Svirikhin, K. Tsukada, K. Tsuruta, A.V. Yeremin

Proc. of the 23rd International Nuclear Physics Conference, Nuc. Phys., **A805** (2008) 516-518

EM calorimeter complex FOREST for the π^0 and η photo-production experiments at LNS-Sendai.

K. Suzuki, H. Fujimura, R. Hashimoto, T. Ishikawa, J. Kasagi, S. Kuwasaki, K. Mochizuki, K. Nawa, Y. Okada, Y. Onodera, M. Sato, H. Shimizu, H. Yamazaki, A. Kawano, Y. Sakamoto, and K. Maeda

Mod. Phys. Lett. **A 24** (2009) 978.

η photo-production on the deuteron at LNS, Tohoku University.

T. Ishikawa

Proceedings of Sendai International Symposium On Strangeness In Nuclear And Hadronic Systems (SENDAI 08) (2009) 101.

Development of 4π electro-magnetic calorimeter complex FOREST for neutral meson photo-production experiments.

K. Suzuki, H. Fujimura, H. Fukasawa, R. Hashimoto, T. Ishikawa, J. Kasagi, S. Kuwasaki, K. Mochizuki, K. Nawa, Y. Okada, Y. Onodera, M. Sato, H. Shimizu, H. Yamazaki, A. Kawano, Y. Sakamoto, and K. Maeda

Proceedings of Sendai International Symposium On Strangeness In Nuclear And Hadronic Systems (SENDAI 08) (2009) 410.

Construction of a cryogenic H2/D2 target fitted to 4 π EM calorimeter FOREST.

R. Hashimoto, H. Fujimura, T. Ishikawa, J. Kasagi, S. Kuwasaki, Y. Okada, M. Sato, K. Suzuki, H. Yamazaki, H. Shimizu, P. Kanda, and K. Maeda

Proceedings of Sendai International Symposium On Strangeness In Nuclear And Hadronic Systems (SENDAI 08) (2009) 390.

Neutral kaon photoproduction at LNS, Tohoku University.

M. Kaneta, N. Chiga, B. Beckford, M. Ejima, T. Fujii, Y. Fujii, T. Fujibayashi, T. Gogami, K. Futatsukawa, O. Hashimoto, K. Hosomi, K. Hirose, A. Iguchi, S. Kameoka, H. Kanda, H. Kato, D. Kawama, T. Kawasaki, C. Kimura, S. Kiyokawa, T. Koike, T. Kon, Y. Ma, K. Maeda, N. Maruyama, A. Matsumura, Y. Miyagi, Y. Miura, K. Miwa, S. N. Nakamura, H. Nomura, A. Okuyama, A. Ohtani, T. Otani, M. Sato, A. Shichijo, K. Shirotori, T. Takahashi, H. Tamura, N. Taniya, H. Tsubota, K. Tsukada, N. Terada, M. Ukai, D. Uchida, T. Watanabe, T. Yamamoto, H. Yamauchi, K. Yokota, T. Ishikawa, T. Kinoshita, H. Miyahara, T. Nakabayashi, H. Shimizu, K. Suzuki, T. Tamae, T. Terasawa, H. Yamazaki, Y. C. Han, T. S. Wang, A. Sasaki, O. Konno, P. Bydžovský, and M. Sotona (NKS and NKS2 Collaborations)

Proceedings of Sendai International Symposium On Strangeness In Nuclear And Hadronic Systems (SENDAI 08) (2009) 63.

A Far-infrared Undulator for Coherent Synchrotron Radiation and Free Electron Laser at Tohoku University.

H. Hama, F. Hinode, M. Kawai, K. Nanbu, F. Miyahara, M. Yasuda

Proc. of SRI2009, Australia, Oct, (2009) pp523–526

Development of Accelerator-Based THz Sources at Tohoku University.

H. Hama, M. Kawai, F. Hinode, K. Nanbu, F. Miyahara, M. Yasuda

Proc. of PAC09, WE5RFP052, Canada, May, (2009) 2386.

Ionic Debye screening in dense liquid plasmas observed for the Li+p,d reactions in liquid Li target

J. Kasagi, H. Yonemura, Y. Toriyabe, A. Nakagawa, T. Sugawara and T. Wang

Proceedings of the 3rd China-Japan-Korea Symposium on Hadron and Nuclear Physics HNP08, Nuclear Physics Review 26 Suppl. (2009) 44–48.

Electronic and ionic screening for low energy nuclear reactions in condensed matter

J. Kasagi and H. Yonemura

Proceedings of International Conference on Heavy Ion Fusion Reaction FUSION08, AIP Conference Proceedings 1098 (2009) 161–168.

π^0 Photoproduction on Deuteron for Photon Energies from 0.6 to 1.15 GeV

F. Miyahara, H. Fukasawa, R. Hashimoto, T. Ishikawa, T. Iwata, H. Kanda, J. Kasagi, H. Kato, T. Kinoshita, K. Maeda, M. Matsuzawa, T. Michigami, K. Motiduki, K. Murakami, T. Nakabayashi, K. Nawa, T. Nomura, K. Okamura, H. Okamura, H. Okuyama, Y. Onodera, Y. Saito, T. Sasaki, H. Shimizu, T. Shishido, S. Suzuki, K. Suzuki, Y. Tajima, S. Takita, H. Ueno, H. Y. Yoshida, S. Yamaguchi, H. Yamazaki

Nucl. Phys. Rev. 26 (2009) 104-108.

Effects of nuclear orientation on fission mass distributions in the reactions of ^{34,36}S+^{238}U.

K. Nishio, S. Hofmann, F.P. Hessberger, H. Ikeoze, D. Ackermann, S. Antalic, V.F. Comas, Z. Gan, S. Heinz, J.A.Heredia, J. Khuyagbaatar, B. Kindler, I. Kojouharov, P. Kuusiniemi, B. Lommel, R. Mann, M. Mazzocco, S. Mitsuoka, Y. Nagame, T. Ohtsuki, A.G. Popeko, S.Saro, H.J. Schoett, B. Sulignano, A. Svirikhin, K. Tsukada, K. Tsuruta, A.V. Yeremin

International Conference on Heavy Ion Collisions Near the Coulomb Barrier., AIP Conference Proceedings **1098** (2009) 289–294.

Effects of Nuclear Orientation on Fusion and Fission Process in Heavy Ion Reactions.

K. Nishio, H. Ikezoe, S. Mitsuoka, I. Nishinaka, Y. Watanabe, Y. Nagame, T. Ohtsuki, K. Hirose, S. Hofmann

Proceedings of the 6th Japan-Italy Symposium on Heavy-Ion Physics., AIP Conference Proceedings **1120** (2009) 275–279.

Effects of nuclear orientation on fission fragment mass distributions for the reactions using actinide target nuclei.

K. Nishio, H. Ikezoe, S. Mitsuoka, I. Nishinaka, Y. Watanabe, Y. Nagame, T. Ohtsuki, K. Hirose, S. Hofmann

Fission2009 “4th Inthernational Workshop on Nuclear Fission and Fission-Product Spectroscopy”, AIP Conference Proceedings **1175** (2009) 111–118.

学位論文 (核理研所属)

博士論文「Design and test of low emittance electron beam for Smith-Purcell backward wave oscillator free electron laser」

Kittipong Kasamsook，平成 20 年，東北大学

修士論文「数値シミュレーションによる超短パルス電子ビームを用いる自由電子レーザーの研究」

安田真冬，平成 20 年，東北大学

修士論文「荷電粒子識別用スパイラルシンチレータホドスコープの開発」

佐藤 衛，平成 20 年 ，東北大学

博士論文「H, D(γ, π^0) 反応を用いた W=1.4〜1.7 GeV 領域の核子共鳴状態の研究」

宮原房史, 平成 21 年, 東北大学

博士論文「超音波キャビテーションを伴う液体金属中での低エネルギー原子核反応の研究」

鳥谷部祐，平成 21 年，東北大学

修士論文「高速 GeV 光子ビームプロファイルモニターの開発」

大串 尚永， 平成 21 年，東北大学

修士論文「前方電磁カロリメータによる γ 線位置の測定」

菅井 裕之，平成 21 年，東北大学

学位論文 (他機関所属)

修士論文「中性 K 中間子スペクトロメータ (NKS2) 用 Vertex Drift Chamber の設計および性能評価」

清川 省吾，平成 20 年，東北大学

修士論文「中性 K 中間子スペクトロメータ中心部検出器の開発と性能評価」

奥山 皓，平成 21 年，東北大学

修士論文「エネルギー領域 670 920MeV 光子ビームによる重陽子からのダブルパイ中間子生成反応の研究」

木村 千草，平成 21 年，東北大学

修士論文「陽子標的を用いた光中間子生成反応による NKS2 システムの性能評価」

藤井 隆穂，平成 21 年，東北大学

Ⅳ. Approved Experiments

平成20年度前期採択課題一覧

課題番号	課　　題　　名	申込責任者	採択シフト数
原子核関連分野			
2621	J-PARC Beamline MWPC および MWDC のテスト	高橋 俊行	6
2622	SPring-8 LEPS 実験用の e^+e^- veto counter の性能評価	河合 秀幸	1
2623	バリオン共鳴 N*(1670) の研究 (1)	清水 肇	68
2624	CsI シンチレータの応答性の測定	石川 貴嗣	8
2625	次期全立体角電磁カロリメータのための大型 BGO 単結晶のエネルギー応答性の測定	清水 肇	7
2626	国際宇宙ステーション搭載用電子、ガンマ線観測装置 (CALET) の基礎開発	鳥居 祥二	4
放射化学関連分野			
2627	宇宙化学的試料および環境試料の光量子放射化分析	大浦 泰嗣	3
2628	半減期変化の系統的研究	大槻 勤	1
2629	選択硫化を用いる使用済燃料の再処理法の研究	佐藤 修彰	1
2630	固体抽出剤を用いた希土類元素とアクチノイド元素の分離に関する研究	鈴木 達也	1
2631	Sm-146 の製造と半減期測定および ^{147}Sm$(\gamma, n)^{146}$Sm 反応の断面積測定	中西 孝	1
2632	放射化分析法による通信用材料中の不純物評価	鹿野 弘二	1
随時申込			
2633	NKS2 バーテックス・チェンバーのテスト	橋本 治	10
2634	J-PARC ハイパー核 γ 線実験のための π^0 同定カウンターおよびビームラインチェレンコフカウンターの性能評価実験	三輪 浩司	3
2635	NKS2 の改良に伴う回路・データ収集系の整備	神田 浩樹	3

平成20年度後期採択課題一覧

課題番号	課　　題　　名	申込責任者	採択シフト数
原子核関連分野			
2636	PWO 及び CsI を用いた γ カウンターのプロトタイプテスト	鈴木 史郎	3
2637	中性ビームラインの γ 線、中性子測定用カロリメータの性能評価	田島 靖久	2
2638	Study of Neutral Kaon Photoproduction on Deuterium Target by NKS2	橋本 治	80
2639	BM5 ラジエータ自動運転のためのデーターベース作成	藤村 寿子	3
2640	バリオン共鳴 N*(1670) の研究 (2)	清水 肇	100
2641	SPring-8 LEPS 実験用 e^+e^- veto counter の性能評価	河合 秀幸	1
放射化学関連分野			
2642	放射化分析法による通信用材料中の不純物評価	鹿野 弘二	1
2643	宇宙化学的試料および環境試料の光量子放射化分析	大浦 泰嗣	2
2644	Sm-146 の製造と半減期測定および ^{147}Sm(γ, n)^{146}Sm 反応の断面積測定	中西 孝	1
2645	固体抽出剤を用いた希土類元素とアクチノイド元素の分離に関する研究	鈴木 達也	1
2646	半減期変化の系統的研究	大槻 勤	2
2647	選択硫化を用いる使用済燃料の再処理法の研究	佐藤 修彰	2
2648	超臨界水利用の MOX 燃料製造と核分裂生成物分離に関する研究	山村 朝雄	1
随時申込			
2649	中性ビームラインのハロー中性子測定用検出器の性能評価	南條 創	1
2650	物理学実験 3 向け γ 線および電子線照射実験	前田 和茂	1
2651	光量子放射化分析法による磁性球粒試料中の微量ニッケルの定量	関本 俊	2
2652	KOTO 実験荷電粒子検出器の性能評価	南條 創	5
2653	J-PARC ハイパー核 γ 線実験のためのビームラインチェレンコフカウンターの性能評価実験	三輪 浩司	2
2654	アルミナ蛍光板によるガンマ線ビームスポットの確認	石川 貴嗣	1

平成21年度前期採択課題一覧

課題番号	課　　題　　名	申込責任者	採択シフト数
原子核関連分野			
2655	バリオン共鳴 N*(1670) の研究（3）	清水 肇	40
2656	アルミナ蛍光板によるガンマ線ビームスポットの確認 II	石川 貴嗣	2
2657	J-PARC E16 実験用 GEM トラッカーのテスト実験	小沢 恭一郎	4
2658	NKS2 バーッテクス・チェンバーのテスト	金田 雅司	10
2659	Study of Neutral Kaon Photoproduction on Deuterium Target by NKS2	金田 雅司	0
2660	$550 < E_\gamma < 920$ MeV 領域における重水素原子核標的での 2π 光生成反応の研究	神田 浩樹	36
2661	J-PARC ハイパー核 γ 線実験のためのビームラインチェレンコフカウンターおよびビームベトカウンターの性能評価実験	三輪 浩司	5
2662	FPGA モジュールを用いた Beam Profile Monitor の開発	藤村 寿子	5
2663	KOTO 実験荷電粒子、光子検出器の性能評価	南條 創	3
2664	KOTO 実験ビームラインサーベイ用 K_L 及びハロー中性子検出器の性能評価	南條 創	5
2676	NKS2 実験のための CDC と STB BM4 Tagger のスタディ	神田 浩樹	2
2677	J-PARC K1.8 ビームラインカウンター、 E15 実験用ガラスチェレンコフカウンターの性能評価	藤岡 宏之	3
2678	偏極陽子標的用ポリエチレン試料に対する低エネルギー電子線照射による不対電子生成の研究	岩田 高広	1
放射化学関連分野			
2665	宇宙化学的試料および環境試料の光量子放射化分析	大浦 泰嗣	3
2666	光量子放射化分析法による磁性球粒試料中の微量ニッケルの定量	関本 俊	2
2667	半減期変化の系統的研究	大槻 勤	3
2668	放射化分析法による通信用材料中の不純物評価	鹿野 弘二	1
2669	固体抽出剤を用いた希土類元素とアクチノイド元素の分離に関する研究	鈴木 達也	1
2670	選択硫化を用いる使用済燃料の再処理法の研究	佐藤 修彰	2
2671	Cr, Y, Tb ターゲットにおける光核反応による生成核種の収率測定	柴田 誠一	0
2672	超臨界水利用の MOX 燃料製造と核分裂生成物分離に関する研究	山村 朝雄	1
2673	陽電子消滅 γ 線ドップラー拡がり測定装置の較正用線源（Sr-85）製造	木野 康志	1
2674	$^{147}\mathrm{Sm}(\gamma, n)^{146}\mathrm{Sm}$ 反応と $^{231}\mathrm{Pa}(\gamma, f)$ 反応の断面積測定	中西 孝	3
2675	$^{99m}\mathrm{Tc}$ の壊変定数の化学形に対する依存性	高宮 幸一	2

平成21年度後期採択課題一覧

課題番号	課　　題　　名	申込責任者	採択シフト数
原子核関連分野			
2690	液体アルゴン検出器の電磁シャワー検出能力の評価	丸山 和純	10
2691	STB 820 MeV 運転における BM4 ガンマビームのスタディ	神田 浩樹	4
2693	J-PARC E14 KOTO 実験の CsI カロリメータの性能評価	山中 卓	10
2694	バリオン共鳴 N*(1670) の研究（4）	清水 肇	50
2695	フォスウィッチ型 BGO クリスタル検出器の開発	石川 貴嗣	2
2696	KOTO 実験用荷電粒子検出器の性能評価	南條 創	2
2697	J-PARC E16 実験用 GEM トラッカーのテスト実験	小沢 恭一郎	5
2698	ミューオン電子転換過程探索におけるカロリメーターの開発	佐藤 朗	5
放射化学関連分野			
2679	^{99m}Tc の壊変定数の化学形に対する依存性	高宮 幸一	1
2680	フィション・トラック法による ^{231}Pa の光核分裂反応断面積の測定	中西 孝	2
2681	放射化分析法による通信用材料中の不純物評価	鹿野 弘二	1
2682	固体抽出剤を用いた希土類元素とアクチノイド元素の分離に関する研究	鈴木 達也	1
2683	宇宙化学的試料および環境試料の光量子放射化分析	大浦 泰嗣	3
2684	韓国原子力分野学生実験プログラム－核燃料サイクルにおける加速器利用と RI 製造	佐藤 修彰	1
2685	選択硫化を用いる使用済燃料の再処理法の研究	桐島 陽	2
2686	光量子放射化分析法による磁性球粒試料中の微量ニッケルの定量	関本 俊	2
2687	半減期変化の系統的研究	大槻 勤	2
2688	超臨界水利用の MOX 燃料製造と核分裂生成物分離に関する研究	山村 朝雄	1
2689	偏極陽子標的用ポリエチレン資料に対する低エネルギー電子線照射による液体窒素温度での不対電子生成の研究	岩田 高広	1
2692	陽電子消滅 γ 線ドップラー拡がり測定装置の較正用線源（Sr-85）製造	木野 康志	1
随時申込			
2699	高レートビームトラッキング用シリコン検出器のテスト	谷田 聖	3

核理研研究報告　第42&43巻

2011年３月発行

発行所　東北大学電子光理学研究センター
仙台市太白区三神峯1-2-1（郵便番号982－0826）
電話　022－743－3400

印刷所　株式会社　東北プリント
仙台市青葉区立町24番24号
TEL　022（263）1166㈹

RESEARCH REPORT OF
LABORATORY OF NUCLEAR SCIENCE
TOHOKU UNIVERSITY

Volume 42&43 March 2011

Research Center for Electron Photon Science, Tohoku University
1-2-1, Mikamine, Taihaku, Sendai 982-0826, Japan

東北大学電子光理学研究センター